Title
Design and Characterization of Catalysts for the Production of Transportation Fuels from Low Molecular Weight Alkenes

Author
Hanna, David

Publication Date
2014

Peer reviewed|Thesis/dissertation

Design and Characterization of Catalysts for the Production of Transportation Fuels from Low Molecular Weight Alkenes

by

David Galil Hanna

A dissertation submitted in partial satisfaction of the

requirements for the degree of

Doctor of Philosophy

in

Chemical Engineering

in the

Graduate Division

of the

University of California, Berkeley

Committee in charge:

Professor Alexis T. Bell, Chair
Professor Roya Maboudian
Professor T. Don Tilley

Spring 2014

Design and Characterization of Catalysts for the Production of Transportation Fuels from Low Molecular Weight Alkenes

by

David Galil Hanna

Abstract

Design and Characterization of Catalysts for the Production of Transportation Fuels from Low Molecular Weight Alkenes

by

David Galil Hanna

Doctor of Philosophy in Chemical Engineering

University of California, Berkeley

Professor Alexis T. Bell, Chair

Low molecular weight alkenes comprise a significant fraction of the effluent from fluid catalytic cracking units and of the C_2-C_5 hydrocarbons produced from Fischer Tropsch synthesis. Yet these products are too volatile to be blended into transportation fuel. Therefore, the aim of this research was to investigate pathways by which light alkenes could be converted to molecules with favorable gasoline or diesel characteristics. This research is relevant because such pathways would allow for the production of fuels from non-petroleum feedstocks such as biomass, coal, and natural gas.

Previous work has identified butanol and 2-ethylhexanol as suitable blending components or replacements for gasoline and diesel, respectively. These molecules can be synthesized via propene hydroformylation to yield butanal which can then be hydrogenated to butanol or can undergo self-condensation followed by hydrogenation to form 2-ethylhexanol. Although many of these reactions are catalyzed effectively by homogeneous catalysts, our research has focused on the development, characterization, and kinetics of heterogeneous, industrially implantable catalysts for these reactions.

Hydroformylation processes are commonly plagued by the separation of the organic products from the homogeneous Rh complexes. Supported Ionic Liquid Phase (SILP) catalysts that immobilize a Rh complex on a support can address this concern; however, little was known about the effects of catalyst preparation on the activity and stability of such catalyst. Our studies have shown that the activity and stability are strongly influenced by the ligand-to-rhodium ratio and the surface density of silanol groups on the silica support. In situ spectroscopic studies suggest that $HRh(CO)_2SX$ (SX, sulphoxantphos) complexes are bound to the support by interactions of the sulfonate groups of SX with silanol groups from the silica support. The function of the ionic liquid is to prevent the formation of catalytically inactive $[Rh(CO)(\mu\text{-}CO)SX]_2$ or $HRh(SX)_2$ species by enhancing the dispersion of the active monomers. The realization that the support interaction was necessary to maintain high dispersion led to the development of ionic liquid-free hydroformylation catalysts ($X\text{-}Rh/SiO_2$, X = xantphos). Reaction kinetics for hydroformylation were investigated and found to be dependent on reaction conditions.

To achieve the tandem hydroformylation-hydrogenation of propene to butanol in a single reactor, a heterogeneous catalyst is needed for the selective hydrogenation of aldehydes in the presence of CO and alkene. An organometallic complex, Shvo's catalyst, was dispersed onto SiO_2. This catalyst meets the necessary criteria because it operates through an outer sphere mechanism, thereby permitting the hydrogenation of butanal but not propene. Reaction kinetics of butanal hydrogenation were investigated and then used to predict the butanol yield in a tandem process that converts a mixture of propene and synthesis gas into butanol.

The aldol condensation of *n*-butanal was investigated over a solid-base organocatalyst and Ti-SBA-15 catalysts. The bifunctional nature of these catalysts is necessary to promote several of the elementary steps of the reaction mechanism. The catalyst was made by grafting site-isolated amines on tailored silica surfaces to allow for a co-operative interaction between basic amine and the weakly acidic silanols. Secondary amine functionalized silica was found to be nearly five times more active than primary amines, whereas grafted tertiary amines exhibited negligible catalytic activity. For secondary amines grafted on silica, it was found that the surface silanol groups serve as adsorption sites for the aldehydes and as a Brønsted acids to activate the carbonyl group of the aldehyde to form enamines. The bifunctional nature of this catalyst was confirmed by experimental evidence and theoretical calculations which demonstrate the need for spatial separation of the weakly acidic silanol and the basic amine groups in order to achieve high catalytic activity.

To understand how the coordination and connectivity of Ti affect the kinetics of aldol condensation, catalysts were made by either incorporation or impregnation of Ti precursors into or onto the SBA surface. Irrespective of the catalyst synthesis procedure, site isolated tetrahedral Ti sites were found to be more active than catalysts containing hexacoordinated Ti oligomers. Furthermore, it was observed that isolated tetrahedral titanols were more active than tetrahedral dimers. Theoretical calculations demonstrated that Ti dimers are less active due to steric constraints.

To my loving God,

and my beautiful fiancé Michelle

Table of Contents

List of Figures v

List of Tables x

List of Schemes xi

Acknowledgements xii

Chapter 1: Introduction 1

Chapter 2: Factors Influencing the Activity, Selectivity, and Stability of Rh-Based Supported Ionic Liquid Phase (SILP) Catalysts for Hydroformylation of Propene 5

Abstract 5

2.1 Introduction 5

2.2 Methods 6

2.2.1 Catalyst Preparation 6

2.2.2 Gas-phase Hydroformylation of Propene 7

2.2.3 Catalyst Characterization 8

2.3 Results and Discussion 8

2.3.1 Choice of Ligand and Ionic Liquid 8

2.3.2 Effect of Silica Pretreatment 9

2.3.3 Effect of Ligand and Ionic Liquid Concentration 9

2.3.4 Characterization of SILP Catalysts 12

2.3.5 Effects of Catalyst Formulation on Catalytic Activity and Selectivity 15

2.4 Conclusions 18

2.5 Acknowledgements 18

2.6 Supporting Information 19

2.7 References 21

Chapter 3: The Kinetics of Gas-Phase Propene Hydroformylation over a Supported Ionic Liquid Phase (SILP) Rhodium Catalyst 23

Abstract 23

3.1 Introduction 23

3.2 Methods 24

3.2.1 Catalyst Preparation 24

3.2.2 Gas-phase Hydroformylation of Propene 25

3.3 Results 25

3.3.1 Catalytic Activity of SX-Rh/SiO_2 SILP Catalysts 25

3.3.2 Kinetics of Propene Hydroformylation 28

3.4 Discussion 30

3.4.1 Rate Expressions for Butanal Synthesis 30

3.4.2 Regioselectivity....32
3.4.3 Entropic Effects on the RDS....33
3.5 Conclusions....34
3.6 Acknowledgements....34
3.7 Supporting Information....35
3.7.1 Derivation of Rate Expressions....36
3.8 References....37

Chapter 4: In situ Formation of Wilkinson-Type Hydroformylation Catalysts: Insights into the Structure, Stability and Kinetics of Triphenyl Phosphine- and Xantphos-Modified Rh/SiO_2....39
Abstract....39
4.1 Introduction....39
4.2 Methods....40
4.2.1 Catalyst Preparation....40
4.2.2 Gas-phase Hydroformylation of Propene....41
4.2.3 Catalyst Characterization....41
4.3 Results....42
4.3.1 Effect of Ligand Composition....42
4.3.2 Effect of L/Rh Molar Ratio....43
4.3.3 Effect of Rh Loading....45
4.3.4 Kinetics of Propene Hydroformylation using L-Rh/SiO_2 Catalysts....45
4.3.5 In Situ FT-IR Spectroscopy of Phosphine-modified Rh/SiO_2 Catalysts....49
4.3.6 ^{31}P MAS NMR Spectroscopy of Phosphine-modified Rh/SiO_2 Catalysts....50
4.3.7 HR-TEM Measurements....53
4.4 Discussion....54
4.5 Conclusions....59
4.6 Acknowledgements....59
4.7 Supporting Information....60
4.8 References....63

Chapter 5: Hydrogenation of Butanal over Silica-Supported Shvo's Catalyst and Its Use for the Gas-Phase Conversion of Propene to Butanol via Tandem Hydroformylation and Hydrogenation....65
Abstract....65
5.1 Introduction....65
5.2 Methods....66
5.2.1 Catalyst Preparation....67
5.2.2 Gas-phase Hydroformylation of Propene....67
5.2.3 Catalyst Characterization....68
5.3 Results and Discussion....68
5.3.1 Catalyst Stability and Kinetics of Butanal Hydrogenation....68
5.3.2 Proposed Mechanism of Butanal Hydrogenation....70

5.3.3 Kinetics of Butanal Hydrogenation 73
5.3.4 Butene hydrogenation over Shvo/SiO_2 75
5.3.5 Tandem hydroformylation and hydrogenation using Rh-SILP and Shvo/SiO2 catalysts 75
5.4 Conclusions 78
5.5 Acknowledgements 78
5.6 Supporting Information 79
5.6.1 Derivation of Rate Expressions 79
5.7 References 82

Chapter 6: Tailoring the Co-operative Acid-Base Effects in Silica Supported Amine Catalysts: Applications in the Continuous Gas-Phase Self Condensation of *n*-butanal 84
Abstract 84
6.1 Introduction 84
6.2 Methods 85
6.2.1 Catalyst Preparation 85
6.2.2 Gas-phase Self-condensation of *n*-butanal 86
6.2.3 Catalyst Characterization 86
6.3 Results and Discussion 87
6.4 Conclusions 99
6.5 Acknowledgements 100
6.6 Supporting Information 100
6.6.1 Catalyst Preparation 100
6.6.2 Theoretical Methods Section 100
6.6.3 Derivation of Rate Expressions 101
6.7 References 110

Chapter 7: An Experimental and Theoretical Study of n-butanal Self-Condensation over Ti Species Supported on Silica 112
Abstract 112
7.1 Introduction 112
7.2 Methods 113
7.2.1 Catalyst Preparation 113
7.2.2 Gas-phase Self-condensation of *n*-butanal 114
7.2.3 Catalyst Characterization 114
7.2.4 Theoretical Calculations 115
7.3 Results and Discussion 116
7.3.1 Catalyst Characterization 116
7.3.2 Catalytic Activity of *x*-Ti–SBA-15 and *x*-Ti/SBA-15 Catalysts 119
7.3.3 Catalytic Mechanism for Aldol Condensation 122
7.3.4 Theoretical Modeling of Tetrahedral Titanol and Ti Dimer Sites 123
7.4 Conclusions 127
7.5 Acknowledgements 128

7.6 Supporting Information.....129
7.7 References.....131

List of Figures

Figure 1.1 Distribution of hydrocarbons produced from Fisher Tropsch Synthesis over Co/SiO_2 catalysts 1

Figure 2.1 Effects of silica pretreatment temperature and silica passivation on the activity and stability of SILP catalysts..... 10

Figure 2.2 Effects of SX/Rh ratio on the activity and stability of SILP catalysts 11

Figure 2.3 Effect of α on the activity and stability of SILP catalysts 11

Figure 2.4 Effects of the manner of catalyst preparation on the activity and selectivity of SILP catalyst 12

Figure 2.5 Solid-state ^{29}Si MAS NMR spectra of SiO_2 pretreated at different temperatures..... 13

Figure 2.6 In situ FT-IR spectra of SILP catalysts showing the formation of monomeric and dimeric complexes (after 30 min in synthesis gas)..... 14

Figure 2.7 Solid-state ^{31}P MAS NMR spectra of SILP catalysts (SX/Rh=10) under different silica pretreatment conditions 15

Figure S2.1 Time on stream studies of SILP catalysts (a) with IL and (b) without IL..... 19

Figure S2.2 TEM images of SiO_2-373 K Rh-SX SILP catalyst, (a) before and (b) after reaction 20

Figure S2.3 Elemental mapping analysis of a SILP catalyst (SiO_2@373 K, α = 0.1, SX/Rh =10) showing the homogeneous dispersion of metal complex and ionic liquid on the silica support surfaces..... 20

Figure 3.1 Time on stream study with SX-Rh/SiO_2 SILP catalysts..... 26

Figure 3.2 Effect of temperature on rate of butanal synthesis and regioselectivity... 27

Figure 3.3 Arrhenius plot showing the apparent activation energies of *n*- and isobutanal formation 27

Figure 3.4 Log-log plot of the effect of reactant partial pressures on the rates of *n*- and isobutanal synthesis 29

Figure 3.5 Rate of *n*- and isobutanal synthesis vs. partial pressure of CO, C_3H_6, and H_2..... 33

Figure S3.1 Differential thermogravimetric analysis of [bmim][$OctSO_4$]/SiO_2, SX/SiO_2, fresh SX-Rh/SiO_2 SILP catalyst. 37

Figure 4.1 The effect of PPh_3/Rh and X/Rh ratios on the rates of butanal synthesis 44

Figure 4.2 The effect of rhodium loading on the rates of butanal synthesis with PPh_3 ligand and Xantphos ligand 47

Figure 4.3 Effect of temperature on rate of *n*-butanal synthesis and regioselectivity over PPh_3-Rh/SiO_2 and X-Rh/SiO_2 catalysts 48

Figure 4.4 In situ FT-IR of PPh_3-Rh/SiO_2 and X-Rh/SiO_2 catalysts in presence of CO and syngas showing the formation of homogeneous catalysts 51

Figure 4.5 Solid-state ^{31}P MAS NMR spectra of PPh_3-modified Rh/SiO_2 (PPh_3/Rh =15) and X- modified Rh/SiO_2 (X/Rh = 15) spent catalyst with 0.05 wt. %, 0.2 wt. % 0.5 wt. %, and 1 wt. %. Rh weight loadings 52

Figure 4.6 High resolution-transmission electron micrographs (HR-TEM) and high angle annular dark field-scanning tunneling electron microscopy (HAADF-STEM) of 1%Rh/SiO_2 and 0.2%Rh/SiO_2 samples 53

Figure S4.1 Comparison of activity between a PPh_3-Rh/SiO_2, X-Rh/SiO_2, and SILP catalysts 60

Figure S4.2 Differential Thermo Gravimetric (DTG) plots of Rh/SiO_2, PPh_3/SiO_2, and PPh_3-Rh/SiO_2 samples 60

Figure S4.3 Solid-state ^{31}P MAS NMR spectra of PPh_3-modified SiO_2 sample (PPh_3/SiO_2), PPh_3-modified Rh/SiO_2 sample (PPh_3-Rh/SiO_2) sample, and Wilkinson catalyst supported SiO_2 sample ($HRh(CO)(PPh_3)_3$/SiO_2) sample 61

Figure S4.4 Formation of *gem*-dicarbonyl rhodium species on a 0.2 wt. % and 1 wt. % Rh/SiO_2 sample 61

Figure S4.5 Correlation of $Rh^I(CO)_2$ formation with depletion of hydroxyl groups for Rh/SiO_2 sample 62

Figure S4.6 Comparison on the rates of butanal synthesis over PPh_3-Rh/SiO_2 and $HRh(CO)(PPh_3)_3$/SiO_2 catalyst under identical reaction conditions 62

Figure 5.1 Time on stream study with Shvo/SiO_2 and SX-Shvo/SiO_2 catalysts 69

Figure 5.2 In situ infrared spectra of Shvo's complex in He at 298 K and Shvo/SiO_2 catalyst under He at 298 K, He at 363 K, H_2 at 363 K, and H_2/CO = 1 at 363 K 72

Figure 5.3 Solid-state ^{31}P MAS NMR spectra of spent SX-Shvo/SiO_2 catalyst..... 73

Figure 5.4 Non-linear regression of partial pressure data using Shvo/SiO_2 and SX-Shvo/SiO_2. Rate of *n*- and isobutanol synthesis vs. partial pressure of butanal, H_2, and CO 74

Figure 5.5 Results from tandem hydroformylation-hydrogenation experiment 76

Figure 5.6 Modeled results of the tandem hydroformylation-hydrogenation experiment..... 77

Figure S5.1 Infrared spectra of SiO_2 exposed to He 80

Figure S5.2 In situ infrared spectra of SX-Shvo/SiO_2 and Shvo/SiO_2 exposed to a 1:1 ratio of H_2 and CO 80

Figure S5.3 Solid-state ^{31}P MAS NMR spectra of SX/SiO_2..... 81

Figure S5.4 Parity plot of the predicted values determined from non-linear regression vs. the experimental data 81

Figure 6.1 The effect of amine composition on the rate of 2-ethylhexenal synthesis over silica-supported amine catalysts..... 88

Figure 6.2 In situ FT-IR spectra of *n*-butanal adsorbed at 343 K on silica-supported amine catalysts: (a) SiO_2-NR_2, (b) SiO_2-NHR, and (c) SiO_2-NH_2..... 89

Figure 6.3 The effect of secondary amine loading on the rate of 2-ethylhexenal synthesis..... 90

Figure 6.4 The effect of the pore size of mesoporous silica-supported secondary amine catalysts on the rate of 2-ethylhexenal synthesis 92

Figure 6.5 The effect of silanol density on the rate of 2-ethylhexenal synthesis over silica-supported silica secondary amine catalysts..... 92

Figure 6.6 Effect of pretreatment temperature on the solid-state ^{13}C CP MAS NMR spectrum of silica-supported secondary amine catalysts: (a) SiO_2-423 K; (b) SiO_2-823 K; and (c) SiO_2-973 K..... 93

Figure 6.7 Effect of linker length on the catalytic activity of silica-supported secondary amine catalysts and comparison with their silylated analogs 94

Figure 6.8 Model active site for the SiO_2-C_3-NHR catalyst 94

Figure 6.9 Enthalpy (343 K) diagram for aldol condensation of *n*-butanal over a SiO_2-C_3-NHR catalyst..... 98

Figure 6.10 Free energy (343 K) diagram for aldol condensation of *n*-butanal over a SiO2-C3-NHR catalyst 99

Figure S6.1 A plot of *L'* vs. *L* is shown below and qualitatively matches the experimental data. 103

Figure S6.2 Solid-state ^{13}C CP MAS NMR spectra of silica supported amine catalysts..... 104

Figure S6.3 Partial pressure dependency of *n*-butanal using SiO_2-NH_2, SiO_2-NHR and SiO_2-NR_2 on the rate of 2-ethylhexenal synthesis 105

Figure S6.4 Solid-state UV-Vis spectra of spent SiO_2-NH_2 catalyst showing the formation of stable imines 106

Figure S6.5 Comparison in catalytic activity of secondary amine supported on amorphous silica, pretreated at 423 K and 823 K, and a mesoporous SBA-15 support.....106

Figure S6.6 Catalytic activity results of secondary amine supported silica catalyst in the absence and presence of co-feeding 2% water 107

Figure S6.7 Enthalpy (343 K) diagram for aldol condensation of n-butanal over a SiO_2-C_3-NHR catalyst..... 108

Figure S6.8 Free energy (343 K) diagram for aldol condensation of *n*-butanal over a SiO_2-C_3-NHR catalyst..... 109

Figure 7.1 XANES spectra of TS1, 0.07-Ti–SBA-15, 0.3-Ti–SBA-15, 0.7-Ti–SBA-15, and TiO_2 anatase 116

Figure 7.2 UV-Vis spectra of 0.02-Ti–SBA-15, 0.07-Ti–SBA-15, 0.3-Ti–SBA-15, 0.7-Ti–SBA-15, and TiO_2 anatase 118

Figure 7.3 Raman spectra of SBA-15, 0.02-Ti–SBA-15, 0.07-Ti–SBA-15, 0.3-Ti–SBA-15, 0.7-Ti–SBA-15, andTiO_2 anatase..... 119

Figure 7.4 Time on stream study over 0.02-Ti–SBA-15 catalyst 121

Figure 7.5 Effect of the Ti site density on the activity of *x*-Ti–SBA-15 catalysts for aldol condensation 121

Figure 7.6 Free-energy (353 K) diagram for aldol condensation over an isolated titanol 125

Figure 7.7 Enthalpy (353 K) diagram for aldol condensation over an isolated titanol 126

Figure 7.8 Energy decomposition analysis of enolate formation over isolated titanol monomer and dimer species 127

Figure S7.1 XRD of x-Ti—SBA-15 catalysts obtained with a Siemens D5000 diffractometer using Cu Kα radiation 129

Figure S7.2 TGA of *n*-butanal soaked 0.07 and 0.7-Ti—SBA-15 catalysts obtained with a TA Instruments TGA 5000 instrument 129

Figure S7.3 UV-Vis Spectra of 0.07-Ti-Cp/SBA-15, 0.3-Ti-Cp/SBA-15, 0.07-Ti-Pr/SBA-15 catalysts 130

Figure S7.4 Raman Spectra of 0.07-Ti-Pr/SiO_2-373K and 0.07-Ti-Pr/SiO_2-1023K catalysts 130

List of Tables

Table 2.1 Results from the hydroformylation of propene using various SILP catalysts 8

Table 2.2 Results from the hydroformylation of propene using different ionic liquids containing Rh-SX SILP catalysts 9

Table S2.1 Textural properties of pretreated silica supports and SILP catalysts. 19

Table 3.1 Activity of different sized particles of SX-Rh/SiO_2 SILP catalyst 26

Table 3.2 Nonlinear regression results for Eq. 2 and Eq. 3 32

Table 4.1 Results from the hydroformylation of propene using various phosphine-modified Rh/SiO_2 catalysts 43

Table 4.2 Comparison in activation energies for the formation of n- and isobutanal over different phosphine-containing rhodium catalysts 46

Table 4.3 Reaction order of propene, CO and H_2 over phosphine-modified Rh/SiO_2 catalysts 46

Table 5.1 Apparent activation energies (kJ mol^{-1}) for the formation of *n*- and isobutanol using Shvo/SiO_2 or SX-Shvo/SiO_2 69

Table 5.2 Apparent reaction orders of *n*-butanol and isobutanol synthesis using Shvo/SiO_2 and SX-Shvo/SiO_2 catalysts 70

Table 5.3 Values of the rate parameters obtained by a best fit to experimental data. 75

Table 7.1 Chemical and physical properties of different *x*-Ti—SBA-15 catalysts.. 117

Table 7.2 Activity (TOF), apparent activation energy (kJ mol^{-1}), and partial pressure dependencies of Ti silica catalysts 120

Table 7.3 Lewis acid and base properties of the isolated titanol monomer and the Ti dimer 126

List of Schemes

Scheme 1.1 Reaction pathway to upgrade low molecular weight alkenes through (1) hydroformyation, (2) hydrogenation, and (3) aldol condensation 1

Scheme 2.1 Bidentate phosphine ligand and ionic liquid used in the hydroformylation of propene 6

Scheme 2.2 Possible interaction of sulfoxantphos ligand and [bmim][$OctSO_4$] ionic liquid on silica support..... 16

Scheme 3.1 Proposed mechanism for the hydroformylation of propene 30

Scheme 4.1 Proposed mechanism for the formation of homogenous catalysts on phosphine-modified Rh/SiO_2 supports. 54

Scheme 4.2 Equilibrium of rhodium catalysts containing PPh_3 and carbonyl ligands 55

Scheme 4.3 Proposed stabilization effect of $HRh(CO)_n(PPh_3)_{4-n}$ catalysts on Rh/SiO_2 supports..... 56

Scheme 4.4 Proposed mechanism for the hydroformylation of propene PPh_3-Rh/SiO_2 57

Scheme 5.1 Proposed mechanism for aldehyde hydrogenation using $Shvo/SiO_2$ catalyst 71

Scheme 6.1 Proposed mechanism for aldol self-condensation of *n*-butanal over silica supported secondary amine catalysts..... 95

Scheme S6.1 Proposed aldol reaction mechanism using tertiary amine supported silica catalysts 109

Scheme 7.1 Cluster model of the tetrahedral isolated titanol and the Ti dimer 115

Scheme 7.2 Mechanism of aldol condensation over an isolated titanol..... 124

Acknowledgements

I moved to Berkeley five years ago as an ambitious and accomplished student eager to learn about science. This dissertation is the achievement of that goal; however, I learned more important things from my PhD than the science of catalysis. In a couple weeks, I will graduate from Berkeley as an adult permanently humbled by the many extraordinary people who have taught me so much about life.

I must acknowledge God first and foremost for blessing me with the opportunity to study at the University of California, Berkeley. I thank Him for supporting me through the numerous intellectual, physical, and emotional trials I have endured. I also thank Him for sending his angels to minister unto me many valuable life lessons.

The first angel I would like to thank is my advisor Professor Alexis T. Bell. Although I have rarely referred to my boss as an angel over the past five years, it is now very obvious how much he has supported me since I joined the group. I remember dreading my weekly meetings with him because I was so intimidated that I could barely speak. I remember feeling so dumb and inadequate that I thought there would be no way to survive five years of these meeting. However, no matter how unintelligible I sounded, Prof. Bell was patient with me and was always supportive of my project. He even selected me to attend a conference in Heidelberg, Germany to present on his behalf after my first of graduate school. He also encouraged me to present at our BP funding review meetings several times within my first two years of joining the group. More importantly, Prof. Bell enhanced my problem solving skills by teaching me how to ask the relevant questions and how to think logically for solutions. I am indebted to him for teaching me these valuable skills which I apply not only to science, but also to other aspects of life.

The second angel I have to thank is Dr. Sankaranarayanapillia Shylesh (Shylesh for short). I was privileged to work on this project with Shylesh for the past five years; he joined the Bell group as a post-doctoral researcher just two months after I joined the group. I believe that without him, I would have likely dropped out of graduate school. The breadth of knowledge and experience that Shylesh provided at the beginning of my graduate school career allowed me not only survive, but to thrive. He taught me all about experimental design, catalyst synthesis, and how to think creatively – whether it be a synthesis technique or a scientific argument. He also taught me precious life lessons like how to remain calm, be content, and to respect other people. Over the past five years, I have never observed Shylesh upset or angry. No matter the circumstances, he is always at peace and expresses happiness. He always respected me as fellow researcher even though he was much older, wiser, and more experienced than me. Rather than belittle me, Shylesh valued our conversation and my ideas, and was a good friend. I am very grateful to him.

I must also acknowledge the contributions of several other members of the Bell lab. Prof. Fuat Celik, Dr. Bean Getosian, Dr. Anton Mlinar, and Dr. Sebastian Werner taught me the basics about catalysis research. I thank them for being reliable guides and friends, whom I could turn to during difficult times. Their profound knowledge and curiosity inspire me to continue learning. I will always remember the good times we shared discussing science, religion, politics, and history.

The next host of angels that I would like to thank belong to the Cal Copts group at Berkeley and Coptic Orthodox community of the San Francisco Bay Area. I must thank Fr. Bishoy Ray and Dr. Angel Ray for their love and for continuing to believe in me despite

my many obvious shortcomings. Their constant support taught me the value of service. I must also recognize Vally Kondos, Sarah Ghabrial, Magi Gabra, Amanda Sadra, Bola Malek, Michel "Archie-Basha" Mikhael, Monica Mikhail, and Benjamin Shenouda for making Berkeley such an amazing place. I will always remember how much fun I had distracting them from their late night studying. I thank those who were involved in the St. Moses the Strong (SMS) Fellowship and The Sojourners – namely, Clara Matta, Paul Kist, Evram Dawd, and Charoo Youssef. I thank all of them for their friendship and for showing me that God can unite seemingly incompatible people to accomplish His will.

I must also recognize my best friend, Abraham Ghattas, who will be graduating from medical school in less than one month! I thank him for maintaining our friendship even though we were thousands of miles apart, especially for dealing with my poor communications skills. Through thick and thin, he has showed me the value of friendship through his dedication and commitment to our relationship. I am very blessed to have such an angel in my life. I must also thank the rest of my friends for their support and love – namely, Jimmy Rizkalla, Ramez Ayoub, George Rizk, Mena Soliman, Mina "Hedo" Wanis, and Mina Tawfik. Special appreciation goes out to Simon Soliman for being a great, but messy roommate. I am blessed that God allowed us to share many great memories together.

Last, but certainly, not least, I must thank my angelic family. I am indebted to my mother, Cecile Hanna, for her continual prayers for my success. I believe that the numerous miracles in my life were the result of her prayers. I am grateful for my father, Galil Hanna, for always believing in me and giving me confidence to face difficult trials. I thank my brother, Ashraf Hanna, for being my role model and inspiring me to be the best. I thank my beautiful nieces, Cecilia and Grace Hanna, and my nephew, Luke Hanna, for their unwavering love. They have been an enormous source of joy, and have shown me that nothing in this world is more important than family.

I hope to practice these values and lessons with my wife-to-be Dr. Michelle Farag, who has been my guardian angel for the past seven years. She has been my rock and closest friend, so I cannot thank her enough for the support and love she has provided. I have become a better person by learning from her example. She has taught me to be resilient, hard-working, openhearted, and to never give up on my goals. Her cheerful personality calms my anxiety and gives me courage to endure life's obstacles. I will always remember how her words of encouragement helped me pass my qualification exam as I was on the verge of an emotional breakdown. I appreciate her strength and dedication to our relationship for making our difficult long-distance relationship succeed. I thank her for spending countless hours on the phone, driving hundreds of miles, purchasing costly airline tickets when she had no money, and flying cross country to visit on a regular basis. I believe that these lovable qualities are just few of the reasons Michelle will be an excellent wife. I am thankful, honored, and blessed to become her husband and cannot wait to spend the rest of our lives together.

Chapter 1

1.1 Introduction

New pathways to produce gasoline, diesel, and jet fuel from non-petroleum feedstocks are necessary to meet the increasing demand for clean, transportation fuel. One option is to reform natural gas, coal, and/or biomass to yield CO and H_2 and then carry out Fisher Tropsch synthesis to produce a distribution of hydrocarbons. As shown in Figure 1.1 the resulting C_5-C_{11}, C_{12}-C_{20} hydrocarbons are suitable for the gasoline and diesel; however, a significant fraction of the products (C_1-C_5, C_{21+}) are either too volatile or too heavy to be blended into gasoline and diesel. Waxes (C_{21+}) can be hydrocracked into smaller molecules appropriate for the gasoline/diesel range. Yet the effluent from fluid catalytic cracking units contains a high fraction of low molecular weight olefins that are not usable as liquid fuel. It is also notable that the C_2-C_5 hydrocarbons produced Fischer Tropsch synthesis are alkene rich. Therefore, the aim of the research reported in this thesis was to investigate alternative pathways by which light alkenes could be converted to products suitable for blending into gasoline or diesel.

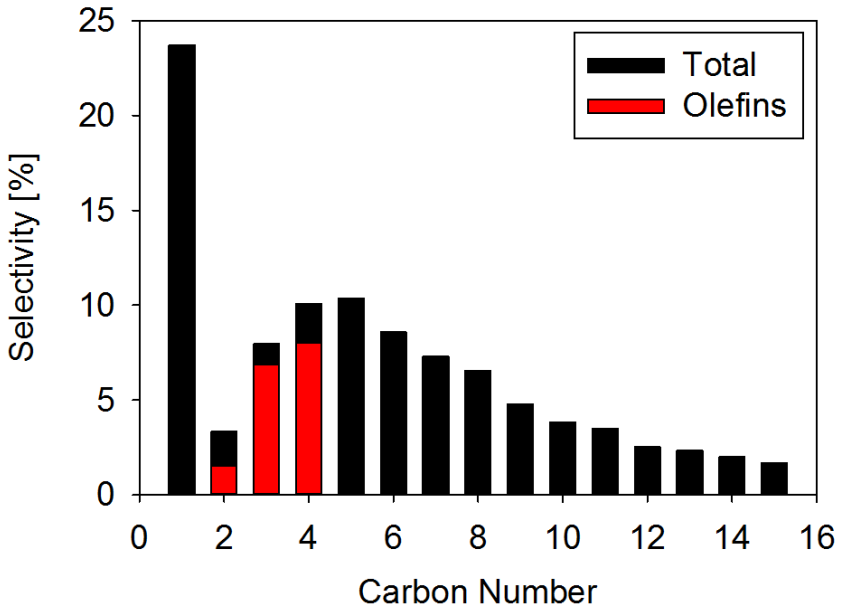

Figure 1.1 Distribution of hydrocarbons produced from Fisher Tropsch Synthesis over Co/SiO_2 catalysts. T = 493 K, P_{Total} = 10 atm, 11% conversion. (courtesy of Gregory Johnson, printed with permission)

A second objective of the present work was to examine pathways for converting ethanol to products suitable for blending into gasoline and diesel. This effort is motivated by the Clean Air Act which mandates that the production of renewable fuel (mostly ethanol) must more than double from the 15 billion gallon mark set in 2012 [1]. Despite the high octane number of ethanol, it is poor fuel because of its corrosivity, high miscibility with water, and low energy density [2]. Furthermore, current infrastructure is unable to tolerate gasoline containing a higher fraction of ethanol. In order to comply

with federal regulations, new pathways to convert ethanol into a gasoline or diesel range molecule must be explored. A viable means to achieve this goal is through multi-step process requiring the dehydration of alcohol to an alkene, (1) the hydroformylation of an alkene to an aldehyde, (2) the hydrogenation of aldehydes to alcohol, or (3) the aldol condensation of aldehydes to form oligomers.

Each step of the sequence shown in Scheme 1.1 was thoroughly investigated and the results are presented in the subsequent chapters of this dissertation. Chapters 2-4 discuss the hydroformylation of propene, Chapter 5 highlights aldehyde hydrogenation and a method by which tandem hydroformylation-hydrogenation can be performed in a reactor, whereas Chapters 6-7 provides insights into the mechanism of aldol condensation. Propene hydroformylation was studied because the products *n*- and isobutanal can be hydrogenated to form the corresponding alcohols, which have high energy density and octane number, and are less miscible with water than ethanol [2].

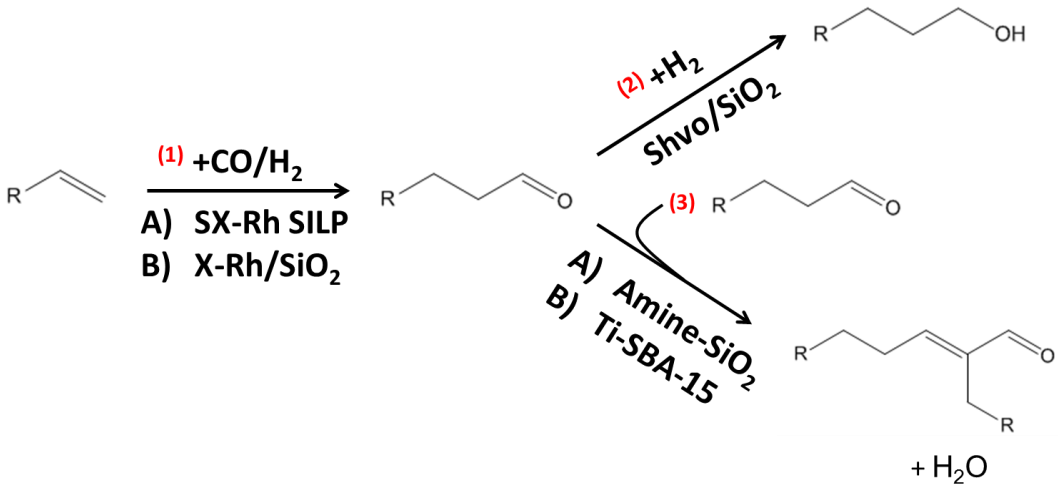

Scheme 1.1 Reaction pathway to upgrade low molecular weight alkenes through (1) hydroformyation, (2) hydrogenation, and (3) aldol condensation.

Strategies for producing heterogeneous hydroformylation catalysts are described in Chapters 2 and 3. Chapter 2 discusses Supported Ionic Liquid Phase (SILP) catalysts. These catalysts consist of a homogeneous Rh complex immobilized on a support material in the presence of ionic liquid. In this manner, a homogeneous catalyst is "heterogenized." However, little was known about the nature of this immobilization and how catalyst preparation could affect the activity and stability. Our experiments have shown that the activity and stability are strongly influenced by the ligand-to-rhodium ratio and the surface density of silanol groups on the silica support. In situ spectroscopic studies suggest that $HRh(CO)_2SX$ (SX, sulphoxantphos) complexes are bound to the support by interactions of the sulfonate groups of SX with silanol groups from the silica support. The function of the ionic liquid is to prevent the formation of catalytically inactive $[Rh(CO)(\mu\text{-}CO)SX]_2$ or $HRh(SX)_2$ species by enhancing the dispersion of the active monomers.

Chapter 3 describes an investigation of the kinetics of hydroformylation over Rh SILP catalysts. This effort was able to rationalize previous discrepancies in the literature concerning measured reaction orders with respect to reactant partial pressures by showing that the rate-determining step is dependent upon reaction temperature. At low temperature, alkyl insertion is the rate-determining but at high temperature, the rate-determining step is the oxidative addition of H_2.

An alternative approach for producing a supported Rh hydroformylation catalyst is described in Chapter 4. Catalysts were prepared by incipient wetness impregnation of a Rh precursor into silica. Following calcination and reduction to form Rh nanoparticles, xantphos was impregnated onto the support. Interestingly, the activity of this catalyst was identical to that of SX-Rh SILP catalysts. Additionally, the similarity between the infrared spectra of both types of catalysts led to the conclusion that a homogenous catalyst was formed in situ under reaction conditions. A mechanism was proposed showing how this transformation occurs in the presence of synthesis gas.

Chapter 5 discusses the hydrogenation of butanal using Shvo's Catalyst dispersed onto SiO_2. Shvo's catalyst is an organometallic complex that reduces aldehydes through an outer sphere mechanism. The kinetics of butanal hydrogenation were investigated and a rate law consistent with the observed partial pressure dependencies was derived. Furthermore, it was shown that Shvo's catalyst could be used in tandem with a hydroformylation catalyst to convert propene to butanol in a single reactor. To the best of our knowledge, this was the first example of teh tandem, gas-phase conversion of an alkene to an alkanal ever reported.

While tandem hydroformylation-hydrogenation can produce molecules in the gasoline range, hydroformylation followed by aldol condensation of the resulting alkanal provides a means for increasing the product molecular weight into the diesel range. This subject is treated in Chapters 6-7. We note that the product of *n*-butanal self-condensation is ethylhexeneal, which can be hydrogenated to produce 2-ethylhexanol, a product that can be blended into diesel [3].

Chapter 6 discusses the synthesis, characterization and performance of bifunctional aldol condensation catalysts, which are inspired by biological systems such as the aldolase enzyme and the amino acids proline and glycine [4]. The catalysts investagated were synthesized by grafting site-isolated amines on tailored silica surfaces to allow for a co-operative interaction between basic amine and the weakly acidic silanol. It was observed that secondary amine functionalized silica is nearly five times more active than grafted primary amines, whereas grafted tertiary amines exhibit negligible catalytic activity. It was found that for secondary amines the surface silanol groups serve as an adsorption site for the aldehydes and as a Brønsted acid to activate the carbonyl group of the aldehyde which leads to a favorable attack of the secondary amines to form enamines. The bifunctional nature of this catalyst was confirmed by experimental evidence and theoretical calculations which demonstrate the need for spatial separation of the weakly acidic silanol and the basic amine groups in order to achieve high catalytic activity.

Metal oxides containing bifunctional moieties and are also effective aldol condensation catalysts. For example, titania anatase contains Lewis acidic Ti^{4+} sites which bind the carbonyl group of the aldehyde and Lewis basic O^{2-} sites which facilitate the α-H abstraction [5]. However, previous studies were unable to precisely identify the

active site [6,7]. Therefore, the purpose of Chapter 7 is to elucidate the effects of coordination and connectivity of Ti on the kinetics of *n*-butanal condensation. Catalysts were synthesized by either incorporation Ti into the framework of SBA-15, a mesoporous silica, or by grafting Ti onto the surface of SBA-15. Irrespective of the catalyst synthesis procedure, site-isolated, tetrahedrally coordinated Ti sites were found to be more active than catalysts containing Ti oligomers. A theoretical analysis was carried out of the reaction energetic for butanal condensation occurring on monomeric and dimeric titania species. This effort reproduced the observed activation energies and helped to explain why the activation energy is significantly higher on the dimer species.

1.2 References

[1] "The Clean Air Act in a Nutshell: How it Works." EPA. http://www.epa.gov/air/caa/pdfs/CAA_Nutshell.pdf (accessed April 28, 2014)

[2] S. Lee, M. O. Cho, C. H. Park, Y. Chung, J. H. Kim, B. Sang, Y. Um. *Energy Fuels* **2008**, 22, 3459-3464.

[3] B. J. Arena, J. S. Holmgren. *Direct Conversion of butyraldehyde to 2-ethylhexanol-1*. US5258558 A, **1992**.

[4] B. Noziere, A. Cordova. *J. Phys. Chem. A* **2008**, 112, 2827-2837.

[5] M. Singh, N. Zhou, D. K. Paul, K. J. Klabunde. *J. Catal.* **2008**, 260, 371-379.

[6] H. Idriss, M. A. Barteau. *Catal. Lett.* **1996**, 40, 147-153.

[7] H. Idriss, K. S. Kim, M. A. Barteau. *J. Catal.* **1993**, 139, 119-133.

Chapter 2

Factors Influencing the Activity, Selectivity, and Stability of Rh-Based Supported Ionic Liquid Phase (SILP) Catalysts for Hydroformylation of Propene

Abtract

An investigation has been carried out on the effects of catalyst preparation on the activity and stability of supported ionic liquid phase (SILP) catalysts for propene hydroformylation. Catalyst activity and stability were found to be strongly influenced by ligand and ionic liquid composition, ligand-to-rhodium ratio, and the surface density of silanol groups on the silica support. Highest activity was achieved using rhodium sulfoxantphos (SX) complexes in the presence of [bmim][$OctSO_4$]. In situ FT-IR and solid-state ^{31}P and ^{29}Si MAS NMR characterization suggest that active Rh centers are not present as homogeneous complexes dissolved in an ionic liquid film, instead are present as $HRh(CO)_2SX$ complexes bound to the support by interactions of the sulfonate groups of SX with silanol groups of the support. The function of the ionic liquid is to inhibit undesired interactions of SX ligands, since such interactions render the phosphine groups unavailable for interaction with the Rh^+ cations. Catalyst deactivation is attributed mainly to the formation of catalytically inactive $[Rh(CO)(\mu\text{-}CO)SX]_2$ or $HRh(SX)_2$ complexes when the SX/Rh ratio is too low or high, respectively.

2.1 Introduction

The hydroformylation of alkenes using homogeneous Rh complexes has received extensive interest because such catalysts can operate under relatively mild conditions (typically 80-393 K, 10-30 atm) [1-3]. For practical application, the products need to be separated from the catalyst, a challenge that continues to be subject of ongoing research. A particularly appealing approach is immobilization of the Rh complex onto a solid support [4-8]. Davis and coworkers have reported the preparation of supported aqueous-phase (SAP) catalysts by forming a thin layer of Rh-tppts (tppts = tri(m-sulfonyl)triphenyl phosphine trisodium salt) dissolved in water onto high-surface-area hydrophilic silica [9,10]. ^{31}P NMR spectra of the catalyst were consistent with the presence of mobile Rh species in the aqueous phase. Liquid-phase hydroformylation of oleyl alcohol and several other high molecular weight alkenes was demonstrated at 373 K. In related studies, Horvath reported that similar SAP catalysts exhibited good activity for hexene, octene, and decene hydroformylation but deactivated via the loss of water [11]. The concept of supported ionic liquid catalysis (SILC) was introduced by Mehnert and coworkers [12,13]. Catalysts were prepared by impregnating a solution of Rh-tppts in [bmim][BF_4] or [bmim][PF_6] into a 1-n-butyl-3-methyl imidazolium modified silica gel support. SILC catalysts were found to be more active for the liquid-phase hydroformylation of 1-hexene than SAP catalysts. However, a loss of Rh was observed at high conversion due to depletion of the supported ionic liquid layer into the reaction medium. Most recently, Wasserscheid and coworkers have reported very stable

supported ionic liquid-phase (SILP) Rh catalysts for the vapor-phase hydroformylation of propene [14,15,16]. In this case, silica dehydrated at 773 K was impregnated with a solution of Rh sulfoxantphos (SX) dissolved in [bmim][OctSO4]. IR and ^{31}P NMR characterization of SILP catalysts suggested that the active form of the catalyst were $Rh(H)(CO)_2SX$ complexes dissolved in a thin layer of the ionic liquid.

The aim of the present study was to investigate the effects of catalyst synthesis on the activity, selectivity, and stability of Rh SILP catalysts for the hydroformylation of propene (Scheme 2.1). Particular attention was given to the effects of (a) ligand composition, (b) ligand/rhodium ratio, (c) ionic liquid composition, (d) ionic liquid loading, and (e) temperature of silica pretreatment. The structure of the catalyst was characterized by in situ FT-IR and by ^{31}P and ^{29}Si MAS NMR. The effects of catalyst formulation on the activity and stability of Rh-based SILP hydroformylation catalysts are interpreted in terms of the observed interactions between the various components and the interaction of each component with silanol groups of the silica support. The results of the present study suggest that the active Rh centers are not present as homogeneous complexes dissolved in ionic liquid, but instead as complexes bound to the support by interactions of the sulfonate groups associated with the sulfoxantphos ligand and the silanol groups of the support. The ionic liquid, rather than serving as a solvent, inhibits the undesired interaction of sulfoxanthos ligands via interactions of the phosphines groups of the ligands with the acidic silanol groups of the support.

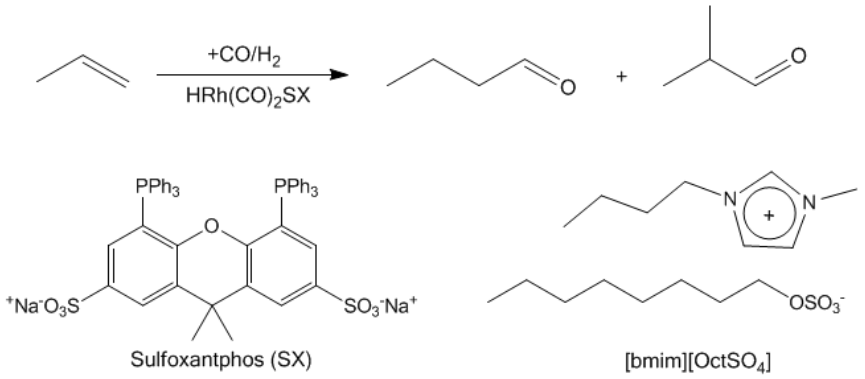

Scheme 2.1 Bidentate phosphine ligand and ionic liquid used in the hydroformylation of propene.

2.2 Methods

2.2.1 Catalyst Preparation

Silica (Silicycle, surface area: 300 $m^2 g^{-1}$, pore volume = 1.15 $cm^3 g^{-1}$) was used as the support. One gram of this material was dried in vacuum at 373 K for 24 h, or at 823 K and 1023 K for 15 h, and then stored in vacuum prior to use. Catalysts were also prepared on silica that had been silylated according to the following procedure. Silylation was performed by dispersing 0.5 g of the silica in 25 mL of dry toluene followed by the addition of 3.75 mmol of methyl trimethoxysilane (Strem) and stirring at 373 K for 12 h under an inert atmosphere. The material was then cooled down to room

temperature, filtered, washed with copious amounts of ethanol, and vacuum dried. The final material is referred to as SiO_2-372 K-Me. SILP catalysts were synthesized according to the procedure described in Ref. 15. The dried silica support or SiO_2-373 K-Me was impregnated with an anhydrous methanolic solution (10 mL, Aldrich) of the ionic liquid [bmim][$OctSO_4$] (0.52 mmol) containing the catalyst precursors $Rh(acac)(CO)_2$ (0.02 mmol, Aldrich) and the bidentate sulfoxantphos [17] ligand (0.19 mmol). A light red colored, free flowing powder was obtained upon removal of methanol by vacuum evaporation followed by drying at 353 K for 12 h.

2.2.2 Gas-phase Hydroformylation of Propene

Gas-phase hydroformylation of propene was performed in a 6.35 mm OD quartz tube with an expanded section (~12.7 mm OD, ~20 mm length). The reactor was packed with quartz wool above and below the catalyst bed to hold the catalyst in place. The feed to the reactor consisted of propene (Praxair, 99.9%), CO (Praxair, 99.99%) and H_2 (Praxair, 99.999%). A reactant ratio of C_3H_6:CO:H_2 of 1:1:1 was used unless specified otherwise. Experiments were carried out at a temperature of 393 K, total gas pressures of 2 atm, total gas flow rate of 120 $cm^3\ min^{-1}$ at STP in order to maintain a constant volumetric flow rate of 60 $cm^3\ min^{-1}$ at pressure. Under these conditions, the conversion of propene was always less than 1%. Reaction products were analyzed using an Agilent 6890N gas chromatograph containing a bonded and crosslinked (5%-phenyl)-methylpolysiloxane capillary column (Agilent, HP-1) connected to a flame ionization detector.

2.2.3 Catalyst Characterization

Infrared spectra were acquired using a Thermo Scientific Nicolet 6700 FT-IR spectrometer equipped with a liquid nitrogen cooled MCT detector. Each spectrum was obtained by averaging 32 scans taken with 1 cm^{-1} resolution. 0.05 g of SILP catalyst was pressed into a 20 mm-diameter pellet (< 1 mm thick) and placed into a custom-built transmission cell equipped with CaF_2 windows, a K-type thermocouple for temperature control, and resistive cartridge heaters. All scans were acquired at 393 K. Experiments at elevated pressure were carried out by throttling a needle valve located downstream from the reactor. The spectrum of the catalyst under He flow was subtracted from all the results reported.

Solid-state ^{31}P MAS NMR and ^{29}Si MAS NMR experiments were performed on a Bruker Avance I-500 MHz spectrometer. ^{31}P MAS NMR spectra were obtained at 202.5 MHz, using 90° pulses of 4.2 μs duration, a recyle delay of 60 s relative to 85% H_3PO_4, and a spinning rate of 10 kHz at room temperature. Samples were sealed into zirconia rotors under nitrogen atmosphere to avoid the possible oxidation of phosphorous in SX ligand. ^{29}Si MAS NMR were acquired at 80 MHz, using 90° pulses of 8.1 μs duration, a recycle delay of 360 s relative to TMS, and a spinning rate of 10 kHz. The resolution obtained in the ^{29}Si NMR spectra was sufficient for accurate peak assignments, and the relative peak area of each site was obtained by the curve-fitting, using a series of Gaussian peaks [8].

2.3 Results and Discussion

2.3.1 Choice of Ligand and Ionic Liquid

It is well known that the activity, stability and selectivity of homogenous rhodium-phosphine complexes used for hydroformylation are sensitive to the structure and concentration of the ligand [2,16]. The effect of various phosphine ligands was investigated using monodentate triphenylphosphine (tpp), sulfonated triphenyl phosphine (tppts), and bidentate xantphos (X) and sulfonated xantphos (SX). Each of these ligands was mixed with [bmim][$OctSO_4$] and immobilized on silica pretreated at 823 K (SiO_2-823 K). Experiments conducted in the absence of ligands showed negligible catalytic activity. Table 2.1 shows that under identical reaction conditions, Rh-SX complexes are about five-fold more active than Rh-tppts complexes, as well as exhibiting a nearly six-fold higher selectivity to the linear product. The higher activity of Rh complexes involving SX over monodentate phosphines can be attributed to the chelating ability of SX, which yields a higher concentration of the coordinated Rh species. Consistent with this interpretation, the molar ratio of *n*-butanal to isobutanal (*n/i*) is higher when SX is used as the ligand due to the wider bite angle [2]. This in turn results in increased complexation of the rhodium center by the diphosphine SX ligand, and the rigid backbone of the ligand compells the phenyl groups of SX to exert a greater degree of steric hindrance on the alkene entering the coordination sphere, thereby favouring linear products [18,19]. Table 2.1 also shows that Rh-tpp and Rh-tppts complexes have comparable activity, the higher *n/i* ratio observed for the Rh-tpp system relative to the Rh-tppts system is due to the formation of $HRh(CO)_2(tpp)_2$ versus $HRh(CO)_3$(tppts) complexes [20]. Table 2.1 also shows that the activity of Rh-SX system is 2.5 times more active than the Rh-X system. As discussed below, the presence of the sulfonate groups on SX enables the Rh-SX complex to interact with the silanol groups of the support, thereby stabilizing the complex in an active form.

Table 2.1 Results from the hydroformylation of propene using various SILP catalysts.

Ligand-IL	L/Rh ratio [a]	α [b]	TOF (h^{-1}) [c]	*n/i*
tppts-[bmim][$OctSO_4$]	10	0.2	15	2.3
tppts-[bmim][$OctSO_4$]	20	0.2	8	3.8
tpp-[bmim][$OctSO_4$]	10	0.2	11	8
SX-[bmim][$OctSO_4$]	10	0.2	84	12
SX-[bmim][$OctSO_4$] [d]	10	0.1	100	13
X-[bmim][$OctSO_4$] [d]	10	0.1	40	11

T = 393 K, P_{Total} = 2 atm, C_3H_6:H_2:CO = 1:1:1, t = 8 h, 0.2 wt% Rh, SiO_2-823 K,
[a] Molar ligand to metal ratio; [b] Pore filling degree of the support as the ratio of IL volume/support pore volume, [c] Turn over frequency in moles aldehyde per mole of Rh per hour, [d] SiO_2 pretreated at 373 K.

The effects of IL composition on the activity and selectivity of SILP catalysts for propene hydroformylation are presented in Table 2.2. The choice of anion associated with [bmim] cation had a strong effect on the catalyst activity but relatively little effect on the *n/i* ratio. Highest and lowest activity was achieved using the $[OctSO_4]^-$ and the $[HSO_4]^-$ anions, respectively. Changing the composition of the cation from $[bmim]^+$ to $[emim]^+$, while maintaining $[MeSO_4]^-$ as the anion, caused a two-fold reduction in the catalyst activity.

Table 2.2 Results from the hydroformylation of propene using different ionic liquids containing Rh-SX SILP catalysts.

IL	L/Rh ratio [a]	α [b]	TOF (h^{-1}) [c]	*n/i*
$[bmim][OctSO_4]$	10	0.2	84	12
$[bmim][MeSO_4]$	10	0.2	32	13
$[bmim][HSO_4]$	10	0.2	3	11
$[bmim][NTf_2]$	10	0.2	26	16
$[emim][MeSO_4]$	10	0.2	15	13

T = 393 K, P_{Total} = 2 atm, C_3H_6:H_2:CO = 1:1:1, t = 8 h, 0.2 wt% Rh, SiO_2-823 K,
[a] Molar ligand to metal ratio; [b] Pore filling degree of the support as the ratio of IL volume/support pore volume, [c] Turn over frequency in moles aldehyde per mole of Rh per hour.

2.3.2 Effect of Silica Pretreatment

The results presented in Figure 2.1, show that SiO_2 pre-treated at 373 K and 823 K (SX/Rh = 10) produces very stable catalysts, whereas pretreatment at 1023 K (SiO_2-1023 K) results in a less active catalyst that deactivates with time on stream. Interestingly, irrespective of pretreatment conditions the *n/i* ratio remained the same throughout each run. These experiments suggest that silanol groups are required to stabilize the active form of the catalyst. To test this hypothesis, the silanol groups were passivated by silylation (SiO_2-373 K-Me) prior to formation of the SILP catalyst (refer to *Section 2.2.1*). While the SILP catalyst prepared on SiO_2-373 K-Me was initially nearly twice as active as that prepared on SiO_2-1023 K, this catalyst deactivated rapidly and became comparable in activity to that prepared on SiO_2-1023 K.

2.3.3 Effect of Ligand and Ionic Liquid Concentration

The effects of SX/Rh ratio and IL concentration were explored for SILP catalysts prepared with SiO_2-823 K. Figure 2.2 shows the effects of varying the SX/Rh ratio from 3 to 15, at a constant Rh loading of 0.2 wt %. The hydroformylation activity increases with increasing SX/Rh ratio, reaching a maximum for SX/Rh = 5 and then decreasing for higher SX/Rh ratios. While the initial activity for SX/Rh = 5 is higher than that for SX/Rh = 10, the activities of these two catalysts approach a common value after 8 h of

time on stream. These results differ from Rh-SX systems investigated in homogenous biphasic systems, for which very stable catalytic activity was observed for SX/Rh ratios of 2-5 [21-23].

The degree of pore filling by IL, α, (defined as the ratio between the volume of ionic liquid used and the pore volume of the support) also had a significant effect on the activity and stability of the SILP catalysts. Figure 2.3 shows that with no added IL, the catalyst increases in activity over 9.5 h of time on stream. The activity of the catalyst increases with α up to 0.2, but then decreases rapidly falling below that observed for no addition of IL. It is also notable that for $\alpha \leq 0.2$ the selectivity of propene to butanal was 100%; however for $\alpha = 0.4$ the selectivity to butanal dropped and large concentrations of aldol condensation products were observed. The value of α influences catalyst stability in addition to activity. For catalysts with $\alpha \leq 0.1$ the activity increased with time on stream, was stable for $\alpha = 0.2$, and decreased with time on stream for $\alpha = 0.4$.

To further understand how the IL interacts with the support, the support was first contacted with the IL ($\alpha = 0.1$) after which the rhodium precursor and SX dissolved in methanol (SX/Rh = 10) were introduced. Figure 2.4 shows that in contrast to the steady increase in hydroformylation activity observed when the Rh precursor, SX, and IL are introduced together, initial introduction of the IL leads to a progressive loss in activity. These results suggest that initial contact of the IL with the silanol groups of the support inhibits the interaction of the catalyst with the support.

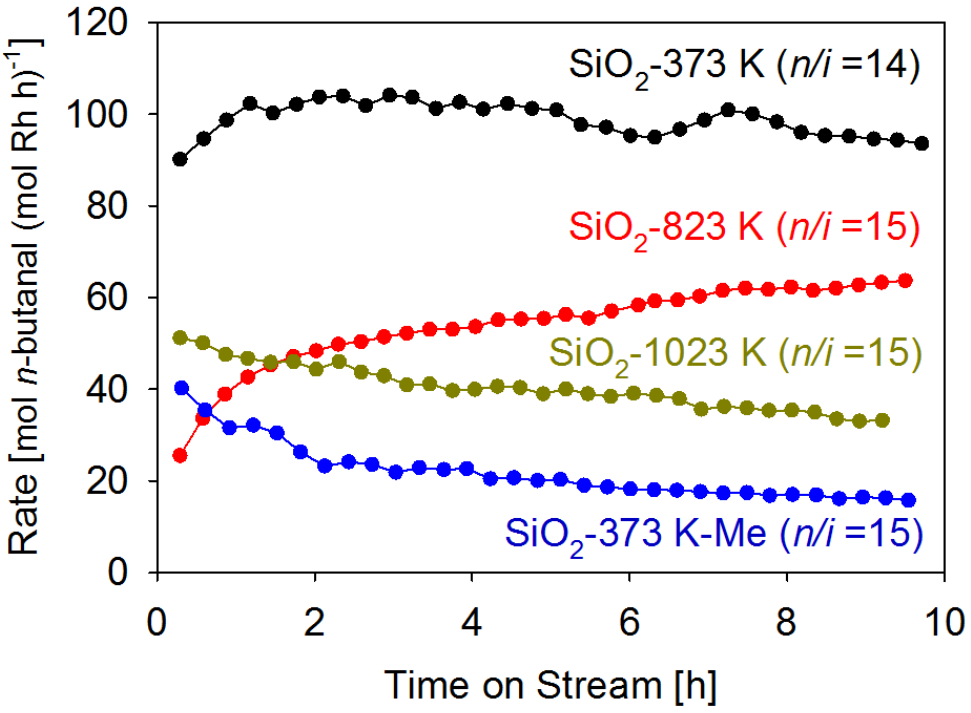

Figure 2.1 Effects of silica pretreatment temperature and silica passivation on the activity and stability of SILP catalysts (SX/Rh = 10, α = 0.1, 0.2 wt. % Rh) for the hydroformylation of propene. T = 393 K, P_{Total} = 2 atm, C_3H_6:H_2:CO = 1:1:1, catalyst mass = 0.3 g, total gas flow rate = 120 cm^3 min^{-1} at STP.

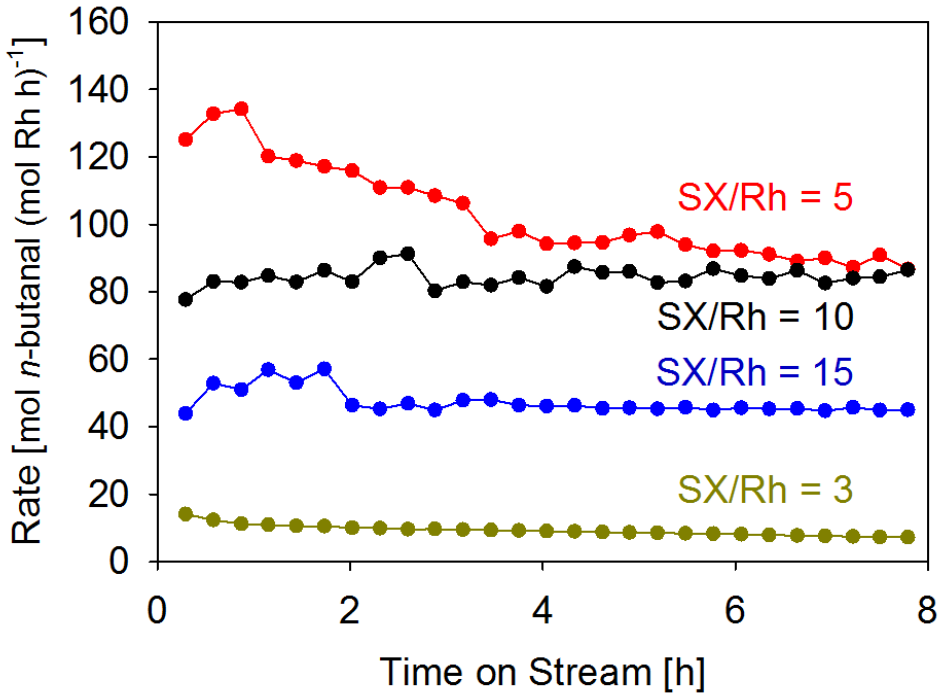

Figure 2.2 Effects of SX/Rh ratio on the activity and stability of SILP catalysts (SiO_2-823 K, α = 0.2, 0.2 wt. % Rh) for the hydroformylation of propene.

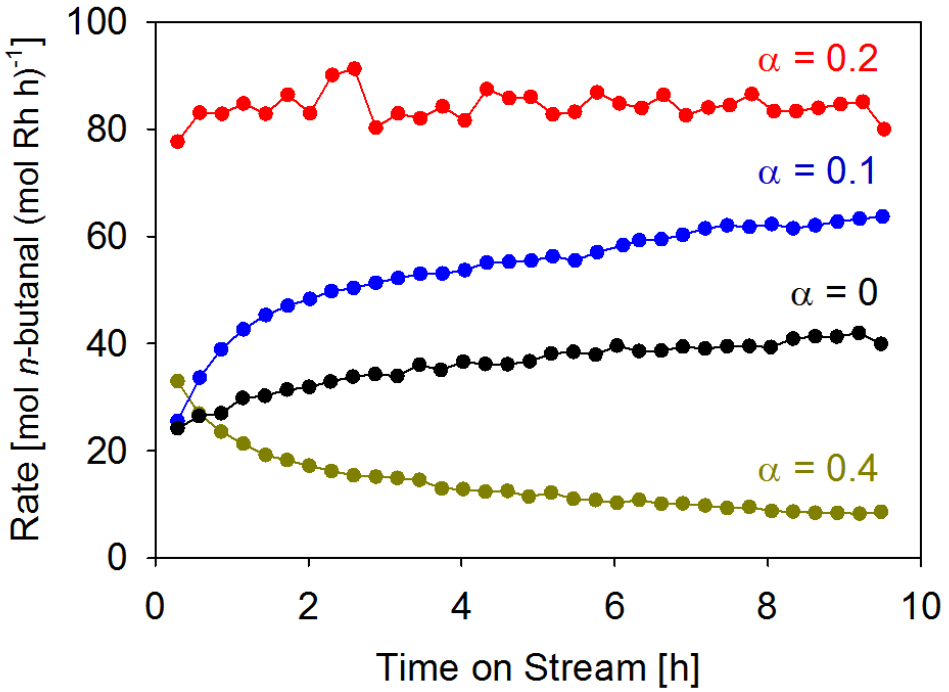

Figure 2.3 Effect of α on the activity and stability of SILP catalysts (SiO_2-823 K, SX/Rh = 10, 0.2 wt. % Rh) for the hydroformylation of propene.*

*T = 393 K, P_{Total} = 2 atm, C_3H_6:H_2:CO = 1:1:1, catalyst mass = 0.3 g , total gas flow rate = 120 cm^3 min^{-1} at STP.

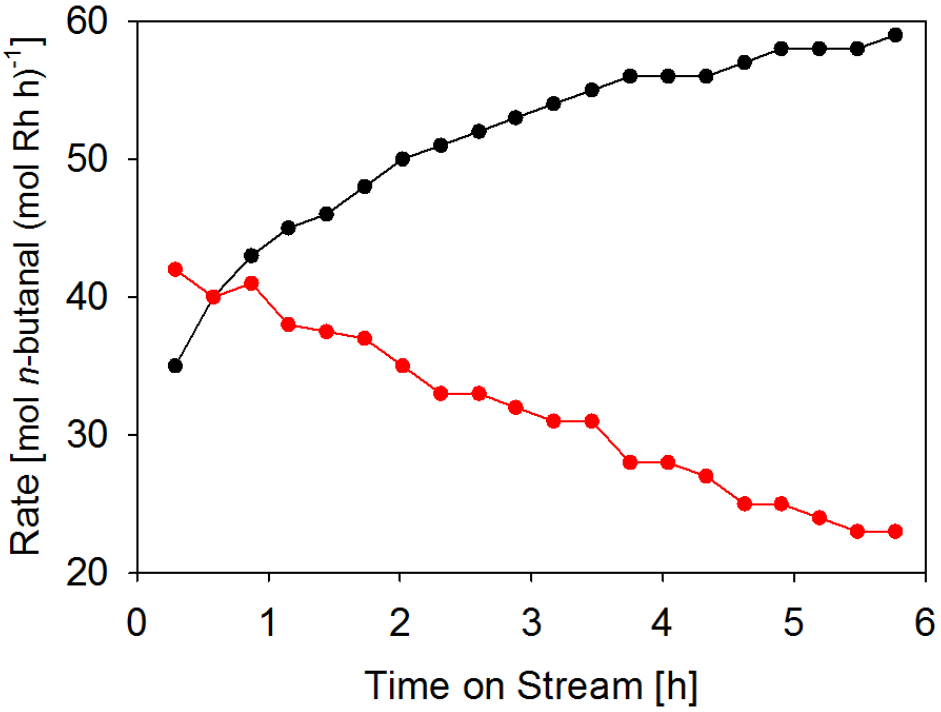

Figure 2.4 Effects of the manner of catalyst preparation on the activity and selectivity of SILP catalyst (SiO_2-823 K, SX/Rh = 10, α = 0.1, 0.2 wt. % Rh) for the hydroformylation of propene: (●) silica support treated with IL followed by the addition of rhodium precursor and SX; (●) simultaneous addition of IL, rhodium precursor and SX to the silica support. T = 393 K, P_{Total} = 2 atm, C_3H_6:H_2:CO = 1:1:1, catalyst mass = 0.3 g, total gas flow rate = 120 cm^3 min^{-1} at STP.

2.3.4 Characterization of SILP Catalysts

The influence of silica dehydration on the structure of the support was probed by ^{29}Si MAS-NMR. Figure 2.5 shows spectra for silica dehydrated at 373 K, 823 K, and 1023 K. These spectra show Q^3 and Q^4 peaks at -100 and -110 ppm, respectively. The Q^3 feature is due to silanol groups whereas the Q^4 feature is due to Si atoms coordinated to four other Si atoms via Si-O-Si bonds. With increasing temperature of dehydration the ratio of Si in silanol groups decreases relative to the concentration of Si in siloxane bonds [15]. The apparent surface concentration of silanol groups determined from these measurements and the corresponding BET surface areas show that the concentration of silanol groups decreases from 4 OH nm^{-2} for SiO_2-373 K, to 3 OH nm^{-2} for SiO_2-823 K, and to 1.6 OH nm^{-2} for SiO_2-1023 K, in agreement with values reported previously for silica treated at similar temperatures [24].

SILP catalysts were characterized by in situ IR and ex situ ^{31}P MAS-NMR. Unless otherwise specified, these experiments were carried out using a SILP catalyst prepared on SiO_2-823 K with SX/Rh = 10 and α = 0.1. IR spectra of the catalyst taken at 1 atm in He, CO/He and CO/H_2 are shown in Figure 2.6. The spectrum recorded in He at 393 K is devoid of features in the carbonyl stretching region, suggesting the CO ligands

associated by the Rh precursor, $Rh(acac)(CO)_2$ were replaced by coordination with the phosphine groups of SX [25]. As noted below, evidence for coordination of SX with Rh at this stage was obtained from ^{31}P MAS-NMR spectra. Upon contacting the catalyst with 0.5 atm CO in He, carbonyl bands appeared at 2007 and 1940 cm^{-1}. The positions of these bands are attributed to the formation of the cationic complex $[SXRh(CO)_2]^+$. Addition of H_2 to CO in the gas stream resulted in the appearance of four carbonyl bands at 2035, 2000, 1973, and 1943 cm^{-1}. These features are identical to those observed for Rh complexes formed with SX dissolved in organic solvents and in ILs [21,22]. The bands at 2035 and 1973 cm^{-1} are attributable to *ee*-$HRh(CO)_2SX$, in which both phosphorous atoms occupy equatorial coordination sites, and the bands at 2000 and 1943 cm^{-1} are attributable to *ea*-$HRh(CO)_2SX$, in which one phosphorous atom is equatorial and the other is apical. No bands were observed in the region characteristic of CO bridging ligands (1800-1700 cm^{-1}) for SILP catalysts prepared with SX/Rh = 10 on SiO_2@823 K. However, bands at 1775 and 1745 cm^{-1} were observed for SILP catalysts prepared on SiO_2@823 K with SX/Rh = 5 and on SiO_2@1023 K with SX/Rh = 10. These features can be attributed to $[Rh(SX)(CO)(\mu\text{-}CO)]_2$ [26-28].

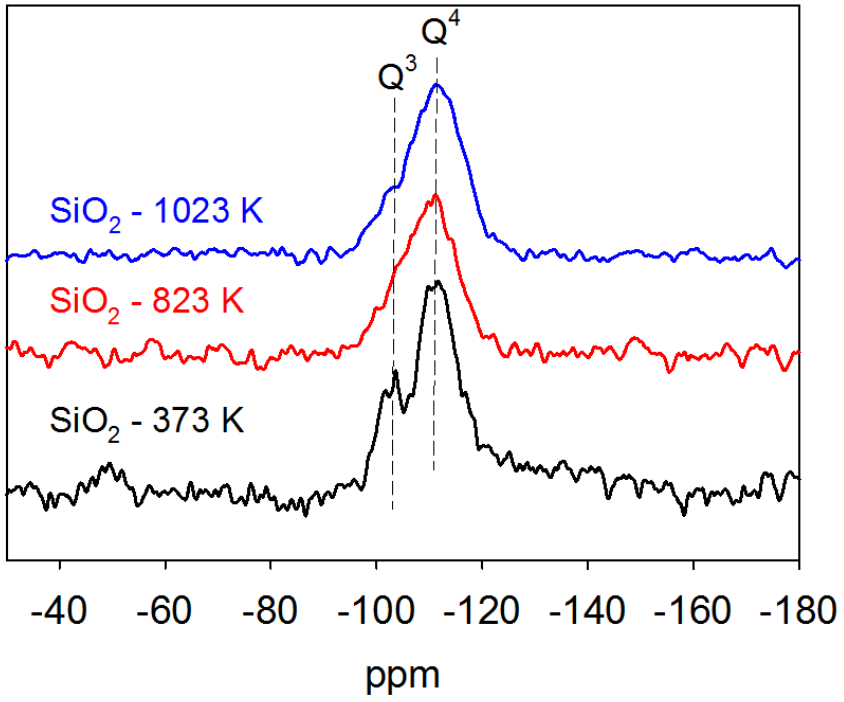

Figure 2.5. Solid-state ^{29}Si MAS NMR spectra of SiO_2 pretreated at different temperatures. (SiO_2-373 K shows Q^3/Q^4 = 0.25, SiO_2-823 K shows Q^3/Q^4 = 0.17 and SiO_2-1023 K shows Q^3/Q^4 = 0.11).

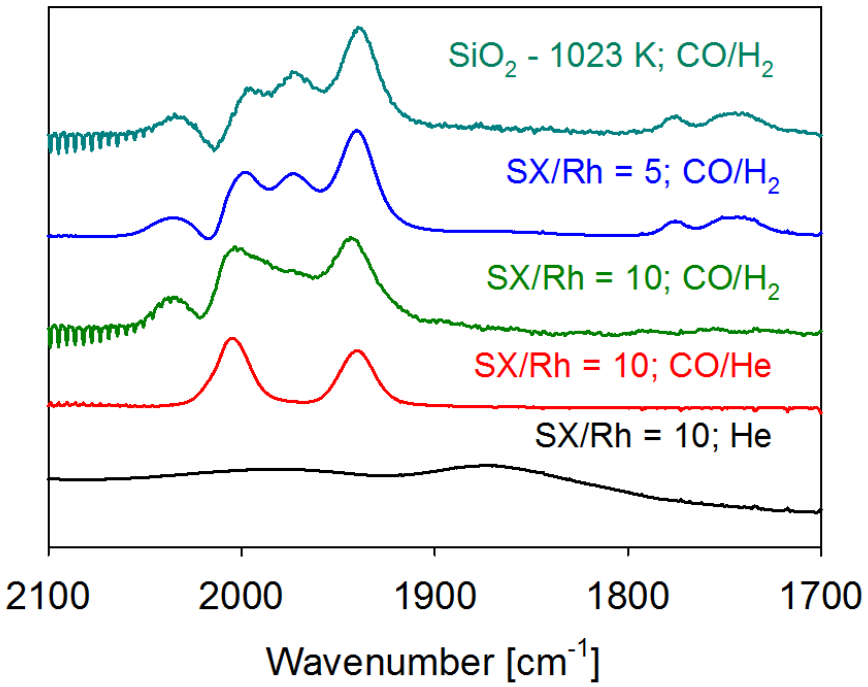

Figure 2.6 In situ FT-IR spectra of SILP catalysts showing the formation of monomeric and dimeric complexes (α = 0.1, SiO_2-823 K, 393 K, after 30 min in synthesis gas).

^{31}P MAS-NMR spectra of SILP catalysts prepared on SiO_2-373 K, SiO_2-823 K, and SiO_2-1023 K with SX/Rh = 10 and α = 0.1 are presented in Figure 2.7. Also shown is the spectrum for pure SX in $CDCl_3$, which exhibits a single peak at -16 ppm. For the catalyst prepared on SiO_2-373 K, this feature is accompanied by a feature at -21 ppm. We attribute the peak at -16 ppm to SX weakly physisorbed on silica, and attribute the peak at -21 ppm to phosphorous atoms in either singly protonated or non-protonated, strongly physisorbed SX groups. These assignments are fully consistent with ^{31}P MAS-NMR observation reported by Grey and coworkers for bidentate $PPh_2(CH_2)_nPPh_2$ (n = 1) adsorbed on HY zeolite [29]. The weak band at 30 ppm is assigned to the phosphine groups of SX interacting with Rh.[15] As the temperature of silica dehydration increases, the peaks attributed to "free" SX and SX interacting with silanol groups meld into one broad feature, whereas the peak due to SX-Rh interactions increases and passes through a maximum for SiO_2-823 K. The distribution of SX between "free" and interacting with silanol groups is also dependent on the SX/Rh ratio. Decreasing the SX/Rh ratio from 10 to 5, decreased the ratio of "free" to silanol-interacting SX from 2.5 to 1.3. The strong broadening in both the "free" to silanol-interacting SX with increasing temperature of silica dehydration suggests that the component described as "free" may be better described as SX interacting with silanol groups via the sulfonate groups. Illustrations of the two forms of SX interaction with silanol are presented in Scheme 2.2 (Conformations **A** and **B**).

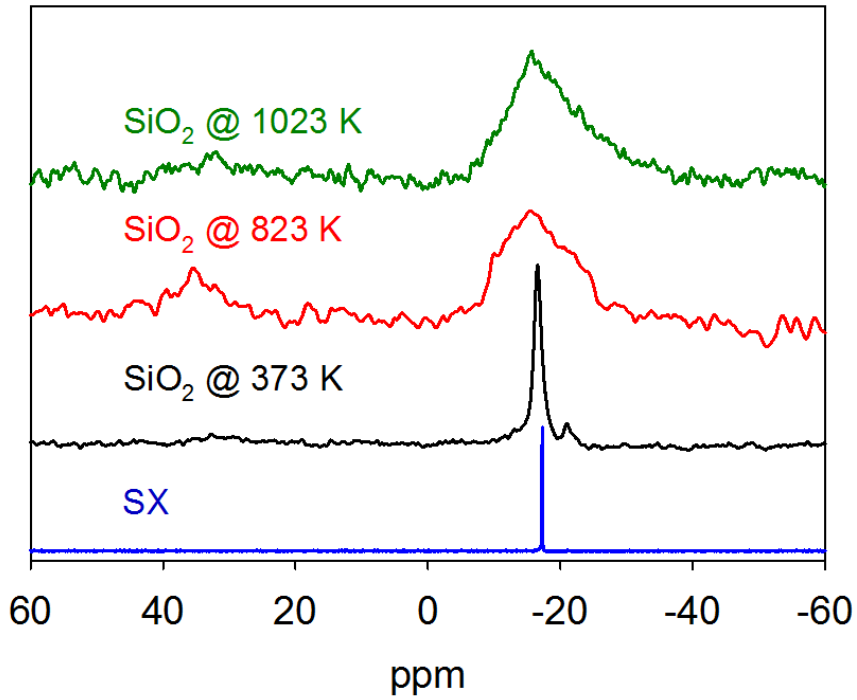

Figure 2.7 Solid-state ^{31}P MAS NMR spectra of SILP catalysts (SX/Rh=10) under different silica pretreatment conditions. SILP-SiO_2-373 K shows peaks for free SX ligand (δ = -16 ppm, 76%), surface bound ligand (δ = -22 ppm, 10%) and to the complexed ligand (δ = 30 ppm, 14%); SILP- SiO_2-823 K shows peaks for free SX ligand (δ = -16 ppm, 54%), surface bound ligand (δ = -22 ppm, 23%) and to the complexed ligand (δ = 30 ppm, 23%); SILP- SiO_2-1023 K shows peaks for free SX ligand (δ = -16 ppm, 47%), surface bound ligand (δ = -22 ppm, 33%) and to the complexed ligand (δ = 30 ppm, 10%) [15].

2.3.5 Effects of Catalyst Formulation on Catalytic Activity and Selectivity

The results of the present study demonstrate that the activity and stability of Rh-based SILP catalyst are highly sensitive to their formulation. Silanol groups on the surface of the support are required to achieve high activity and stability. Dehydration of the support at 1023 K or removal of silanol groups by silylation reduces the propene hydroformylation activity by a factor of 5. Highest activity and stability are attained for an SX/Rh ratio of 10, and both lower and higher ratios lead to less active catalysts. The IL loading also has an effect on catalyst activity and stability; catalysts with α = 0.2 are most active. A qualitative interpretation of the effects of catalyst composition on catalyst performance can be developed on the basis of the observed interactions of SX and [bmim][$OctSO_4$] with the support.

^{31}P MAS-NMR spectra of the SILP catalysts indicate that SX interacts with the silanol groups of silica via the modes shown in Scheme 2.2 (conformation **A** and **B**). The resonance observed at -16 ppm, previously attributed to free SX can be better assigned to SX interacting with silanol groups via their sulfonate groups (conformation **B** in Scheme 2.2); however, consistent with previous studies, the resonance observed at -22 ppm is

attributed to SX interacting with silanol groups via their phosphine groups (conformation **A** in Scheme 2.2) [15,29].

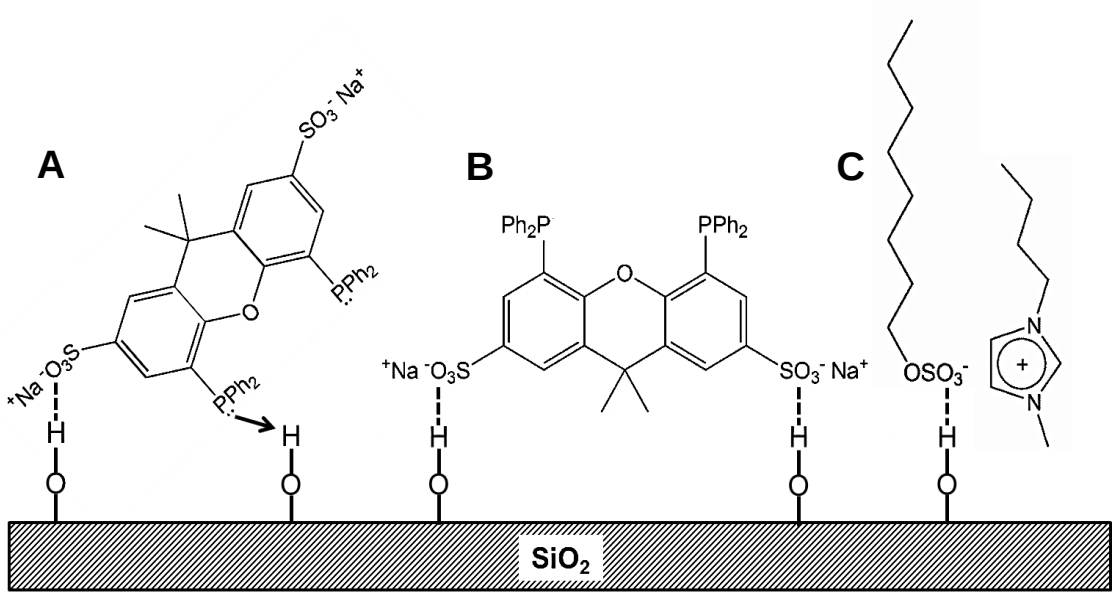

Scheme 2.2 Possible interaction of sulfoxantphos ligand (A and B) and [bmim][OctSO4] ionic liquid (C) on silica support.

The concentration of silanol groups decreases from 4 OH nm^{-2} for silica dehydrated at 373 K to 1.6 OH nm^{-2} as the dehydration temperature was increased to 1023 K. Dehydration increases the fraction of isolated silanol groups and their Brønsted acidity [30,31]. Consequently, the Lewis acid-base interaction between the silanol groups and the phosphine groups of SX is enhanced. For a Rh loading of 0.02 mmol g^{-1} and an SX/Rh ratio of 10, the apparent surface density of SX is always lower (~0.4 SX nm^{-2}) than that of silanol groups. The ^{31}P MAS-NMR spectra suggest that as the surface concentration of silanol groups decreases, an increasing fraction of SX is bound via its phosphine groups, making these groups unavailable for coordination with Rh^+ cations. By contrast, SX interacting with silanol groups via their sulfonate groups can form complexes with Rh^+ cations. Unbound SX would also coordinate with Rh^+ cations; however, since the concentration of Rh is high in the liquid comprised of SX and IL, it is likely that free $HRh(CO)_2SX$ dimerize to form $[Rh(CO)(\mu\text{-}CO)SX]_2$ complexes or $HRh(SX)_2$ complexes, which are inactive for propene hydroformylation [25,26]. The proposal that $HRh(SX)_2$ complexes may results in less active catalysts is supported by observations of Van Eldik and coworkers, who demonstrated the low catalytic activity of $HRhL_4$ type species in hydroformylation reactions [32]. Therefore, it is proposed that the role of silanol groups on silica is to stabilize SX mainly in the form of conformation **B** (Scheme 2.2), thereby producing isolated $HRh(CO)_2SX$ complexes. The in situ IR spectra presented in Figure 2.6 provide evidence for the formation of such complexes.

The dependence of propene hydroformylation activity on SX/Rh ratio seen in Figure 2.2 can be interpreted in the following manner. For SX/Rh = 0, no catalytic activity was observed, indicating an SX-Rh complex is necessary to initiate the hydroformylation of propene. For SX/Rh = 3, a very low activity is observed, because a

large fraction of the SX interacts with the support via its phosphine groups, i.e., conformation **A** in Scheme 2.2. As the SX/Rh ratio is raised a greater fraction of SX is bound to the support in the form of conformation **B**, enabling the formation of catalytically active $HRh(CO)_2SX$ complexes. Above SX/Rh = 5, it is conceivable that free SX now interacts with the isolated complexes to form $HRh(SX)_2$ complexes, which are expected to be less active for propene hydroformylation [30,31]. It is important to note that an optimal concentration of SX/Rh has also been reported in studies of $HRh(CO)_2SX$ complexes dissolved in various solvents [22-24]. The near constancy of the *n/i* ratio as the concentration of SX varied suggests that CO dissociation from both the *ee*- and *ea*- isomers of $HRh(CO)_2SX$ result in the same reactive four coordinate HRh(CO)SX intermediates in the hydroformylation cycle [19].

While previous studies of Rh-based SILP propene hydroformylation catalyst have suggested that the IL acts as a solvent for homogeneously dispersed $HRh(CO)_2SX$ complexes, we propose an alternative interpretation [14-16]. Figure 2.3 and 4 demonstrate that there is an optimal loading of IL necessary for achieving high catalyst activity and stability, and that introduction of IL prior to introducing $Rh(CO)_2(acac)$ and SX results in a less active catalyst. As noted above, this suggests that the IL interacts with the silanol groups of the support, thereby interfering with the interaction of SX to form conformation **B**. Evidence for interactions of $[bmim][OctSO_4]$ was obtained from IR spectra taken before and after treatment of SiO_2-823 K with IL ($\alpha = 0.2$). Prior to introduction of the IL, the only feature observed was a sharp silanol band at 3740 cm^{-1}. After contacting the support with IL, the intensity of this band decreased significantly and a broad band appeared at 3650 cm^{-1}. A similar pattern was observed when SX/SiO_2 was contacted with IL. We attribute the observed changes in the spectrum to interactions of the sulfonate groups of $[bmim][OctSO_4]$ with the silanol groups of the support [6]. We note that evidence for such interaction has been reported by Antonietti and coworkers who showed that $[BF_4]^-$ anions of $[bmim][BF_4]$ IL form hydrogen bonds with the silanol groups of mesoporous silica [33]. It is quite possible that the higher catalytic activity observed using $[bmim][OctSO_4]$ compared to other anions is attributable to the strength of anion interaction with the support [34]. For $[RSO_4]^-$ anions (R = H, Me, Oct) the strength of interaction of the anion with silanol groups of the support would be expected to increase with an increase in the pKa of the conjugate Brønsted acid. Thus, the low activity observed in Table 2.2 when $[bmim][HSO_4]$ was used as the IL could be ascribed to excessive interaction of the IL with the support, thereby inhibiting the association of SX with the support to form conformation **B**.

All these observations lead to the hypothesis that IL molecules spatially distribute $HRh(CO)_2SX$ complexes on the support surfaces at lower α values while they compete with SX ligands for silanol groups at high α values. We note that for SX/Rh = 10, $\alpha = 0.1$ to 0.4 corresponds to IL/SX = 1 to 4. Since an optimal hydroformylation activity is achieved for $\alpha = 0.2$ for a SILP catalyst prepared on SiO_2-823 K with SX/Rh = 10, this indicates that the optimum IL/SX ratio in this case is 2. For higher IL/SX ratios, it is likely that the excess IL displaces SX attached to the support in the form of conformation **B**. Further evidence for the interaction of IL with the support is suggested by the dependence of catalyst activity on IL composition. As noted in Table 2.2, propene hydroformylation activity depends primarily on the composition of the IL anion, and to a lesser extent the composition of the cation.

The mechanism of catalyst deactivation observed in Figures 1-3 can be explained as follows. Greatest evidence for a decline in activity with time on stream is seen for SILP catalysts prepared on SiO_2-1023 K with SX/Rh = 10 and $\alpha = 0.1$, SiO_2-823 K with SX/Rh = 5 and $\alpha = 0.1$, and SiO_2-823 K with SX/Rh = 10 and $\alpha = 0.4$. These examples suggest that deactivation most likely occur when catalysts are prepared with a low concentration of SX in the form of conformation **B**. The gradual loss of $HRh(CO)_2SX$ complexes on the support could lead to the formation of $[Rh(CO)(\mu\text{-}CO)SX]_2$ dimer complexes that are inactive for propene hydroformylation. Evidence for bridging CO, characteristic of such complexes was observed in in-situ IR spectra taken of SILP catalysts prepared on SiO_2-1023 K with SX/Rh = 10 and $\alpha = 0.1$ and on SiO_2-823 K with SX/Rh = 5 and $\alpha = 0.1$.

2.4 Conclusions

The results of this study provide important insights into the factors influencing the activity and stability of Rh-based SILP catalysts for the hydroformylation of propene prepared on high surface area silica. Catalyst activity and stability are found to be strong functions of ligand and IL composition, as well as ligand-to-Rh ratio, IL loading, and temperature of support pretreatment. Highest activity is achieved with SX as the ligand and $[bmim][OctSO_4]$ as the IL supported on silica pretreated at 373 K and using an SX/Rh ratio of 10 and IL loading corresponding to $\alpha = 0.2$. Characterization of SILP catalysts by various techniques suggests that the active form of the catalyst consists of $HRh(CO)_2SX$ complexes stabilized by the support through interactions of the sulfonate groups of the SX ligand with silanol groups of the support. Pretreatment of the support at temperatures above 373 K decreases the surface density of silanol groups and increases the acidity of these groups. These results in an increasing fraction of SX binding to the support through its phosphine groups, thereby reducing the availability of these groups to coordinate Rh^+ cations. High IL loadings are undesirable, since the interaction of IL with the silanol groups of the support can inhibit interaction of silanol groups with the sulfonate groups of SX, resulting in the formation of $[Rh(CO)(\mu\text{-}CO)SX]_2$ species that are catalytically inactive. The SX/Rh ratio also has a large effect on the catalytic activity and stability. If SX/Rh is much less than 10, the fraction of SX bound to the surface via phosphine groups is high and therefore the concentration of $HRh(CO)_2SX$ complexes stabilized by the support through interactions of the sulfonate groups of the SX ligand is low. By contrast for SX/Rh ratios greater than 10, the excess SX may form $HRh(SX)_2$ complexes that are less active for propene hydroformylation.

2.5 Acknowledgements

This work was supported by the XC^2 program funded by BP. The authors would like to thank Dr. Chris Canlas (Berkeley NMR facility) for his assistance in acquiring the NMR spectra, Dr. Boon Jason Yeo for the EDX elemental mapping studies and Dr. Zhengmeng Peng for the TEM images. The authors also wish to express their appreciation to Prof. Peter Wasserscheid of the Friedrich-Alexander Universität Erlangen-Nürnberg for providing the sulfoxantphos ligand.

2.6 Supporting Information

Table S2.1 Textural properties of pretreated silica supports and SILP catalysts.

Sample	BET Surface Area (m^2 g^{-1})	Pore Volume (mL g^{-1})	Average Pore Diameter (nm)
SiO_2-373 K	300	1.15	6
SiO_2-823 K	378	0.867	3.8
SiO_2-1023 K	475	0.723	3.5
SILP-SiO_2-373 K [a]	216	0.545	3.3
SILP-SiO_2-1023 K [a]	255	0.215	1.7

[a] SX/Rh = 10, α = 0.1, [bmim][$OctSO_4$].

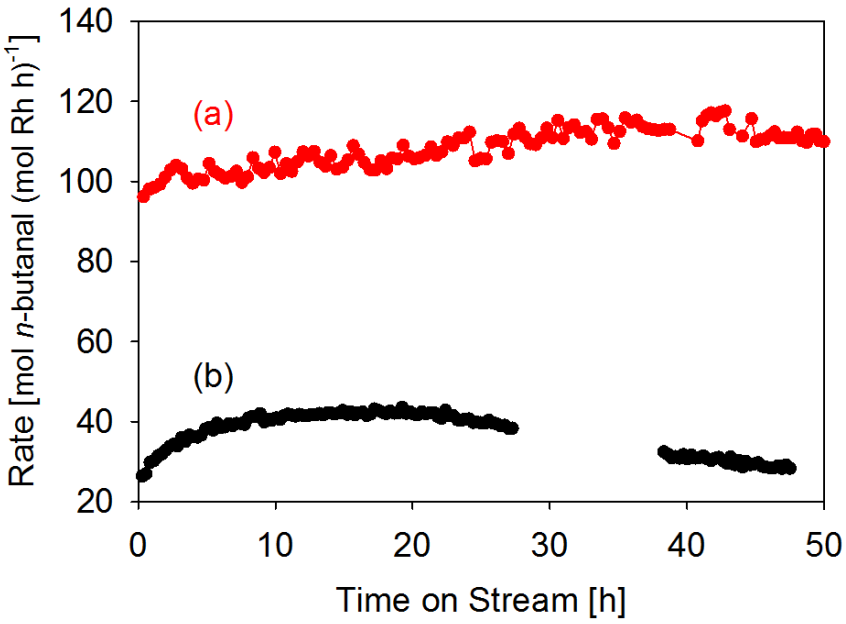

Figure S2.1 Time on stream studies of SILP catalysts (a) with IL and (b) without IL. T = 393 K, P_{Total} = 2 atm, C_3H_6:H_2:CO = 1:1:1, catalyst mass = 0.3 g, total gas flow rate = 120 cm^3 min^{-1} at STP. SiO_2-373 K, SX/Rh = 10, α = 0.1, 0.2 wt. % Rh.

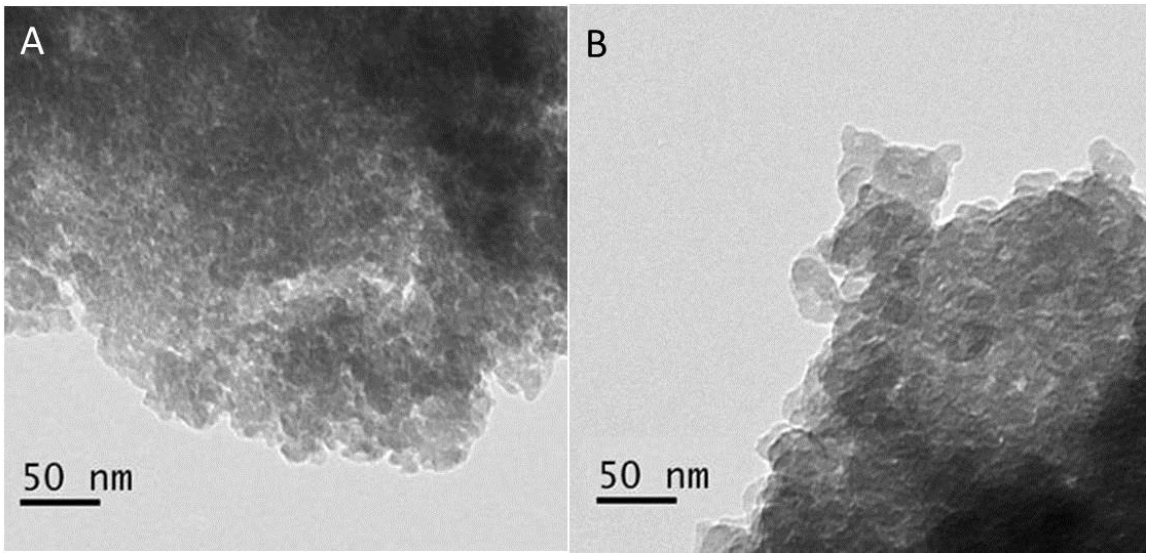

Figure S2.2 TEM images of SiO_2-373 K Rh-SX SILP catalyst, (a) before and (b) after reaction.

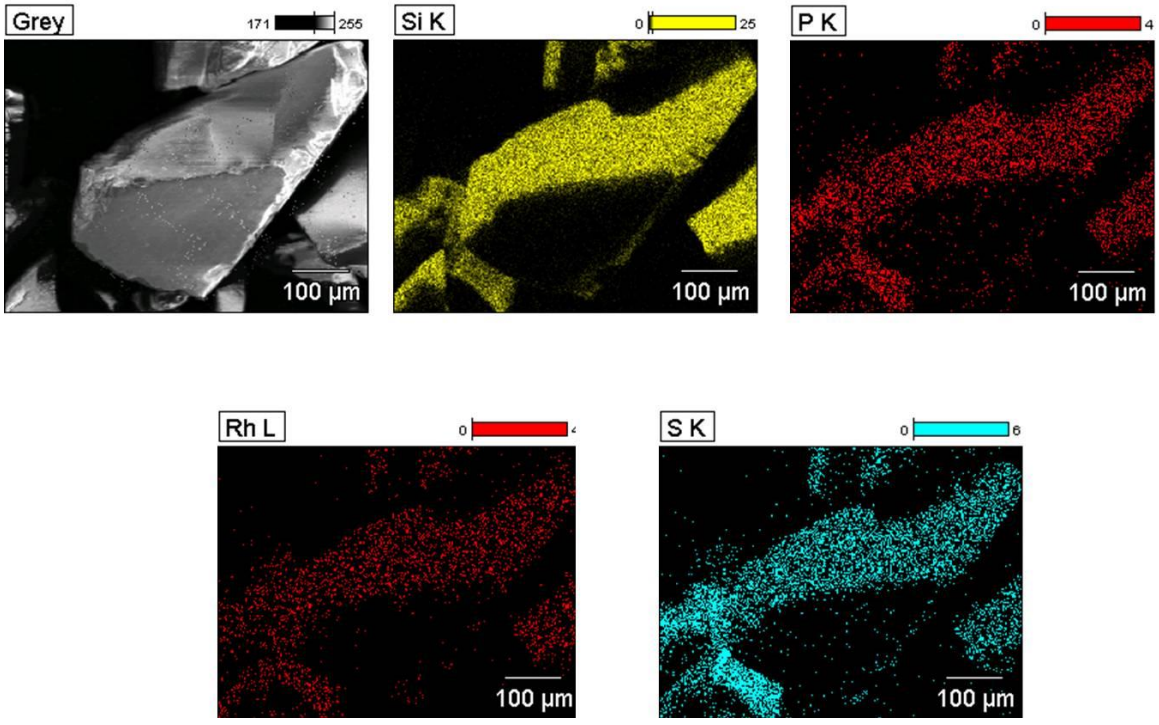

Figure S2.3 Elemental mapping analysis of a SILP catalyst (SiO_2@373 K, α = 0.1, SX/Rh =10) showing the homogeneous dispersion of metal complex and ionic liquid on the silica support surfaces.

2.7 References

[1] W. A. Hermann, B. Cornils. *Angew. Chem. Int. Ed*. **1997**, 36, 1048-1067.

[2] P. W. N. M. van Leeuwen, C. Claver. in: *Rhodium Catalyzed Hydroformylation*, Kluwer Academic Publishers, AA Dordrecht, **2000**.

[3] M. Beller, B. Cornils, C. D. Frohning, C. W. Kohlpainter. *J. Mol. Catal. A: Chem*. **1995**, 104, 17-85.

[4] D. J. Cole Hamilton. *Science* **2003**, 299, 1702-1706.

[5] A. J. Sandee, J. N. H. Reek, P. C. J. Kamer, P. W. N. M. van Leeuwen. *J. Am. Chem. Soc*. **2001**, 123, 8468-8476.

[6] C. Bianchini, D. G. Burnaby, J. Evans, P. Frediani, A. Meli, W. Oberhauser, R. Psaro, L. Sordelli, F. Vizza. *J. Am. Chem. Soc*. **1999**, 121, 5961-5971.

[7] K. Mukhopadhyay, A. B. Mandale, R. V. Chaudhari. *Chem. Mater*. **2003**, 15, 1766-1777.

[8] L. Xijie, Z. Weiping, L. Yan, Y. Ding, X. Han, L. Lin, B. Bao. *J. Phys. Chem. C* **2009**, 113, 6589-6595.

[9] J. P. Arhanchet, M. E. Davis, J. S. Merola, B. E. Hanson. *Nature* **1989**, 339, 454-455.

[10] J. P. Arhanchet, M. E. Davis, B. E. Hanson. *J. Catal*. **1991**, 129, 94-99.

[11] I. T. Horvath. *Catal. Lett*. **1990**, 6, 43-48.

[12] C. P. Mehnert, R. A. Cook, N. C. Dispenziere, M. Afeworki. *J. Am. Chem. Soc*. **2002**, 124, 12932-12933.

[13] C. P Mehnert. *Chem. Eur. J*. **2005**, 11, 50-56.

[14] A. Riisager, P. Wasserscheid, R. van Hal, R. Fehrmann. *J. Catal*. **2003**, 219, 452-455.

[15] A. Riisager, R. Fehrmann, S. Flicker, R. van Hal, M. Haumann, P. Wasserscheid. *Angew. Chem. Int. Ed*. **2005**, 44, 815-819.

[16] A. Riisager, R. Fehrmann, M. Haumann, P. Wasserscheid. *Eur. J. Inorg. Chem*. **2006**, 695-706.

[17] W. P. Mul, K. Ramkisoensing, P. C. J. Kamer, J. N. H. Reek, A. J. van der Linden, A. Marson, P. W. N. M. van Leeuwen. *Adv. Synth. Catal.* **2002**, 344, 293-298.

[18] P. W. N. M. van Leeuwen, P. C. J. Kamer, J. N. H. Reek, P. Dierkes. *Chem. Rev*. **2000**, 100, 2741-2769.

[19] L. A. van der Veen, M. D. K. Boele, F. R. Bregman, P. C. J. Kamer, P. W. N. M van Leeuwen, K. Goubitz, J. Fraanje, H. Schenk, C. Bo. *J. Am. Chem. Soc*. **1998**, 120, 11616-11626.

[20] I. T. Horvath, R. V. Kastrup, A. A. Oswald, E. J. Mozeleski. *Catal. Lett*. **1989**, 2, 85-90.

[21] S. M. Silvia, R. P. J. Bronger, Z. Freixa, J. Dupont, P. W. N. M. van Leeuwen. *New J. Chem*. **2003**, 27, 1294-1296.

[22] A. J. Sandee, V. F. Slagt, J. N. H. Reek, P. C. J. Kamer, P. W. N. M. van Leeuwen. *Chem. Commun*. **1999**, 1633-1634.

[23] J. Dupont, S. M. Silva, R. F. De Souza. *Catal. Lett*. **2001**, 77, 131-133.

[24] S. Ek, A Root, M. Peussa, L. Niinisto. *Thermochim. Acta* **2001**, 379, 201-212.

[25] D. Semeril, D. Matt, L. Toupet, W. Oberhauser, C. Bianchini. *Chem. Eur. J*. **2010**, 16, 13443-13849.

[26] B. R. James, D. Mahajan, S. R. Retting, G. M. Williams. *Organometallics* **1983**, 2, 1452-1458.

[27] W. R. Moser, C. J. Papile, D. A. Brannon, R. A. Duwell. *J. Mol. Catal*. **1987**, 41, 271-292.

[28] A. Castellanos-Paez, S. Castillon, C. Claver, P. W. N. M. van Leeuwen, W. G. de Lange. J. *Organometallics* **1998**, 17, 2543-2552.

[29] L. Peng, P. J. Chupas, C. P. Grey. *J. Am. Chem. Soc*. **2004**, 126, 12254-12255.

[30] R. K. Iler. in: *The Chemistry of Silica*, John Wiley & Sons, New York, **1979**.

[31] G. Crepeau, V. Montouillout, A. Vimont, L. Mariey, T. Cseri, F. Mauge. *J. Phys. Chem. B.* **2006**, 110, 15172-15185.

[32] A. M. Trzeciak, J. J. Ziolkowski, S. Aygen, R. Van Eldik. *J. Mol. Catal*. **1986**, 34, 337-343.

[33] Y. Zhou, J. H. Schattka, M. Antonietti. *Nano Lett.* **2004**, 4, 477-481

[34] L. Cammarata, S. G. Kazarian, P. A. Salter, T. Welton. *Phys. Chem. Chem. Phys*. **2001**, 3, 5192-5200.

Chapter 3

The Kinetics of Gas-Phase Propene Hydroformylation over a Supported Ionic Liquid Phase (SILP) Rhodium Catalyst

Abtract

An investigation of the kinetics of propene hydroformylation in the gas-phase has been conducted over a silica-supported Rh-sulfoxantphos complex stabilized by the ionic liquid [bmim][$OctSO_4$]. The reaction temperature was found to have a strong effect on the kinetics of *n*- and isobutanal formation. For both products, it was observed that increasing the temperature decreased the apparent activation energy, altered the reaction orders with respect to reactants, and decreased the molar ratio of *n*- to isobutanal. The observed changes in the kinetics are discussed in terms of the generally accepted mechanism for olefin hydroformylation and are attributed to a change in the rate-determining step (RDS). It is concluded that at low temperature the RDS is alkene insertion into an Rh-H bond, but becomes the oxidative addition of H_2 at high temperature. The change in the RDS is rationalized in terms of a change in the elementary step with the largest Gibbs free energy of activation ($\Delta G^{\ddagger}$). A greater loss in entropy for the oxidative addition of H_2 over alkene insertion causes the $\Delta G^{\ddagger}$ of the oxidative addition to be greater than the $\Delta G^{\ddagger}$ of alkene insertion at high temperature.

3.1 Introduction

The liquid-phase hydroformylation of alkenes to aldehydes, catalyzed by Rh complexes, is used extensively to produce intermediates for a number of commodity chemicals (e.g., plasticizers, detergents, etc.) [1]. Two of the ongoing challenges with the use of homogeneous Rh complexes are separation of the organic products from the catalyst and loss of Rh due to leaching [2]. Biphasic systems such as the Ruhrchemie/Rhône-Poulenc process are currently used to facilitate product separation and reduce Rh leaching for propene hydroformylation [1]. The reaction is carried out in an aqueous phase containing the solubilized Rh complex, whereas an organic phase is used to extract the product aldehyde. Although satisfactory for propene hydroformylation, this process is not suitable for longer chain olefins due to decreased alkene solubility in the aqueous phase [2,3]. Another disadvantage of such systems is the cost for recovering the alkene from the organic phase [3].

To circumvent the issues associated with using biphasic systems, a number of authors have examined the possibility of dispersing the active Rh complex in a liquid contained within the pores of a high surface area solid or grafting the complex to the surface of a support material [4-7]. In the early 1980's, Gerritsen and coworkers showed that molten triphenlyphosphine could be used as a solvent for $HRh(CO)(PPh_3)$ supported on γ-alumina and silica [8]. Subsequent work by Davis and coworkers led to the development of supported aqueous-phase (SAP) catalysts in which an aqueous solution of a Rh complex is supported on microporous glass [9]. Such catalysts proved effective

for the hydroformylation of water-insoluble alkenes in non-polar solvents [10]. However, subsequent work revealed that SAPs are not suitable for gas-phase hydroformylation due to evaporation of the aqueous phase [11]. Since ionic liquids have negligible vapor pressure, Mehnert and coworkers developed supported ionic liquid catalysts (SILC) by impregnating a solution of Rh-tppts in [bmim][BF_4] or [bmim][PF_6] into a 1-n-butyl-3-methyl imidazolium modified silica gel support [12]. In later studies conducted by Wasserscheid and coworkers, analogous supported ionic liquid phase (SILP) catalysts were found to be exceptionally stable and active under continuous gas-phase reaction conditions [13,14]. The stability, high activity, and facile separation of the products from the Rh complex make SILP catalysts particularly promising for the commercial application of propene hydroformylation.

While previous studies of SILP catalysts have suggested that the Rh complex is homogeneously dispersed in an IL film [12-15], our recent study using ^{31}P MAS NMR and in situ FT-IR suggests that interactions of the IL and metal complex with the support are required to yield a stable catalysts [16] (refer to Chapter 2). As shown in Scheme 2.2, the phosphine ligand, sulfoxantphos (SX), interacts with the slightly acidic silanol groups via the lone pair of electrons on phosphorus (conformation **A**) or in an ion-dipole interaction with the charged sulfonate group (conformation **B**). Similarly, the IL ([bmim][$OctSO_4$]) interacts with the silanol groups via the sulfonate group of the anion ([$OctSO_4$]) (conformation **C**). Conformation **B** is desired to yield active catalysts because the phosphine groups on SX are free to coordinate to the Rh cations.

In this work, we report an investigation of the kinetics for the gas-phase hydroformylation of propene over a SILP catalyst. Previous studies have suggested that the oxidative addition of H_2 is the RDS [7,17,18] despite arguments that the RDS occurs earlier in the hydroformylation cycle [19,20]. Other authors have claimed that the RDS is dependent upon the partial pressures of propene and hydrogen [21]. We show that the kinetics for forming *n*- and isobutanal are functions of the reaction temperature suggesting that the rate-determining step (RDS) is also dependent upon the reaction temperature. Rate equations were developed based upon the Wilkinson mechanism for olefin hydroformylation [22] and an explanation was given to rationalize the temperature effects on the RDS.

3.2 Methods

3.2.1 Catalyst Preparation

SILP catalysts were prepared following the procedure described in Ref. [15]. In brief, 5 mg of $Rh(CO)_2(acac)$ (Fluka, purum) was dissolved in 10 mL of anhydrous methanol (Aldrich, 99.8%) and then approximately 150 mg of Sulfoxantphos (SX) [23] was added to this solution to achieve a molar ratio of SX/Rh = 10. After 10 min of stirring, 120 mg of [bmim][$OctSO_4$] [24] was added to the mixture. The volume of IL added to solution was 10% of the pore volume of the silica support. After another 1 h of stirring, 1 g of silica (Silicycle, 500 m^2 g^{-1}, average pore diameter 60 Å) stored under vacuum at 353 K was added to solution and was stirred for an additional 1 h. Methanol was then slowly removed under vacuum in a rotary evaporator. The resulting catalyst is a red colored, free flowing powder containing 0.002 g Rh (g SiO_2)$^{-1}$.

3.2.2 Gas-phase Hydroformylation of Propene

Measurements of reaction rates were performed in a 6.35 mm OD quartz tube with an expanded section (~12.7 mm OD, ~20 mm length). The reactor was packed with quartz wool below the catalyst bed to hold the powder in place. The reactor was placed inside a resistively heated ceramic furnace with external temperature control and the catalyst bed temperature was measured with a K-type thermocouple sheathed in a quartz capillary placed in direct contact with the catalyst bed.

Prior to reaction, the 0.3 g of catalyst was heated to the reaction temperature at a rate of 2 K min^{-1} in pure He (Praxair, 99.999%) flowing at 20 cm^3 min^{-1} at STP. The feed to the reactor consisted of propene (Praxair, 99.9%), CO (Praxair, 99.99%), H_2 (Praxair, 99.999%). A reactant ratio of C_3H_6:CO:H_2 of 1:1:1 was used unless specified otherwise. Experiments were carried out at total gas pressures of 2 atm by throttling a needle valve located downstream from the reactor. Total gas flow rate was typically 120 cm^3 min^{-1} at STP. Using these conditions, the conversion of propene was always less than 1%. Reaction products were analyzed using an Agilent 6890N gas chromatograph containing a bonded and crosslinked (5%-Phenyl)-methylpolysiloxane capillary column (Agilent, HP-1) connected to a flame ionization detector.

3.3 Results

3.3.1 Catalytic Activity of SX-Rh/SiO_2 SILP Catalysts

To avoid artifacts due to catalyst deactivation, catalyst stability with time on stream was examined. Figure 3.1 shows a representative example of the results, demonstrating that the catalyst is stable for 40 h. The only products observed under any of the conditions investigated were *n*- and isobutanal.

Figure 3.2 shows the effects of reaction temperature on the catalytic activity and the molar *n*/*i* ratio. The rates of *n*- and isobutanal formation increase as the reaction temperature increases. At 403 K, the rate of *n*-butanal formation begins to plateau while the rate of isobutanal formation continues to rise. Thus, the *n/i* ratio decreases from 24 at 343 K to 6 at 413 K, demonstrating that temperature can be used as a parameter to control the *n/i* isomer ratio. Above 413 K, a loss in catalytic activity was observed due to ligand decomposition, as identified by differential thermal gravimetric analysis (refer to Figure S3.1 in the Supporting Information).

An Arrhenius plot for propene hydroformylation in the temperature interval 353-413 K is shown in Figure 3.3. The apparent activation energy for *n*-butanal formation is 60 kJ mol^{-1} measured over the interval 353-373 K and 24 kJ mol^{-1} measured over the interval 383-413 K. The value measured at low temperature for *n*-butanal is in agreement with previous reports for SILP catalysts [14]. The apparent activation energy for isobutanal formation is greater than that for *n*-butanal and decreases from 72 kJ mol^{-1} measured over the interval 353-373 K to 55 kJ mol^{-1} measured over the interval 383-413 K. To determine whether the decrease in activation energy was due to internal mass transfer limitations, the catalyst (> 150 μm) was crushed and sieved into small particles (< 50 μm). Table 1 shows that the activities at low and high temperature are independent of particle size, leading to the conclusion that the catalytic activity remains kinetically

controlled at high temperature. As discussed below, the observed decrease in the apparent activation at high temperature can be ascribed to a change in the rate-determining step (RDS) in the mechanism of propene hydroformylation.

Table 3.1 Activity of different sized particles of SX-Rh/SiO_2 SILP catalyst.

Particle Size	Rate (h^{-1}) [a]	
(μm)	363 K	413 K
< 50	32	151
> 150	35	155

[a] mol *n*-butanal (mol Rh h)$^{-1}$

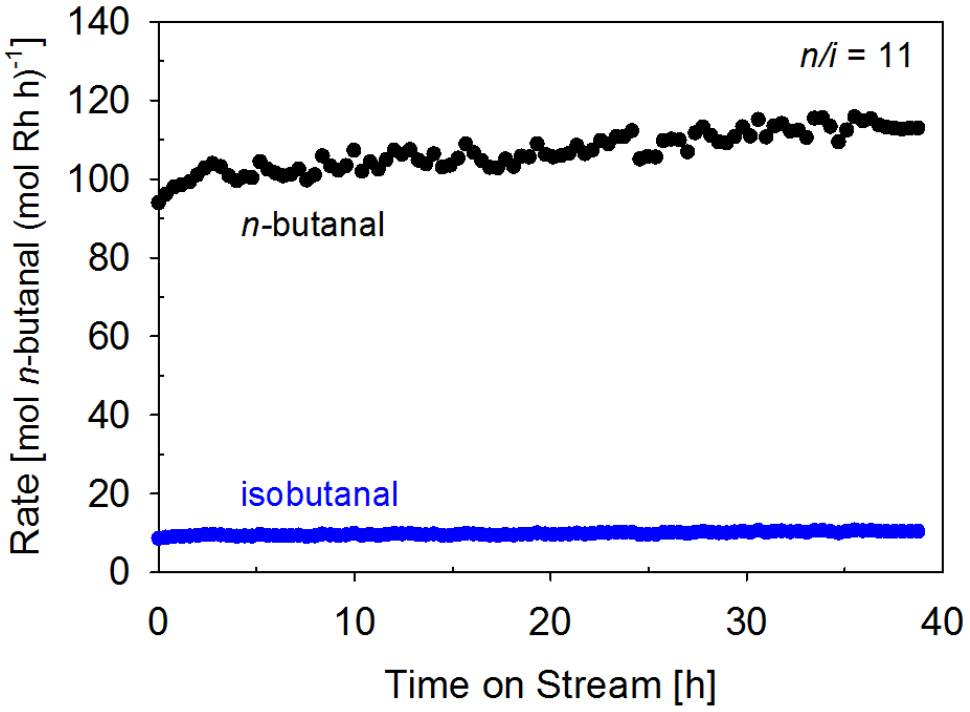

Figure 3.1 Time on stream study with SX-Rh/SiO_2 SILP catalysts. T = 393 K, P_{Total} = 2 atm, C_3H_6:H_2:CO = 1:1:1, catalyst mass = 0.3 g, total gas flow rate = 120 cm^3 min^{-1} at STP.

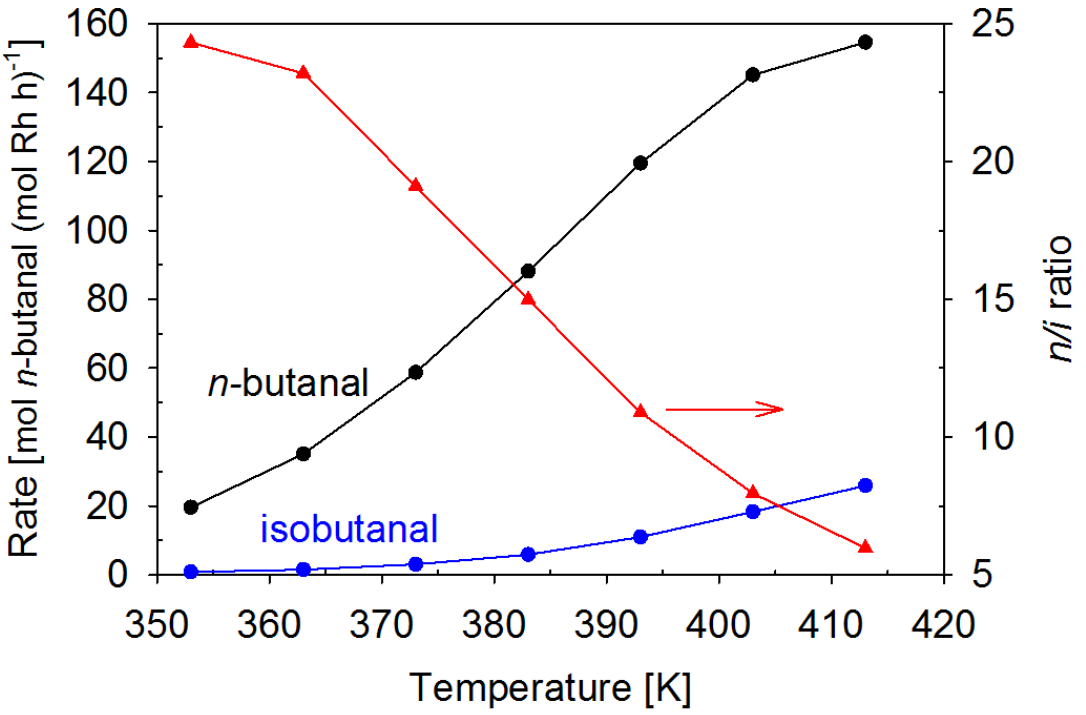

Figure 3.2 Effect of temperature on rate of butanal synthesis and regioselectivity. (●,●) Rate, (▲) *n/i* ratio, P_{Total} = 2 atm, C_3H_6:H_2:CO = 1:1:1, catalyst mass = 0.3 g, total gas flow rate = 120 cm^3 min^{-1} at STP.

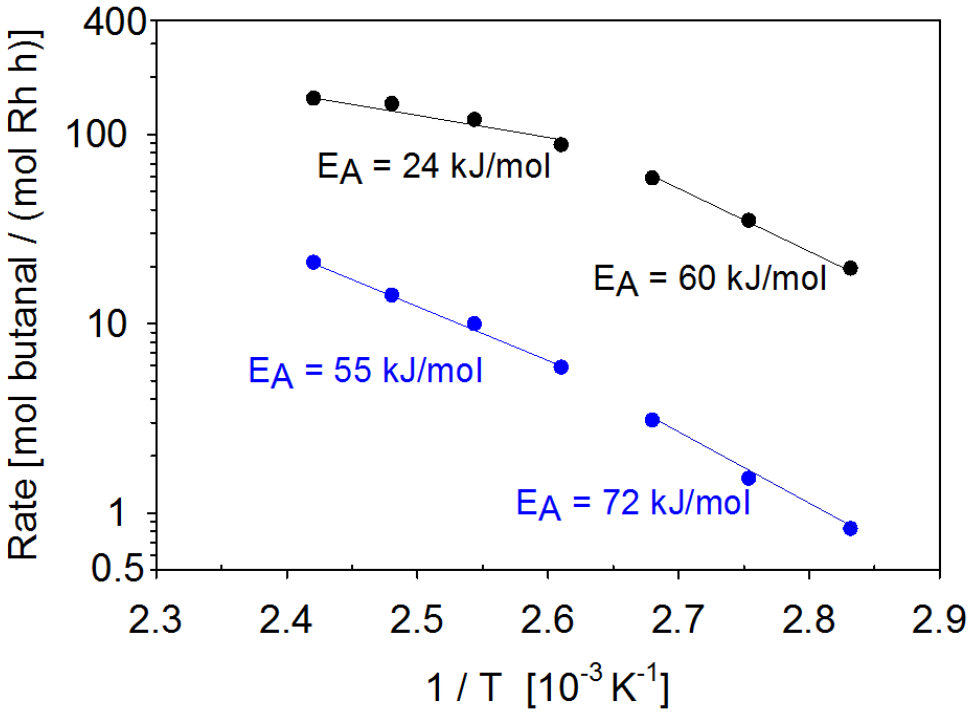

Figure 3.3 Arrhenius plot showing the apparent activation energies of (●) *n*- and (●) isobutanal formation. P_{Total} = 2 atm, C_3H_6:H_2:CO = 1:1:1, catalyst mass = 0.3 g, total gas flow rate = 120 cm^3 min^{-1} at STP.

3.3.1 Kinetics of Propene Hydroformylation

The dependences of the rate of *n*- and isobutanal formation on the partial pressures of propene, CO, and H_2 were measured by holding the partial pressures of two components at 0.67 atm while the partial pressures of the third reactant and He were varied. The total gas flow rate and pressure were kept constant at 60 cm^3 $min^{-1}$and 2 atm (120 cm^3 min^{-1} at STP).

Figure 3.4a-f illustrates the effect of varying the partial pressures of C_3H_6, CO, and H_2 partial pressures on the catalytic activity at 363 K and 413 K. The molar *n/i* ratio was also found to be a weak function of the reactant partial pressures, changing by less than ~10% over the pressure range investigated. The order of reaction with respect to H_2, CO, and C_3H_6 for *n*-butanal and isobutanal formation are similar and follow the same trend. As shown in Figure 3.4a-b, the partial pressure dependence of H_2 on the rate of *n*- and isobutanal formation is nearly zero order at 363 K but is nearly first order at 413 K. At an intermediate temperature of 393 K, the partial pressure dependence of H_2 is 0.3. The partial pressure dependence on CO shown in Figures 3.4c-d is roughly -0.5 at 363 K but increases to nearly zero at 413 K. As shown in Figure 3.4e-f, the order with respect to C_3H_6 decreases slightly from 0.9 to 0.7 when measured at 363 K and 413 K, respectively.

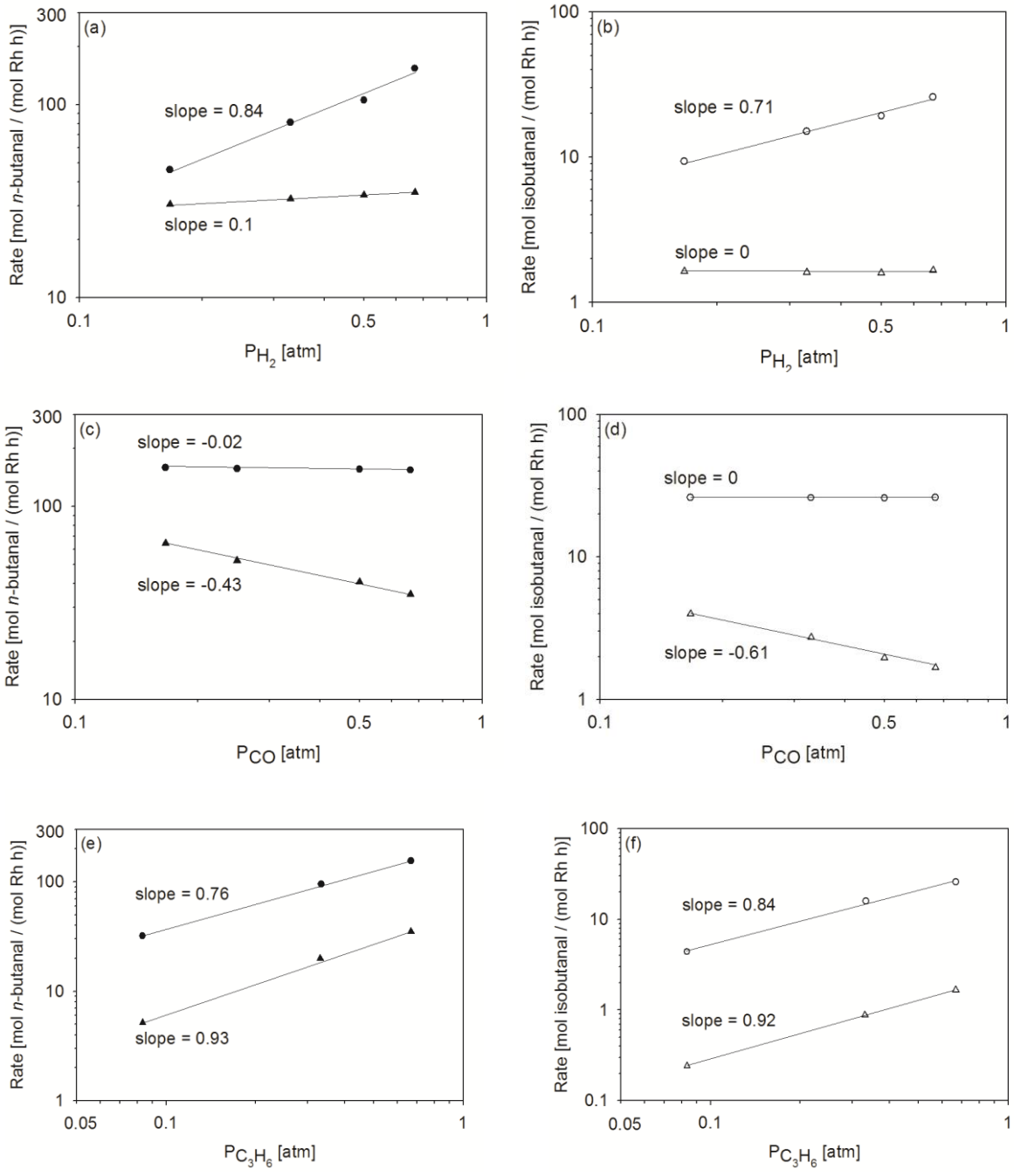

Figure 3.4 Log-log plot of the effect of reactant partial pressures on the rates of (●,▲) *n*- and (○,△) isobutanal synthesis. (●,○) T = 413 K, (▲,△) T = 363 K. P_{Total} = 2 atm, (a,b) $P_{CO} = P_{C_3H_6}$ = 0.67 atm, balance He, (c,d) $P_{C_3H_6} = P_{H_2}$ = 0.67 atm, balance He, (e,f) $P_{CO} = P_{H_2}$ = 0.67 atm, balance He. Catalyst mass = 0.3 g, total gas flow rate = 120 cm^3 min^{-1} at STP.

3.4 Discussion

3.4.1 Rate Expressions for Butanal Synthesis

The kinetics of butanal formation can be interpreted using the mechanism proposed by Heck and Breslow [25] adapted by Wilkinson [22]. As shown in Scheme 3.1, the hydroformylation of propene is initiated by the loss of a CO ligand from $HRh(CO)_2SX$ (species **A**) to form the 16-electron species **B** via Reaction 1. Propene then coordinates to species **B** to form a η^2-Rh complex (species **C**)**.** Migratory insertion into the Rh-H bond forms a propyl-Rh complex (species **D**) via Reaction 3. CO then adds to species **D** to form an 18-electron intermediate species **E** in Reaction 4. Migratory insertion of the propyl to a carbonyl group leads to the formation of an acyl intermediate (species **F**) via Reaction 5. Oxidative addition of H_2 (Reaction 6) forms the 18-electron Rh(III) species **G**, followed by the reductive elimination of butanal (Reaction 7). Isobutanal is formed in a catalytic cycle by an analogous mechanism, in which species **D-G** involve a secondary, rather than a primary, alkyl species.

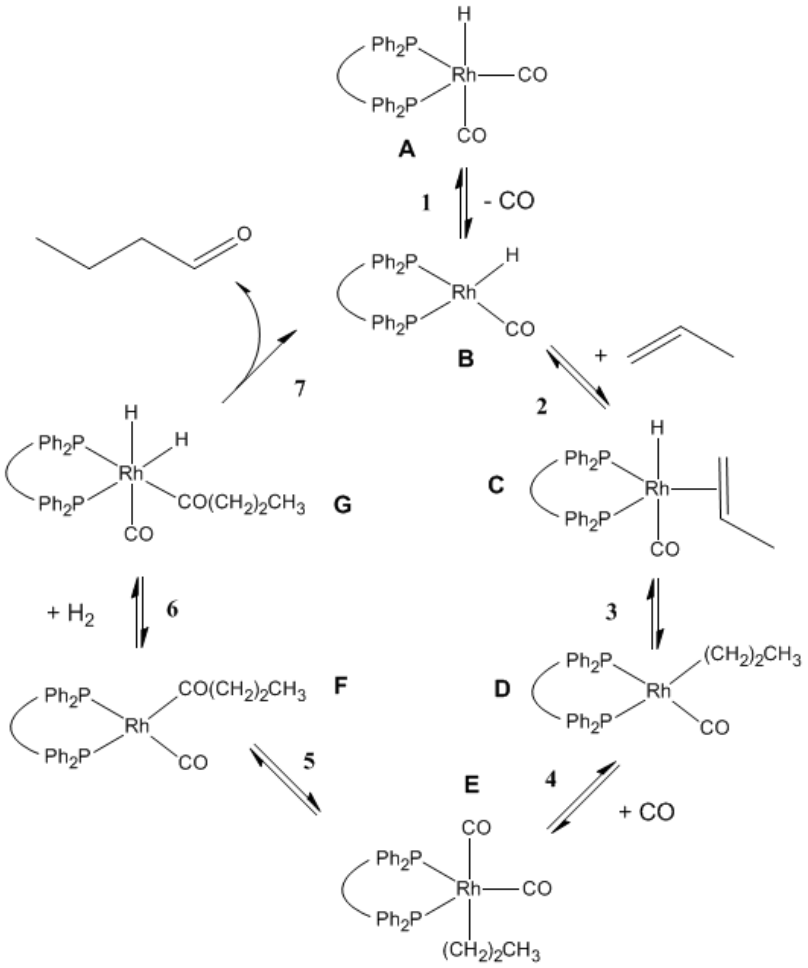

Scheme 3.1 Proposed mechanism for the hydroformylation of propene.

The observed reaction orders at 363 K suggest that the RDS is either alkene coordination (Reaction 2) or alkene insertion (Reaction 3) into the Rh-H bond. Support for Reaction 3 being the RDS can be drawn from the work of van Leeuwen and coworkers using homogeneous Rh-xantphos complexes [26]. While isotopic experiments ($^{1}H/^{2}H$ and $^{12}C/^{13}C$) were unable to determine the RDS irrefutably, their hybrid quantum mechanical/molecular mechanical (QM/MM) calculations suggested that alkene insertion is the RDS. In agreement with van Leeuwen's conclusion that olefin chemisorption is a barrierless process, other theoretical studies were unable to locate a transition state for olefin coordination to $HRh(PH_3)_2CO$ complexes [27,28]. For these reasons, alkene insertion into the Rh-H bond is taken as the RDS. If Reaction 1 and 2 are assumed to be quasi-equilibrated and Reaction 3 is the irreversible, rate-limiting step, then the rate of butanal formation is given by the following relation:

$$r_{butanal} = \frac{K_1 K_2 k_3 P_{C_3H_6}[Rh]}{P_{CO} + K_1 + K_1 K_2 P_{C_3H_6}} \qquad (2)$$

where k_i is the rate coefficient for Reaction i, K_i is the equilibrium constant for Reaction i, P_j is the partial pressure of species j, and *[Rh]* is the total moles of Rh. Implicit in this rate equation is the assumption that the concentrations of species **D-G** are negligible.
Eq. 2 is consistent with the observed kinetics at 363 K. Similar kinetics have been reported for homogenous hydroformylation Rh complexes [29-31]. The rate of butanal synthesis is zero order in the partial pressure of H_2 and less than first order in the partial pressure of C_3H_6. As the partial pressure of C_3H_6 increases, the $K_1K_2P_{C_3H_6}$ term in the denominator becomes increasingly significant, thereby reducing the effective order from unity. The experimentally observed, inhibitory effect of CO is also represented effectively by Eq. 2. Since the order of CO is -0.4, the remaining terms in the denominator are significant in magnitude compared to P_{CO}.

At 413 K, the partial pressure dependence on H_2 and CO becomes nearly first order and zero order, respectively, suggesting a change in the RDS from olefin insertion (Reaction 3) to oxidative addition of H_2 (Reaction 6). If Reaction 6 is considered to be the irreversible, rate-limiting step and Reactions 1-5 are considered quasi-equilibrated, then the rate of butanal formation will be given by the following relation:

$$r_{butanal} = \frac{K_1 K_2 K_3 K_4 K_5 k_6 P_{C_3H_6} P_{H_2}[Rh]}{1 + (K_1 K_2 K_3 K_4 + K_1 K_2 K_3 K_4 K_5) P_{C_3H_6}} \qquad (3)$$

Terms in the denominator inversely proportional to the partial pressure of CO must be negligible in order to be consistent with the experimental results. The less than first order dependence observed for propene suggests that the terms in the denominator proportional to the partial pressure of propene are significant in magnitude relative to unity. Further evidence for a change in the RDS is provided by the observation of a partial pressure dependence on H_2 of 0.3 at 393 K. At this intermediate temperature, Eqns. 2 and 3 contribute to the overall rate, resulting in an increase in the order with respect to H_2 found at 363 K.

MATLAB was used to estimate the parameters appearing in Eq. 2 and Eq. 3. Values for the parameters or groups of parameters are listed in Table 3.2 for *n*- and isobutanal formation. As seen in Figure 5a-d, the derived rate expressions (Eqns. 2 and 3) adequately describe the data acquired at 363 K and 413 K. The coefficient of determination, R^2, was above 90% for all cases considered.

3.4.2 Regioselectivity

The decrease in *n/i* molar ratio with increasing temperature shown in Figure 3.2 can be rationalized in terms of the RDS in each temperature regime and the corresponding rate expressions for *n*- and isobutanal formation. The regioselectivity is determined by the alkene insertion into the Rh-H bond to form either a primary or secondary alkyls. At low temperature, alkene insertion is the RDS and the apparent activation energies measured for *n*- and isobutanal formation are 60 and 72 kJ mol^{-1}, respectively. Therefore, the resulting *n/i* ratio is high because primary alkyls are favored kinetically over secondary alkyls. Theoretical studies by Bo and coworkers have demonstrated that the transition for the formation of secondary alkyls is approximately 9 kJ mol^{-1} greater than primary alkyls due to the steric effects from the phenyl groups of the phosphine ligand [32]. To a first approximation, the ratio of rate constants for alkene insertion to form either a primary or secondary alkyl (k_3) can effectively model the temperature effect on the *n/i* ratio. However, the model begins to fail above 383 K due to the change in the RDS. The deviations arise due the influence of equilibrium constants corresponding to Reactions 3-5. The decrease in the *n/i* ratio at high temperature is due to a shift in the equilibrium from the thermodynamically favorable primary alkyl complex [33] to the less favorable secondary alkyl complex. Our results are consistent with previous deutroformylation studies which found that Rh-alkyl formation is irreversible at low temperature, but is reversible at higher temperatures [34,35].

Table 3.2 Nonlinear regression results for Eq. 2 and Eq. 3.

363 K				413 K			
$r_{butanal} = \frac{K_1K_2k_3P_{C_3H_6}[Rh]}{P_{CO} + K_1 + K_1K_2P_{C_3H_6}}$				$r_{butanal} = \frac{aP_{C_3H_6}P_{H_2}[Rh]}{1 + (K_1K_2K_3K_4 + K_1K_2K_3K_4K_5)P_{C_3H_6}}$			
Parameter	Product		Unit	Parameter	Product		Unit
	n- [a]	iso [b]			*n*- [a]	iso [b]	
K_1	0.16	0.05	atm	$a = K_1K_2K_3K_4K_5k_6$	589	85.6	$atm^{-2}\ h^{-1}$
K_2	2.7	3.9	atm^{-1}	$b = K_1K_2K_3K_4$	0.89	0.22	atm^{-1}
k_3	134	10.7	h^{-1}	K_5	0.20	1.8	--
				$k_6 = a(bK_5)^{-1}$	3287	210	$atm^{-1}\ h^{-1}$

[a] n-butanal, [b] isobutanal

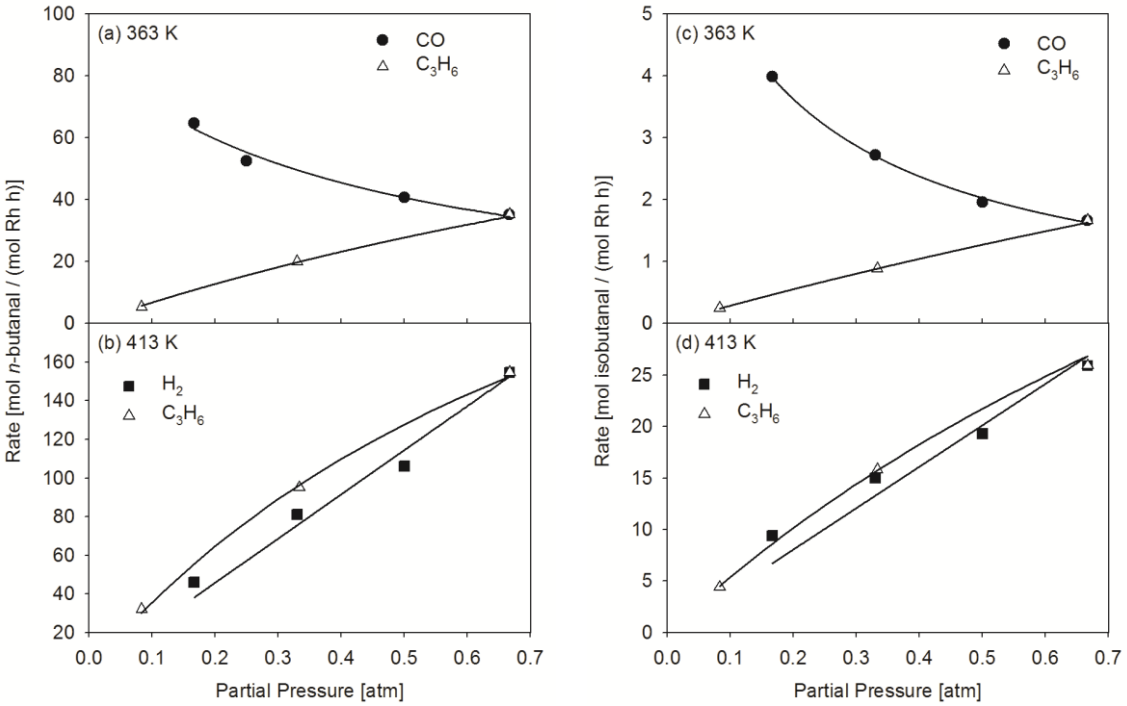

Figure 3.5 Rate of (a,b) *n*- and (c,d) isobutanal synthesis vs. partial pressure of (●) CO, (△) C_3H_6, (■) H_2. Experimental points are indicated by data markers. Spline curves indicate predicted values. P_{Total} = 2 atm, catalyst mass = 0.3 g, total gas flow rate = 120 cm^3 min^{-1} at STP.

3.4.3 Entropic Effects on the RDS

The shift in the RDS with increasing temperature can be ascribed to a change in the elementary step with the largest Gibbs free energy of activation ($\Delta G^{\ddagger} = \Delta H^{\ddagger} - T\Delta S^{\ddagger}$). At 363 K, the $\Delta G^{\ddagger}$ for alkene insertion is greater than $\Delta G^{\ddagger}$ for oxidative addition due to a larger enthalpic barrier. Theoretical analysis of alkene hydroformylation on $HRh(PH_3)_2(CO)$ has shown that the activation enthalpy barrier for alkene insertion is 40 kJ mol^{-1} larger than for oxidative addition of H_2 [27]. However, the contribution of the entropic term to $\Delta G^{\ddagger}$ becomes more significant with increasing temperature. The intrinsic entropy of activation is expected to be more negative for oxidative addition of H_2 (Reaction 6) than for alkene insertion (Reaction 3) due to the loss in entropy resulting from the binding of gas-phase H_2. The value of $\Delta S^{\ddagger}$ for oxidative addition was estimated to be approximately -100 J mol^{-1} K^{-1} based upon the removal of translational and rotational degrees of freedom of H_2 [36]. This value of $\Delta S^{\ddagger}$ is sufficient to cause the magnitude of $\Delta G^{\ddagger}$ for the oxidative addition step to become greater than that of alkene insertion at 393 K given the difference in the enthalpic barriers and assuming that $\Delta S^{\ddagger}$ of alkene insertion is negligible. Hence, the change in the RDS from alkene insertion to the oxidative addition of H_2 can be ascribed to a change in the entropic contribution to the intrinsic rate parameter.

3.5 Conclusions

The kinetics of propene hydroformylation over a silica-supported Rh-sulfoxantphos complex has been investigated. Reaction temperature was found to have profound effects on the regioselectivity and the nature of the rate-determining step (RDS). Evidence for this change was observed by performing kinetic experiments at 363 K and 413 K. At low temperature, the RDS is alkene insertion into the Rh-H bond, but at high temperature the oxidative addition of H_2 becomes rate-limiting. Although the partial pressure dependence of C_3H_6 was roughly unaltered by temperature, the partial pressure dependences of H_2 and CO were found be to substantially dependent on temperature. The partial pressure dependence of H_2 was nearly zero order at low temperature, but is nearly first order at high temperature. The partial dependence of CO was -0.4 at low temperature, but was zero order at high temperature. Based upon the mechanism for hydroformylation, rate expressions were derived in the high and low temperature regime. The parameters appearing in these rate expressions were estimated by nonlinear regression. Variation in the RDS can be rationalized in terms of the elementary step with largest Gibbs free energy of activation. The enthalpic barrier of activation is greater for alkene insertion than oxidative addition, which causes alkene insertion to be the RDS at low temperature. However, the greater loss in entropy for the oxidative addition reaction causes the oxidative addition of H_2 to become the RDS at high temperature.

3.6 Aknowledgements

This work was supported by the XC^2 program funded by BP. The authors would like to thank the Wasserscheid Group in Erlangen, Germany for providing the sulfoxantphos ligand and Eric Bloch for his assistance in performing dTGA.

3.7 Supporting Information

3.7.1 Derivation of Rate Expressions

Assuming alkene insertion to be the rate-determining step (RDS), the rate of butanal formation is:

1) $r_3 = k_3[C]$

where [*I*] represents the concentration of species *I* shown in Scheme 3.1. The concentration of the reactive intermediates can be determined using the quasi-equilibrium assumption:

2) $[C] = K_2[B]P_{C_3H_6}$
3) $[B] = K_1[A]P_{CO}^{-1}$

Substituting Eqn. 2 and 3 into Eq. 1 yields:

4) $r_3 = K_1K_2k_3[A]P_{C_3H_6}P_{CO}^{-1}$

In order to solve for the concentration of [*A*], perform a Rh balance:

5) $[Rh] = [A] + [B] + [C] + [D] + [E] + [F] + [G]$

Assuming the intermediates prior to the RDS are the most abundant intermediates, we neglect [*D*]-[*G*].

6) $[Rh] = [A] + [B] + [C]$

Performing algebraic manipulations to solve for [*A*]:

7) $[A] = [Rh]\left(1 + \frac{[B]}{[A]} + \frac{[C]}{[A]}\right)^{-1}$

Substituting equilibrium expression Eqns. 2 and 3 into Eq. 7 yields:

8) $[A] = [Rh]\left(1 + K_1P_{CO}^{-1} + K_1K_2P_{C_3H_6}P_{CO}^{-1}\right)^{-1}$

Substituting Eq. 8 into Eq. 4 yields the final rate expression:

9) $r_3 = \frac{K_1K_2k_3P_{C_3H_6}[Rh]}{P_{CO}+K_1+K_1K_2P_{C_3H_6}}$

In order to derive the rate expression when the oxidative-addition of hydrogen is the RDS, follow the same procedure as outlined above. First, express the rate as a function of the RDS:

10) $r_6 = k_6[F]P_{H_2}$

The concentration of the reactive intermediates can be determined using the quasi-equilibrium assumption:

11) $[F] = K_5[E]$
12) $[E] = K_4[D]P_{CO}$
13) $[D] = K_3[C]$

Substituting Eqns. 11, 12, 13 into Eq. 10 yields:

14) $r_6 = K_1K_2K_3K_4K_5K_6k_6[A]P_{C_3H_6}P_{H_2}$

A Rh balance yields:

15) $[Rh] = [A] + [B] + [C] + [D] + [E] + [F]$

Solving for $[A]$ yields:

16) $[A] = [Rh]\left(1 + \frac{[B]}{[A]} + \frac{[C]}{[A]} + \frac{[D]}{[A]} + \frac{[E]}{[A]} + \frac{[F]}{[A]}\right)^{-1}$

Assuming terms proportional to the CO partial pressure are negligible and the remaining terms correspond to the most abundant surface intermediates, the expression for the concentration of $[A]$ is:

17) $[A] = [Rh]\left(1 + K_1K_2K_3K_4P_{C_3H_6} + K_1K_2K_3K_4K_5P_{C_3H_6}\right)^{-1}$

Substituting Eq. 17 into Eq. 14 yields the final rate expression.

18) $r_6 = \frac{K_1K_2K_3K_4K_5K_6k_6P_{C_3H_6}P_{H_2}[Rh]}{1+K_1K_2K_3K_4P_{C_3H_6}+K_1K_2K_3K_4K_5P_{C_3H_6}}$

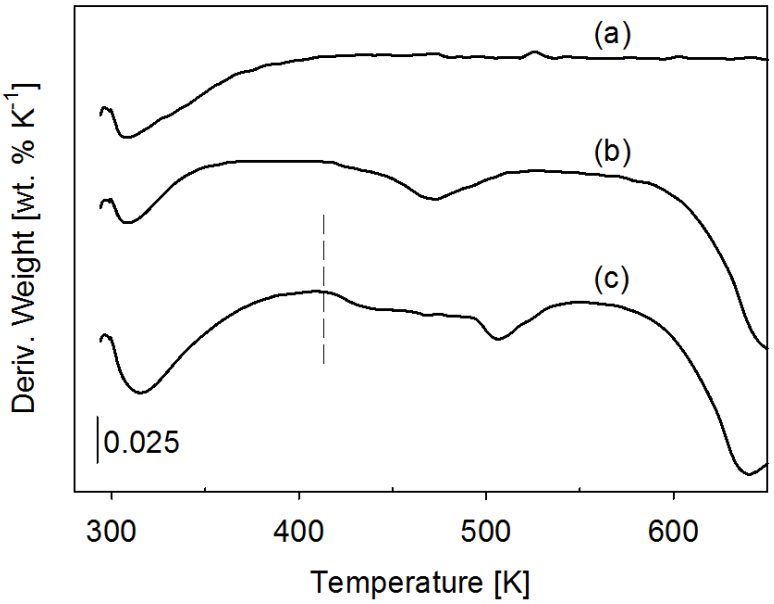

Fig. S3.1 Differential thermogravimetric analysis of (a) [bmim][$OctSO_4$]/SiO_2, (b) SX/SiO_2, (c) fresh SX-Rh/SiO_2 SILP catalyst. Analysis was conducted on a TA instrument TGA 5000. Approximately 15 mg of the sample was loaded into a platinum pan under N_2 (25 cm^3 min^{-1}) atmosphere. The temperature was increased from ambient conditions to 773 K at a rate of 10 K min^{-1}.

3.8 References

[1] C. W. Kolpainter, R. W. Fischer, B. Cornils. *Appl. Catal. A.* **2001**, 221, 219-225.

[2] D. J. Cole Hamilton. *Science* **2003**, 299, 1702-1706.

[3] P. W. N. M. van Leeuwen, C. Claver. in: *Rhodium Catalyzed Hydroformylation*, Kluwer Academic Publishers, AA Dordrecht, **2000**, 189.

[4] R. J. Davis, J. A. Rossin, M. E. Davis. *J. Catal.***1986**, 98, 477-487.

[5] A. J. Sandee, L. A. van der Veen, J. N. H. Reek, P. C. J. Kamer, M. Lutz, A. L. Spek, P. W. N. M. van Leeuwen. *Angew. Chem. Int. Ed.* **1999**, 38, 3231-3235.

[6] L. Yan, Y. J. Ding, L. W. Lin, H. J. Zhu, H. M. Yin, X. M. Li, Y. Lu. *J. Mol. Catal. A: Chem.* **2009**, 300, 116-120.

[7] T. Kim, F. E. Celik, D. G. Hanna, S. Shylesh, S. Werner, A. T. Bell. *Top. Catal.* **2011**, 54, 299-307.

[8] L. A. Gerritsen, A. van Meerkerk, M. H. Vreugdenhil, J. J. F. Scholten. *J. Mol. Catal.* **1980**, 9, 139-155.

[9] J. P. Arhancet, M. E. Davis, B. E. Hanson. *J. Catal.* **1990**,129, 94-99.

[10] C. Disser, C. Muennich, G. Luft. *Appl. Catal., A.* **2005**, 296, 201-208.

[11] J. P. Arhancet, M. E. Davis, J. S. Merola, B. E. Hanson. *Nature.* **1989**, 339, 454-455.

[12] C. P. Mehnert, R. A. Cook, N. C. Dispenziere, M. J. Afeworki. *J. Am. Chem. Soc.* **2002**, 124, 12932-12933.

[13] A. Riisager, K. M Eriksen, P. Wasserscheid, R. Fehrmann. *Catal. Lett.* **2003**, 90, 149-153.

[14] A. Riisager, R. Fehrmann, M. Haumann, B. S. K Gorle, P. Wasserscheid. *Ind. Eng. Chem. Res.* **2005**,44, 9853-9859.

[15] A. Riisager, R. Fehrmann, S. Flicker, R. van Hal, M. Haumann, P. Wasserscheid. *Angew. Chem. Int. Ed*. **2005**, 44, 815-819.

[16] S. Shylesh, D. G. Hanna, S. Werner. A. T. Bell. *ACS Catal.* **2012**, 2, 487-493.

[17] R. M. Deshpande, R. V. Chaudhari. *Ind. Eng. Chem. Res.* **1988**, 27, 1996-2002.

[18] D. Y. Murzin, A. Bernas, T. J. Salmi. *J. Mol. Catal. A: Chem.* **2010**, 315, 148-154.

[19] P. W. N. M. van Leeuwen, C. Claver. in: *Rhodium Catalyzed Hydroformylation*, Kluwer Academic Publishers, AA Dordrecht, **2000**.

[20] L. A. van der Veen, P. H. Keeven, G. C. Shoemaker, J. N. H. Reek, P. C. J. Kamer, P. W. N. M. van Leeuwan, M. Lutz, A. L. Spek. *Organometallics*. **2000**, 19, 872-883.

[21] P. C. J. Kamer, A. van Rooy, G. C. Schoemaker, P. W. N. M. van Leeuwen. *Coord. Chem. Rev.* **2004**, 248, 2409-2424.

[22] C. K. Brown, G. Wilkinson. *J. Chem. Soc. A* **1970**, 2753-2764.

[23] W. P. Mul, K. Ramkisoensing, P. C. J. Kamer, J. N. H Reek, A. J. van der Linden, A. Marson, P. W. N. M. van Leeuwen. *Adv. Synth. Catal.* **2002**, 344, 293-298.

[24] P. Wasserscheid, R. van Hal, A. Bosmann. *Green Chem.* **2002**, 4, 400-404.

[25] R.F. Heck, D.S. Breslow. *J. Am. Chem. Soc.* **1962**, 84, 2499-2502.

[26] E. Zuidema, L. Escorihuela, T. Eichelsheim, J. J. Carbo, C. Bo , P. C. J. Kamer, P. W. N. M van Leeuwen. *Chem. Eur. J.* **2008**, 14, 1843-1853.

[27] S. A. Decker, T. R. Cundari. *Organometallics.* **2001**, 20, 2827-2841.

[28] T. Matsubara, N. Koga, Y. Ding, D.G. Musaev, K. Morokuma. *Organometallics.* **1997**, 16, 1065-1078.

[29] G. Kiss, E. J. Mozeleski, K. C. Nadler, E. VanDriessche, C. DeRoover. *J. Mol. Catal. A: Chem.* **1999,**138, 155-176.

[30] R. M. Deshpande, B. M. Bhanage, S. Kanagasabapathy, R. V. Chaudhari. *Ind. Eng. Chem. Res.* **1998**, 37, 2391-2396.

[31] S. S. Divekar, R. M. Desphande, R. V. Chaudhari. *Catal. Lett.* **1993**, 21, 191-200.

[32] J. J. Carbo, F. Maseras, C. Bo, P. W. N. M. van Leeuwen. *J. Am. Chem. Soc.* **2011**, 123, 7630-7637.

[33] R. H. Crabtree. The Organometallic Chemistry of the Transition Metals, 4th ed, John Wiley & Sons, Inc., Hoboken, 2005, p. 194.

[34] R. Lazzaroni, R. Settambolo, A. Raffaelli, S. Pucci, G. Vitulli, J. *Organomet. Chem.* **1988**, 339, 357-365.

[35] C. P. Casey, L. M. Petrovich. *J. Am. Chem. Soc.* **1995**, 117, 6007-6014.

[36] D. A. McQuarrie. in: Statistical Mechanics, University Science Books, Sausalito, **2000**, 108.

Chapter 4

In situ Formation of Wilkinson-Type Hydroformylation Catalysts: Insights into the Structure, Stability and Kinetics of Triphenyl Phosphine- and Xantphos-Modified Rh/SiO_2

Abtract

An investigation has been carried out to identify the effects of catalyst preparation on the activity, selectivity, and stability of phosphine-modified rhodium-silica catalysts (Rh/SiO_2) for propene hydroformylation. High selectivity to aldehydes was achieved, without the formation of propane or butanol. Catalyst activity and selectivity was found to depend strongly on the nature and concentration of the phosphine ligands and the amount of rhodium dispersed on the silica support. Screening of different ligands showed that a bidentate xantphos (X) ligand was approximately two fold more active than the monodentate phosphine ligand (PPh_3) screened at a ligand to rhodium ratio of 15:1. Investigation of the effects of reaction temperature, reactant partial pressures, and phosphine to rhodium ratio indicates that the kinetics of propene hydroformylation over X-promoted Rh/SiO_2 is nearly identical to those for sulfoxantphos modified rhodium-containing supported ionic liquid phase (SX-Rh SILP) catalysts. In situ FT-IR and solid-state ^{31}P MAS NMR characterization provide evidence for the formation of $HRh(CO)_n(PPh_3)_{4-n}$ species on PPh_3-modified Rh/SiO_2, and $HRh(CO)_2(X)$ species on xantphos-modified Rh/SiO_2. The high catalytic activity observed over rhodium-containing silica catalysts is attributed to formation of $Rh^I(CO)_2$ species by the process of corrosive chemisorption of Rh nanoparticles by CO and the subsequent ligation of phosphine ligands to the dicarbonyl species. Evidence is also presented suggesting that the active form of the catalyst resides on the surface of the Rh nanoparticles.

4.1 Introduction

The hydroformylation of alkenes to produce aldehydes is carried out on a large scale using an aqueous solution of a Rh-tppts complex (tppts = tri(*m*-sulfonyl) triphenyl phosphine trisodium salt) [1-3]. While this process is highly effective it is limited to alkenes with fewer than four carbon atoms due to the low solubility of higher molecular weight alkenes. The need to separate the reaction products from the catalyst solution presents additional challenge for carrying out alkene hydroformylation using homogeneous complexes [4]. Heterogenization of homogeneous catalysts on solid supports can easily mitigate these problems and enable alkene hydroformylation to be carried out in the gas phase or in the liquid phase without need for a solvent [5,6]. Several attempts have been made to achieve this goal. Davis and coworkers have shown that a supported aqueous phase (SAP) catalyst can be prepared by dispersing tppts to $Rh(acac)(CO)_2$ dissolved in a thin aqueous layer within the pores of a high-surface area silica [7]. Exposure of this impregnated solid to synthesis gas (H_2/CO = 1) at atmospheric pressure and room temperature produced an active catalyst for propene

hydroformylation. Wasserscheid and coworkers have shown that supported ionic liquid phase (SILP) catalysts can be prepared by dispersing a solution of the catalyst complex in an ionic liquid (IL) as a thin film on the internal surface of a porous solid [8-11]. The advantage to using ILs over water is the near zero vapor pressure of ILs, which virtually eliminates the loss of solvent under reaction conditions. Such SILP catalysts have been demonstrated to be highly effective for propene hydroformylation. The factors influencing the activity and stability of Rh-based SILP catalysts for the gas-phase hydroformylation of propene have been discussed by Shylesh et al. [12]. Evidence from in situ FT-IR and ^{31}P MAS NMR suggests that interactions of the IL and metal complex with the support are required to yield a stable catalyst. Catalyst activity is found to be a strong function of IL composition, as well as ligand-to-Rh ratio, IL loading, and temperature of support pretreatment. Ding and coworkers have reported a different approach for producing an active catalyst for propene hydroformylation. In this case, silica-supported Rh nanoparticles are promoted with PPh_3 [13, 14], and Kim et al. have recently shown that the highest activity for PPh_3-modified Rh/SiO_2 is achieved for PPh_3/Rh = 15 [15]. Due to the similarities in activation energies, partial and total pressure dependences of the reaction rates for PPh_3-modified Rh/SiO_2 and homogeneous $HRh(CO)(PPh_3)_3$ catalysts suggests that the active species in both systems are identical [15].

Here, we report the characterization and catalytic activity of a monodentate and bidentate phosphine-modified rhodium-silica (L-Rh/SiO_2, L = triphenyl phosphine (PPh_3) and xantphos (X)) catalysts for the gas-phase hydroformylation of propene under mild reaction conditions. The objective of this work was to explore how the catalytically active species are formed under reaction conditions, the effects of ligand composition, ligand/rhodium ratio, and rhodium loading affect the catalytic activity, selectivity, and stability of L-Rh/SiO_2 catalyst relative to silica-supported Wilkinson-type catalyst ($HRh(CO)(PPh_3)_3/SiO_2$). The kinetics of propene hydroformylation on bidentate xantphos-modified Rh/SiO_2 catalyst (X-Rh/SiO_2) and PPh_3-modified Rh/SiO_2 catalyst (PPh_3-Rh/SiO_2) are also discussed. In situ FT-IR characterization of the phosphine-modified Rh/SiO_2 catalyst was performed in order to obtain evidence for the formation of active species under the reaction conditions. These observations were complemented by ex-situ characterization of the catalysts by ^{31}P MAS NMR and HR-TEM. Results of the present study provide additional experimental evidence for in-situ formation of homogenous catalysts and the interactions of the homogenous catalyst with the rhodium nanoparticles dispersed on the support surfaces.

4.2 Methods

4.2.1 Catalyst Preparation

The preparation of PPh_3-modified Rh/SiO_2 was as follows. 0.2 wt. % Rh/SiO_2 was prepared by incipient-wetness impregnation of mesoporous SiO_2 (Silicycle, 500 m^2 g^{-1}, average pore diameter 60 Å) with a solution of rhodium (III) acetyl acetonate (Aldrich, 97%) dissolved in toluene (Alfa Aesar, anhydrous 99.8%). After impregnation, the solid was dried at 393 K for 12 h, then calcined in 100 cm^3 min^{-1} of 10% O_2/He (Praxair, certified standard) for 4 h at 673 K (2 K min^{-1}), and finally reduced in 100 cm^3

min^{-1} of 9% H_2/He (Praxair, certified standard) at 673 K for 4 h. Using incipient-wetness impregnation, a solution of PPh_3 (Aldrich, 99%) in toluene was absorbed onto the SiO_2-supported Rh under nitrogen atmosphere. After the impregnation, the solid was dried for 2 h at ambient temperature in nitrogen and then dried in a vacuum oven at 353 K for 12 h. The PPh_3/toluene solution concentration was varied to obtain final molar ratios of PPh_3/Rh between 5 and 20, and the rhodium loading was varied from 0.05 to 1 wt. %. A similar incipient-wetness impregnation procedure using toluene as a solvent was used for the preparation of xantphos-modified Rh/SiO_2 catalysts (X-Rh/SiO_2).

4.2.2 Gas-phase Hydroformylation of Propene

Gas-phase hydroformylation of propene was performed in a 6.35 mm OD (~4 mm ID) quartz tube containing an expanded section (~12.7 mm OD, ~20 mm length). The reactor was packed with quartz wool above and below the catalyst bed to hold the catalyst in place. The feed to the reactor consisted of propene (Praxair, 99.9%), CO (Praxair, 99.99%) and H_2 (Praxair, 99.999%). A reactant ratio of C_3H_6:CO:H_2 of 1:1:1 was used unless specified otherwise. Experiments were carried out at 393 K, total gas pressures of 2 atm, total gas flow rate of 120 cm^3 min^{-1} at STP in order to maintain a constant volumetric flow rate of 60 cm^3 min^{-1} at pressure. Under these conditions, the conversion of propene was always less than 1%. Reaction products were analyzed using an Agilent 6890N gas chromatograph containing a bonded and crosslinked (5%-phenyl)-methylpolysiloxane capillary column (Agilent, HP-1) connected to a flame ionization detector.

4.2.3 Catalyst Characterization

Infrared spectra were acquired using a Thermo Scientific Nicolet 6700 FT-IR spectrometer equipped with a liquid nitrogen cooled MCT detector. Each spectrum was obtained by averaging 32 scans taken with 1 cm^{-1} resolution. 0.05 g of SILP catalyst was pressed into a 20 mm-diameter pellet (< 1 mm thick) and placed into a custom-built transmission cell equipped with CaF_2 windows, a K-type thermocouple for temperature control, and resistive cartridge heaters. All scans were acquired at 393 K. Experiments at elevated pressure were carried out by throttling a needle valve located downstream from the reactor. The spectrum of the catalyst under He flow was subtracted from all the results reported.

Solid-state ^{31}P MAS NMR experiments were performed on a Bruker Avance I-500 MHz spectrometer using a frequency of 202.5 MHz, 90° pulse in 4.2 μs, and a delay of 60 s relative to 85% H_3PO_4. High-resolution transmission electron microscopy (HR-TEM) characterizations were conducted on the TEAM 0.5 high-resolution electron microscope, a modified FEI Titan 80-300 TEM equipped with a gun mono-chromator, operated at 80 KV at the National Center for Electron Microscopy (NCEM). Scanning transmission electron microscopy (STEM) images were taken on a FEI Tecnai F20 microscope operated at 200 KV and incorporated with a guan monochromator.

4.3 Results

4.3.1 Effect of Ligand Composition

It is known that the activity, selectivity, and stability of homogenous rhodium-phosphine complexes used for hydroformylation reactions are sensitive to the structure and concentration of the ligand [1]. The role of various phosphine ligands was therefore investigated at a fixed ligand to rhodium molar ratio of 15 (L/Rh = 15) and a rhodium loading of 0.2 wt.%. The ligands screened include triphenylphosphine (PPh_3), triphenyl phosphite ($P(OPh)_3$), fluorinated triphenyl phosphine (*3F*-PPh_3), methoxy triphenylphosphine (*OMe*-PPh_3) and bidentate xantphos (X). Table 4.1 shows that ligand composition had a strong effect on the catalyst activity and *n/i* ratio. Under identical reaction conditions, Rh/SiO_2 modified by bidentate xantphos was approximately two fold more active than the Rh/SiO_2 modified by monodentate phosphine ligands. The catalytic activity and *n/i* ratio observed for X-Rh/SiO_2 catalyst were similar to that observed over sulfoxantphos containing Rh-SILP (supported ionic liquid phase) catalysts [12] (refer to Figure S4.1 in the Supporting Information).

The higher activity of Rh complexes involving xantphos over monodentate phosphines can be attributed to the chelating ability of xantphos, which yields a higher concentration of the coordinated rhodium species [1]. Quite interestingly, an *n/i* ratio of 3 was observed over the phosphite-modified Rh/SiO_2 catalysts. Use of derivatives of triphenylphosphine with substituents typically in the para positions can obviate the problems of simultaneously changing the electronic and steric features of phosphine ligands [16]. For instance, electron-withdrawing groups in the para position decrease the basicity of the triphenylphosphine groups whereas electron-donating groups decrease the electrophilicity over the rhodium center without altering the steric confinement around the rhodium site. Accordingly, it should be noted that the *n/i* ratio of the aldehyde increased as the electron density around the rhodium was decreased by using electron-withdrawing substituents in the modifying phosphine ligand (-F *vs* -OMe, Table 4.1). In other words, less basic triaryl phosphines enhance the formation of linear products, whereas the more basic triaryl phosphine groups lead to lower *n/i* ratios.

Table 4.1 Results from the hydroformylation of propene using various phosphine-modified Rh/SiO_2 catalysts.

Catalyst	L/Rh ratio [a]	Rate (h^{-1}) [b]	*n/i*
X-Rh/SiO_2	15	78	13
PPh_3-Rh/SiO_2	15	35	9
3F-PPh_3-Rh/SiO_2	15	31	12
OMe- PPh_3-Rh/SiO_2	15	15	8
$P(OPh)_3$-Rh/SiO_2	15	24	3
SX-Rh/SILP	15	83	13

Reaction conditions: C_3H_6:H_2:CO = 1:1:1, P_{Total} = 2 atm, T = 393 K, t = 8 h, 0.2 wt. % Rh metal loading. [a] Molar ligand to metal ratio, [b] Rate in moles aldehyde per mole of Rh per hour.

4.3.2 Effect of L/Rh Molar Ratio

To investigate the role of phosphine ligands on the catalytic performance of Rh/SiO_2 catalysts, the L/Rh molar ratio (L = PPh_3 and X) was varied from 5-20 at a fixed rhodium loading of 0.2 wt.%. In the absence of ligands, Rh/SiO_2 is inactive for hydroformylation clearly showing the importance of phosphine ligands for promoting hydroformylation. Neither propane nor butanol was observed in the reaction products indicating that the phosphine-modified Rh/SiO_2 catalysts are highly selective towards the formation of aldehydes. The results in Figure 4.1 show that the hydroformylation rate increased rapidly with increasing L/Rh ratio up to a molar ratio of 15, and above this value the activity towards both products declined. The observed patterns were qualitatively similar for PPh_3 and X, but the catalytic activity was roughly two-fold higher for X. Irrespective of the L/Rh composition, bidentate xantphos-modified Rh/SiO_2 exhibited an almost constant *n/i* ratio of 12. It is important to note that an optimal X/Rh ratio has also been reported in studies of $HRh(CO)_2(X)$ complexes dissolved in various solvents [17,18]. By contrast, for PPh_3-modified Rh/SiO_2, the rate of linear product formation grew more rapidly than the rate of branched product formation up to a PPh_3/Rh ratio of 20, increasing the *n/i* ratio from approximately 3 to 13 (Figure 4.1a). The high *n/i* ratio observed in the present study for $PPh_3/Rh \geq 15$ is consistent with studies conducted with $HRh(CO)(PPh_3)_3$ in homogeneous solutions [15].

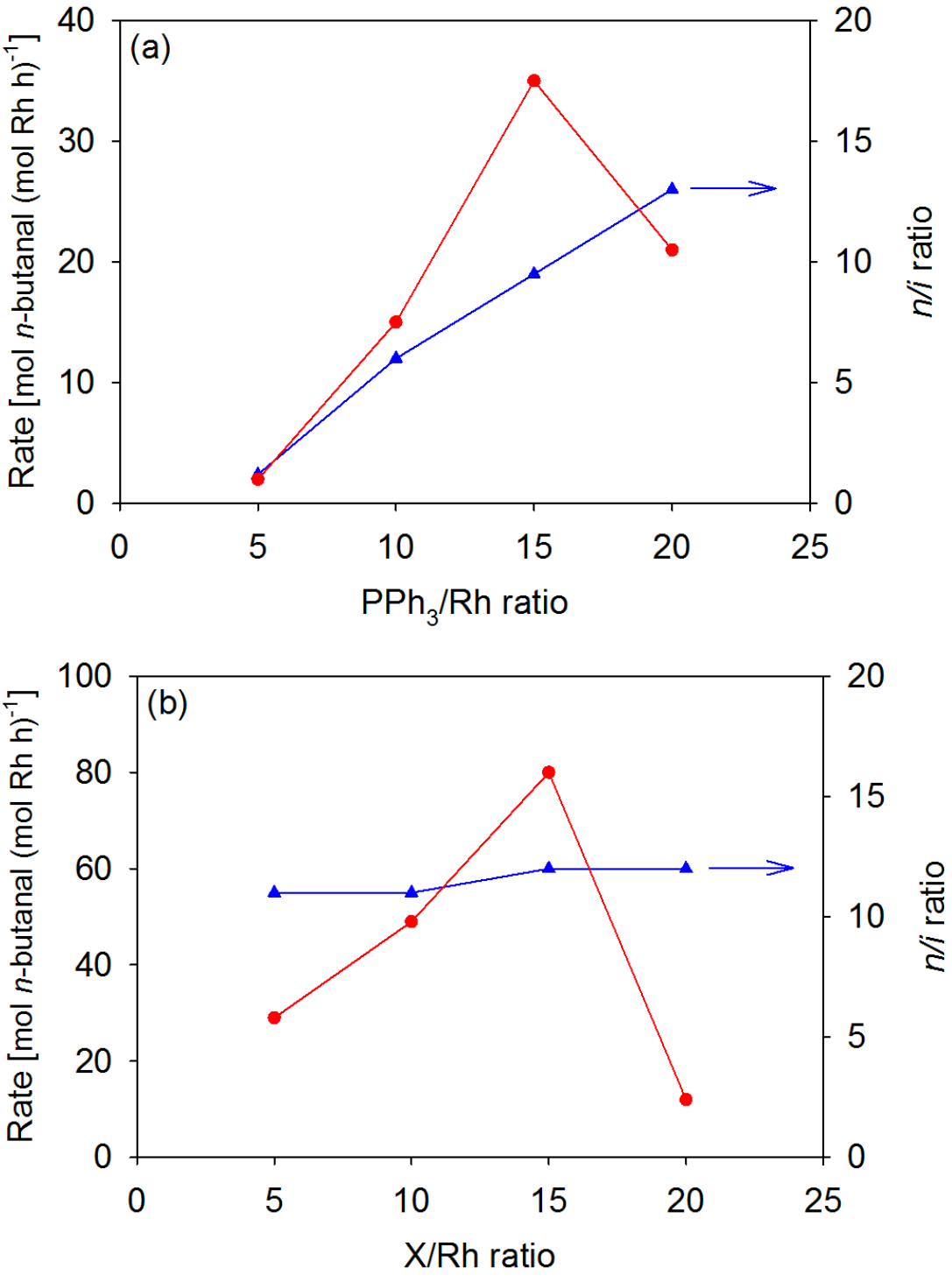

Figure 4.1 The effect of (a) PPh_3/Rh and (b) X/Rh ratios on the rates of butanal synthesis. P_{Total} = 2 atm, C_3H_6:CO:H_2 = 1:1:1, T = 393 K, L/Rh molar ratio = 5-20, 0.2 wt. % Rh, catalyst mass = 0.3 g, total gas flow rate = 60 cm^3 min^{-1} at pressure, 120 cm^3 min^{-1} at STP.

4.3.3 Effect of Rh Loading

The role of rhodium loading on the phosphine-modified Rh/SiO_2 catalyst was investigated by varying the rhodium concentration on the silica support from 0.05 to 1 wt.% at a fixed L/Rh molar ratio of 15. Figure 4.2 shows that, irrespective of ligand composition, the rate per rhodium atom increased almost four fold as the loading of rhodium decreased from 1 to 0.05 wt. %. It was also found that the *n/i* ratio decreased from approximately 9 to 4 with a decrease in the rhodium weight loading with the PPh_3-modified Rh/SiO_2 catalysts, whereas the *n/i* ratio remained constant at approximately 13 for the bidentate xantphos-modified Rh/SiO_2 catalysts.

4.3.4 Kinetics of Propene Hydroformylation using L-Rh/SiO_2 Catalysts

Time-on-stream studies demonstrated that the L-Rh/SiO_2 catalysts were stable for 30 h and no deactivation was observed under the reaction conditions. There is no loss in the rhodium content on phosphine-modified Rh/SiO_2 catalysts as analyzed from the ICP-OES analysis. The only products observed under any of the conditions investigated were *n*- and isobutanal. Figure 4.3 shows the effects of reaction temperature on the catalytic activity and the *n/i* ratio of the phosphine-modified Rh/SiO_2 catalyst (PPh_3-Rh/SiO_2) and xantphos-modified Rh/SiO_2 catalyst (X-Rh/SiO_2) for an L/Rh molar ratio of 15. For PPh_3-Rh/SiO_2 catalysts the rate of *n*-butanal formation increased with temperature up to 393 K, after which the rate decreased. The ratio of *n*- to isobutanal peaked a maximum value of 24 at 363 K and then decreased sharply to 3 at 413 K. The decrease in the rate of *n*-butanal formation above 393 K is attributable to decomposition of PPh_3, which is confirmed by TGA analysis (refer to Figure S4.2 in the Supporting Information). For X-Rh/SiO_2 catalysts, the rates of *n*- and isobutanal formation increased as the reaction temperature increased. At 403 K, the rate of *n*-butanal formation begins to plateau while the rate of isobutanal formation continues to rise. Thus, the *n/i* ratio decreases from 15 at 353 K to 8 at 413 K, demonstrating that temperature can be used to control the *n/i* ratio. Above 413 K, a loss in catalytic activity was noted due to ligand decomposition, as identified by thermal gravimetric analysis.

The apparent activation energy calculated from the Arrhenius plot for PPh_3-Rh/SiO_2 in the temperature interval 353-413 K are 65 and 56 kJ mol^{-1}, respectively (Table 4.2). For X-Rh/SiO_2, the apparent activation energy measured over the interval 353-413 K for *n*-butanal formation is 65 kJ mol^{-1}, while the apparent activation energy for iso-butanal formation is 75 kJ mol^{-1}. These values are approximately 5 kJ mol^{-1} higher than those previously reported for a sulfoxantphos ligand containing Rh- SILP catalysts [19].

The dependences of the rate of *n*- and isobutanal formation on the partial pressures of propene, CO, and H_2 were measured by holding the partial pressures of two components at 0.67 atm while varying the partial pressures of the third reactant and He. The total gas flow rate and pressure were kept constant at 60 cm^3 min^{-1} and 2 atm (120 cm^3 min^{-1} at STP). Table 4.3 shows the effect of varying the partial pressures of C_3H_6, CO, and H_2 partial pressures on the catalytic activity at 363 K of phosphine ligand-modified Rh/SiO_2 catalysts and a sulfoxantphos-containing Rh-SILP catalyst. As shown in Table 4.3, for X-Rh/SiO_2 the partial pressure dependence of H_2 on the rate of *n*-butanal formation is 0.12, the partial pressure dependence on CO is -0.47 and the partial pressure dependence on C_3H_6 is 0.86. The order of reaction with respect to the partial pressures of

H_2, CO, and C_3H_6 for *n*- and isobutanal formation are similar. The partial pressure dependences observed for X-Rh/SiO_2 are similar to those observed for the sulfoxantphos-containing Rh-SILP catalysts (Table 4.3). By contrast, a first order dependence in C_3H_6, CO and H_2 was noted with the phosphine-modified, PPh_3-Rh/SiO_2 catalysts [15].

Table 4.2 Comparison in activation energies for the formation of n- and isobutanal over different phosphine-containing rhodium catalysts.

Catalyst	Reaction Phase	E_A (kJ mol^{-1})	Temperature (K)	Pressure (atm)	Reference
X-Rh/SiO_2	Gas	65.0 [a] 75.0 [b]	353-373	2	This work
PPh_3-Rh/SiO_2	Gas	65.0 [a] 57.0 [b]	353-373	2	[15]
SX-Rh-SILP	Gas	60.0 [a] 72.0 [b]	353-373	2	[19]

[a] *n*-butanal, [b] isobutanal

Table 4.3. Reaction order of propene, CO and H_2 over phosphine-modified Rh/SiO_2 catalysts.

Catalyst	Reactant		
	C_3H_6	CO	H_2
X-Rh/SiO_2	0.86 [a] 0.76 [b]	-0.47 -0.40	0.12 0.12
PPh_3-Rh/SiO_2	1.01 [a] 0.99 [b]	1.12 0.90	1.02 0.85
SX-Rh- SILP	0.93 [a] 0.92 [b]	-0.43 -0.61	0.10 0.00

[a] *n*-butanal, [b] isobutanal

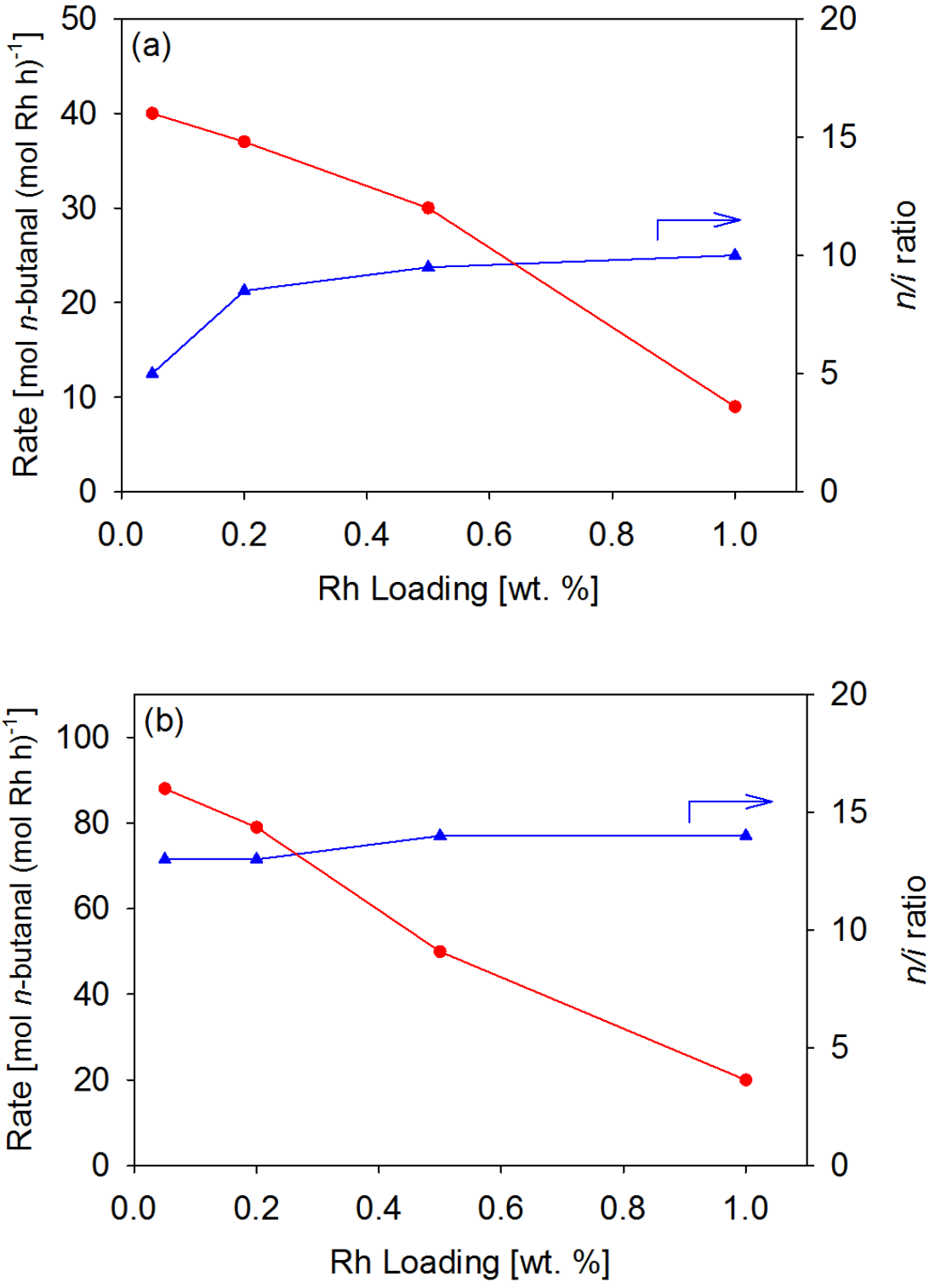

Figure 4.2 The effect of rhodium loading on the rates of butanal synthesis, (a) PPh_3 ligand and (b) Xantphos ligand. P_{Total} = 2 atm, C_3H_6:CO:H_2 = 1:1:1, T = 393 K, L/Rh molar ratio = 5-20, 0.2 wt. % Rh, catalyst mass = 0.3 g, total gas flow rate = 60 cm^3 min^{-1} at pressure, 120 cm^3 min^{-1} at STP.

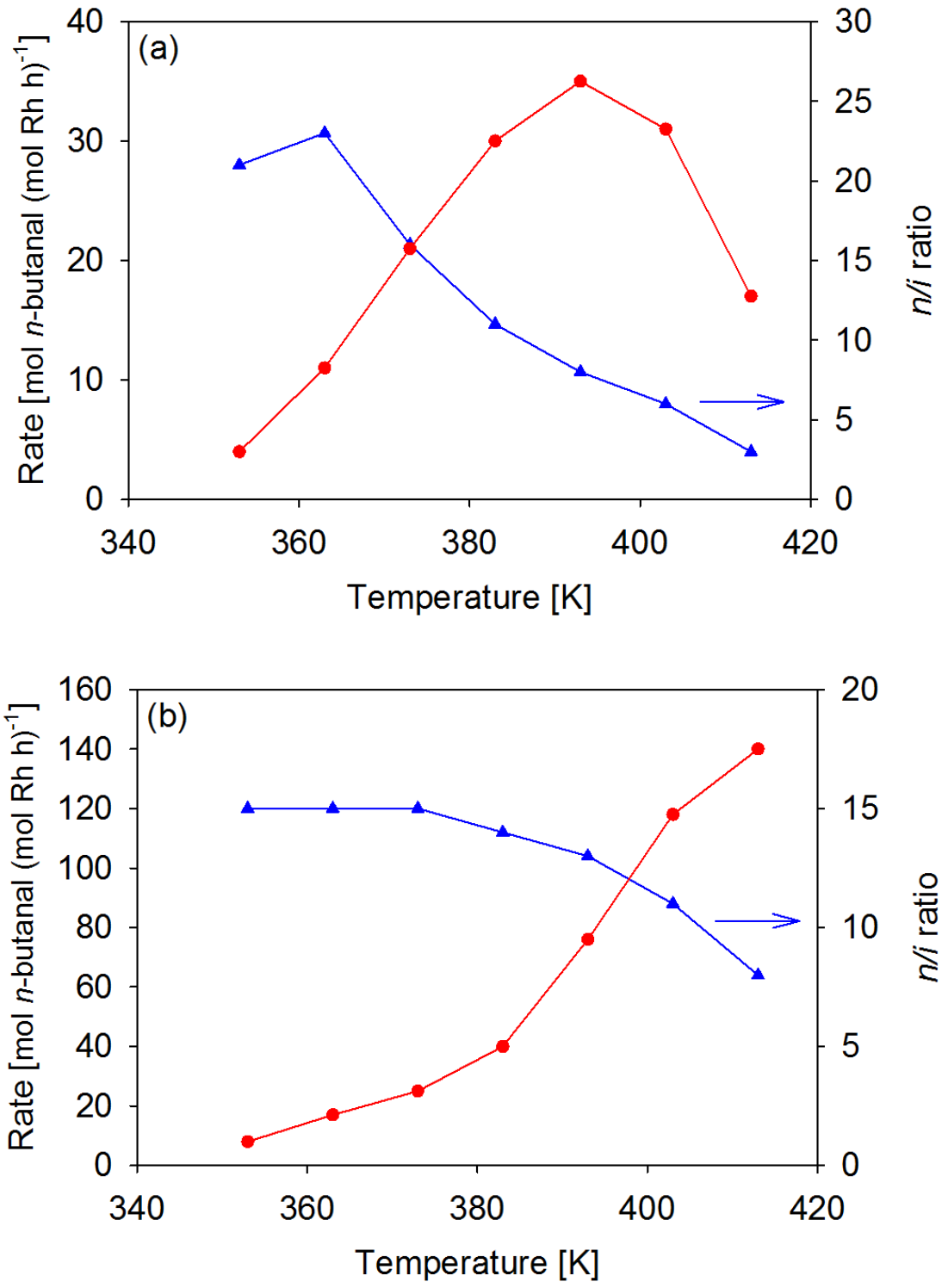

Figure 4.3 Effect of temperature on rate of *n*-butanal synthesis and regioselectivity over (a) PPh_3-Rh/SiO_2 and (b) X-Rh/SiO_2 catalysts. P_{Total} = 2 atm, C_3H_6:CO:H_2 = 1:1:1, T = 393 K, L/Rh molar ratio = 5-20, 0.2 wt. % Rh, catalyst mass = 0.3 g, total gas flow rate = 60 cm^3 min^{-1} at pressure, 120 cm^3 min^{-1} at STP.

4.3.5 In Situ FT-IR Spectroscopy of Phosphine-modified Rh/SiO_2 Catalysts

In situ FT-IR was used to identify how the phosphine-modified Rh/SiO_2 (L-Rh/SiO_2, L = PPh_3 and X) changed upon exposure to CO and then a mixture of CO and H_2. At very low CO partial pressure (0.2 atm), the IR spectra of PPh_3-modified 1%Rh/SiO_2 (PPh_3/Rh = 15) showed a sharp band at 1970 cm^{-1} as well as narrow bands at 2000 and 1940 cm^{-1}. As the CO partial pressure was increased to 1 atm, the intensity of these bands increased further with nearly constant relative intensities. The broad peak at 1970 cm^{-1} arises from linear Rh(CO), whereas the band at 2000 and 1940 cm^{-1} are due to $Rh(CO)_2$ species red-shifted due to the presence of adsorbed PPh_3 [20]. Coordination of electron-donating PPh_3 ligand enhances the electron density around the rhodium center resulting in substantial back donation to CO ligands, thereby lowering the CO vibration frequency. Addition of H_2 to CO in the gas stream resulted in the appearence of bands at 2045, 2010, 1990 and 1950 cm^{-1}. The position of these bands are identical to those observed for soluble $HRh(CO)_n(PPh_3)_{4-n}$ complexes. The peaks at 2045 cm^{-1} and 1990 cm^{-1} are attributable to *ee* $HRh(CO)_2(PPh_3)_2$, whereas the peaks at 2010 cm^{-1}, 1950 cm^{-1} are attributable to *ea* $HRh(CO)_2(PPh_3)_2$ complexes [21,22]. The band at 1900 cm^{-1} can be assigned to $HRh(CO)(PPh_3)_3$ species downshifted due to the presence of three PPh_3 groups [21]. The growth of bands associated with $HRh(CO)(PPh_3)_3$ and $HRh(CO)_2(PPh_3)_2$ with increasing partial pressure provides evidence for in situ formation of homogeneous catalysts. The nearly linear growth of these bands with increasing synthesis gas pressure also indicates that an equilibrium exist between gaseous CO, Rh metal, and homogeneous $HRh(CO)_n(PPh_3)_{4-n}$ species [15]. Notably, no bands were observed in the region of 1850-1700 cm^{-1} characteristic of bridging CO ligands, suggesting the absence of dimeric rhodium complexes.

The IR spectra of PPh_3-modified 0.2 wt. % Rh/SiO_2 (PPh_3/Rh = 15) differed from those of PPh_3 – modified 1%Rh/SiO_2 due to the different amount of PPh_3 ligands (per gram of support) on the silica support. This leads to the formation of PPh_3 rich $HRh(CO)(PPh_3)_3$ homogeneous species in 1 wt. % Rh samples while the 0.2 wt. % Rh sample leads to ligand lean $HRh(CO)_3(PPh_3)$ type species. This leads to the difference in the IR spectra of both samples. As seen in Figure 4.4a, contacting the catalyst with CO in He (1 atm) produced sharp CO bands at 2090, 2030, 2000 and 1940 cm^{-1}. As noted above, the band at 2000 and 940 cm^{-1} are due to $Rh(CO)_2$ species red-shifted due to the presence of adsorbed PPh_3 whereas the intense bands at 2090 and 2030 cm^{-1} arise from the geminal-dicarbonyl rhodium species. Addition of H_2 to CO in the gas stream produced peaks at 2045, 2010, 1990 and 1940 cm^{-1} associated with $HRh(CO)_2(PPh_3)_2$ species. It is remarkable that no evidence was observed for phosphine rich $HRh(CO)(PPh_3)_3$ species, as were observed in the spectrum of PPh_3-modified 1%Rh/SiO_2. More interestingly, this catalyst showed the presence of a broad peak at 1820 cm^{-1}, characteristic of bridging CO present in rhodium dimers.

IR spectra of bidentate xantphos-modified 0.2 wt. % Rh/SiO_2 catalyst (X-Rh/SiO_2, X/Rh=15) in presence of synthesis gas are presented in Figure 4.4b. Upon contacting the catalyst with CO in He, carbonyl bands appeared at 2005 and 1940 cm^{-1}. The positions of these bands are attributed to the formation of the rhodium carbonyl phosphine complexes [12]. Addition of H_2 to CO to the gas stream resulted in the formation of four carbonyl bands at 2035, 1995, 1970, and 1940 cm^{-1}. These features are

identical to those observed for Rh complexes formed with xantphos dissolved in organic solvents, ionic liquids and in supported ionic liquid phase (SILP) catalytic systems [22]. The bands at 2035 and 1970 cm^{-1} are attributable to *ee*-$HRh(CO)_2(X)$, in which both phosphorous atoms occupy equatorial coordination sites, and the bands at 1995 and 1940 cm^{-1} are attributable to *ea*-$HRh(CO)_2(X)$, in which one phosphorous atom is equatorial and the other is apical. No bands were observed in the region characteristic of CO bridging ligands (1800-1700 cm^{-1}) suggesting the absence of dimeric $[Rh(X)(CO)(\mu\text{-}CO)]_2$ species for catalysts prepared with xantphos ligand on Rh/SiO_2.

4.3.6 ^{31}P MAS NMR Spectroscopy of Phosphine-modified Rh/SiO_2 Catalysts

Further evidence for in situ formation of homogenous complexes over the phosphine-modified Rh/SiO_2 catalysts was obtained by solid-state ^{31}P MAS NMR spectroscopy. The spectrum of a PPh_3-modified silica support (PPh_3/SiO_2) exhibits a band at -5.6 ppm ascribed to PPh_3 adsorbed on the silica surface [13]. By contrast, PPh_3-Rh/SiO_2 showed the presence of physisorbed phosphine at -5.6 ppm and a broad, less intense, peak centered at 33 ppm due to phosphine adsorbed on rhodium nanoparticles. The position of this peak is similar to the peak observed at 36 ppm in the ^{31}P MAS NMR spectra of $HRh(CO)(PPh_3)_3/SiO_2$, which is attributed to the coordination of Rh^+ ion and PPh_3 of rhodium complex [13] (refer to Figure S4.3 in the Supporting Information). Figure 4.5 shows the ^{31}P MAS NMR spectrum of the spent PPh_3-modified Rh/SiO_2 and the xantphos-modified Rh/SiO_2 catalysts. The spent PPh_3-0.05%Rh/SiO_2 catalyst showed a sharp peak at approximately 38 ppm, and with increasing rhodium loading, a progressive upfield shift of this band is observed. Free phosphines characterized by a peak at -5.6 ppm was observed in the spent PPh_3-1%Rh/SiO_2 catalyst, whereas free phosphine was absent for catalysts prepared with lower rhodium loadings. This result suggests that PPh_3-1%Rh/SiO_2 contains free phosphines and homogenous species mainly as $HRh(CO)(PPh_3)_3$. Indeed, a phosphine-modified $HRh(CO)(PPh_3)_3/SiO_2$ (Rh = 1%) spent catalyst also showed a peak at 30 ppm. By contrast, X-Rh/SiO_2 exhibited peaks at 36 ppm, -16 ppm and -22 ppm, similar to the features observed for sulfoxantphos-modified rhodium SILP catalysts [12]. The peak at -16 ppm is attributable to xantphos weakly physisorbed on silica, while the broad peak at -22 ppm is attributable to phosphorous atoms in either singly-protonated or non-protonated, strongly physisorbed xantphos ligands. The peak at 35 ppm is assigned to the phosphine groups of xantphos interacting with Rh. These results are indicative of in situ formation of homogenous $HRh(CO)_n(L)_{4-n}$ species on phosphine-modified Rh/SiO_2.

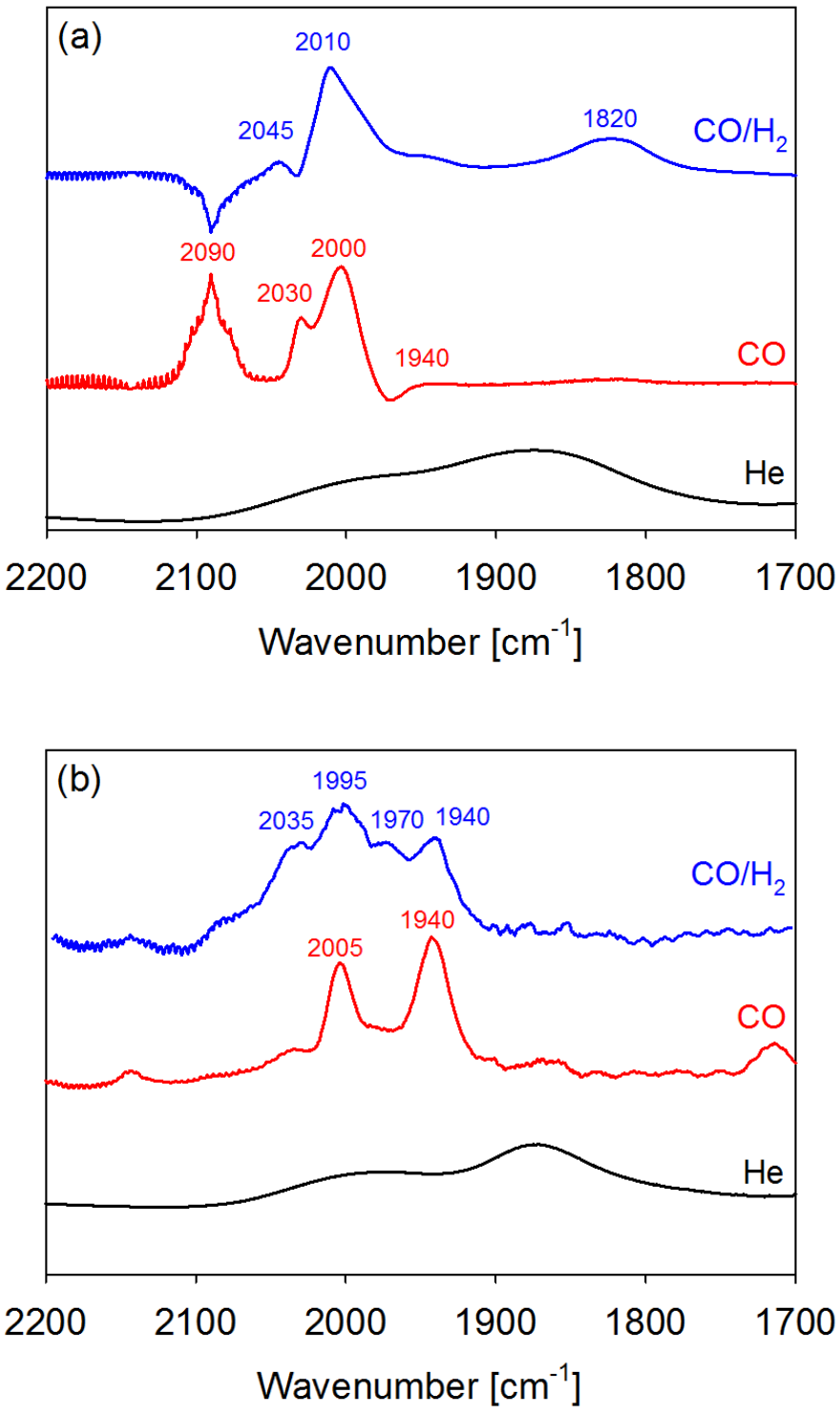

Figure 4.4 In situ FT-IR of (a) PPh_3-Rh/SiO_2 and (b) X-Rh/SiO_2 catalysts in presence of CO and syngas showing the formation of homogeneous catalysts, L/Rh = 15, 0.2 wt. % Rh, *T* = 393 K.

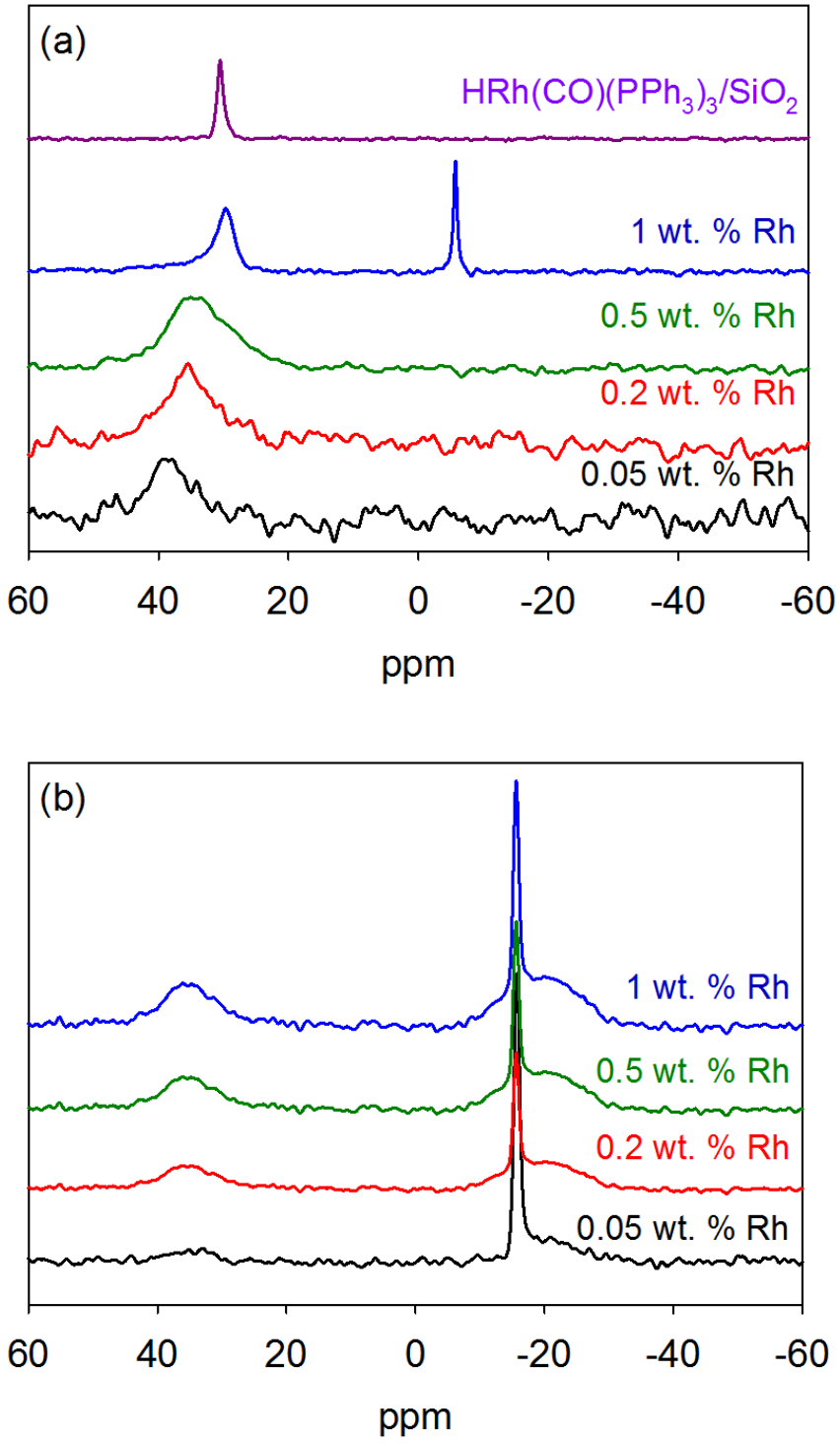

Figure 4.5 Solid-state ^{31}P MAS NMR spectra of (a) PPh_3-modified Rh/SiO_2 (PPh_3/Rh =15) and (b) X- modified Rh/SiO_2 (X/Rh = 15) spent catalyst with 0.05 wt. %, 0.2 wt. % 0.5 wt. %, and 1 wt. %. Rh weight loadings.

4.3.7 HR-TEM Measurements

HR-TEM image of 1%Rh/SiO_2 showed rhodium nanoparticles approximately 5 nm in diameter, whereas the 0.2%Rh/SiO_2 catalyst showed particles 1.5 nm in diameter. In both cases the particles are well distributed over the support surfaces as shown in Figure 4.6. Further confirmation for the high dispersion of rhodium nanoparticles on the silica support surfaces was obtained by the high angle annular dark field-scanning tunneling electron microscopy (HAADF-STEM). A spent catalyst showed no difference in the size of the rhodium nanoparticle highlighting that the particle remains unchanged under the reaction conditions.

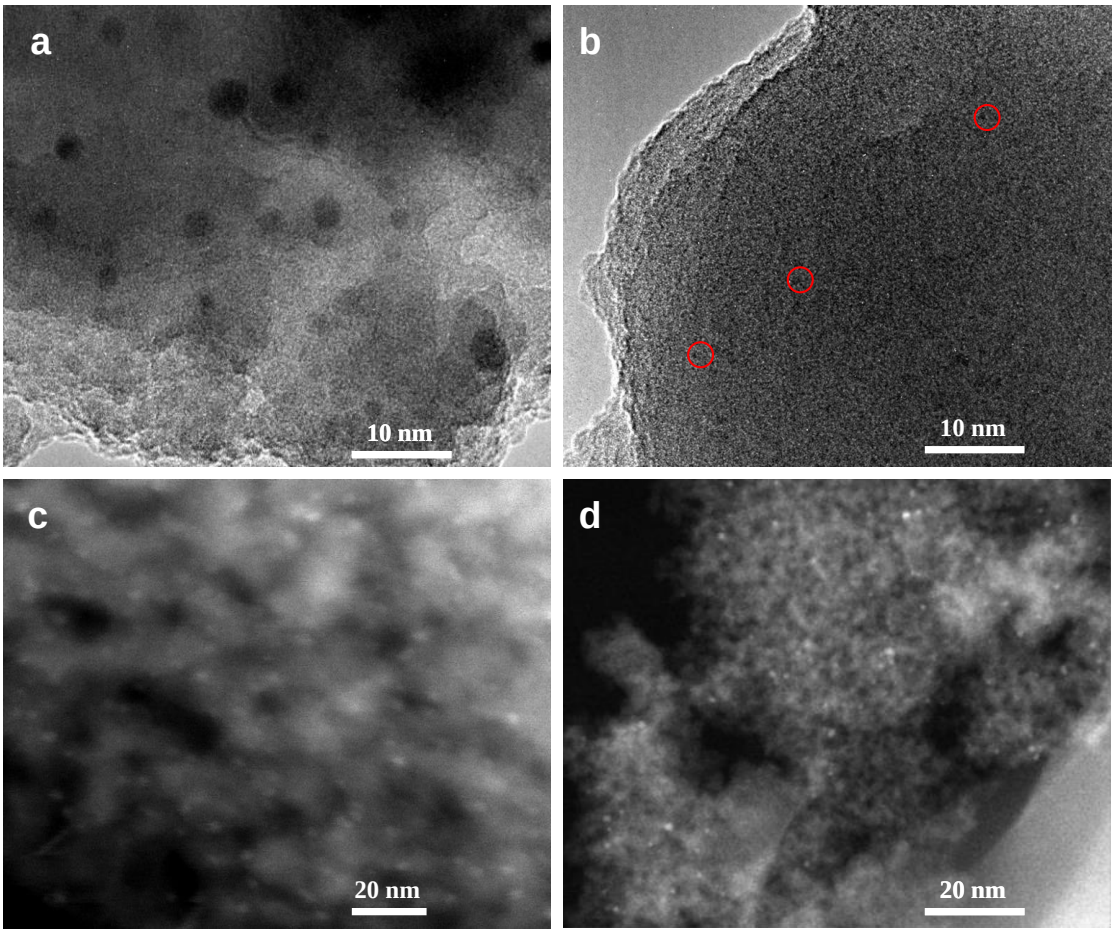

Figure 4.6. (a, b) High resolution-transmission electron micrographs (HR-TEM) and (c, d) high angle annular dark field-scanning tunneling electron microscopy (HAADF-STEM) of (a, c) 1%Rh/SiO2 and (b, d) 0.2%Rh/SiO2 samples. Red circles represent rhodium nanoparticles of ~1 nm.

4.4 Discussion

The strong similarities in the rate parameters for hydroformylation of propene over phosphine- and xantphos-modified Rh/SiO_2 and the corresponding homogeneous species of the type $HRh(CO)_n(L)_{4-n}$ [15] suggest that Rh complexes are produced in situ. The manner in which this occurs is as follows. Nanoparticles of Rh supported on silica or alumina are known to undergo corrosive chemisorption in the presence of CO to produce Rh (I) gem-dicarbonyl species ($Rh^{(I)}(CO)_2$) exhibiting bands at 2090 and 2030 cm^{-1} [20]. It has been proposed that such species are formed from supported Rh nanoparticles by the adsorption of CO on the surface of the particle, which leads to a weakening of Rh-Rh bonds due to the higher strength of Rh-CO bonds (185 kJ) than Rh-Rh bonds (44.5 kJ) [23]. Neutral Rh dicarbonyl species formed via this process can then interact with the hydroxyl groups of the support to release H_2 and produce $\equiv$Si-O-$Rh^{(I)}(CO)_2$ species, as shown in Scheme 4.1. Evidence for the formation of such species can be drawn from the results of in situ IR spectroscopy. The IR spectra for both 0.2 wt% and 1 wt% Rh/SiO_2 exposed to CO at 393 K showed bands for *gem*-rhodium dicarbonyl bands at 2090 and 2030 cm^{-1} and the concurrent decrease in the intensity of the band at 3660 cm^{-1} due to $\equiv$Si-O-H vibrations (refer to Figure S4.4 in the Supporting Information). Interaction of H_2 with the $\equiv$SiO-$Rh^{(I)}(CO)_2$ species leads to the formation of mobile $HRh(CO)_2$ species and a restoration of hydroxyl groups [24]. We envisage that, under reaction conditions, the phosphine ligands interact with these species to generate *in situ* $HRh(CO)_2(X)$ species in presence of xantphos ligand and $HRh(CO)_n(PPh_3)_{4-n}$ species in the presence of PPh_3 (Scheme 4.1).

$$Rh^0 + 2\,CO \longrightarrow Rh^0(CO)_2$$

$$2\,Rh^0(CO)2 + 2\,Si\text{-}OH \longrightarrow 2\,Si\text{-}O\text{-}Rh^I(CO)_2 + H_2$$

$$Si\text{-}O\text{-}Rh^I(CO)_2 + H_2 \longrightarrow HRh^I(CO)_2 + Si\text{-}OH$$

$$HRh^I(CO)_2 + 2\,PPh_3 \longrightarrow HRh^I(CO)_2(PPh_3)_2$$

Scheme 4.1 Proposed mechanism for the formation of homogenous catalysts on phosphine-modified Rh/SiO_2 supports.

The effect of PPh_3/Rh ratio on the rate of *n*- and isobutanal formation can be attributed to the equilibrium shown in Scheme 4.2. Due to the low CO partial pressures used, formation of $HRh(CO)_4$ species is unlikely under our experimental conditions, which explains the absence of catalytic activity without PPh_3 ligands. The increase in catalytic activity with increasing PPh_3/Rh ratio is due to an increase in the concentration of $HRh(CO)_n(PPh_3)_{4-n}$ species (Figure 4.1). The need for excess PPh_3 arises from the relatively weak Rh-PPh_3 binding [25]. Hence, in order to maintain a high activity and regioselectivity excess PPh_3 is required to drive the equilibrium in favor of $HRh(CO)(PPh_3)_2$. Consequently, as the ligand concentration increases, the equilibria in Scheme 4.2 shift to the left, the steric bulk of the complexes increase contributing to the

formation of complexes that produce higher *n/i* ratios. Stated another way, the enhancement in linear aldehyde selectivity observed at high PPh_3/Rh ratios may be due to the hydroformylation cycle in which each intermediate contain two phosphines per rhodium derived from $HRh(CO)(PPh_3)_3$. The decreased activity for PPh_3/Rh>15 is related to the difficulty of $HRh(CO)_n(PPh_3)_{4-n}$ 18-electron complexes to lose a PPh_3 ligand to form the 16-electron species or to the formation of $HRh(L)_4$ type species [15]. By contrast, the bidentate xantphos ligand favor the formation of $HRh(CO)_2(X)$ 18-electron species which then dissociates a CO ligand to form the catalytically active, regioselective 16-electron HRh(CO)(X) species.

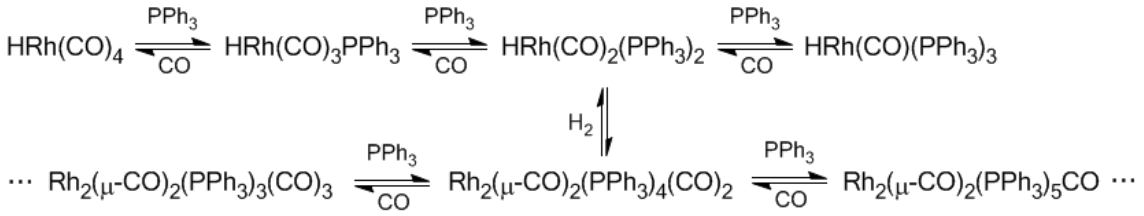

Scheme 4.2 Equilibrium of rhodium catalysts containing PPh_3 and carbonyl ligands.

The dependence of propene hydroformylation activity and stability on rhodium loading can be interpreted in the following manner. It is known that the ratio of surface atoms located at edges and vertices relative to those in planes increases significantly as the size of the nanoparticle becomes small. Our TEM observations show that the size of the Rh particles supported on SiO_2 decreases with decreasing Rh loading. Since the Rh atoms located at the particle corners and edges are more coordinatively unsaturated, they are more susceptible to corrosive chemisorption than Rh atoms located on the planar surfaces of the particles. Thus, we attribute the higher specific activity per Rh site observed with decreasing Rh weight loading to an increase in the facility with which corrosive chemisorption releases Rh atoms from Rh nanoparticles, which in turn increases the concentration of $Rh^{(I)}(CO)_2$ species. Thus the highly dispersed and smaller nanoparticles (preferably cluster sized) leads to an ease of formation of the homogenous complexes in presence of syngas than larger particles. This result is clearly confirmed from the comparison between the size of the rhodium nanoparticles that the highly dispersed and smaller nanoparticles showed a higher rate than the larger Rh nanoparticles (Figure 4.2).

The higher catalytic activity of bidentate xantphos-modified Rh/SiO_2 compared to monodentate PPh_3-modified Rh/SiO_2 can be related to the chelating ability of xantphos, which yields a higher concentration of the coordinated Rh species [1]. This in turn results in increased complexation of the rhodium center by the diphosphine X ligand, and the rigid backbone of the ligand compells the phenyl groups of xantphos to exert a greater degree of steric hindrance on the alkene entering the coordination sphere, favouring linear products. Usage of different ligands suggests that as the electron density on the rhodium atom is reduced by increasing the electron-withdrawing functionality in the phosphine ligand (*3F-PPh*$_3$-Rh/SiO_2 vs *OMe-PPh*$_3$-Rh/SiO_2), the selectivity to linear

aldehydes increased with a significant change in the activity. Since para substituted aryl phosphines were utilized in the present study, the steric environment around the active rhodium center is nearly constant [16]. Hence the catalytic activity differences can be correlated nicely with the electronic properties of the phosphine ligands. If the ligand has good back-bonding ability, the equilibrium in Scheme 4.2 will shift to the left to favor $HRh(CO)(L)_3$ in order to prevent excess charge building up on $Rh^{(I)}$ cations. These results suggest that electron-withdrawing phosphine ligands tend to form the 18-electron $HRh(CO)_n(PPh_3)_{4-n}$ species and then rapidly lose a ligand to form the coordinatively unsaturated, active 16-electron $HRh(CO)_n(PPh_3)_{3-n}$ species. Consistent with this interpretation, electron-withdrawing substituents in phosphine ligands increase the carbonyl stretching frequencies which provide direct evidence that the M-CO bond is weakened as the electron with-drawing ligands reduce M-CO dπ-pπ interactions [16]. The low *n*-aldehyde selectivity obtained with the phosphite ligands suggests that the electronegativity difference of the groups attached to the phosphorous will change the σ donor and π acceptor properties of the ligands leading to a change in the overall performance of the catalysts [25].

The catalytic activity, *n/i* ratio, and stability of phosphine-modified Rh/SiO_2 (PPh_3-Rh/SiO_2) and $HRh(CO)(PPh_3)_3/SiO_2$ differ significantly. Phosphine-modified Rh/SiO_2 is stable under reaction conditions, whereas $HRh(CO)(PPh_3)_3/SiO_2$ progressively loses activity under identical reaction conditions (refer to Figure S4.6 in the Supporting Information). These observations suggest that the interaction of the Rh complex with the rest of the catalyst is different in the two samples. As discussed earlier, we envisage that the formation of geminal rhodium dicarbonyl species provide a favourable stabilizing effect, as proposed by Augustine and co-workers using heteropolyacid as linkers (Scheme 4.3) [26]. Comparison of the IR spectra of PPh_3-Rh/SiO_2 and $HRh(CO)(PPh_3)_3/SiO_2$ shows a greater red shift (~1945 cm^{-1}) for the CO resonances of homogeneous species in PPh_3-Rh/SiO_2 than the Wilkinson catalyst supported silica sample (~1975 cm^{-1}). The sharp decrease in activity of the $HRh(CO)(PPh_3)_3/SiO_2$ catalyst thus relates to the weak interaction of the homogenous catalyst with the silica surface and thereby to the easy formation of inactive dimers/clusters [12,13].

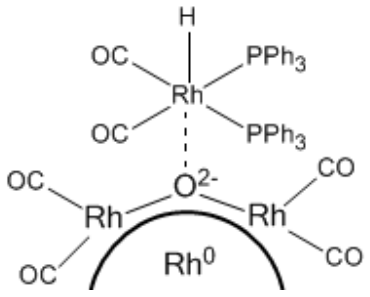

Scheme 4.3 Proposed stabilization effect of $HRh(CO)_n(PPh_3)_{4-n}$ catalysts on Rh/SiO_2 supports.

The kinetics of butanal formation observed for monodentate PPh_3-modified and bidentate xantphos-modified Rh/SiO_2 catalysts can be interpreted using the mechanism proposed by Heck and Breslow [27]. $HRh(CO)(PPh_3)_3$ (**A**) and $HRh(CO)_2(PPh_3)_2$ (**B**) species exist in equilibrium for phosphine-modified PPh_3-Rh/SiO_2 catalysts and hydroformylation is initiated with the loss of a CO ligand to form the 16-electron species, $HRh(CO)(PPh_3)_2$ (**C**) (Scheme 4.4). Propene then coordinates to species **C** to form a η^2-Rh complex (species **D**)**.** Migratory insertion into the Rh-H bond forms a propyl-Rh complex (species **E**). CO then adds to species **E** to form an 18-electron intermediate species **F**. Migratory insertion of the propyl to a carbonyl group leads to the formation of an acyl intermediate (species **G**). Oxidative addition of H_2 forms the 18-electron Rh(III) species **H**, followed by the reductive elimination of butanal. For X-Rh/SiO_2 catalysts, hydroformylation of propene is initiated by the loss of a CO ligand from $HRh(CO)_2(X)$ (species **A**) to form the 16-electron species HRh(CO)(X**) (B)** (Scheme 3.1). Isobutanal is formed in a catalytic cycle by an analogous mechanism, in which species **D-G** involve a secondary, rather than a primary alkyl species.

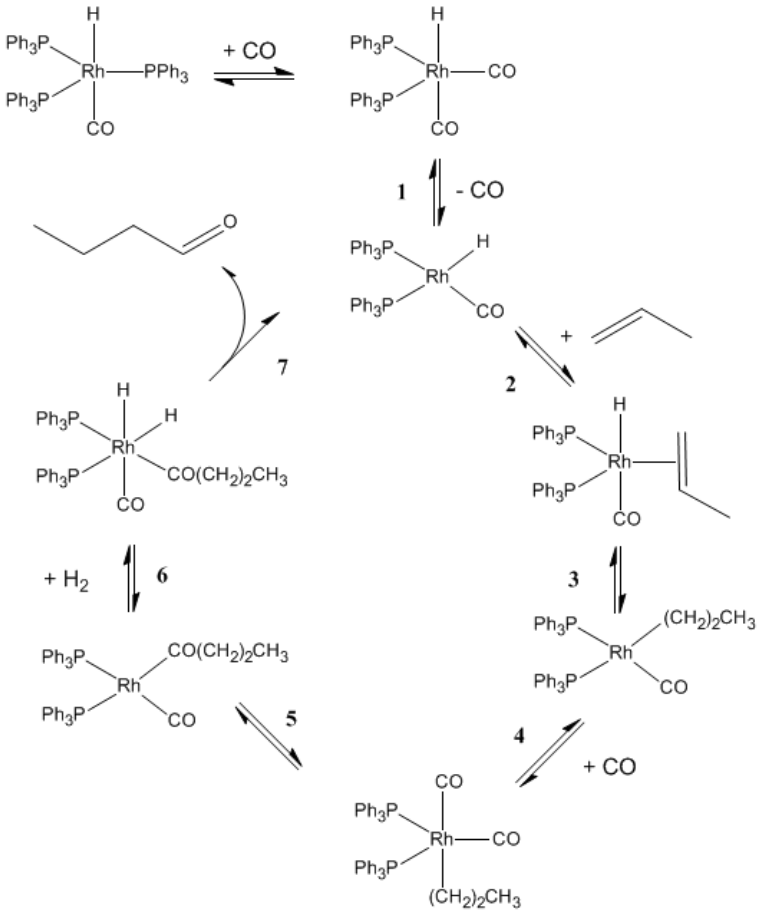

Scheme 4.4 Proposed mechanism for the hydroformylation of propene PPh_3-Rh/SiO_2.

The observed reaction orders at 363 K for PPh_3-Rh/SiO_2 catalyst were first order in C_3H_6, CO and H_2, suggesting that the rate-determining step (RDS) is the oxidative addition of hydrogen. Under this assumption, the rate of butanal formation can be written as follows:

$$r_{butanal} = \frac{\prod_{i=1}^{6} K_i \, k_7 P_{C_3H_6} P_{CO} P_{H_2} / [PPh_3]}{1 + K_1 P_{CO} / [PPh_3]} \qquad (1)$$

where k_i is the rate coefficient for Reaction *i*, K_i is the equilibrium constant for Reaction *i*, P_j is the partial pressure of species *j*, [PPh_3] is the concentration of PPh_3 species and [Rh] is the total moles of Rh. If it is assumed that the second term in the denominator of equation (1) is small relative to unity, then the rate expression is consistent with the observed kinetics at 363 K. Similar positive order kinetics have been reported earlier for hydroformylation reactions carried out at pressures lower than those described as typical hydroformylation conditions (343-393 K, 10-30 atm) [15,28].

The apparent reaction orders observed at 363 K for xantphos-modified Rh/SiO_2 catalyst were first order in propene, negative order in CO and nearly zero order in H_2. These results suggest that the rate-determining step (RDS) now becomes alkene insertion, in good accordance with the kinetics reported for hydroformylation over sulfoxantphos-containing Rh-SILP catalysts [19]. Further support for alkene insertion as the RDS for diphosphine ligands can be drawn from the work of van Leeuwen and co-workers [29]. Based upon the hydroformylation reaction mechanism and considering alkene insertion be the irreversible, rate-limiting step, the rate of butanal formation is given by the following relation:

$$r_{butanal} = \frac{K_1 K_2 k_3 P_{C_3H_6}}{P_{CO} + K_1 + K_1 K_2 P_{C_3H_6}} \qquad (2)$$

where k_i is the rate coefficient for Reaction *i*, K_i is the equilibrium constant for Reaction *i*, P_j is the partial pressure of species *j*, and [Rh] is the total moles of Rh.
Equation (2) is consistent with the observed kinetics at 363 K. The rate of butanal synthesis is zero order in the partial pressure of H_2 and less than first order in the partial pressure of C_3H_6. As the partial pressure of C_3H_6 increases, the $K_1K_2P_{C_3H_6}$ term in the denominator becomes increasingly significant, thereby reducing the effective order from unity. The experimentally observed, inhibitory effect of CO is also effectively represented by Equation (2). Since the order of CO is -0.4, the remaining terms in the denominator are significant in magnitude compared to P_{CO}.

The decrease in *n/i* ratio from low temperature to high temperature over the phosphine-modified Rh/SiO_2 catalysts can be explained as follows. PPh_3-Rh/SiO_2 catalysts show very high *n/i* ratio of 22 at 353 K, which decreases to 3 at 413 K. Preference for forming linear versus branched aldehydes in PPh_3-Rh/SiO_2 catalysts can be attributed to the preferred isomerization of $HRh(CO)(PPh_3)_2$ to the structure in which both phosphine groups are coordinated in the equatorial plane [15]. The high *n/i* ratio observed with PPh_3-Rh/SiO_2 at low temperatures is consistent with studies conducted with $HRh(CO)(PPh_3)_3$ in homogenous solutions. For X-Rh/SiO_2 catalysts, a decrease in

n/i molar ratio from 15 at 353 K to approximately 8 at 413 K was observed. For the bidentate xantphos ligand, the regioselectivity is determined by alkene insertion into the Rh-H bond to form either primary or secondary alkyls [1]. The apparent activation energies measured for *n*- and isobutanal formation are 65 and 75 kJ mol^{-1}, respectively. Therefore, the resulting *n/i* ratio is high because primary alkyls are favored kinetically over secondary alkyls. Indeed, theoretical studies demonstrate that the transition for the formation of secondary alkyls is approximately 9 kJ mol^{-1} greater than that for the formation of primary alkyls due to the steric effects exerted from the phenyl groups of the phosphine ligand [30]. The decrease in the *n/i* ratio at high temperature is due to a shift from the thermodynamically favorable primary alkyl complex to the less favorable secondary alkyl complex. These results are in agreement with previous deuteroformylation studies, which found that Rh-alkyl formation is irreversible at low temperature, but reversible at higher temperatures [19,31].

4.5 Conclusion

The results of this study provide a detailed understanding of the factors influencing the activity, selectivity, and stability of phosphine-modified Rh/SiO_2 catalysts for the hydroformylation of propene. Catalyst performance and stability are found to be strong functions of the nature and concentration of ligand and rhodium loading. The catalysts produced are very stable and exhibit 100% selectivity to butyraldehydes; no propane or alcohols were detected. Higher catalytic activity and *n/i* ratios were observed over xantphos-modified Rh/SiO_2 than over phosphine-modified Rh/SiO_2. The reaction temperature has a strong effect on the activity and regioselectivity of PPh_3-Rh/SiO_2. A first order dependence on the partial pressures of propene, CO and H_2 were observed for PPh_3-Rh/SiO_2, whereas X-Rh/SiO_2 catalysts showed first-order partial pressure dependence in propene, negative order in CO and zero order in H_2. Differences in the kinetics between the monodentate and the bidentate phosphine ligands are related to the difference in the rate limiting steps. Oxidative addition of hydrogen is the rate-limiting step for PPh_3-Rh/SiO_2, whereas alkene insertion is the rate-limiting step over the X-Rh/SiO_2. In situ FT-IR and ^{31}P MAS NMR indicate the in situ formation of $HRh(CO)_2(X)$ species on the xantphos-modified Rh/SiO_2 catalyst and $HRh(CO)_n(PPh_3)_{4-n}$ species on the phosphine-modified Rh/SiO_2. In each case, isolated $Rh^{(I)}(CO)_2$ species are produced via corrosive chemisorption as shown in Scheme 4.1.

4.6 Acknowledgements

This work was supported by the XC2 program funded by BP. The authors would like to thank Dr. Chris Canlas (Berkeley NMR facility) for his assistance in acquiring the NMR spectra, Eric Bloch for the TGA results, Dr. Zhengmeng Peng for the HR-TEM results.

4.7 Supporting Information

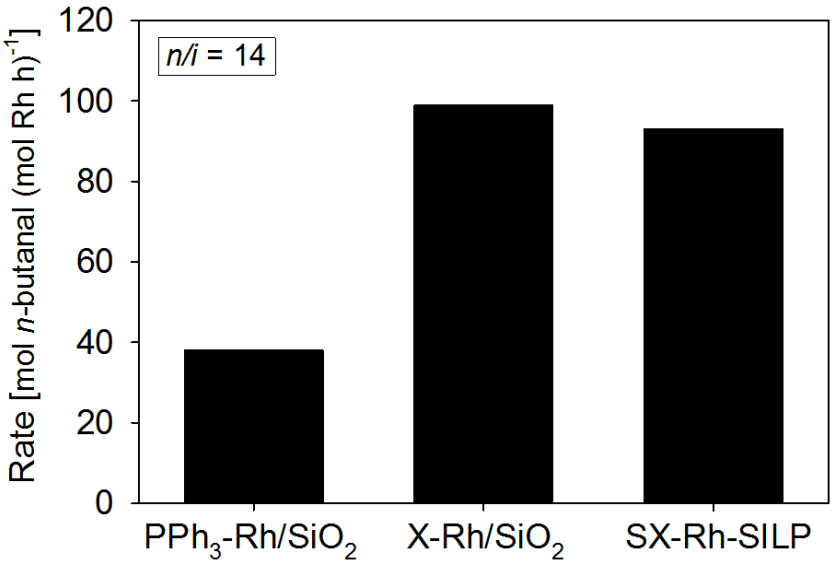

Figure S4.1 Comparison of activity between a PPh_3-Rh/SiO_2, X-Rh/SiO_2, and SILP catalysts. P_{Total} = 2 atm, C_3H_6:CO:H_2 = 1:1:1, T = 393 K, catalyst mass = 0.3 g, 0.2 wt. % Rh, L/Rh molar ratio = 15, total gas flow rate = 60 cm^3 min^{-1} at pressure, 120 cm^3 min^{-1} at STP.

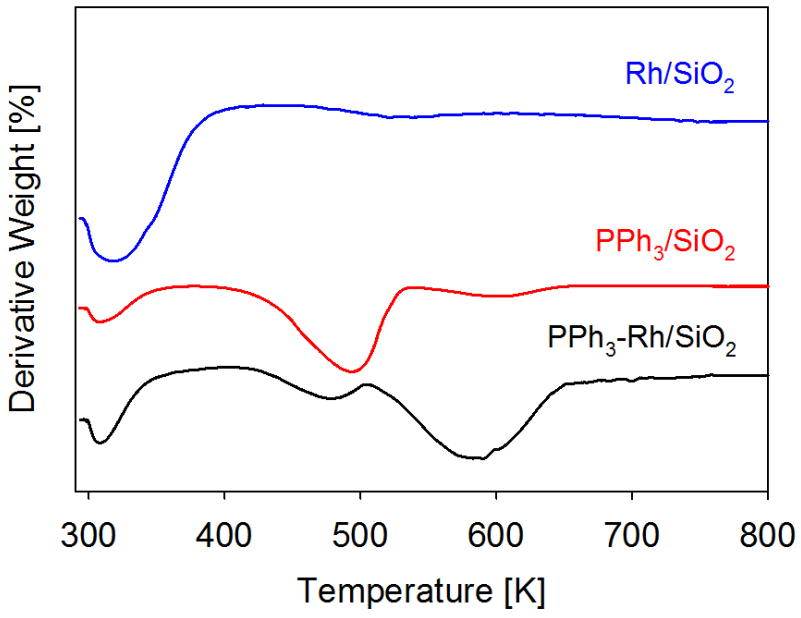

Figure S4.2 Differential Thermo Gravimetric (DTG) plots of Rh/SiO_2, PPh_3/SiO_2, and PPh_3-Rh/SiO_2 samples.

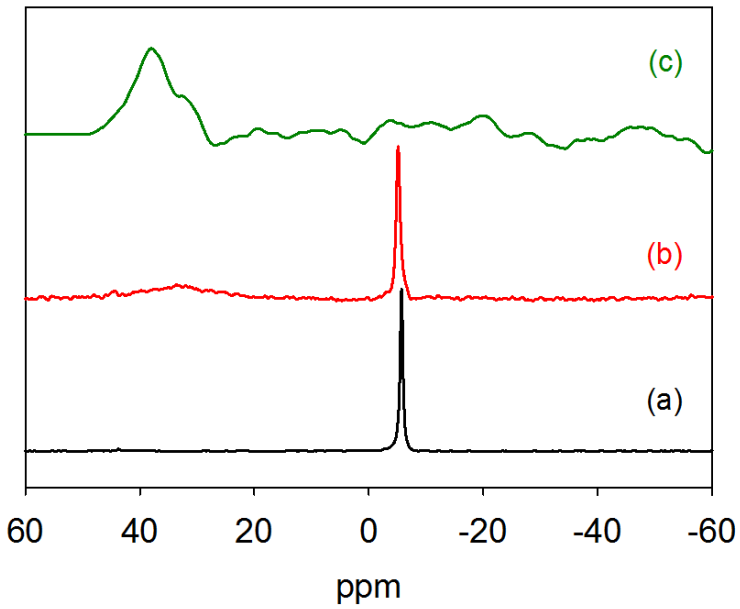

Figure S4.3 Solid-state ^{31}P MAS NMR spectra of (a) PPh_3-modified SiO_2 sample (PPh_3/SiO_2), (b) PPh_3-modified Rh/SiO_2 sample (PPh_3-Rh/SiO_2) sample, and (c) Wilkinson catalyst supported SiO_2 sample ($HRh(CO)(PPh_3)_3/SiO_2$) sample.

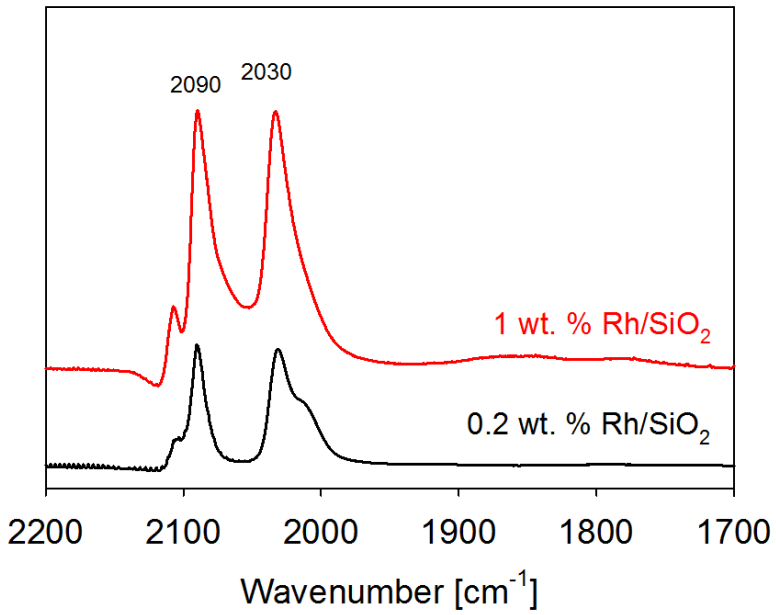

Figure S4.4 Formation of *gem*-dicarbonyl rhodium species on a 0.2 wt. % and 1 wt. % Rh/SiO_2 sample.

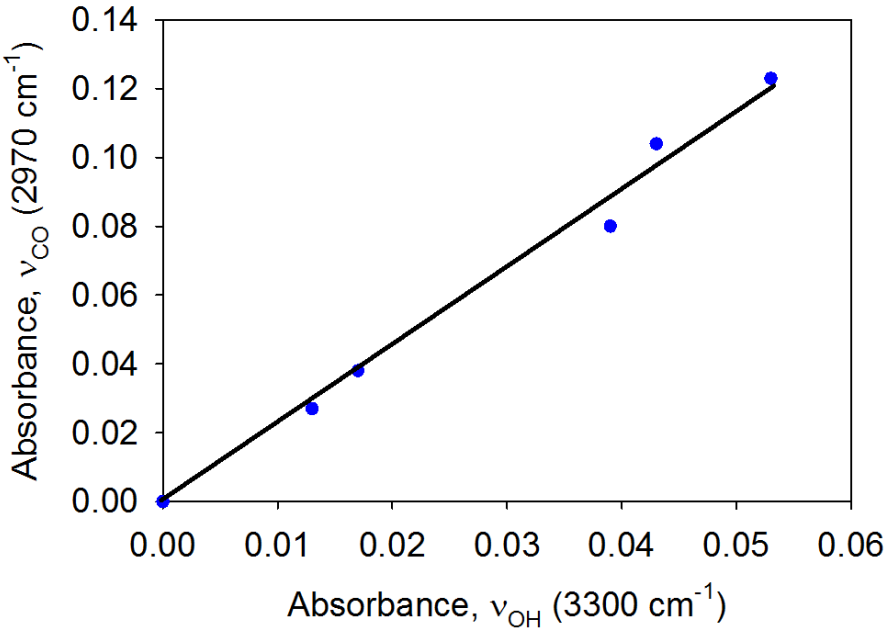

Figure S4.5 Correlation of $Rh^{I}(CO)_2$ formation with depletion of hydroxyl groups for Rh/SiO_2 sample.

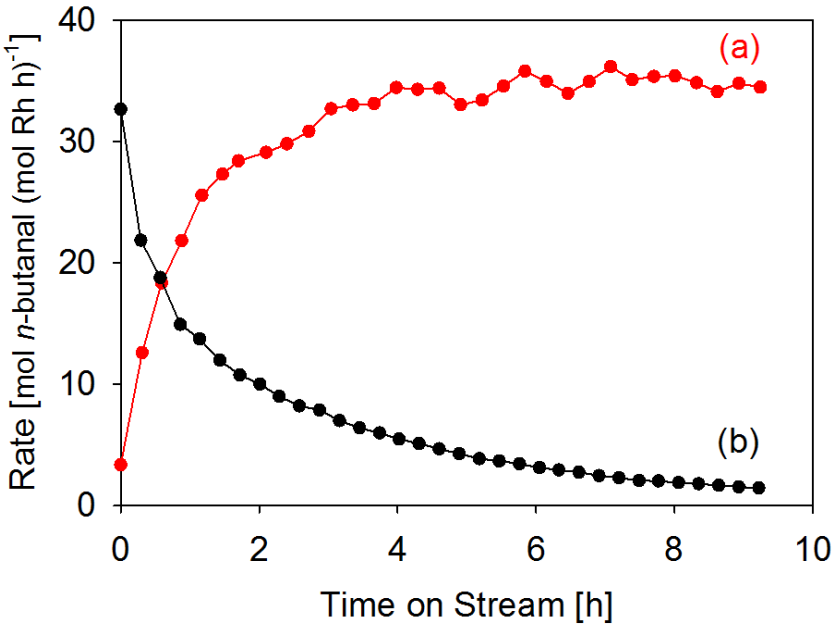

Figure S4.6 Comparison on the rates of butanal synthesis over (a) PPh_3-Rh/SiO_2 and (b) $HRh(CO)(PPh_3)_3/SiO_2$ catalyst under identical reaction conditions. P_{Total} = 2 atm, C_3H_6:CO:H_2 = 1:1:1, T = 393 K, catalyst mass = 0.3 g, 0.2 wt. % Rh, PPh_3/Rh = 15, total gas flow rate = 60 cm^3 min^{-1} at pressure, 120 cm^3 min^{-1} at STP.

4.8 References

[1] P. W. N. M. van Leeuwen, C. Claver. in: *Rhodium Catalyzed Hydroformylation*, Kluwer Academic Publishers, AA Dordrecht, **2000**, 189.

[2] B. Cornils, W. A. Hermann, M. Rasch. *Angew. Chem. Int. Ed*. **1994**, 33, 2144-2163.

[3] D. J. Cole Hamilton. *Science* **2003**, 299, 1702-1706.

[4] M. Beller, B. Cornils, C. D. Frohning, C. W. Kohlpainter. *J. Mol. Catal. A: Chem*. **1995**, 104, 17-85.

[5] A. J. Sandee, J. N. H. Reek, P. C. J. Kamer, P. W. N. M. van Leeuwen. *J. Am. Chem. Soc*. **2001**, 123, 8468-8476.

[6] C. P. Mehnert, R. A. Cook, N. C. Dispenziere, M. Afeworki. *J. Am. Chem. Soc*. **2002**, 124, 12932-12933.

[7] J. P. Arhanchet, M. E. Davis, B. E. Hanson. *J. Catal*. **1991**, 129, 94-99.

[8] A. Riisager, P. Wasserscheid, R. van Hal, R. Fehrmann. *J. Catal*. **2003**, 219, 452-455.

[9] A. Riisager, R. Fehrmann, S. Flicker, R. van Hal, M. Haumann, P. Wasserscheid. *Angew. Chem. Int. Ed*. **2005**, 44, 815-819.

[10] A. Riisager, R. Fehrmann, M. Haumann, B. S. K Gorle, P. Wasserscheid. *Ind. Eng. Chem. Res.* **2005**,44, 9853-9859.

[11] A. Riisager, R. Fehrmann, M. Haumann, P. Wasserscheid. *Eur. J. Inorg. Chem*. **2006**, 695-706.

[12] S. Shylesh, D. G. Hanna, S. Werner. A. T. Bell. *ACS Catal.* **2012**, 2, 487-493.

[13] L. Yan, Y. J. Ding, H. J. Zhu, J. M. Xiong, T. Wang, Z. D. Pan, L. W. Lin. *J. Mol. Catal. A: Chem*. **2005**, 234, 1-7.

[14] H. J. Zhu, Y. J. Ding, L. Yan, J. M. Xiong, Y. Lu, L. W. Lin. *Catal. Today* **2004**, *93*, 389-393.

[15] T. Kim, F. E. Celik, D. G. Hanna, S. Shylesh, S. Werner, A. T. Bell. *Top. Catal.* **2011**, 54, 299-307.

[16] W. R. Moser, C. J. Papile, D. A. Brannon, R. A. Duwell. *J. Mol. Catal*. **1987**, 41, 271-292.

[17] A. J. Sandee, V. F. Slagt, J. N. H. Reek, P. C. J. Kamer, P. W. N. M. van Leeuwen. *Chem. Commun*. **1999**, 1633-1634.

[18] J. Dupont, S. M. Silva, R. F. De Souza. *Catal. Lett*. **2001**, 77, 131-133.

[19] D. G. Hanna, S. Shylesh, S. Werner, A. T. Bell. *J. Catal.* **2012**, 292, 166-172

[20] A. C.Yang, C. W. Garland. *J. Phys. Chem*. **1957**, *61*, 1504-1512.

[21] D. Evans, G. Yagupsky, G. Wilkinson. *J. Chem. Soc*. **1968**, 2660-2663

[22] S. M. Silvia, R. P. J. Bronger, Z. Freixa, J. Dupont, P. W. N. M. van Leeuwen. *New J. Chem*. **2003**, 27, 1294-1296.

[23] H. F. J. Vant Blik, J. B. A. D. Van Zon, T. Huizinga, J. C. Vis, D. C. Koningsberger, R. Prins. *J. Am. Chem. Soc*. **1985**, 107, 3139-3145

[24] P. Basu, D. Panayotov, J. T. Yates Jr. *J. Am. Chem. Soc*. **1988**, 110, 2074-2081.

[25] R. L. Pruett, J. A. Smith. *J. Org. Chem*. **1969**, 34, 327-330.

[26] R. Augustine, S. Tanielyan, S. Anderson, H. Yang. *Chem. Commun*. **1999**, 1257-1258

[27] R.F. Heck, D.S. Breslow. *J. Am. Chem. Soc.* **1962**, 84, 2499-2502.

[28] R. M. Deshpande, B. M. Bhanage, S. Kanagasabapathy, R. V. Chaudhari. *Ind. Eng. Chem. Res*. **1998**, 37, 2391-2396.

[29] E. Zuidema, L. Escorihuela, T. Eichelsheim, J. J. Carbo, C. Bo , P. C. J. Kamer, P. W. N. M van Leeuwen. *Chem. Eur. J.* **2008**, 14, 1843-1853.

[30] J. J. Carbo, F. Maseras, C. Bo, P. W. N. M. van Leeuwen. *J. Am. Chem. Soc.* **2011**, 123, 7630-7637.

[31] C. P. Casey, L. M. Petrovich. *J. Am. Chem. Soc.* **1995**, 117, 6007-6014.

Chapter 5

Hydrogenation of Butanal over Silica-Supported Shvo's Catalyst and Its Use for the Gas-Phase Conversion of Propene to Butanol via Tandem Hydroformylation and Hydrogenation

Abtract

The objective of the present study was to develop a heterogeneous catalyst for the hydrogenation of butanal that could function in the presence of CO and propene and, hence, could be used in a tandem reactor to enable the gas-phase conversion of propene and synthesis gas to butanol. To this end, we investigated the activity of silica-supported Shvo's catalyst (Shvo/SiO_2) for the gas-phase hydrogenation of butanal. Experiments were performed to determine the kinetics of *n*- and isobutanal hydrogenation. The apparent activation energies and the apparent partial pressure dependencies of *n*- and isobutanal, H_2, and CO on the rates of *n*- and isobutanol formation were determined. A mechanism for butanal hydrogenation was proposed to rationalize the observed kinetics and some of the reaction intermediates were observed by in situ infrared and ^{31}P MAS NMR spectroscopy. It was found that Shvo/SiO_2 was inhibited by SX (SX = sulfoxanthphos) and CO, and is inactive for alkene hydrogenation. The tandem catalytic conversion of propene and synthesis gas to butanol was then carried out using a SX-Rh supported ionic liquid phase (SILP) catalyst to promote the hydroformylation of propene to butanal and Shvo/SiO_2 to promote the hydrogenation of butanal to butanol. The rate expressions describing the kinetics of each of the catalysts were then used to predict operating conditions required to achieve high conversion of propene to butanol. Under the most favorable conditions examined (H_2/CO = 10), an overall yield of 13% to butanol was achieved with 15% propene conversion and 90% aldehyde conversion at a temperature of 413 K.

5.1 Introduction

Roughly 2 x 10^6 tons of butanol are produced annually [1] for use as a plasticizer, an industrial solvent, and an intermediate in the production of butyl acetate, a key ingredient in lacquers and varnishes [2]. The demand for butanol is expected to increase in the future as a consequence of recent studies showing that butanol is a viable alternative to ethanol as an additive to gasoline [3,4].

While many processes exist for the production of butanol, such as the aldol condensation of ethanal [5], oxidation of butane [6], or the enzymatic fermentation of sugars [3,7], the overwhelming majority of butanol is produced in a three-step process involving the homogeneously catalyzed hydroformylation of propene, separation of the resulting butanal, and subsequent hydrogenation of butanal. Separation of butanal is necessary because aldehyde hydrogenation catalysts such as supported Pt and Pt-Sn [8], Rh-Sn [9], and Ni [10] are poisoned by CO, as well as being active for alkene hydrogenation. Therefore, it would be highly desirable to develop a catalyst system for

the tandem, gas-phase conversion of propene and synthesis gas to butanol. Achievement of this goal requires identification of a heterogeneous hydroformylation catalyst and a heterogeneous aldehyde hydrogenation catalyst that functions in the presence of CO and is inactive for alkene hydrogenation.

Recent studies have shown that the gas-phase hydroformylation of propene can be carried out on a heterogeneous catalyst prepared by impregnating a Rh-phosphine complex dissolved in ionic liquid onto a silica support [11,12]. Such catalysts, referred to as supported ionic liquid phase (SILP) catalysts, are stable and active under continuous gas-phase reaction conditions. We have recently shown that the exceptional stability of these catalysts is due to the interaction of the Rh-phosphine complex with silanol groups present on the support surface and have discussed the mechanism and kinetics propene hydroformylation over this catalyst [13,14].

Several attempts to perform the tandem conversion of C_n alkenes and synthesis gas to the C_{n+1} alcohol in a single reactor system have been reported. Drent and coworkers have shown that chloride anion promoted palladium-phosphine complexes could be used to convert propene to *n*- and isobutanol with 85% selectivity [15]. High turnovers (1000 hr^{-1}) and selectivity (99%) were also observed in the conversion of C8-C10 internal alkenes into their corresponding alcohols [15]. A halogen-free system studied by Zakzeski et al. demonstrated that the conversion of hexene to heptanol could be achieved utilizing $HRh(PPh_3)_2(CO)$ as the hydroformylation catalyst and $H_2Ru(PPh_3)_3CO$ as the hydrogenation catalyst [16]. It was noted, though, that the hydrogenation of the aldehyde would only occur after the CO was consumed or removed from the reactor because the Ru complex was inhibited by CO [16]. More recently, Nozaki and coworkers have demonstrated that it is possible to carry out the hydroformylation of propene to butanal and the subsequent hydrogenation of butanal to butanol in a solution containing a Rh complex, Shvo's catalyst, and bidentate phosphine ligand, sulfoxantphos (SX) [17]. Using this approach, butanol yields of up to 85% were obtained [17]. The authors suggest that the presence of excess SX influences the activity and/or the chemoselectivity of Shvo's catalyst to preferentially hydrogenate aldehydes [17]. These findings motivated us to explore the possibility of supporting Shvo's catalyst on silica in order to produce a heterogeneous catalyst that could be used in a tandem, gas-phase hydroformylation-hydrogenation process. In this work, we report the successful preparation of a silica-supported Shvo's catalyst, present the kinetics of *n*- and isobutanal hydrogenation, and discuss the effects of CO on the hydrogenation activity. The activity of SX- modified silica-supported Shvo's catalyst was also investigated to test whether the presence of a phosphine ligand enhances the activity and/or improves the CO tolerance. We also show that silica-supported Shvo's catalyst can be used in tandem with a SX-Rh SILP catalyst to carry out the direct synthesis of butanol from propene and synthesis gas.

5.2 Methods

5.2.1 Catalyst Preparation

Approximately, 0.06 g of 1-hydroxytetraphenylcyclopentadienyl(tetraphenyl-2,4-cyclopentadien-1-one)-μ-hydrotetracarbonyldiruthenium(II), Shvo's catalyst, (Strem, 98%) was dissolved in 10 mL of anhydrous methanol (Aldrich, 99.8%). After 10 min of

stirring, 1 g of silica (Silicycle, 500 m^2 g^{-1}, average pore diameter 60 Å) stored under vacuum at 353 K was added to solution and stirred for an additional 1 h. Methanol was then slowly removed under vacuum in a rotary evaporator. The resulting catalyst is a yellowish-orange colored powder containing 0.4 wt. % Ru. SX-Shvo/SiO_2 was prepared in a similar manner except that in this case, sulfoxantphos (SX) [18] was added to the solution prior to the addition of SiO_2. Approximately 434 mg of SX was used to achieve a molar ratio of SX/Ru = 5.

5.2.2 Gas-phase Hydroformylation of Propene

Measurements of reaction rates were performed in a 6.35 mm OD quartz tube containing an expanded section (~12.7 mm OD, ~20 mm length). A plug of quartz wool was placed below the catalyst bed to hold the powder in place. The reactor was heated by a ceramic furnace with external temperature control and the catalyst bed temperature was measured with a K-type thermocouple sheathed in a quartz capillary placed in direct contact with the catalyst bed.

Prior to reaction, 0.3 g of catalyst was heated to the reaction temperature at a rate of 2 K min^{-1} in pure He (Praxair, 99.999%) flowing at 20 cm^3 min^{-1} at STP. The feed to the reactor consisted of *n*-butanal (Aldrich, 98%), isobutanal (Aldrich, 99%), H_2 (Praxair, 99.999%), and He (Praxair, 99.999%). CO (Praxair, 99.99%) was passed through a trap packed with 3.2 mm pellets of 3 Å molecular sieve in order to remove iron pentacarbonyl formed within the cylinder [19] and was then co-fed with the other reactants. An equimolar mixture of *n*- and isobutanal was placed in a 5 mL syringe connected to a syringe pump (Cole-Palmer, 74900 series). The liquid mixture was injected into a heated port subjected to continuous flow of He. A molar ratio of butanal to H_2 of 1:1 was used unless specified otherwise. Experiments were carried out at a total gas pressure of 1 atm. The total gas flow rate was typically 100 cm^3 min^{-1} at STP. Using these conditions, the conversion of aldehyde was always less than 10%. Reaction products were analyzed using an Agilent 6890N gas chromatograph containing a bonded and crosslinked (5%-Phenyl)-methylpolysiloxane capillary column (Agilent, HP-1) connected to a flame ionization detector (FID).

The continuous gas-phase hydrogenation of butene was also examined in order to determine the activity of Shvo/SiO_2 for alkene hydrogenation. Prior to reaction, 0.3 g of Shvo/SiO_2 catalyst was heated to 363 K at a rate of 2 K min^{-1} in pure He (Praxair, 99.999%) flowing at 20 cm^3 min^{-1} at STP. The feed to the reactor was then switched to one containing 1-butene (Praxair, 99.9%), H_2 (Praxair, 99.999%), and He (Praxair, 99.999%). A 1:1 stoichiometric ratio of 1-butene to H_2 was introduced to reactor at 1 atm. The partial pressure of 1-butene and He were 0.05 atm and 0.9 atm respectively. The total gas flow rate was 100 cm^3 min^{-1} at STP. Reaction products were analyzed using a gas chromatograph-mass spectrometer (Varian, Model 320) equipped with a 14-port sampling valve and three sample loops. One sample loop was injected into an Alumina PLOT column for the FID and mass spectrometer, and the other sample loop was injected into a Hayesep and Mol Sieve packed columns.

Tandem hydroformylation and hydrogenation experiments were conducted using a procedure similar to that described previously. A bi-layered catalyst bed consisting of Rh-SILP and Shvo/SiO_2 catalysts was utilized. The SILP catalyst was prepared as described in Refs. [13,14]. Shvo/SiO_2 and Rh-SILP were loaded sequentially into the

reactor (so that SILP catalyst was at the top) along with an intermediary layer of quartz wool to minimize the mixing of the two catalysts. Prior to reaction, the reactor was heated to 413 K at a rate of 2 K min^{-1} in pure He (Praxair, 99.999%) flowing at 20 cm^3 min^{-1} at STP. Experiments were carried out at total gas pressures varying from 1-3 atm and the feed to the reactor consisted of propene (Praxair, 99.9%), CO (Praxair, 99.99%), H_2 (Praxair, 99.999%), and He (Praxair, 99.999%). The total gas flow rate varied from 20-60 cm^3 min^{-1} at STP in order to maintain a constant residence time. The reaction products were analyzed by a Agilent 6890N gas chromatograph equipped with a HP-1 column connected to a FID.

5.2.3 Catalyst Characterization

Infrared spectra were acquired using a Thermo Scientific Nicolet 6700 FTIR spectrometer equipped with a liquid nitrogen cooled MCT detector. Each spectrum was obtained by averaging 32 scans taken with 1 cm^{-1} resolution. 0.015 g of Shvo/SiO_2 or SX-Shvo/SiO_2 was pressed into a 20 mm-diameter pellet (< 1 mm thick) and placed into a custom-built transmission cell equipped with CaF_2 windows, a K-type thermocouple for temperature control, and resistive cartridge heaters similar to that described in Ref. [20]. All scans were acquired at 363 K and 1 atm. All absorption spectra were taken relative to the empty transmission cell. The spectrum of the catalyst under He flow was subtracted from all the results reported.

Solid-state ^{31}P MAS NMR experiments were performed on a Bruker Avance I-500 MHz spectrometer. Data were obtained by measuring the samples using a frequency of 202.5 MHz, 90° pulse in 4.2 μs, and a delay of 60 s.

5.3 Results and Discussion

5.3.1 Catalyst Stability and Kinetics of Butanal Hydrogenation

To investigate the stability of SX-Shvo/SiO_2 and Shvo/SiO_2 with time-on-stream, experiments were conducted using an equimolar gas mixture of H_2 and *n*-butanal. As shown in Figure 5.1a, both catalysts were stable, although the activity of SX-Shvo/SiO_2 was nearly 50% lower than that of Shvo/SiO_2. Figure 5.1b shows that the addition of CO to the feed after 2 h of time on stream decreased the butanal hydrogenation activity of both catalysts quite substantially. The turnover frequency of SX-Shvo/SiO_2 and Shvo/SiO_2 dropped from roughly 8 h^{-1} to 3 hr^{-1} and 4 h^{-1} to 2 h^{-1}, respectively.

Table 5.1 lists the apparent activation barriers for Shvo/SiO_2 and SX-Shvo/SiO_2 catalysts measured in the temperature range 343-373 K. The apparent activation energy for aldehyde hydrogenation to *n*-butanol and isobutanol with Shvo/SiO_2 are 50 kJ mol^{-1} and 49 kJ mol^{-1}, respectively. Similar activation energies were also measured for SX-Shvo/SiO_2, 46 kJ mol^{-1} and 51 kJ mol^{-1} for *n*- and isobutanol, respectively.

To determine the apparent reaction orders of *n*- and isobutanal, H_2, and CO on the rate of butanol formation, the partial pressures of two components were fixed while the partial pressures of the third reactant and He were varied. The total gas flow rate was kept at 100 cm^3 min^{-1} at STP in order to maintain a constant residence time. Table 5.2 shows the effects of varying the partial pressures of H_2, *n*- and isobutanal, and CO on the rate of formation of *n*- and isobutanol over Shvo/SiO_2 and SX-Shvo/SiO_2. The partial

pressure dependencies and catalytic rates are nearly equal for *n*- and isobutanol formation. The orders with respect to H_2, *n*-butanal, and CO on the rate of formation of *n*-butanol are 0.26, 1.0, and -0.59, respectively. Similarly, the orders with respect to H_2, isobutanal, and CO on the rate of formation of isobutanol are 0.29, 1.1, and -0.58, respectively. The apparent reaction orders of H_2 and CO increased in the presence of SX. The partial pressure dependencies of H_2, *n*-butanal, and CO on the rate of formation of *n*-butanol are 0.42, 0.98, and -0.29, respectively while the partial pressure dependencies of H_2, isobutanal, and CO on the rate of isobutanol formation are 0.45, 0.95, and -0.31, respectively over SX-Shvo/SiO_2 catalysts.

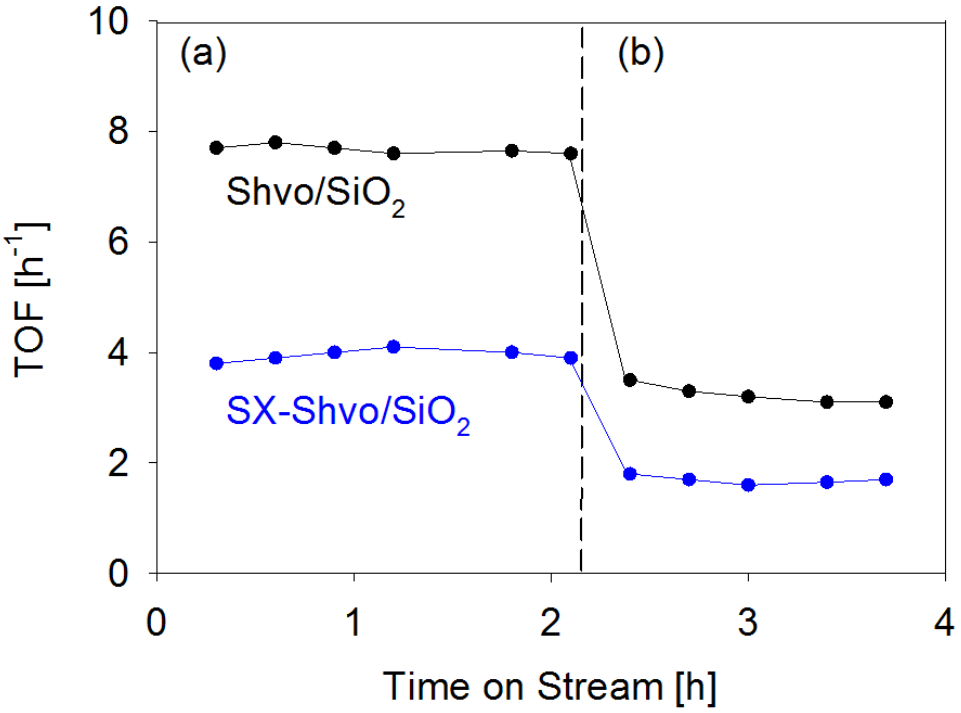

Figure. 5.1. Time on stream study with Shvo/SiO_2 and SX-Shvo/SiO_2 catalysts, T = 363 K, P_{Total} = 1 atm, catalyst mass = 0.3 g, total gas flow rate at STP = 100 cm^3 min^{-1}. (a) $P_{H_2} = P_{butanal}$ = 0.05 atm, balance He. (b) $P_{CO} = P_{H_2} = P_{butanal}$ = 0.05 atm, balance He.

Table 5.1. Apparent activation energies (kJ mol^{-1}) for the formation of *n*- and isobutanol using Shvo/SiO_2 or SX-Shvo/SiO_2. T = 343-373 K, P_{Total} = 1 atm, $P_{H_2} = P_{butanal}$ = 0.05 atm, balance He. total gas flow rate = 100 cm^3 min^{-1}, catalyst mass = 0.3 g

Catalyst	Apparent Activation Energy (kJ mol^{-1})	
	n-butanol	isobutanol
Shvo/SiO_2	49	50
SX-Shvo/SiO_2	46	51

Table 5.2 Apparent reaction orders of *n*-butanol and isobutanol synthesis using Shvo/SiO_2 and SX-Shvo/SiO_2 catalysts. T = 363 K, P_{Total} = 1 atm, catalyst mass = 0.3 g, total gas flow rate = 100 cm^3 min^{-1}.

Reaction Product	Catalyst	Apparent Reaction Order		
		H_2[a]	butanal[b]	CO[c]
n-butanol	Shvo/SiO_2	0.26	1.0	-0.59
	SX-Shvo/SiO_2	0.42	0.98	-0.29
isobutanol	Shvo/SiO_2	0.29	1.1	-0.58
	SX-Shvo/SiO_2	0.45	0.95	-0.31

[a] P_{H_2} = [0.05-0.15 atm], $P_{n-butanal} = P_{isobutanal}$ = 0.025 atm, balance He.
[b] $P_{n-butanal} = P_{isobutanal}$ = [0.025-0.075 atm], P_{H_2} = 0.05 atm, balance He.
[c] P_{CO} = [0.05-0.15 atm], $P_{H_2} = 2P_{n-butanal} = 2P_{isobutanal}$ = 0.05 atm, balance He.

5.3.2 Proposed Mechanism of Butanal Hydrogenation

The kinetics of butanal formation can be interpreted using the mechanism proposed by Shvo and coworkers [21,22] shown in Scheme 5.1. Shvo's catalyst operates through a concerted, outer-sphere mechanism in which the aldehyde is reduced in one elementary step despite not being bound directly to the metal [23]. The reaction sequence begins with the dissociation of the dimeric Ru complex (Shvo's catalyst, species **A**) into the constitutive monomers species **B** and **C** (Reaction 1). Butanal coordinates to the outer sphere of the complex by aligning the polarity of the acetyl group (partially positively charged carbon and partially negatively charged oxygen) with the hydridic (H-Ru) and acidic hydrogen (H-O) present on species **C**. The bound aldehyde is then reduced to alcohol, which converts species **C** into species **B** (Reaction 3). The catalytic cycle is closed by reaction of H_2 with species **B** to yield species **C** (Reaction 2). Species **B** has a vacant coordination site and therefore can react with either ligand, CO or SX, via Reactions 4 or 5 respectively to fulfill the vacancy. Species **D** and **E** are both saturated species which must dissociate a ligand to be catalytically active.

Evidence for the existence of several of the intermediates shown in Scheme 5.1 was provided by in situ infrared spectroscopy. Figure 5.2 shows IR spectra of the pristine Shvo's complex and Shvo/SiO_2 under exposure of He at 298 K, He at 363 K, an equimolar mixture of H_2 and He at 363 K, and an equimolar mixture of H_2, CO, and He at 363 K. The peak in spectra A and B at 1713 cm^{-1} is ascribed to the bridging O-H-O bond present in the Ru dimer [21,24] while the broad peak at 1875 cm^{-1} in spectrum B is from the SiO_2 support as shown by Figure S1 in the Supporting Information. Spectrum C shows that as the reaction temperature was increased to 363 K, the band at 1713 cm^{-1} disappeared while bands at 1965, 2005, and 2030 cm^{-1} became better resolved. The disappearance of the 1713 cm^{-1} band with increased temperature indicates that the Ru dimer complex has dissociated into its constitutive monomers. The bands appearing at 1965, 2005, and 2030 cm^{-1} are characteristic of carbonyl ligands bound to species **B** and species **C** [25,26] and are sharper in spectrum B than in spectrum A due to the removal of physisorbed water on the SiO_2 surface at elevated temperature. The appearance of a broad band at 1630 cm^{-1} is attributed to the oxo functionality present on the cyclopentadienyl ligand of species **B** which is another indication that the Ru dimer has

dissociated into Ru monomer units. Once the catalyst is treated with H_2 (spectrum D), a negative band appears at 1630 cm^{-1} upon subtraction from spectrum B signifying the conversion of species **B** into species **C** via Reaction 2. Exposure of the catalyst to CO, as shown in spectrum E, causes two new bands to appear at 2100 and 2050 cm^{-1}, while the band at 1965 cm^{-1} becomes negative upon subtraction from spectrum B. The new bands in the carbonyl stretching region are attributed to the transformation of species **B** into a tricarbonyl Ru complex species **E**.

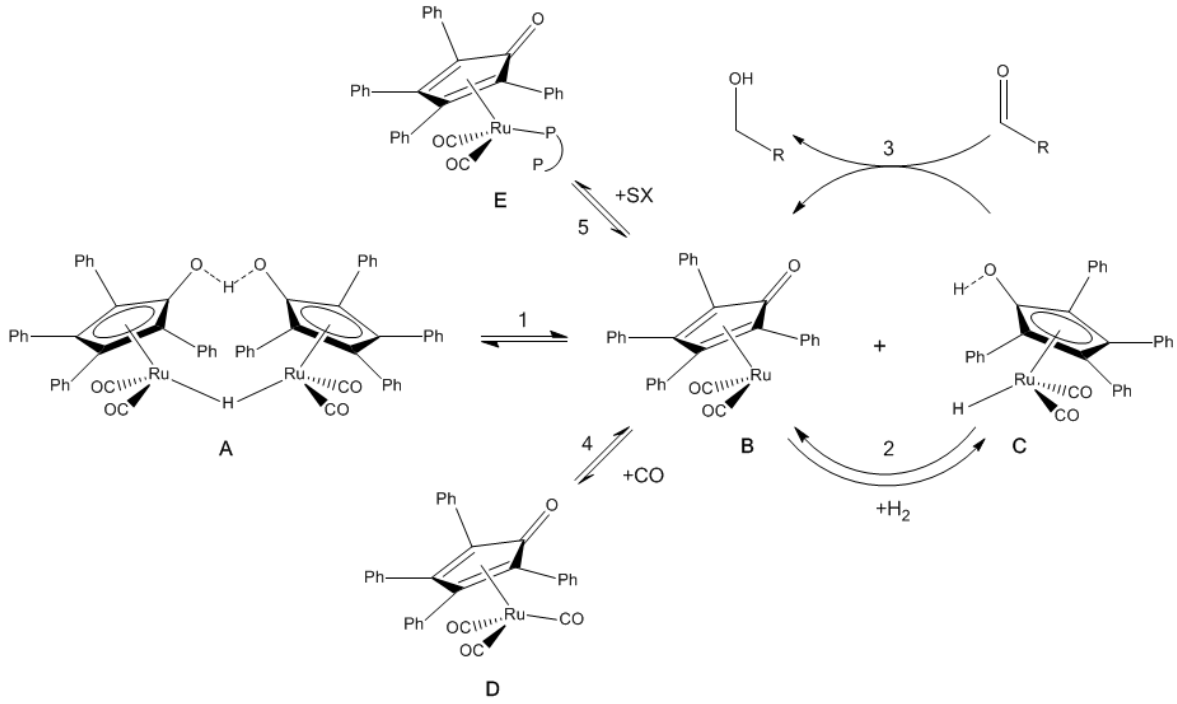

Scheme 5.1 Proposed mechanism for aldehyde hydrogenation using Shvo/SiO_2 catalyst.

The spectra for SX-Shvo/SiO_2 exhibit similar bands to those observed for Shvo/SiO_2. The most notable difference between the catalysts is that the carbonyl stretching region is red-shifted by 5-10 cm^{-1} in the presence of SX because phosphines are better sigma donors than carbonyl ligands [27]. The higher electron density on Ru enables greater pi-backbonding to the carbonyl groups, thereby reducing the frequency of the carbonyl stretching frequency. A comparison of the spectra for Shvo/SiO_2 and SX-Shvo/SiO_2 is provided in the Supporting Information.

Further evidence for the coordination of SX to Shvo's catalysts under reaction conditions was obtained from ^{31}P NMR spectroscopy. Figure 3 shows the results of solid-state ^{31}P MAS NMR measurements of spent SX-Shvo/SiO_2 which exhibits the same spectral features of the fresh SX-Shvo/SiO_2. The broad peak observed at -13 ppm can be ascribed to the free SX adsorbed on the silica surface [13], while the broad peak centered at 34 ppm is due to the phosphine bonded to Ru as shown in species **E** [17]. Although many of species shown in Scheme 5.1 could undergo ligand exchange with SX, Reaction 5 is the most facile because of the vacant coordination site on species **B**. Previous reports

that have shown by solution ^{31}P NMR that singly coordinated phosphorus to Ru (species **E** of Scheme 5.1) results from the reaction of species **B** with SX [17]. However, the possibility that both phosphorus atoms of SX are coordinated to Ru cannot be ruled out on the basis of the present data. While there have reports indicating that Shvo's catalyst modified with PPh_3 can complete the catalytic cycle, this occurs at much slower rates than with the unmodified catalysts [28]; thus, all of the catalytic activity is attributed to unmodified species **C**. The data and the literature, therefore, indicate that SX-Shvo/SiO_2 is less active than Shvo/SiO_2 because coordination of SX reduces the concentration of species **C** available for the catalytic cycle.

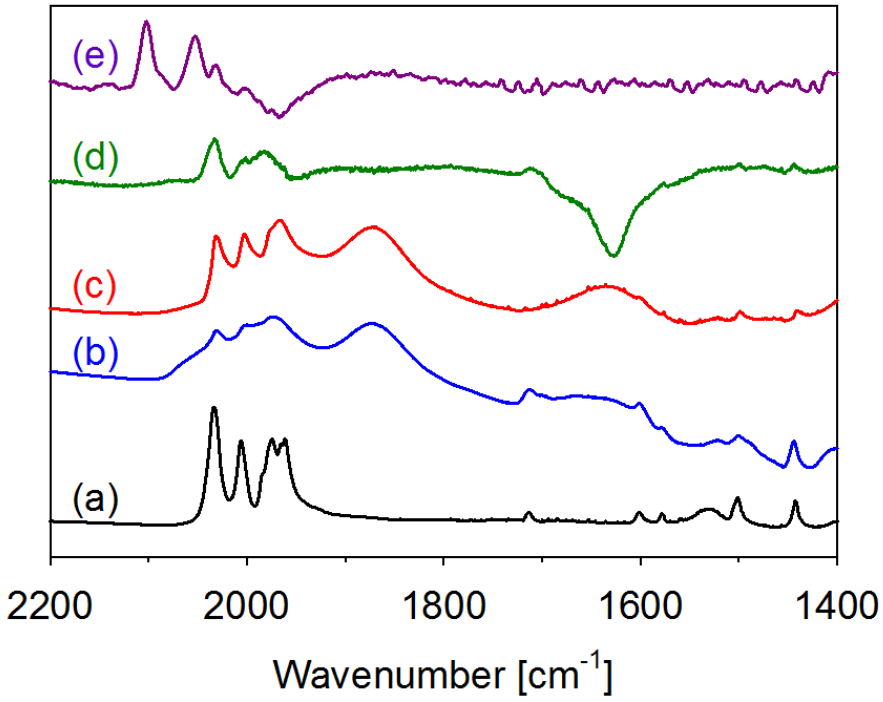

Figure 5.2 In situ infrared spectra of (a) Shvo's complex in He at 298 K and Shvo/SiO_2 catalyst under (b) He at 298 K, (c) He at 363 K, (d) H_2 at 363 K, and (e) H_2/CO = 1 at 363 K.

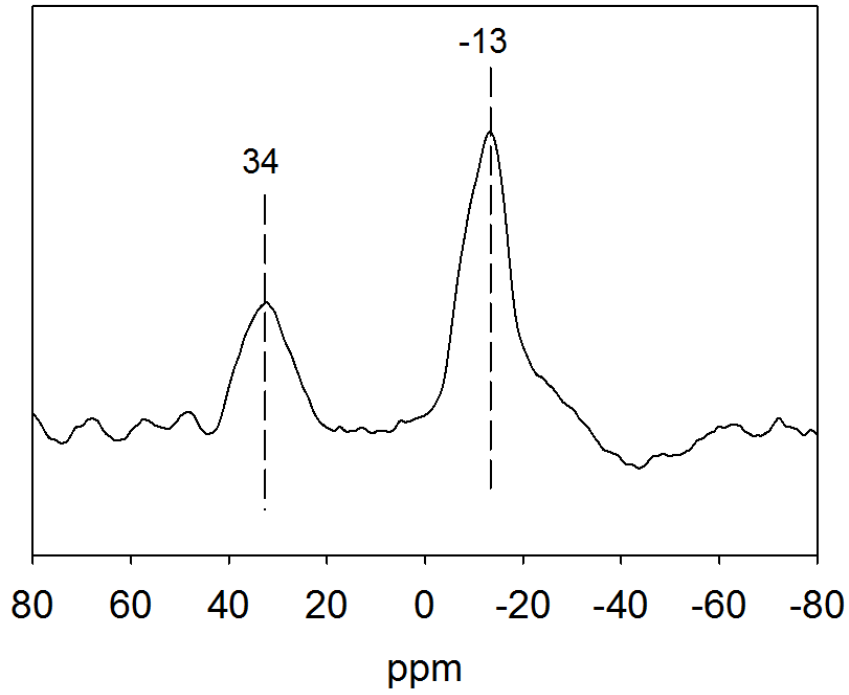

Figure 5.3 Solid-state ^{31}P MAS NMR spectra of spent SX-Shvo/SiO_2 catalyst.

5.3.3 Kinetics of Butanal Hydrogenation

If it is assumed that at reaction temperature, species **A** dissociates completely to species **B** and **C**, that Reactions 2, 4, and 5 are quasi-equilibrated, and that Reaction 3 is the irreversible, rate-limiting step, then the rate of butanol formation is given by the following relation:

$$r_{butanol} = \frac{K_2 k_3 P_{butanal} P_{H_2} [Ru]}{1 + K_2 P_{H_2} + K_4 P_{CO} + K_5 [SX]} \qquad (1)$$

where k_3 is the rate coefficient for Reaction 3, K_i is the equilibrium constant for Reaction i, P_j is the partial pressure of species j, and $[Ru]$ is the total surface concentration of Ru. The derivation of Eq. 1 is provided in the Supporting Information.

Eq. 1 is consistent with the experimentally observed partial pressure dependencies and those found in literature. Casey and coworkers have reported that the order with respect to benzaldehyde and H_2 in a homogenous solution of Shvo's Catalyst to be 1 and 0, respectively [28] The rate of butanal synthesis is first order in butanal due to the $P_{butanal}$ term in the numerator of Eq. 1. The 0-1 order in the partial pressure of H_2 depends on the magnitude of the $K_2 P_{H_2}$ in the denominator of Eq. 1. As the value of $K_2 P_{H_2}$ increases, the order with respect to H_2 tends towards zero. Thus, the value for $K_2 P_{H_2}$ in solution must be high in order to explain the zero order dependence observed in Ref. [28]. The inhibitory effect of CO and SX is represented by the $K_4 P_{CO}$ and the $K_5 [SX]$ terms in the

denominator, respectively. The order with respect to CO becomes less negative in presence of SX due to the term $K_5[SX]$ also present in the denominator of Eq. 1.

The parameters appearing in Eq. 1 for Shvo/SiO_2 and SX-Shvo/SiO_2 were estimated using the data fitting routine (i.e. "nlinfit" function) in MATLAB with the initial guesses of the parameters set to zero. Values for the parameters are listed in Table 5.3 for *n*- and isobutanol formation. As seen in Figure 4a-d, the derived rate expression given in Eq. 1 describes the experimental data effectively. The coefficient of determination, R^2, is above 90% for all cases considered.

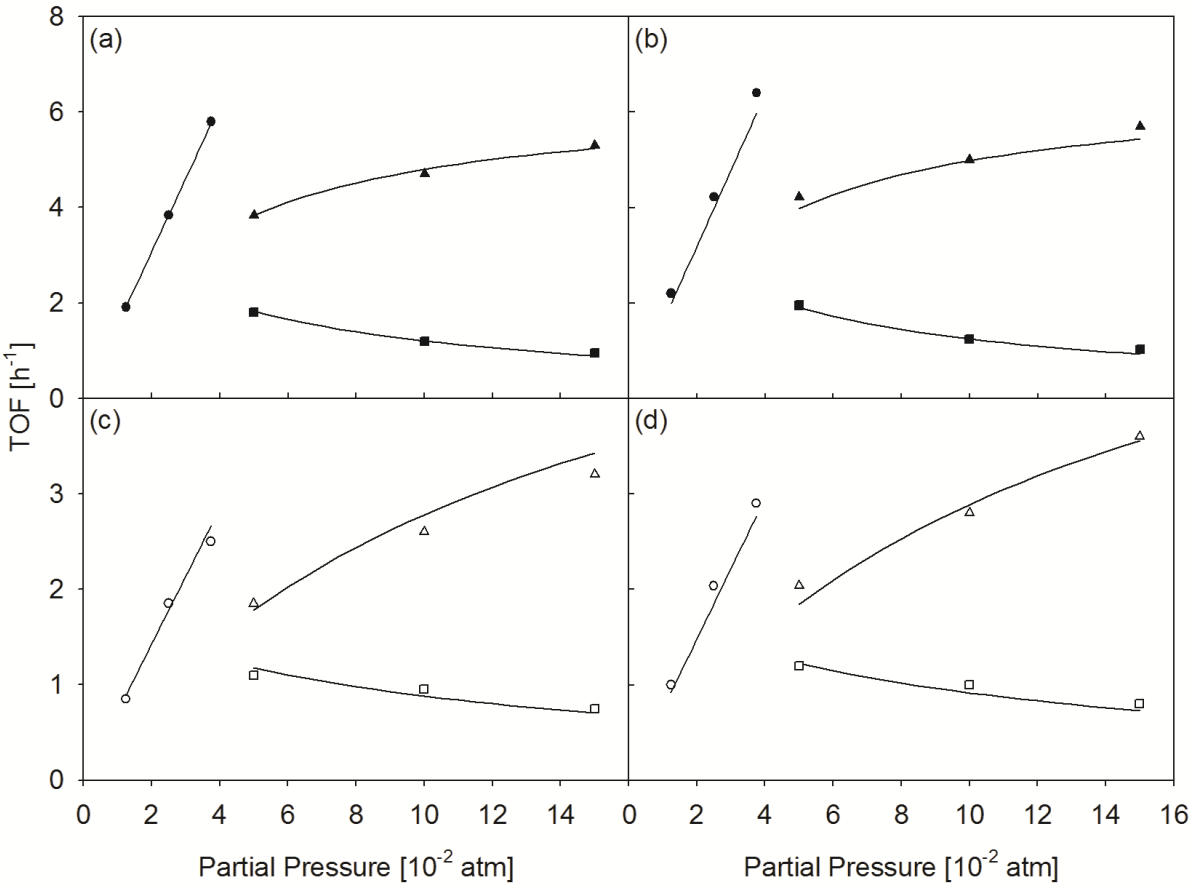

Figure 5.4 Non-linear regression of partial pressure data using (a,b) Shvo/SiO_2 and (c,d) SX-Shvo/SiO_2. Rate of (a,c) *n*- and (b,d) isobutanol synthesis vs. partial pressure of (●,○) butanal, (▲,△) H_2, and (■,□) CO. Experimental points are indicated by data markers. Spline curves indicate predicted values. T = 363 K, P_{Total} = 1 atm, catalyst mass = 0.3 g, total gas flow rate = 100 cm^3 min^{-1}.

Table 5.3 Values of the rate parameters obtained by a best fit to experimental data.

$$r_{butanol} = \frac{K_2 k_3 P_{butanal} P_{H_2} [Ru]}{1 + K_2 P_{H_2} + K_4 P_{CO} + K_5 [SX]}$$

Parameter	Value	Unit
K_2	30	atm^{-1}
K_4	55	atm^{-1}
K_5	7.3×10^6	$m^2\ atm^{-1}$
k_3	255[a] 325[b]	$atm^{-1}\ h^{-1}$

[a] *n*-butanol, [b] isobutanol

5.3.4 Butene hydrogenation over Shvo/SiO_2

The hydrogenation of 1-butene was investigated in order to determine activity of Shvo/SiO_2 for hydrogenation of alkenes. It was observed that the 1-butene hydrogenation activity was 0.4 h^{-1}, which is more than an order of magnitude lower than the activity for butanal hydrogenation under comparable conditions. Consistent with our results, Shvo and coworkers demonstrated that the alkenes are unreactive for hydrogenation in the presence of Shvo's Catalyst and formic acid [29]. The difference in hydrogenation activity between 1-butene and butanal is attributable to the non-polarity of 1-butene. Accordingly, 1-butene is unable to coordinate to the hydridic and acidic hydrogen atoms on the Ru cluster as effectively as the polar carbonyl of butanal.

5.3.5 Tandem hydroformylation and hydrogenation using Rh-SILP and Shvo/SiO_2 catalysts

The direct conversion of propene to butanol was investigated using a bi-layered catalyst bed of SX-Rh SILP and Shvo/SiO_2. The SX-Rh SILP catalyst was selected because of its high activity and stability for propene hydroformylation [13]. From our previous study of Rh-SILP catalysts, we showed that catalysts with SX were almost six times more active than catalysts with triphenylphosphine or sulfonated triphenyl phosphine [13]. Furthermore, we demonstrated that the kinetics of hydroformylation were dependent upon the reaction temperature [14]. At 363 K, the apparent partial pressure dependencies of propene, H_2, and CO were 0.93, 0.1, and -0.43. However, the apparent partial pressure dependencies of propene, H_2, and CO were 0.76, 0.84, and zero, respectively at 413 K. Since the kinetics of butanal hydrogenation exhibit a nearly first order dependence on H_2 and an inverse dependence on the partial pressure of CO (see Table 5.2), a high ratio of H_2 to CO partial pressures is desired. The reaction temperature was set to 413 K to exploit first order and zero order dependence of H_2 and CO on the rates of propene hydroformylation and to lower the molar ratio of *n*-butanal to isobutanal (*n/i*) formation. A low *n/i* ratio is desirable for fuel production because the anti-knock index of isobutanol is much greater than *n*-butanol [4]. The CO and propene partial pressure were fixed at 0.25 atm while the H_2 partial pressure was varied from 0.25 to 2.5

atm. As shown in Figure 5.5, the propene conversion to butanal and the aldehyde conversion to butanol rises as the H_2/CO molar ratio is increased. Also shown in Figure 5.5 is the predicted propene and aldehyde conversion as calculated from the rate laws presented in this work and in Ref. [14]. The values of the parameters in the hydroformylation rate expression measured at 413 K are provided in Table 3.2. As expected from our previous work on hydroformylation and this work, the molar ratios of *n*-butanal to isobutanal and *n*-butanol to isobutanol were both approximately 7. Under the most favorable conditions examined (H_2/CO = 10), 15% propene conversion and 90% aldehyde conversion was observed; thus, a 13% yield to butanol was achieved. The results presented in Figure 5.5 illustrate, to the best of our knowledge, the first example of the direct conversion of propene to butanol by means of the tandem hydroformylation and hydrogenation reactions carried out in the gas phase using heterogeneous catalysts.

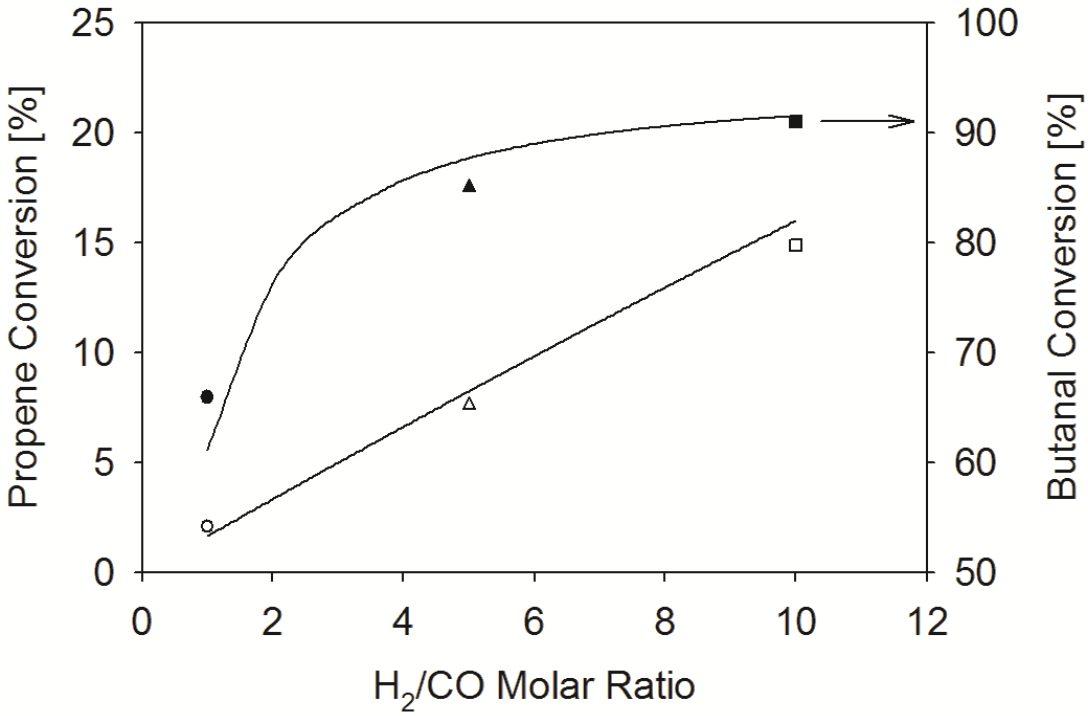

Figure 5.5 Results from tandem hydroformylation-hydrogenation experiment. T = 413 K. (○, △, □) Propene conversion to butanal. (●, ▲, ■) Butanal conversion to butanol. $P_{C_3H_6} = P_{CO}$ = 0.25 atm. (○, ●) $P_{H_2} = P_{He}$ = 0.25 atm, (△, ▲) P_{H_2} = 1.25 atm, (□, ■) P_{H_2} = 2.5 atm. SX-Rh SILP catalyst mass = 0.4 g (0.2 wt. % Rh), Shvo/SiO_2 = 0.8 g (1 wt. % Ru). The solid lines represent conversions determined from the rate expressions for propene hydroformylation and butanal hydrogenation (Eq. 1).

The rate expressions of hydroformylation and hydrogenation were also used to predict the conditions necessary to achieve a high yield of butanol from propene over SX-Rh SILP and Shvo/SiO_2 catalysts. Figure 5.6 shows the effects of varying the total pressure on the minimum amount of hydroformylation catalyst and hydrogenation catalyst necessary to achieve 99% conversion in each reaction. In all of the cases examined, the initial molar flow rate of the feed is set to 54 mmol h^{-1} and the inlet feed consists of a 1:1:2 molar ratio of C_3H_6:CO:H_2. Under these conditions, Shvo/SiO_2 operates in the absence of CO because 99% of the propene and CO are consumed in the hydroformylation reaction. Figure 5.6 shows the amount of catalyst necessary to achieve a 98% yield of butanol decreases substantially as the total pressure is increased. While the span of experimental conditions predicted are beyond the limitations of the apparatus available for the present study, it is evident that a high yield of butanol could be achieved starting with a stoichiometric feed of propene and synthesis gas.

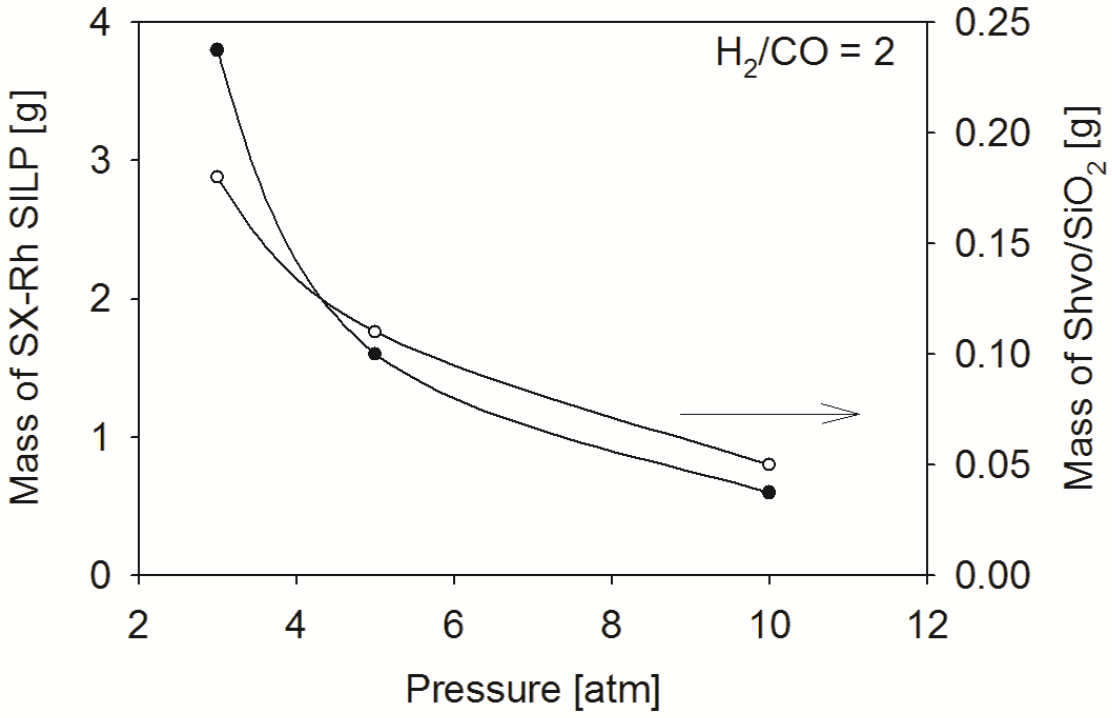

Figure 5.6 Modeled results of the tandem hydroformylation-hydrogenation experiment. (●) mass of SX-Rh SILP catalyst and (○) mass of Shvo/SiO_2 catalyst necessary to achieve 98% yield to butanol as a function of total pressure. T = 413 K, $\dot{N}_T$= 54 mmol h^{-1}, $2P_{C_3H_6} = 2P_{CO} = P_{H_2}$.

5.4 Conclusion

The kinetics of butanal hydrogenation over Shvo/SiO_2 and SX-Shvo/SiO_2 have been investigated. The activity of SX-Shvo/SiO_2 was lower than the activity of Shvo/SiO_2, but the apparent activation energies for hydrogenation of *n*- and isobutanol were nearly identical (~50 kJ mol^{-1}) for both catalysts. This result suggests that the catalytically active species is the same for both catalysts. The partial pressure dependence on butanal is roughly first order for both catalysts, while the partial pressure dependence on H_2 is ~ 0.3 and 0.4 for Shvo/SiO_2 and SX-Shvo/SiO_2, respectively. Similarly, the partial pressure dependence on CO increases from -0.6 in the absence of SX to -0.3 in the presence of SX. The differences in the orders in the partial pressures of H_2 and CO are ascribed to the coordination of SX to Ru, which was confirmed by in situ infrared spectroscopy and ^{31}P MAS NMR. Infrared spectroscopy also provided evidence for several of the intermediates appearing in the mechanism shown in Scheme 5.1. Based upon the proposed mechanism, the ability of Shvo's catalyst to function in the presence of CO is attributed to the competition between a vacant coordination site and the addition of a H_2 to the Ru complex. A rate law was derived assuming that the reduction of aldehyde is the rate-determining step (Reaction 3 in Scheme 5.1) and that the other elementary steps are quasi-equilibrated. The rate coefficients appearing in Eq. 1 were obtained by non-linear regression (see Table 5.3) and found to describes the experimental data very well.

The direct gas-phase conversion of propene to butanol was demonstrated for the first time using a bi-layered, packed-bed reactor containing SX-Rh SILP and Shvo/SiO_2 catalysts. Under the conditions investigated, the overall yield a 13% to *n*- and isobutanol (*n/i* = 7) was achieved using a feed molar ratio of H_2/CO = 10. This proof-of-concept experiment demonstrates the feasibility of converting propene to butanol in a single reactor. The rate expressions describing the kinetics of propene hydroformylation and butanal hydrogenation were also used to predict the amount of each catalyst required to achieve a 98% yield of butanol as a function of total pressure for an assumed stoichiometric feed and initial molar flow rate.

5.5 Acknowledgements

This work was supported by the XC2 program funded by BP.

5.6 Supporting Information

5.6.1 Derivation of Rate Expressions

Assuming aldehyde reduction (reaction 3) to be the rate-determining step (RDS), the rate of butanol formation is:

1) $r_3 = k_3[C]P_{butanal}$

where [*I*] represents the concentration of species *I* shown in Scheme 5.1. The concentration of the reactive intermediates can be determined using the quasi-equilibrium assumption:

2) $[C] = K_2[B]P_{H_2}$

Substituting Eq. 2 into 1 yields:

3) $r_3 = K_2k_3[B]P_{H_2}P_{butanal}$

In order to solve for the concentration of [*B*], perform a Ru balance:

4) $[Ru] = [B] + [C] + [D] + [E]$

Assuming that [*A*] is negligible at high temperature as stated in the manuscript. Performing algebraic manipulations to solve for [*B*].

5) $[B] = [Ru]\left(1 + \frac{[C]}{[B]} + \frac{[D]}{[B]} + \frac{[E]}{[B]}\right)^{-1}$

Using the equilibrium expressions for Reaction 2, 4, and 5 yields Eq. 6, 7, and 8, respectively.

6) $\frac{[C]}{[B]} = K_2P_{H_2}$
7) $\frac{[D]}{[B]} = K_4P_{CO}$
8) $\frac{[E]}{[B]} = K_5[SX]$

Substituting Eqs. 6, 7, and 8 into Eq. 5 yields:

9) $[B] = [Ru]\left(1 + K_2P_{H_2} + K_4P_{CO} + K_5[SX]\right)^{-1}$

Substituting Eq. 9 into Eq. 3 yields the final rate expression:

10) $r_{butanol} = \frac{K_2k_3P_{butanal}P_{H_2}[Ru]}{1+K_2P_{H_2}+K_4P_{CO}+K_5[SX]}$

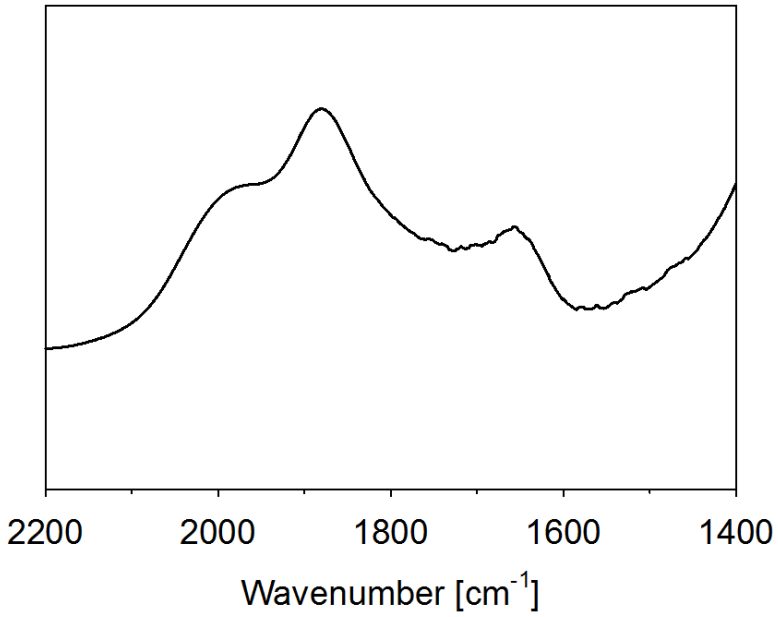

Figure S5.1 Infrared spectra of SiO_2 exposed to He at 298 K and P_{Total} = 1 atm.

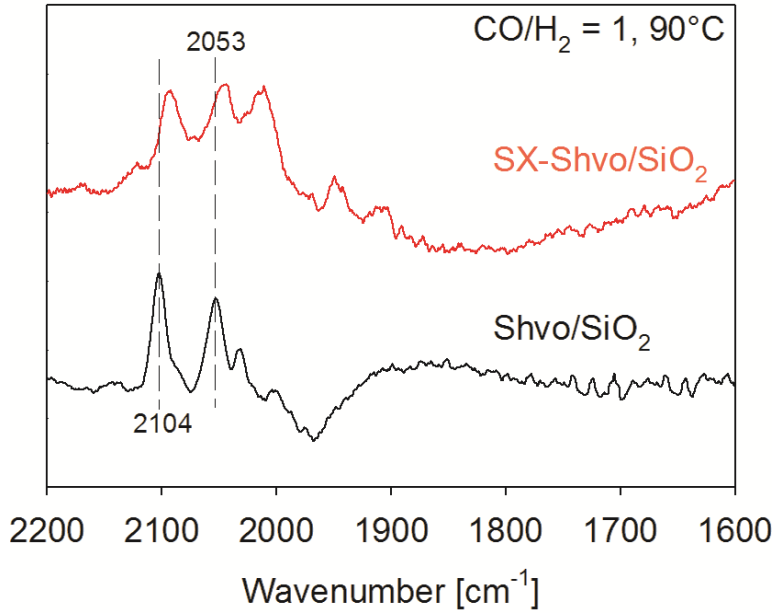

Figure S5.2 In situ infrared spectra of (—) SX-Shvo/SiO_2 and (—) Shvo/SiO_2 exposed to a 1:1 ratio of H_2 and CO at 363 K. P_{Total} = 1 atm.

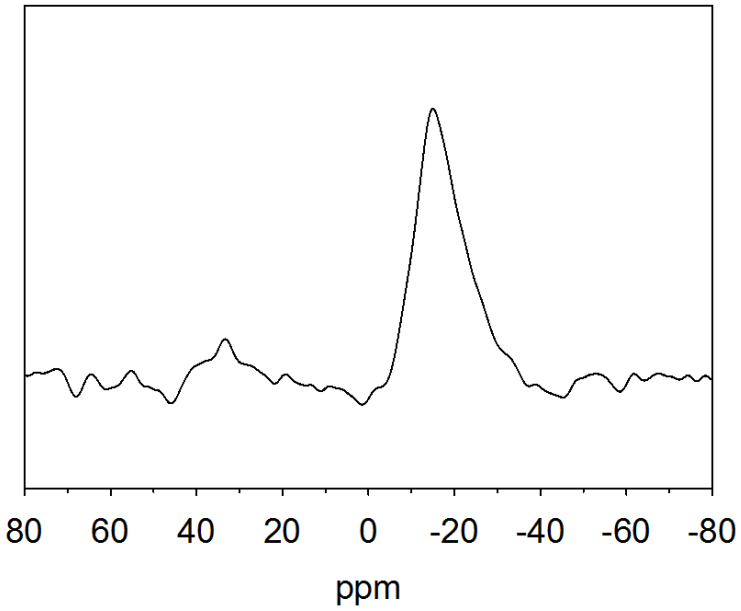

Figure S5.3 Solid-state ^{31}P MAS NMR spectra of SX/SiO_2.

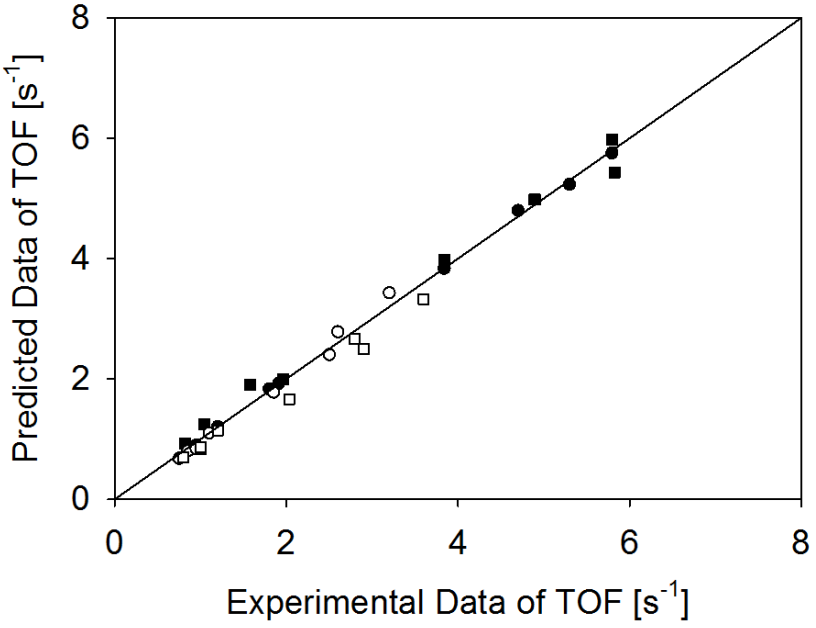

Figure S5.4 Parity plot of the predicted values determined from non-linear regression vs. the experimental data. (●,■) Shvo/SiO_2, (○, □) SX-Shvo/SiO_2 , (●,○) *n*-butanal (■ , □) isobutanal, T = 363 K, P_{Total}= 1 atm, catalyst mass = 0.3 g, total gas flow rate = 100 cm^3 min^{-1}.

5.7 References

[1] A. Chauvel, G. Lefebvre. in: *Petrochemical Processes, 2nd ed*., Editions Technip, Paris, **1989**, 81-90.

[2] P. Durre. *Annals of the New York Academy of Sciences*. **2008**, 1125, 353-362.

[3] S. Lee, M. O. Cho, C. H. Park, Y. Chung, J. H. Kim, B. Sang, Y. Um. *Energy Fuels*. **2008**, 2 3459-3464.

[4] E. Christensen, J. Yanowitz, M. Ratcliff, R. L. McCormick. *Energy Fuels.* **2011**, 25, 4723-4733.

[5] J. E. Rekoske, M. A. Barteau. *Ind. Eng. Chem. Res.* **2011**, 50, 41-51.

[6] S. Marengo, P. Comotti, G. Galli. *Catal. Today.* **2003**, 81, 205-213.

[7] Y. Lee, J. H. Park, S. H. Jang, L. K. Nielsen, J. Kim, K. S. Jung. *Biotechnol. Bioeng.* **2008**, 101, 209-228.

[8] F. Coloma, A. Sepulveda-Escribano, J. L. G. Fierro, F. Rodriguez-Reinoso. *Appl. Catal., A.* **1996**, 136, 231-248.

[9] P. Reyes, M. C. Aguirre, J. L. G. Fierro, G. Santori, O. J. Ferretti. *Mol. Catal. A: Chem.* **2002**,184, 431-441.

[10] J. K. Jeon, J. H. Yim, Y. K. Park. *Chem. Eng. J.* **2008**, 140, 555-561.

[11] A. Riisager, K. M. Eriksen, P. Wasserscheid, R. Fehrmann. *Catal. Lett.* **2003**, 90, 149-153.

[12] A. Riisager, R. Fehrmann, M. Haumann, B. S. K. Gorle, P. Wasserscheid. *Ind. Eng. Chem. Res.* **2005**, 44, 9853-9859.

[13] S. Shylesh, D. G. Hanna, S. Werner, A. T. Bell. *ACS Catal.* **2012**, 4, 487-493.

[14] D. G. Hanna, S. Shylesh, S. Werner, A. T. Bell. J. Catal. **2012**, 292, 166-172.

[15] D. Konya, K. Q. Almeida Lereno, E. Drent. *Organometallics.* **2006**, 23, 3166-3174.

[16] J. Zakzeski, H. R. Lee, Y. L. Leung, A. T. Bell. *Appl. Catal., A.* **2010**, 374, 201-212.

[17] K. Takahashi, M. Yamashita, T. Ichihara, K. Nakano, K. Nozaki. *Angew. Chem. Int. Ed.* **2010**, 49, 4488-4490.

[18] W. P. Mul, K. Ramkisoensing, P. C. J. Kamer, J. N. H. Reek, A. J. van der Linden, A. Marson, P. W. N. M. van Leeuwen. *Adv. Synth. Catal.* **2002**, 344, 293-298.

[19] L. Q. Xu, V. L. Zholobenko, L. M. Kustov, W. M. H. Sachtler. *J. Mol. Catal.* **1993**, 83, 391-395.

[20] J. F. Joly, N. Zanier-Szydlowski, S. Colin, F. Raatz, J. Saussey, J. C. Lavalley, *Catal. Today*. **1991**, 9, 31-38.

[21] Y. Shvo, D. Czarkie, Y. Rahamim. *J.Am. Chem. Soc.* **1986**, 108, 7400-7402.

[22] N. Menashe, Y. Shvo. *Organometallics.* **1991**, 10, 3885-3891.

[23] J. S. M. Samec, J. E. Backvall, P. G. Andersson, P. Brandt. *Chem. Soc. Rev.* **2006**, 35, 237-248.

[24] J. E. Caton, C. V. *Banks. Inorg. Chem.* **1967**, 6, 1670-1675.

[25] M. J. Mays, M. J. Morris, P. R. Raithby, Y. Shvo, D. Czarkie. *Organometallics.* **1989**, 8, 1162-1167.

[26] C. P. Casey, S. E. Beetner, J. B. Johnson. *J. Am. Chem. Soc.* **2008**, 130, 2285-2295.

[27] R. H. Crabtree. in: *The Organometallic Chemistry of the Transistion Metals, 4th ed.*, John Wiley & Sons, Inc., Hoboken, **2005**, 101.

[28] C. P. Casey, N. A. Strotman, S. E. Beetner, J. B. Johnson, D. C. Priebe, T. E. Vos, B. Khodavandi, I. A. Guzei. *Organometallics.* **2006**, 25, 1230-1235.

[29] N. Menashe, E. Salant, Y. Shvo. *J. Organomet. Chem.* **1996**, 514, 97-102.

Chapter 6

Tailoring the Co-operative Acid-Base Effects in Silica Supported Amine Catalysts: Applications in the Continuous Gas-Phase Self Condensation of *n*-butanal

Abtract

A highly efficient solid-base organocatalyst for the gas-phase aldol self-condensation of *n*-butanal to 2-ethylhexenal was developed by grafting site-isolated amines on tailored silica surfaces. The catalytic activity depends largely on the nature of amine species, the surface concentration of amine and silanol groups, and the spatial separation between the silanol and amine groups. In situ FT-IR measurements shows that the formation of nucleophilic enamines leads to the enhanced catalytic activity of secondary amine catalysts, whereas the formation of imines (stable up to 473 K) leads to the low activity observed for silica-supported primary amines. Blocking the silanol groups on the silica support by silylation or co-feeding water into the reaction stream drastically decreases the reaction rates, demonstrating that weaker acidic silanol groups participate cooperatively with the amine groups to catalyze the condensation reaction. This work demonstrates that the spatial separation of the weakly acidic silanols and amines can be tuned by the controlled dehydration of the supporting silica and by varying the linker length of the amine organosilane precursor used to graft the amine to the support surface. A mechanism for aldol condensation is proposed and then analyzed using density functional theory (DFT). DFT analysis of the reaction pathway suggests that the rate-limiting step in aldol condensation is carbon-carbon bond formation, which is consistent with the observed kinetics. The calculated apparent activation barrier that follows from this analysis agrees reasonably with that measured experimentally.

6.1 Introduction

Enzymes accelerate chemical reactions by the co-operative interaction between two or more functional groups accurately positioned within their active sites [1]. For example, serine protease significantly enhances (~10^{12} times) the hydrolysis of amides through the co-operative catalytic triad nucleophilic alcohol, basic imidazole, and acidic carboxylic acid interactions [2]. To achieve high activity, mutually incompatible groups, e.g., acids and bases, must be positioned in order to suppress direct proton transfer; however, the distance between the two active moieties must be close enough so that they can function synergistically [3]. This paradigm of biological transformations has inspired the synthesis of a large library of homogeneous acid-base bifunctional catalysts that exhibit excellent activity in many organic transformations [4].

Solid base catalysts synthesized by functionalization of organosilanes or nitridation of inorganic oxides constitute a new class of heterogeneous catalysts capable of catalyzing various carbon-carbon bond formation such as the Knoevenagel, Henry, and aldol condensation reactions [3,5]. Since organic amines (base sites) supported on silica surfaces (acid sites) can activate nucleophiles and electrophiles, respectively, several

synthetic approaches have been reported for tailoring the spatial separation between the antagonist functional groups [6]. The later feature is crucial for co-operative catalysis because the functional groups must be close enough to each other to achieve co-operativity without mutual neutralization. For example, Kubota and coworkers have shown that higher rates of aldol condensation can be achieved when homogeneous amines are used with mesoporous silica containing weakly acidic silanol groups [7]. Katz and coworkers have shown the pivotal role of silanol groups in the acid-base co-operativity between the silanol and amines groups by demonstrating that the activity of such acid-base pairs is greatly reduced when the silanol groups are passivated [8]. The structure of the support can also influence the performance of acid-base pairs. Shimizu and coworkers have observed that amines supported on mesoporous silica (FSM-16) are nearly twice as active as amines supported on mesoporous silica and five times more active than homogenous amines [9]. The superior performance of mesoporous silica was attributed to the enrichment of reactants inside the ordered channels of this support. The influence of acidity of the acid groups in acid-base pairs has been explored by Davis and coworkers [10]. These authors noted that the activity of the bifunctional materials increased with increasing pK_a of the organic acid component, and the material containing weakly acidic carboxylic acid and amine groups exhibited the highest activity for aldol condensation. By contrast, Jones and coworkers have recently shown that an organosilane possessing carboxylic acid and amine groups are less active than surface silanols and amines [6,11].

The present study was focused on identifying the factors governing the catalytic activity of silica-supported primary, secondary and tertiary amine catalysts for the gas-phase self-condensation of *n*-butanal to 2-ethylhexenal. We report here experiments conducted with the aim of establishing the roles of amine groups and their surface density, the size of the pores in the mesoporous silica support, the surface density of silanol groups on the surface of the support, and the influence of the spatial separation between the acid and base groups to the catalytic activity of silica supported amine catalysts for aldol self condensation of *n*-butanal. The mechanism and kinetics of *n*-butanal condensation were also investigated in detail.

6.2 Methods

6.2.1 Catalyst Preparation

The preparation of silica-supported amine catalysts was carried out in the following manner. One gram of silica (Silicycle, surface area: 500 m^2 g^{-1}, average pore diameter 6 nm) was dried in vacuum at 423 K for 24 h, or pretreated at 823 K and 973 K for 5 h, and then stored in vacuum prior to use. The silylating agents used were 3-aminopropyl trimethoxysilane (APTS), 3-(N-methylaminopropyl) trimethoxysilane (MAPTS) and 3-(N,N-diethylaminopropyl) trimethoxysilane (DEAPTS) and methyl trimethoxysilane (MMTS) obtained from Gelest, Inc. Typically, grafting of organoamines onto silica was done by stirring 1 g of silica with the required amount of amino organosilanes in 100 ml of ethanol at 343 K for 15 h under inert atmosphere. The hot solution was then cooled to room temperature, filtered, washed with copious amounts of ethanol, and then dried in a vacuum oven at 373 K overnight. Silica-supported primary

(SiO_2-NH_2), secondary (SiO_2-NHR) and tertiary amines (SiO_2-NR_2) were prepared with nearly identical amine loadings (~0.4 amines nm^{-2}, according to elemental analysis). A similar synthesis procedure was used for grafting of a secondary amine onto mesoporous silicas (MCM-41, SBA-15, surface area: 800-1300 m^2 g^{-1}, pore diameter 2.5-12 nm) [12,13]. Silylation of amine supported silica catalysts was performed by dispersing 1 g of the catalyst in 25 mL of dry toluene followed by the addition of 3.75 mmol of methyl trimethoxysilane and stirring at 373 K for 15 h under an inert atmosphere. The final material is referred to as Sil-SiO_2-NHR.

6.2.2 Gas-phase Self-condensation of n-butanal

Gas-phase self-condensation of *n*-butanal was performed in a 6.35 mm OD (~ 4 mm ID) quartz tube containing an expanded section (~12.7 mm OD, ~20 mm length). The reactor was packed with quartz wool above and below the catalyst bed to hold the catalyst in place. The feed to the reactor consisted of *n*-butanal (0.02 cm^3 h^{-1}) and He. The catalysts were pretreated at 423 K before passing the feed. Experiments were carried out at 343 K, total gas pressures of 1 atm, total gas flow rate of 150 cm^3 min^{-1}. Under these conditions, the conversion of *n*-butanal was less than 10%. Reaction products were analyzed using an Agilent 6890N gas chromatograph containing a bonded and crosslinked (5%-phenyl)-methylpolysiloxane capillary column (Agilent, HP-1) connected to a flame ionization detector.

6.2.3 Catalyst Characterization

Infrared spectra were acquired using a Thermo Scientific Nicolet 6700 FT-IR spectrometer equipped with a liquid nitrogen cooled MCT detector. Each spectrum was obtained by averaging 32 scans taken with 1 cm^{-1} resolution. A 0.05 g portion of silica-supported amine was pressed into a 20 mm-diameter pellet (<1 mm thick) and placed into a custom-built transmission cell equipped with CaF_2 windows, a K-type thermocouple for temperature control, and resistive cartridge heaters. Unless otherwise mentioned, all scans were acquired at 343 K. The spectrum of the catalyst under He was subtracted from the results reported.

Solid-state ^{13}C CP MAS NMR and ^{29}Si MAS NMR experiments were performed on a Bruker Avance I 500 MHz spectrometer equipped with a H/X double resonance magic angle spinning probe which uses 4 mm O.D. rotors. ^{13}C cross-polarization, tuned to 125.79 MHz, MAS NMR experiments were obtained using a ^1H 90º pulse width of 4.2 μs, 2 ms contact time, 60 kHz decoupling field and 2-5 s recycle delay at a spinning rate of 7-13 kHz. All ^{13}C spectra were referenced against the chemical shifts of adamantane at 38.48 and 29.45 ppm. The ^{29}Si with ^1H decoupling MAS NMR spectra were acquired at 99.37 MHz, using a ^{29}Si 90º pulse width of 7.5 μs, recycle delay of 600 s, and spinning rate of 10-11 kHz. All ^{29}Si spectra were referenced against polydimethylsiloxane at -22 ppm (relative to TMS at 0 ppm). The resolution obtained in the ^{29}Si NMR spectra was sufficient for accurate peak assignments, and the relative peak area of each site was obtained by the curve-fitting, using a series of Gaussian peaks [14].

6.3 Results and Discussion

The successful grafting of the respective organosilanes onto the silica supports was confirmed by ^{13}C CP MAS NMR (refer to Figure S6.1 in the Supporting Information). The observed chemical shifts of the organic amine groups agree well with those of the corresponding organosilane precursors measured in solution [15]. Small peaks were also observed at δ = 62 and 20 ppm and attributed to ethoxy carbon atoms formed by partial esterification of surface silanol groups by ethanol [16]. ^{29}Si MAS NMR further confirmed the presence of organic functional groups grafted on the silica support. Peaks at δ = -110, -100, -90, -65, and -55 ppm were assigned to the $Q^4(Si(OSi)_4)$, $Q^3(Si(OH)(OSi)_3)$, $Q^2(Si(OH)_2(OSi)_2)$, $T^3(SiR(OSi)_3)$, and $T^2(Si(OH)\ R(OSi)_2)$ sites, respectively. The presence of a sharp peak for T^3 sites confirms the formation of a strong covalent linkage between the organic amine groups and the support surface [12].

The catalytic activity of silica-supported amines was evaluated for the self-condensation of *n*-butanal to 2-ethylhexenal. As shown in Figure 6.1, the catalyst prepared with secondary amine were approximately five times more active than that prepared with primary amine, whereas the catalyst prepared with tertiary amine showed negligible activity. Control experiments with silica displayed no catalytic activity, indicating that the surface-bound organic amine functional groups are responsible for the observed catalytic activity. The only products observed under the conditions investigated were the condensation product, 2-ethylhexenal. Despite the stronger basicity of alkyl-substituted tertiary amines, the poor catalytic activity observed with silica supported tertiary amine suggests that aldol condensation does not occur according to a general base-catalyzed mechanism (refer to Scheme S6.1 in the Supporting Information). Instead, the order of the activity (secondary >> primary > tertiary) suggests that the reaction proceeds via an enamine mechanism involving a carbinolamine intermediate [8, 17].

The apparent activation energies calculated from Arrhenius plots for primary, secondary and tertiary amines in the temperature interval 333-353 K are 97, 82, and 115 kJ mol^{-1}, respectively. The partial pressure dependence on the rate of formation of 2-ethyl hexenal was measured by varying the partial pressure of *n*-butanal while keeping the total gas flow rate and pressure constant at 150 $cm^3\ min^{-1}$ and 1 atm. The order of reaction rate with respect to the partial pressures of *n*-butanal for primary and secondary amine catalysts was 0.40 and 0.43, respectively. By contrast, a first order dependence in *n*-butanal was noted for the silica-supported tertiary amine catalysts (see Figure S6.3 in the Supporting Information).

In situ IR spectroscopy was used to obtain information about the mechanism of *n*-butanal self-condensation on silica-supported amine catalysts and to identify differences in the chemistry of primary, secondary and tertiary amine catalysts. Figure 6.2 show the spectrum of the catalyst exposed to *n*-butanal and recorded at 343 K. SiO_2-NHR (spectrum b), exhibits bands at 1705, 1650 and 1630 cm^{-1}. The first of these peaks is attributable to carbonyl vibrations of *n*-butanal adsorbed on the silanol groups, while the second two peaks are attributable to the C=O and C=C vibrations of the product, 2-ethyl hexenal [18]. The shoulder at 1680 cm^{-1} is tentatively assigned to iminium species, the formation of which is frequently reported for homogenous secondary amine catalysts [17]. By contrast, the spectrum of SiO_2-NH_2 (spectrum c) during contact with *n*-butanal exhibits sharp peaks at 1705 and 1670 cm^{-1}. The first of these peaks is assigned to

carbonyl vibrations of *n*-butanal adsorbed on the silanol groups, while the second peak is assigned to the formation of imine (-HC=N-) species [19]. This species was found to be stable up to 473 K. The formation of stable imines was further confirmed using UV-Vis spectroscopy and solid-state ^{13}C CP MAS NMR of the spent catalysts (refer to Figure S6.4 in the Supporting Information). The only feature observed in the spectrum of SiO_2-NR_2 (spectrum a) was a band at 1705 cm^{-1}, attributable to interactions of *n*-butanal with the silanol groups of the support.

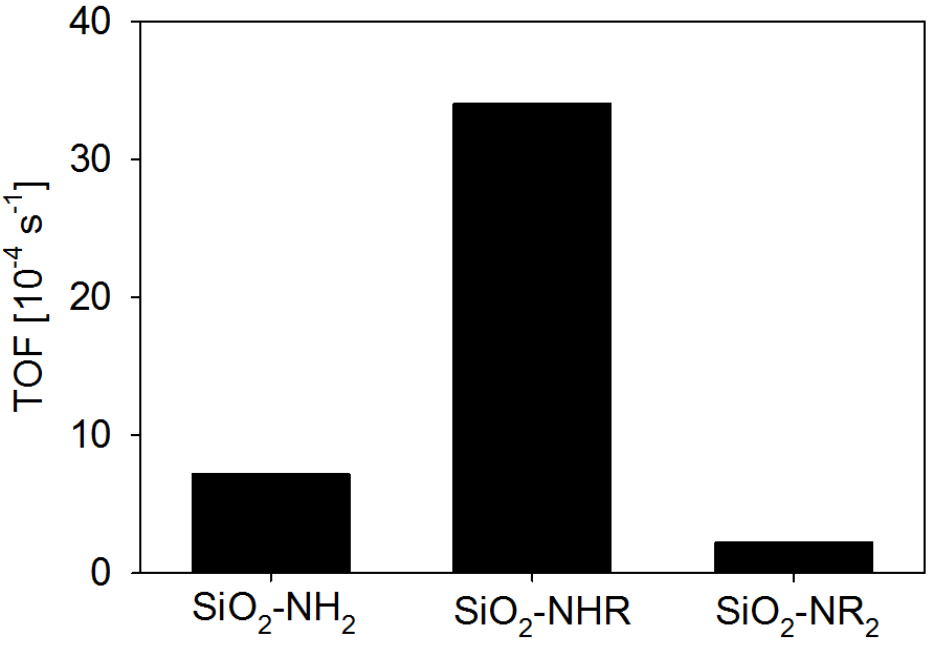

Figure 6.1 The effect of amine composition on the rate of 2-ethylhexenal synthesis over silica-supported amine catalysts. P_{Total} = 1 atm, $P_{n\text{-}butanal}$ = 0.2 kPa, balance He. total gas flow rate = 150 cm^3 min^{-1}, T = 343 K, amine loading = 0.4 -amine nm^{-2}.

The low catalytic activity observed for SiO_2-NH_2 is attributed to the formation of stable imines, which are known to be inhibitors for enamine catalysis [5,19]. The absence of imines or enamines in the spectrum of SiO_2-NR_2 suggests that the reaction proceeds through an ion-pair mechanism, with the formation of enolate species in the rate-determining step. The ion-pair mechanism involves the abstraction of a proton from the methylene carbon by a base, forming a carbanion, which then attacks the carbonyl carbon of another aldehyde to form the C-C bond-forming step with the release of a proton from the base to form the product. Corma and coworkers have shown that the ion-pair mechanism give rise to kinetics that are first order in aldehyde if proton abstraction is assumed to be the rate-limiting step [20]. This finding is consistent with the first order partial pressure dependency on *n*-butanal observed with the tertiary amine catalysts and suggests that aldol condensation on the tertiary amine catalysts proceeds through a general base-catalyzed mechanism.

Having established that silica-supported secondary amines exhibit the highest activity for self-condensation reaction of *n*-butanal, the density of secondary amine groups on the silica surfaces was varied in order to investigate the effect of amine loading

on the catalytic activity. As seen from Figure 6.3, increasing the amine surface density on the silica surface progressively decreased the catalytic activity. Even though an increase in the amine surface density leads to a decrease in the silanol surface density, the least active amine catalyst, which contains 0.6 -NHR nm^{-2} still possess a ten-fold excess of silanol relative to amine groups. This suggests that at low amine loadings, efficient amine-silanol catalytic co-operativity exists because the amine groups are isolated from one another and cannot interact through hydrogen bonding as a consequence of clustering of the amine groups near the pore mouth in the silica support [6].

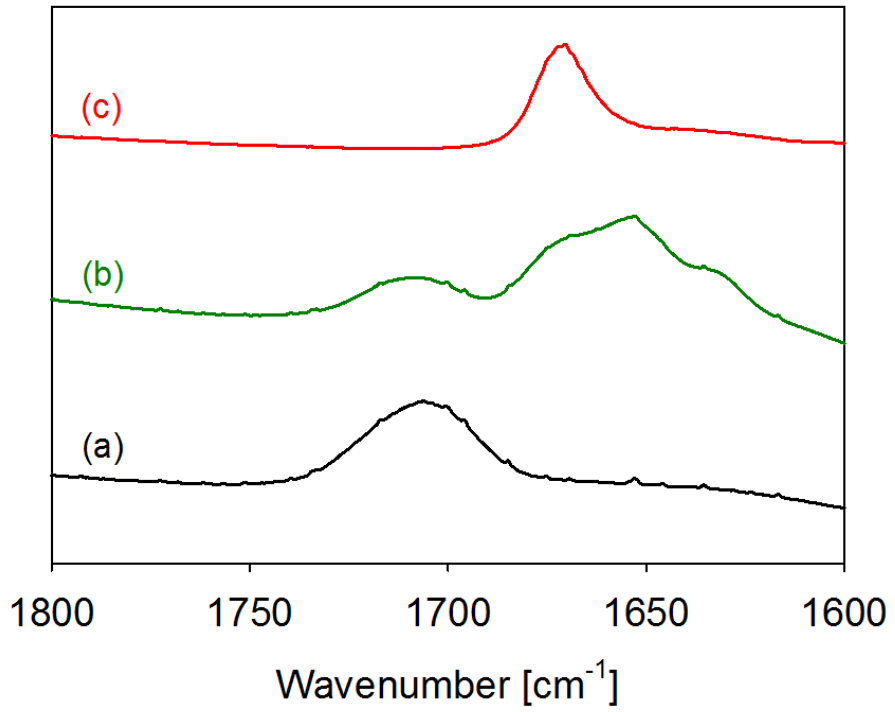

Figure 6.2 In situ FT-IR spectra of *n*-butanal adsorbed at 343 K on silica-supported amine catalysts: (a) SiO_2-NR_2, (b) SiO_2-NHR, and (c) SiO_2-NH_2.

To determine how the spatial confinement of amine groups enhances the catalytic activity, secondary amines were supported on high surface area mesoporous silicas having pore diameters of 2.5 nm to 12 nm. The catalytic activity increased for mesoporous silicas up to a pore diameter of ~6 nm, whereafter the activity remained nearly constant (Figure 6.4). Remarkably, a three fold increase in catalytic activity was noted when the pore size of the support was changed from 2.5 nm to 6 nm. These results suggest that the rate of reaction is limited by molecular diffusion of the products when the reaction is conducted with mesopores of less than 6 nm. Comparison of the activities of secondary amines (0.4 -NHR nm^{-2}) supported mesoporous SBA-15 and amorphous silica (average pore diameter = ~ 6 nm) revealed that the mesoporous SBA-15 has a two-fold higher catalytic activity than the amorphous silica. The higher activity obtained with SBA-15 may be attributed to the (a) higher silanol content of SBA-15 (5 -OH nm^{-2}) than of amorphous silica (3.8 -OH nm^{-2}) and/or (b) to the difference in acidity of silanols

between mesoporous and amorphous silicas [21]. To better understand whether the high density of the silanol groups or the acidity of these groups contributes to the high activity of the secondary amine supported SBA-15, each of these factors was evaluated separately.

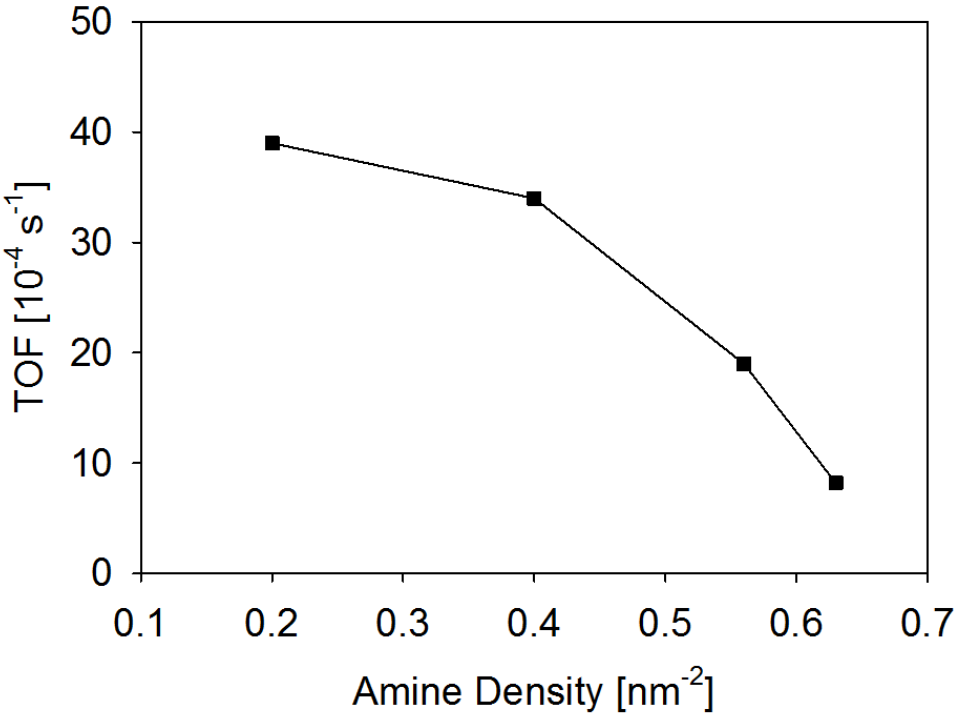

Figure 6.3 The effect of secondary amine loading on the rate of 2-ethylhexenal synthesis. P_{Total} = 1 atm, $P_{n\text{-}butanal}$ = 0.2 kPa, balance He. total gas flow rate = 150 cm^3 min^{-1}, T = 343 K, amine loading = 0.4 -amine nm^{-2}.

To assess the influence of silanol group concentration, the surface concentration of silanol groups was reduced by grafting methyl trimethoxysilane onto the amine supported silica. Irrespective of the support material (SBA-15 or amorphous silica), blocking the silanol groups by silylation decreased the rate seven-fold, confirming that silanols act co-operatively with amines in the aldol condensation of *n*-butanal. ^{29}Si MAS NMR corroborated that silylation decreased the total concentration of silanol groups by ~35%. To further ascertain the role of silanol groups, an experiment was performed by co-feeding water with *n*-butanal into the reaction stream. A 20-fold decrease in the rate of aldol condensation was noted after 6 h time on stream relative to that observed without the addition of water (refer to Figure S6.5 and S6.6 in the Supporting Information). IR spectra of SiO_2-NHR catalysts in presence of co-fed water with *n*-butanal confirms that water interferes with the adsorption of *n*-butanal on the silanol groups.

The role of silanol groups on the amorphous silica support surface was further probed by changing the surface density of silanol groups by varying the temperature at which dehydration of the silica support was carried out, prior to grafting the secondary amines. Dehydration temperatures of 423 K, 823 K and 973 K were used. The apparent surface concentration of the silanols determined from ^{29}Si MAS NMR spectroscopy and

the BET surface areas show that the concentration of silanol groups decreases from 4 OH nm^{-2} for SiO_2-423 K to 2.8 OH nm^{-2} for SiO_2-823 K and to 1.6 OH nm^{-2} for SiO_2-973 K [14]. As shown in Figure 6.5, the catalytic activity passed through a maximum as the concentration of silanol groups decreased. Secondary amine supported on silica pre-treated at 823 K was nearly two times more active than that supported on silica pretreated at 423 K, and four times more active than that supported on silica pretreated at 973 K.

It is known that an increase in the calcination temperature of silica not only reduce the concentration of silanol groups on the silica surface but also increase the acidity of the remaining silanol groups. For instance, the pK_a of isolated silanols is reported to be ~2-4 (Q^3 sites) whereas the pK_a of geminal silanols (Q^2 sites) is ~6-8 [22]. To ascertain whether the acidity of the silanol groups enhances the rate, ^{13}C CP MAS NMR spectra were taken of secondary amine groups supported on silica pretreated at different temperatures. As shown in Figure 6.6, ^{13}C CP MAS NMR spectra did not show an up-field shift in the terminal carbon peak position indicating that amines do not interact with the acidic silanol groups. This result is corroborated by the adsorption of homogenous triethyl amine (NEt_3) on silica. Irrespective of the pre-treatment procedures, an up-field shift of the terminal carbon atoms of organic amine catalysts did not occur confirming that acidity of the silanol groups does not contribute to the enhanced catalytic activity of the catalyst prepared on silica dehydrated at 823 K [23]. Further indication that the dehydration temperature has no effect on the acidity of the silanols was obtained from the absence of a shift in the position of the 1705 cm^{-1} peak for *n*-butanal adsorbed on silanol groups. All these results taken together indicate that the temperature of silica dehydration does not alter the acidity of the silanol groups for the conditions used in this study.

The influence of the spatial separation between the amine and silanol groups was examined in order to determine its effect on the activity of acid-base pairs. The average distance between silanols in a silica pretreated at 423 K is ~0.3-0.4 nm while the propyl amine linker has a chain length of ~0.5 nm [24]. This means that amines can reach over the silanols in SiO_2-423 K, making all the amine groups unavailable for the catalysis. By contrast, for the SiO_2-823 K support, the silanols are separated by an average distance of ~0.6-0.7 nm, which means that the amine groups cannot interact strongly with silanol groups, leading to an enhanced catalytic activity. Consequently, for secondary amine supported SiO_2-973 K catalysts, moving the silanols farther apart lead to an inactive catalyst, since the high catalytic efficiency depends on the co-operative activation of reactants by the amines and the silanols. These studies clearly demonstrate how the spatial separation between acid and base groups influences their catalytic activity. In an alternate way to confirm that an accurate spatial separation between the amines and the silanols leads to an enhanced catalytic activity, secondary amine catalyst having a methyl linker (SiO_2-C_1-NHR) were grafted onto SiO_2-823 K support, instead of the propyl linker (SiO_2-C_3-NHR) [25]. Remarkably, constrained methyl linker showed a ten-fold decrease in activity relative to that for the propyl linker showing that an accurate distance between the silanols and propyl amine groups, on SiO_2-823 K support, leads to an active and stable catalyst for the self-condensation of *n*-butanal (Figure 6.7). These results are consistent with those reported recently by Jones and coworkers in which it was shown that the activity of acid-base pairs catalysts can be tuned by altering the linker length of the amine.

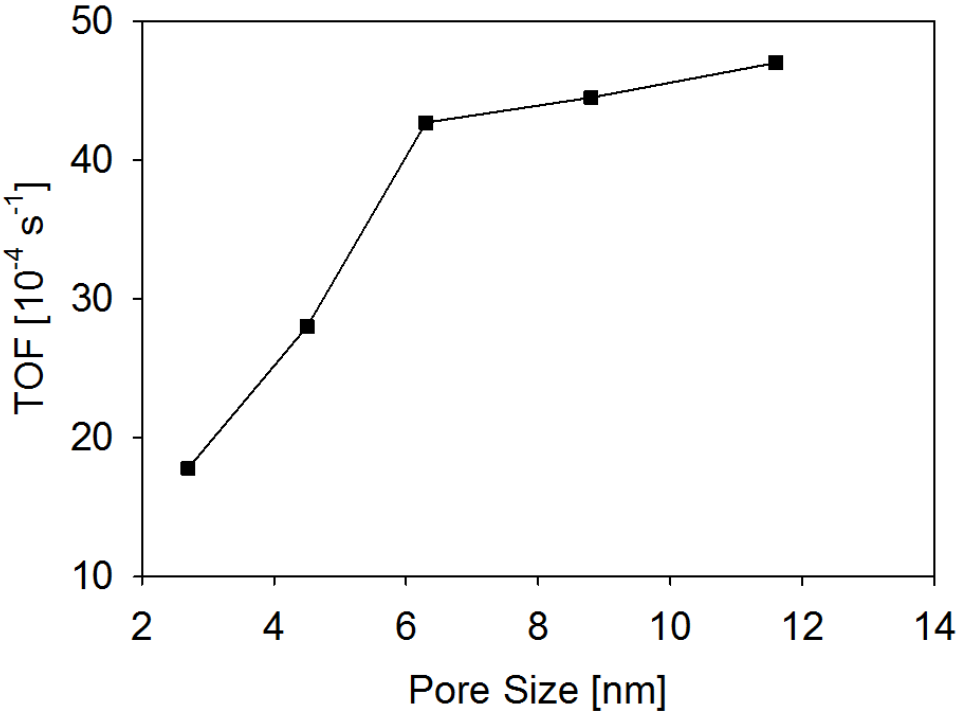

Figure 6.4 The effect of the pore size of mesoporous silica-supported secondary amine catalysts on the rate of 2-ethylhexenal synthesis.*

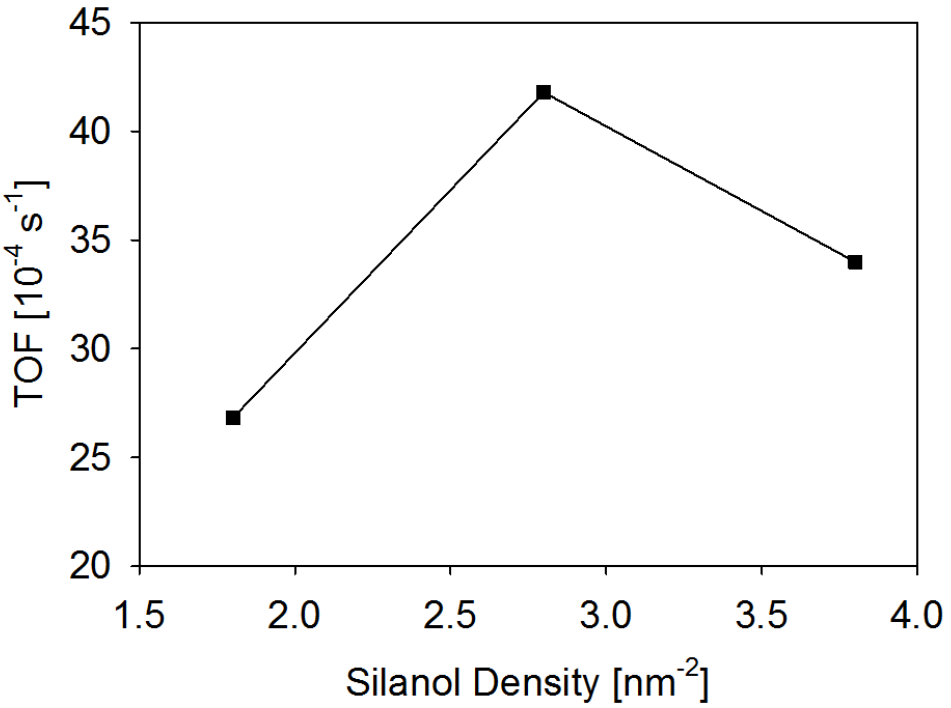

Figure 6.5 The effect of silanol density on the rate of 2-ethylhexenal synthesis over silica-supported silica secondary amine catalysts.*

*P_{Total} = 1 atm, $P_{n\text{-}butanal}$ = 0.2 kPa, balance He. total gas flow rate = 150 cm^3 min^{-1}, T = 343 K, amine loading = 0.4 -amine nm^{-2}.

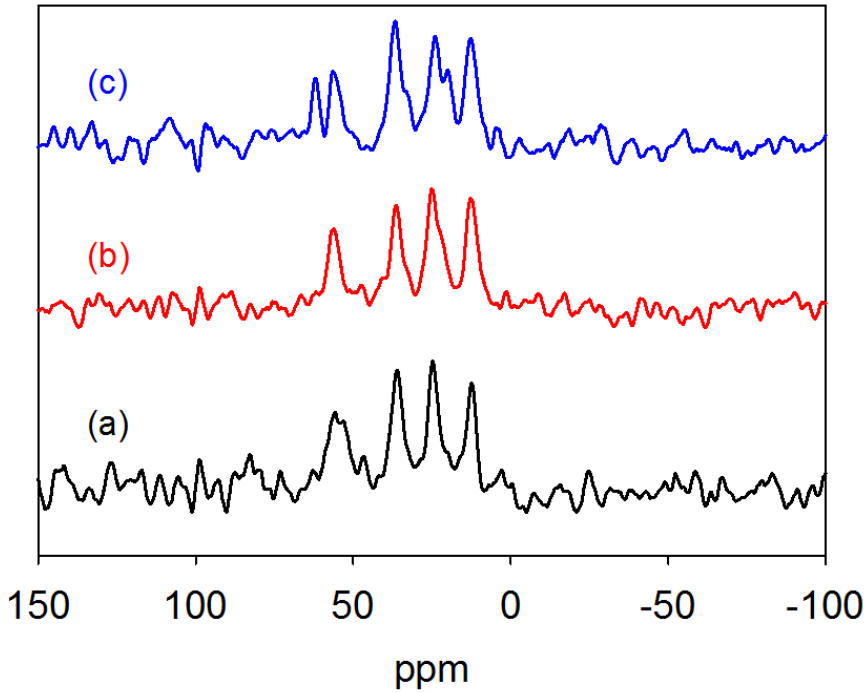

Figure 6.6 Effect of pretreatment temperature on the solid-state ^{13}C CP MAS NMR spectrum of silica-supported secondary amine catalysts: (a) SiO_2-423 K; (b) SiO_2-823 K; and (c) SiO_2-973 K.

The acid-base co-operativity was further demonstrated by silylating the silanol groups on the SiO_2-C_3-NHR and SiO_2-C_1-NHR. Interestingly, silylation decreased the catalytic activity of the SiO_2-C_3-NHR by ten times, whereas the activity of silylated SiO_2-C_1-NHR remained similar to that of non-silylated SiO_2-C_1-NHR (Figure 6.7). These results suggest that silica-supported propyl amines exhibit co-operative interactions with the silanol groups for rate enhancements whereas the constrained methyl amine lacks the acid-base cooperativity. Alternatively, the low activity observed with SiO_2-C_1-NHR suggests that the reaction does not proceed through a silanol assisted acid-base bifunctional mechanism rather this may proceed through the general base catalyzed mechanism. A first order dependence on *n*-butanal partial pressure and a higher activation barrier (122 kJ mol^{-1}) support the proposal that aldol condensation on SiO_2-C_1-NHR proceeds via a general base-catalyzed mechanism. Thus short alkyl linkers like methyl inhibits the beneficial amine-silanol co-operativity on silica surfaces resulting in lower catalytic activity.

The accumulated data suggest that the self-condensation of *n*-butanal over SiO_2-C_3-NHR proceeds via a concerted mechanism involving the basic amine groups and the weakly acidic silanol groups, as shown in Scheme 6.1. A theoretical analysis of the aldol condensation reaction pathway was carried out to test the plausibility of this mechanism and to determine the rate-limiting step. The active site model for these steps contains both a grafted amine group ($C_3H_6NHCH_3$) and a silanol group (Si-OH), as represented by the cluster shown in Figure 6.8. A model of amorphous silica containing 4 tetrahedral silicon atoms (T4) was obtained from the crystal structure of the zeolite H-MOR [29], with all

silicon atoms terminated in oxygen. The cleaved structure gives an O-O silanol separation of 0.5 nm, consistent with experimental measurement from the most active SiO_2-C_3-NHR catalyst. To create the dual-site model containing the grafted amine adjacent to a silanol group, two terminal Si-O fragments are substituted for Si-OH and Si-$C_3H_6NHCH_3$, respectively. The remaining terminal O atoms are replaced by H and fixed in their crystallographic positions during subsequent optimization. The resulting cluster model has stoichiometry of $C_4H_{19}NO_4Si_4$. (Further details concerning the computational method are provided in the Supporting Information).

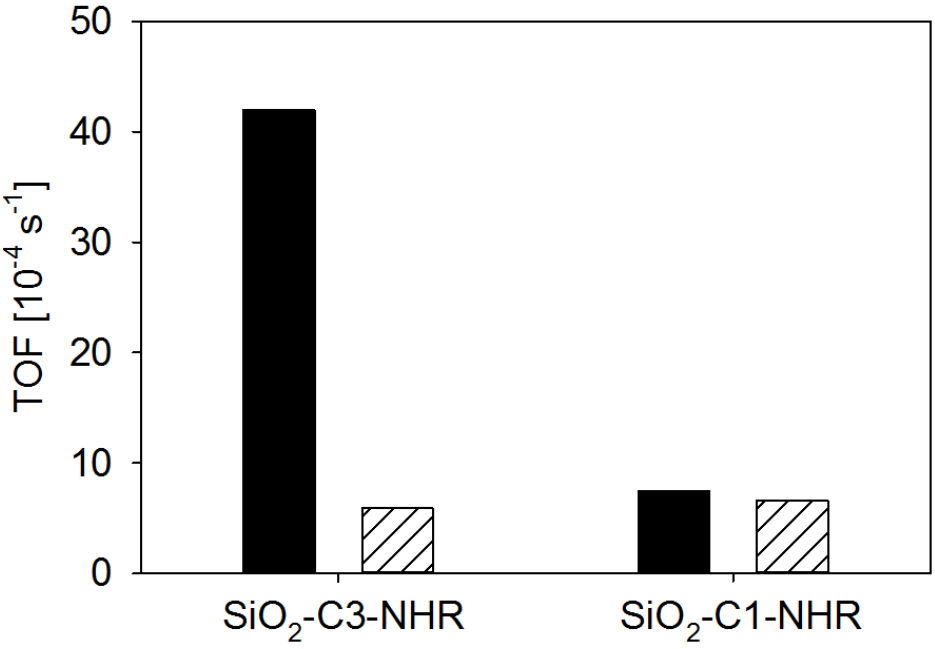

Figure 6.7 Effect of linker length on the catalytic activity of silica-supported secondary amine catalysts (solid bars) and comparison with their silylated analogs (stripped bars). P_{Total} = 1 atm, $P_{n\text{-}butanal}$ = 0.2 kPa, balance He. total gas flow rate = 150 cm^3 min^{-1}, T = 343 K, amine loading = 0.4 -amine nm^{-2}.

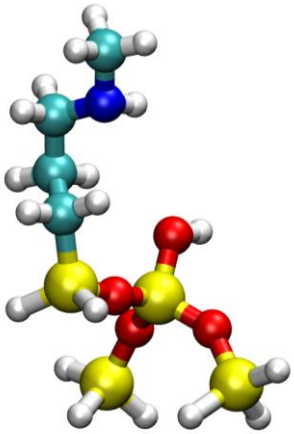

Figure 6.8 Model active site for the SiO_2-C_3-NHR catalyst.

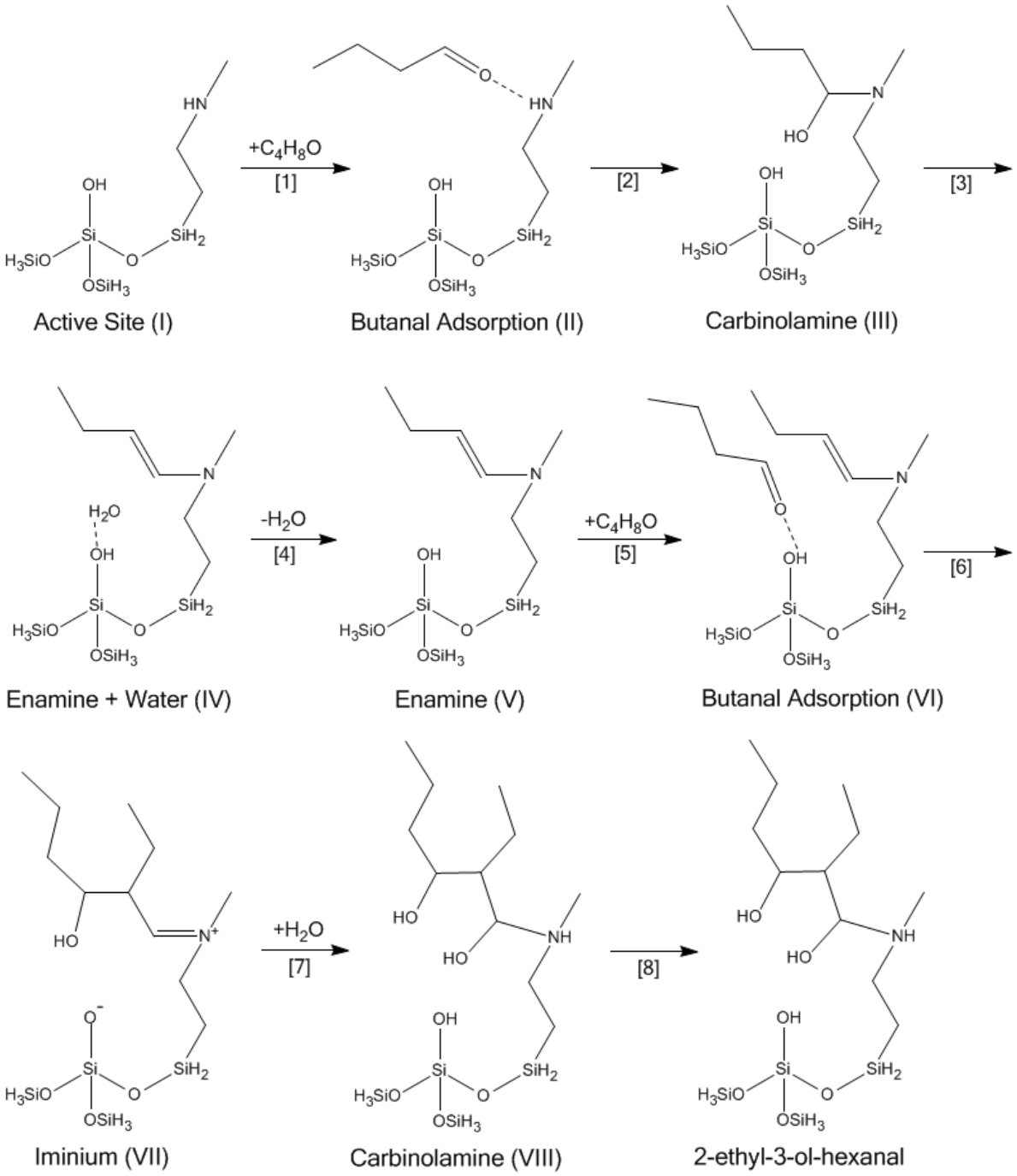

Scheme 6.1 Proposed mechanism for aldol self-condensation of *n*-butanal over silica supported secondary amine catalysts.

The changes in enthalpy (343 K) along the reaction pathway calculated at the ωB97X-D/6-311++G(3df,3pd) level of theory are shown in Figure 6.9 and the corresponding free energy (343 K) changes are shown in Figure 6.10. The adsorption of *n*-butanal to the bare catalyst surface is exothermic (ΔH = -25 kJ mol^{-1}) and is characterized by a weak hydrogen bonding interaction between *n*-butanal and the grafted amine. The formation of a carbinolamine species proceeds through a concerted C-N bond formation and proton transfer reaction. The transition-state structure for carbinolamine formation is similar to one found for proline-catalyzed aldol condensation [26]. The enamine state is produced by intramolecular water elimination. The iminium state can be formed by the protonation of the enamine by the silanol group, but is omitted from this diagram due to its instability relative to the enamine state (ΔH = +35 kJ mol^{-1}). The desorption of water exhibits a favorable free energy change due to the additional gain in entropy. The adsorption of *n*-butanal in the presence of the enamine resting state is exothermic (ΔH = -32 kJ mol^{-1}) and is promoted by hydrogen bonding between the silanol group and the carbonyl group of *n*-butanal. The formation of the C-C bond ($\Delta H^{\ddagger}$ = +116 kJ mol^{-1}) proceeds by the protonation of the *n*-butanal carbonyl group by the silanol group and C-C bond formation between the enamine and the alpha-carbon of *n*-butanal in a concerted fashion, and produces a second iminium species. The hydrolysis proceeds from the second iminium by the attack of water on the complex. This process leads to a concerted proton transfer from the water molecule to the deprotonated silanol group, leaving the final product, 2-ethyl-3-ol-hexenal, in the chemisorbed state. The product then desorbs to reform the catalyst (SiO_2-C_3-NHR) and leave 2-ethyl-3-ol-hexenal in the physisorbed state. The final step of the reaction pathway is desorption of 2-ethyl-3-ol-hexenal into the gas phase. The theoretical analysis of the *n*-butanal self-condensation pathway leads to the conclusion that the transition state for C-C bond formation is the rate-limiting step along the free energy pathway [26-28]. The resting state of the catalyst during reaction is the enamine state, since it is the lowest-lying intermediate on the free energy surface, consistent with the characterization of the spent SiO_2-NHR catalysts. The apparent activation barrier is calculated as the difference in enthalpy between the rate-limiting step and the resting state of the catalyst. The calculated apparent activation energy for this process is 85 kJ mol^{-1}, in good agreement with the value of 82 kJ mol^{-1} determined experimentally.

Based upon the proposed reaction mechanism and considering that reactions prior to the rate-limiting C-C bond-forming step are quasi-equilibrated, the rate of 2-ethylhexenal formation can be expressed as follows:

$$r_P = \frac{\alpha P_{butanal}^2 L L_1/(L_1 + L)}{P_{H_2O} + \beta P_{butanal} + \gamma P_{H_2O} P_{butanal} + K_4 P_{H_2O}^2 + \delta P_{butanal}^2 + \varepsilon P_{H_2O}^2 P_{butanal} + \lambda P_{H_2O} P_{butanal}^2} \quad (1)$$

where α, β, γ, δ, ε, and λ represent lumped equilibrium and rate parameters, K_4 is the equilibrium constant for reaction 4, P_j is the partial pressure of species *j*, and L and L_1 represents the total number of surface silanol and amine groups, respectively. A detailed derivation of Eq. 1 is provided in the Supporting Information.

Eq. 1 can be used to rationalize the experimental results. Under the exper-imental conditions used in this study, the partial pressure of H_2O was negligible because the conversion was less than 10%. Therefore, Eq. 1 simplifies to Eq. 2.

$$r_P = \frac{K_5 k_6 P_{butanal} L L_1/(L_1 + L)}{1 + K_5 P_{butanal}} \quad (2)$$

The form of Eq. 2 is consistent with the observation that the rate of 2-ethylhexenal formation is 0.4 order in *n*-butanal, suggesting that both terms in the denominator contribute to the overall rate.

The P_{H_2O} terms of Eq. 1 in the denominator describe the inhibitory effect of water observed experimentally. Water vapor inhibits the catalytic reaction by hydrolyzing the carbon-carbon double bond of the enamine, thereby decreasing concentration of the enamine intermediate by shifting equilibrium of reaction 3 to the left. Additionally, water vapor competes with aldehyde for vacant silanol groups.

The proposed mechanism for *n*-butanal condensation demonstrates that for efficient catalysis, the basic amine groups must work in concert with the acidic silanol groups. Strong acids are undesirable since they can protonate the amine group, thereby lowering their nucleophilicity, which is essential for formation of enamine species. It is thus essential that the distance between the acid and base sites should be large enough to avoid mutual neutralization but close enough so that the acid and base groups can interact with the reactant molecule for co-operative catalysis to occur. This effect is accurately modeled by the two-site rate equation indicating that a lone silanol or amine site cannot exclusively catalyze the reaction. By increasing the density of amine, the value of the $L' = LL_1/(L + L_1)$ term rises to a maximum and then decreases. This trend qualitatively explains the effect of amine site density on the rate of aldol condensation reaction (see Supporting Information).

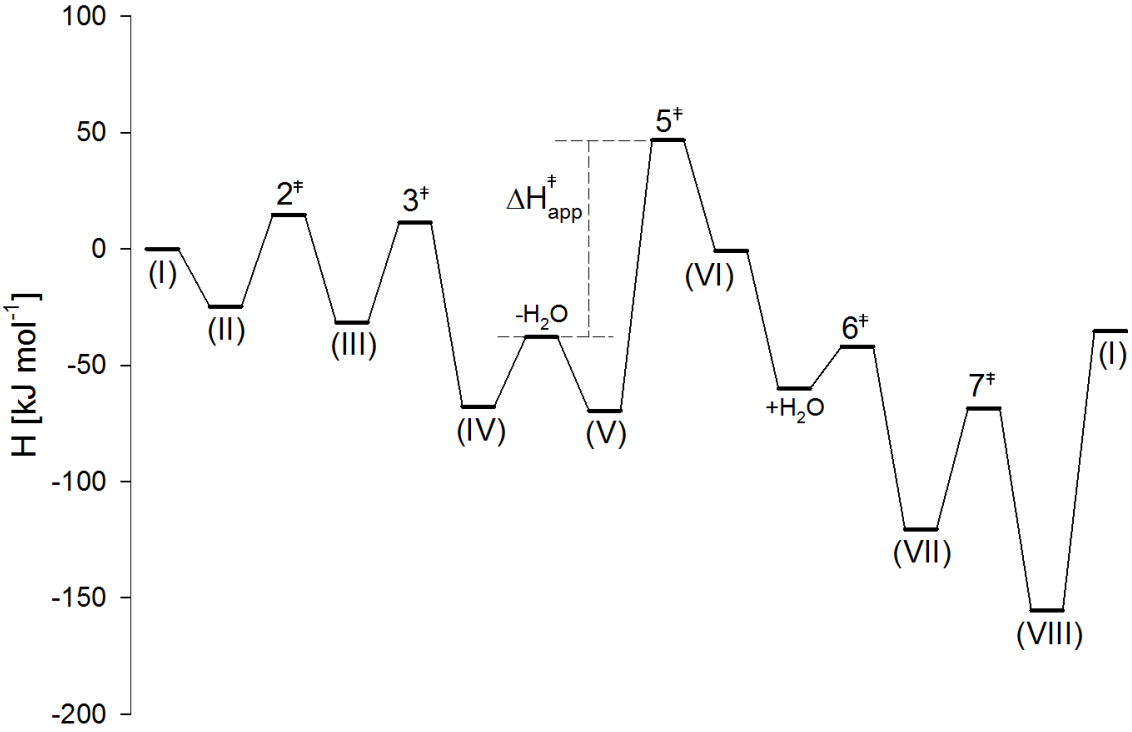

Figure 6.9 Enthalpy (343 K) diagram for aldol condensation of *n*-butanal over a SiO_2-C_3-NHR catalyst calculated at the ωB97X-D/6-311++G(3df,3pd) level of theory [kJ mol^{-1}]. The elementary steps are labeled according to the reaction mechanism in Scheme 6.1. The calculated apparent activation energy ($\Delta H_{app}^{\ddagger}$) is 85 kJ mol^{-1}.

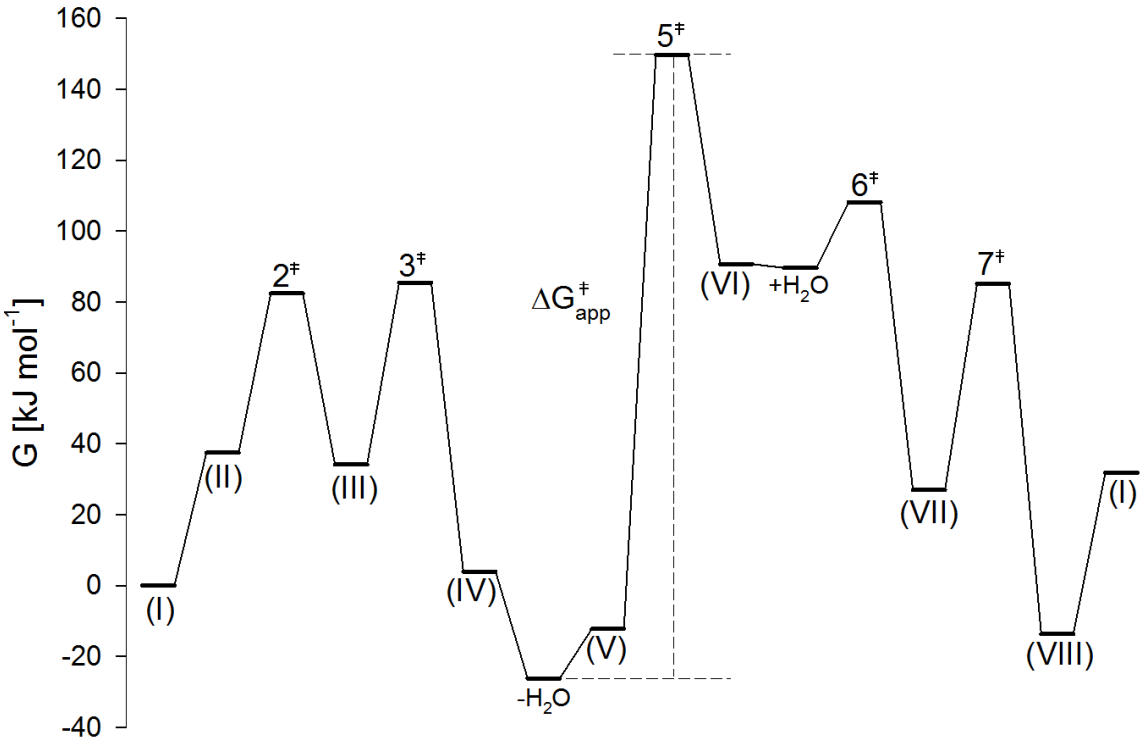

Figure 6.10 Free energy (343 K) diagram for aldol condensation of *n*-butanal over a SiO_2-C_3-NHR catalyst calculated at the ωB97X-D/6-311++G(3df,3pd) level of theory [kJ mol^{-1}]. The elementary steps are labeled according to the reaction mechanism in Scheme 6.1. The difference in free energy between the resting state (IV, -H_2O) and the rate limiting transition state ($5^{\ddagger}$) is denoted as $\Delta G_{app}{}^{\ddagger}$.

6.4 Conclusions

The results presented in this study provide a comprehensive understanding of the factors influencing the acid-base co-operativity of amine supported silica catalysts for carbon-carbon bond formation during the self-condensation of *n*-butanal. Secondary amine functionalized silica is nearly five times more active than the primary amines and tertiary amines exhibit negligible catalytic activity. Formation of nucleophilic enamines leads to enhanced catalytic activity of secondary amine catalysts whereas the formation of stable imines (up to 473 K) leads to the low activity of primary amine supported silica catalysts. Secondary amines in combination with the isolated silanol groups provide the best acid-base pair and the spatial separation between acid-base groups can be tailored by simple calcination treatment of the silica support or by varying the linker length of organosilane for catalytic enhancements. Detailed experimental as well as theoretical analysis of the *n*-butanal self-condensation pathway leads to the conclusion that carbon-carbon bond formation is the rate-limiting step in the aldol condensation of *n*-butanal over silica-supported secondary amines.

6.5 Acknowledgements

This work was supported by the XC^2 program funded by BP.

6.6 Supporting Information

6.6.1 Catalyst Preparation

Cetyltrimethyl ammonium bromide (CTAB), Pluronic P123 triblock copolymer (poly(ethylene glycol)-poly(propylene glycol)-poly (ethylene glycol), tetraethyl orthosilicate (TEOS, 98%), 3-aminopropyl trimethoxysilane (APTS, 97%,), methyl trimethoxysilane, ethanol and hexanes (reagent grade) were obtained from Sigma-Aldrich. 3-(N-methylaminopropyl) trimethoxysilane (MAPTS) and 3-(N,N-diethylaminopropyl) trimethoxysilane (DEAPTS) were obtained from Gelest, Inc. All reagents were used as received without any further purification.

The preparation of silica supported amine catalyst was as follows. Silica (Silicycle, surface area: 300 m^2 g^{-1}, average pore diameter 6 nm) was used as the support. One gram of this support material was dried in vacuum at 423 K for 24 h, or pretreated at 823 and 973 K for 5 h, and then stored in vacuum prior to use. Typically, the postgrafting of organoamines onto silica was done by stirring 1 g of silica using the required amount of aminoorganosilanes (APTS, MAPTS, or DEAPTS) in 100 ml of ethanol at 343 K for 16 h. The hot solution was then cooled down to room temperature, filtered, washed with copious amounts of ethanol, and then dried in vaccum oven at 373 K for overnight. A similar synthesis procedure was used for the synthesis of secondary amine heterogenized mesoporous silicas and silica-alumina supports. Silylation of amine supported silica catalysts was performed by dispersing 1 g of the catalyst in 25 mL of dry toluene followed by the addition of 3.75 mmol of methyl trimethoxysilane and stirring at 373 K for 12 h under an inert atmosphere. The final material is referred to as Sil-SiO_2-NHR.

6.6.2 Theoretical Methods Section

A model of amorphous silica containing 4 tetrahedral silicon atoms (T4) was obtained from the crystal structure of the zeolite H-MOR [29], with all silicon atoms terminated in oxygen. The cleaved structure gives an O-O silanol separation of 0.5 nm, consistent with experimental measurement from the most active SiO_2-C_3-NHR catalyst. To create the dual-site model containing the grafted amine adjacent to a silanol group, two terminal Si-O fragments are substituted for Si-OH and Si-$C_3H_6NHCH_3$, respectively. The remaining terminal O atoms are replaced by H and fixed in their crystallographic positions during subsequent optimization. The resulting cluster model has stoichiometry of $C_4H_{19}NO_4Si_4$.

Geometry optimizations were performed with the exchange-correlation functional ωB97X-D using the double-zeta, polarized valence 6-31G(d,p) basis set. During geometry optimization, energies were converged to 10^{-6} Ha (hartree) and the maximum norm of the Cartesian gradient was converged to 10^{-3} Ha $bohr^{-1}$. The final potential energy surface was obtained by single point energy calculations performed at the ωB97X-D/6-311++G(3df,3pd) level theory. Transition states for each elementary reaction step were first located approximately using the Freezing String Method [30], then subsequently optimized to the true saddle point. Frequency analysis was performed

to confirm the nature of each stationary point: there must be zero imaginary frequencies for potential energy minima and one for potential energy saddle point. Terminal hydrogen atoms frozen during optimization were given a fictitiously high mass in order to remove their contribution to vibrational modes. Vibrational frequencies calculated at each optimized geometry are used to obtain enthalpy and free energy corrections. All calculations were done using a standard version of the Q-Chem 4.0 [31] software package.

The calculated enthalpy and free energy (343 K) surfaces of aldol condensation catalyzed by SiO_2-C_3-NHR are shown in Figures 9 and 10 of the main article. The resting state of the catalyst is the enamine state, it is shown to be the lowest-lying intermediate on the free energy surface. The rate-limiting step of the reaction is C-C bond formation, shown to be the highest lying transition state on the free energy surface. The apparent activation barrier is calculated as the difference in enthalpy between the rate-limiting step and the resting state of the catalyst. The calculated apparent activation energy for this mechanism is 85 kJ mol^{-1}, in good agreement with the experimentally determined value of 82 kJ mol^{-1}. In this study, we considered a second reaction mechanism where water produced during enamine formation (Step 3, Scheme 6.1) is present during C-C bond formation steps. The enthalpy and free energy surfaces of this reaction mechanism are given in Figures S6.7 and S6.8. The adsorption of water to a silanol group occurs after water elimination, and is energetically preferable to n-butanal adsorption. The adsorption of n-butanal to the catalyst occurs through a hydrogen bonded network between silanol, water, and n-butanal. The protonation of the n-butanal carbonyl group that precedes C-C bond formation occurs through a proton-shuttling mechanism mediated by water. In the water-mediated mechanism, C-C bond formation is also the rate-limiting step. An apparent activation barrier of 90 kJ mol^{-1} is calculated, similar to the barrier found without water. The adsorption of water to the surface of the catalyst results in the loss of translational and rotational degrees of freedom, resulting in a higher free energy barrier relative to when water is removed to the gas phase ($\Delta\Delta G$ = +12 kJ mol^{-1}). For this reason, we assume that water desorbs from the catalyst before the rate-limiting step when deriving the rate equation for this process.

6.6.3 Derivation of Rate Expressions

Based on Scheme 6.1, the elementary steps up to the kinetically-relevant step are written below. Where:

1. $A + S \leftrightarrow A - S$
2. $A - S \leftrightarrow B - S$
3. $B - S \leftrightarrow C - S + H$
4. $H + S_1 \leftrightarrow H - S_1$
5. $A + S_1 \leftrightarrow A - S_1$
6. $A - S_1 + C - S \leftrightarrow F - S_1 + E - S$

$A \equiv$ Butanal, $H \equiv$ Water, $S \equiv$ Amine, $S_1 \equiv$ Silanol, $L \equiv$ total # of amines,
$L_1 \equiv$ total # of silanols

Assuming reaction 6 is kinetically-relevant, the rate of 2-ethylhexenal formation is:

(1) $r_P = k_6\theta_{A1}\theta_C LL_1/(L_1 + L)$

Assuming reactions 1-5 are quasi-equilibrated, the coverage of the various surface species may be determined.

(2)
$\theta_{A_1} = K_5\theta_{S_1}P_A$
$\theta_H = K_4\theta_{S_1}P_H$
$\theta_C = K_3\theta_B P_H^{-1}$
$\theta_B = K_2\theta_A$
$\theta_A = K_1 P_A\theta_S$

Substituting Eq. 2 into Eq. 1 yields:

(3) $r_P = K_1K_2K_3K_4K_5k_6P_A^2P_H^{-1}\theta_S\theta_{S_1}LL_1/(L_1 + L)$

Performing a site-balance on the amine and silanol groups yields:

(4)
Site balance for *S*:

$\theta_S = (1 + K_1P_A + K_1K_2P_A + K_1K_2K_3P_AP_H^{-1})^{-1}$

Site balance for S_1:

$\theta_{S_1} = (1 + K_4P_H + K_5P_A)^{-1}$

Substituting (4) into (3) yields the final rate expression (5):

(5) $r_P = \frac{\alpha P_A^2 LL_1/(L_1+L)}{P_H+\beta P_A+\gamma P_AP_H+K_4P_H^2+\delta P_A^2+\varepsilon P_AP_H^2+\lambda P_A^2P_H}$

where:

$\alpha = K_1K_2K_3K_5k_6$
$\beta = K_1K_2K_3$
$\gamma = K_1+K_5 + K_1K_2 + K_1K_2K_3K_4$
$\delta = K_1K_2K_3K_5$
$\varepsilon = K_1K_4 + K_1K_2K_4$
$\lambda = K_1K_5 + K_1K_2K_5$

The rate expression derived previously is based upon a 2-site model. The $L' = LL_1/(L_1 + L)$ term is a consequence of the fact that neither a silanol or amine can

exclusively catalyze the reaction. As mentioned previously, $L \equiv$ total # of amines and $L_1 \equiv$ total # of silanols.

Assuming that the initial concentration of silanol groups, $L_{1,0}$ = 3 OH/nm2 and that each amine grafts to ~3 silanol groups, the L' term can be rewritten:

$$L' = \frac{L(L_{1,0} - 3L)}{L_{1,0} - 2L}$$

A plot of L' vs. L is shown below and qualitatively matches the experimental data.

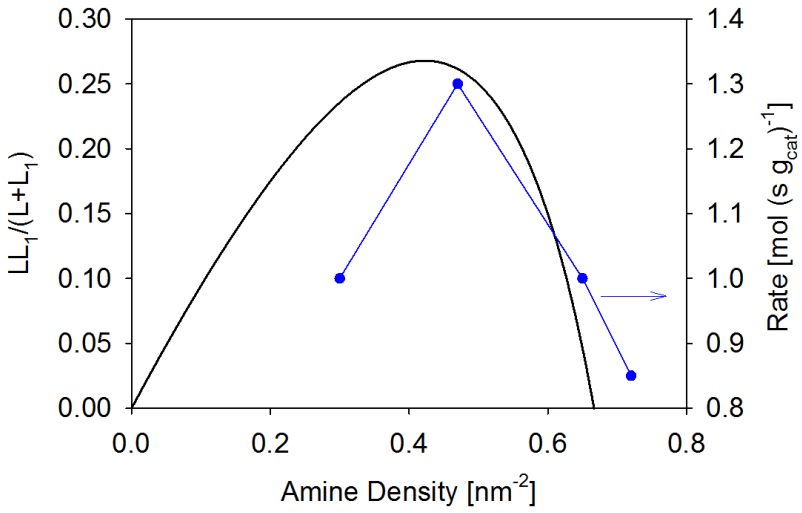

Figure S6.1 A plot of L' vs. L is shown below and qualitatively matches the experimental data.

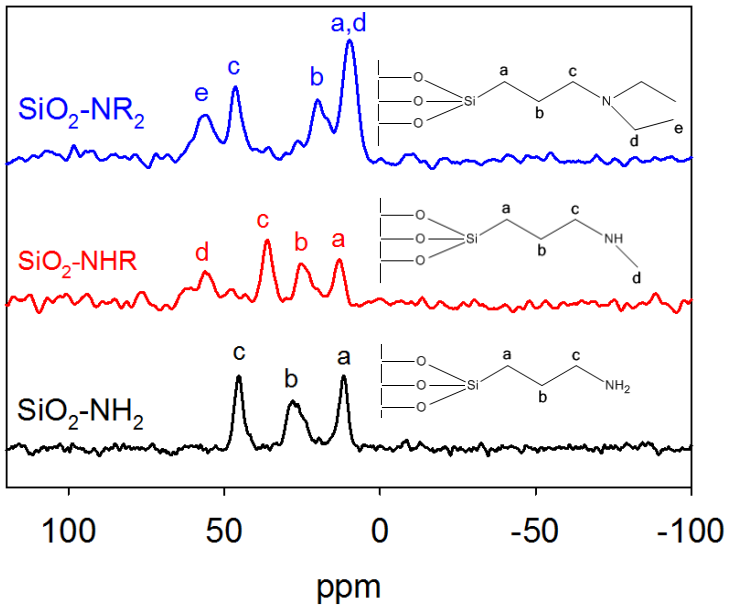

Figure S6.2 Solid-state ^{13}C CP MAS NMR spectra of silica supported amine catalysts.

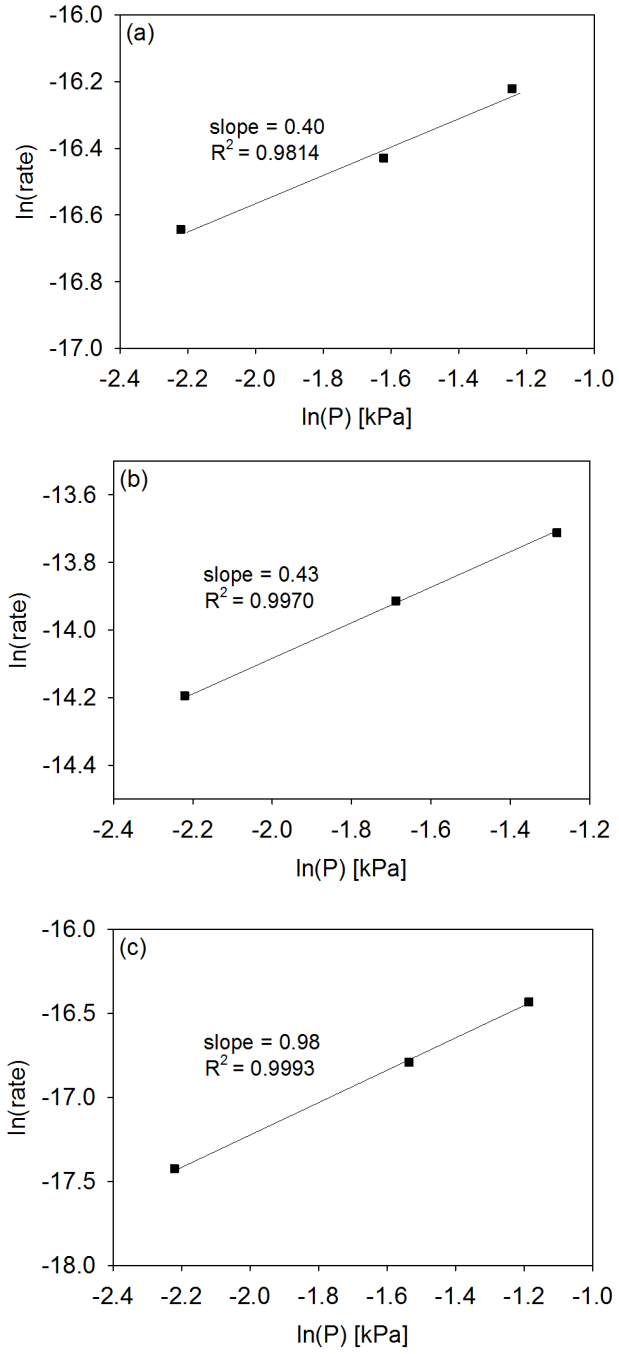

Figure S6.3 Partial pressure dependency of *n*-butanal using (a) SiO_2-NH_2, (b) SiO_2-NHR and (c) SiO_2-NR_2 on the rate of 2-ethylhexenal synthesis. P_{Total} = 1 atm, total gas flow rate = 150 cm^3 min^{-1}, T = 343 K, amine loading = 0.4 -amine nm^{-2}.

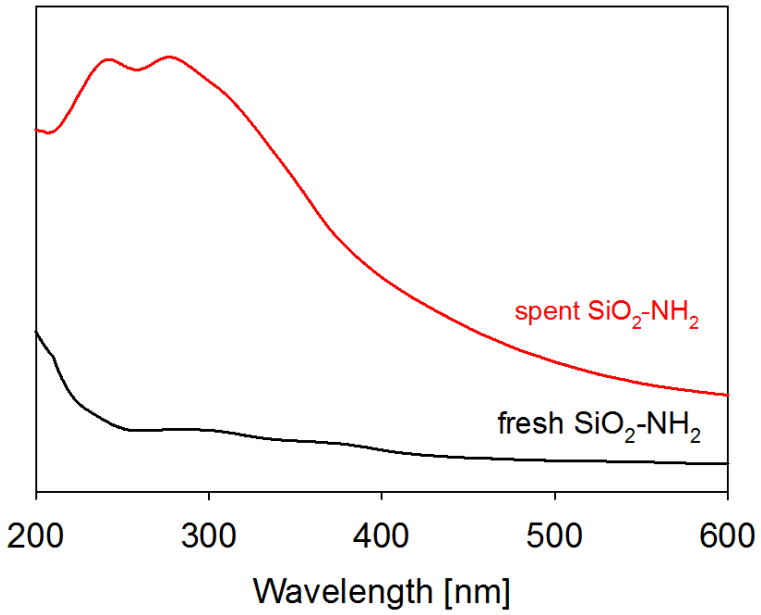

Figure S6.4 Solid-state UV-Vis spectra of spent SiO_2-NH_2 catalyst showing the formation of stable imines.

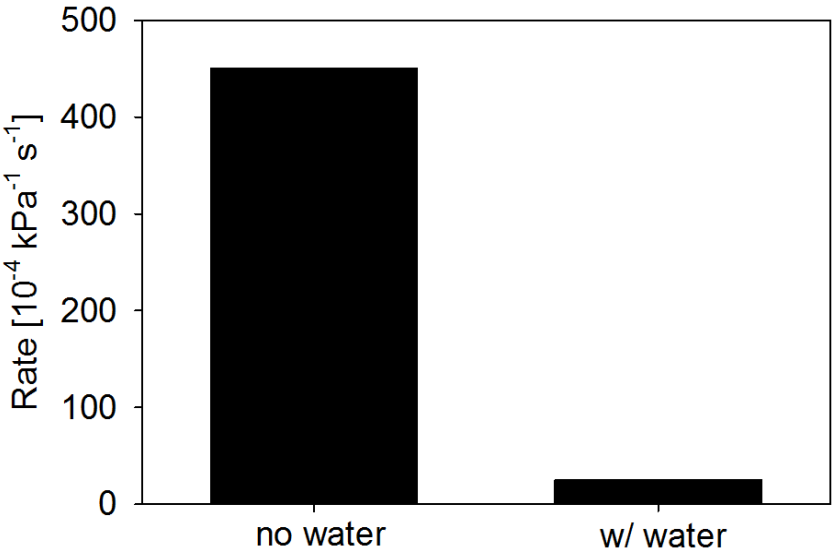

Figure S6.5 Comparison in catalytic activity of secondary amine supported on amorphous silica, pretreated at 423 K and 823 K, and a mesoporous SBA-15 support. P_{total} = 1 atm; $P_{n\text{-butanal}}$ = 0.2 kPa, balance He; total gas flow rate = 150 cm^3min^{-1}; T = 343 K; amine loading = ~0.4 –amine nm^{-2}.

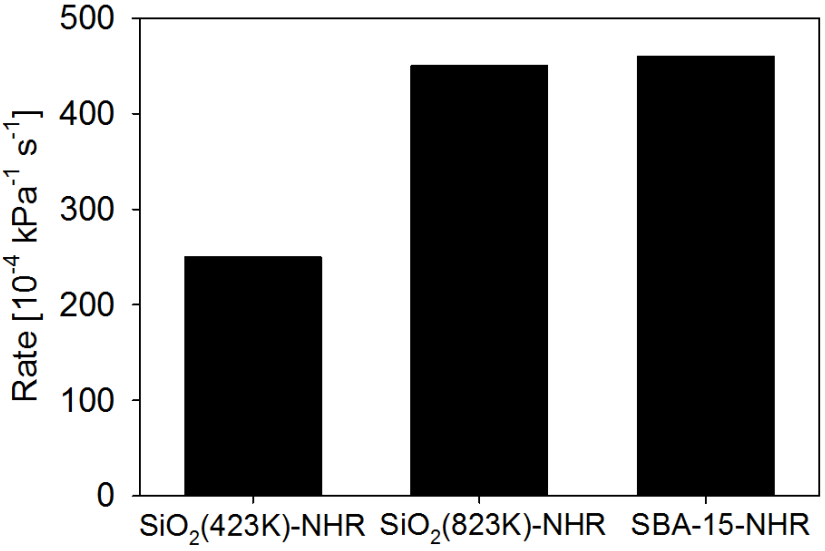

Figure S6.6 Catalytic activity results of secondary amine supported silica catalyst in the absence and presence of co-feeding 2% water. P_{total} = 1 atm; $P_{n\text{-}butanal}$ = 0.2 kPa, balance He; total gas flow rate = 150 cm^3min^{-1}; T = 343 K; amine loading = ~0.4 –amine nm^{-2}.

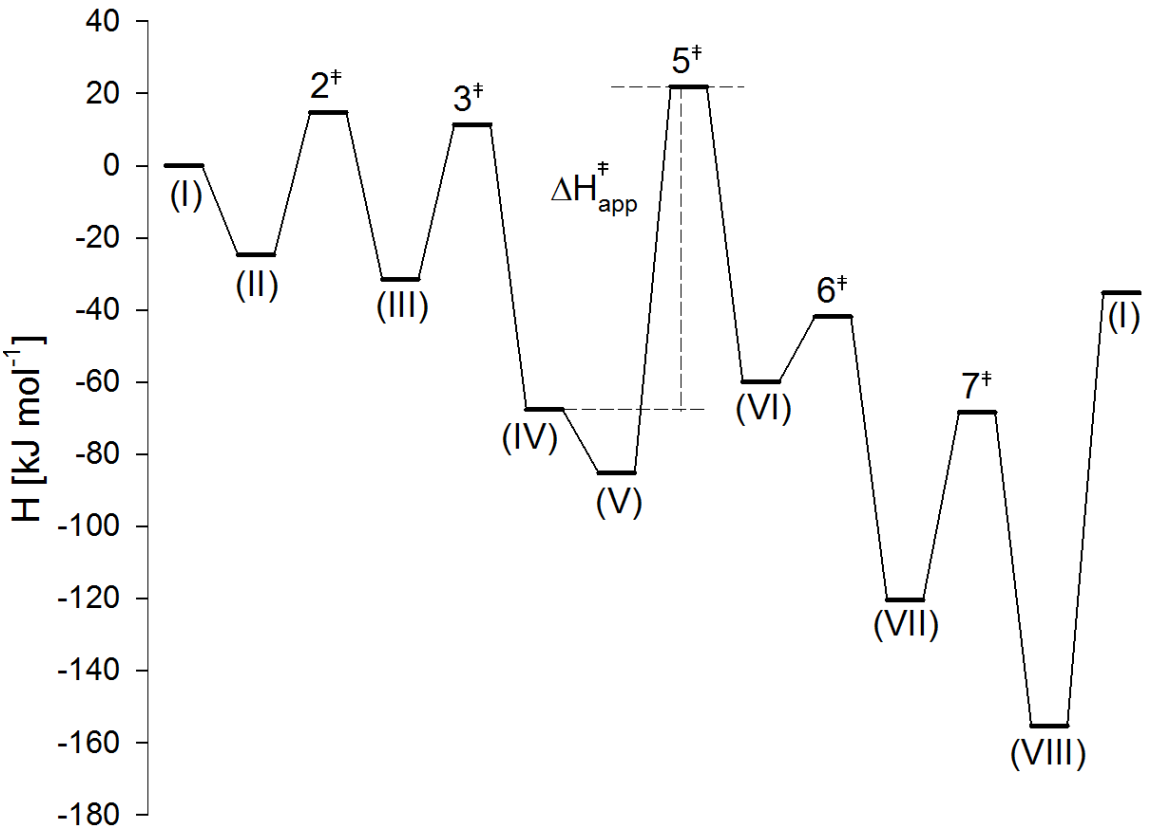

Figure S6.7 Enthalpy (343 K) diagram for aldol condensation of *n*-butanal over a SiO_2-C_3-NHR catalyst calculated at the ωB97X-D/6-311++G(3df,3pd) level of theory [kJ mol^{-1}]. The elementary steps are labeled according to the reaction mechanism in Scheme 6.1. The C-C bond formation step ($5^{\ddagger}$) is done in the presence of water. The calculated apparent activation energy ($\Delta H_{app}^{\ddagger}$) is 90 kJ mol^{-1}.

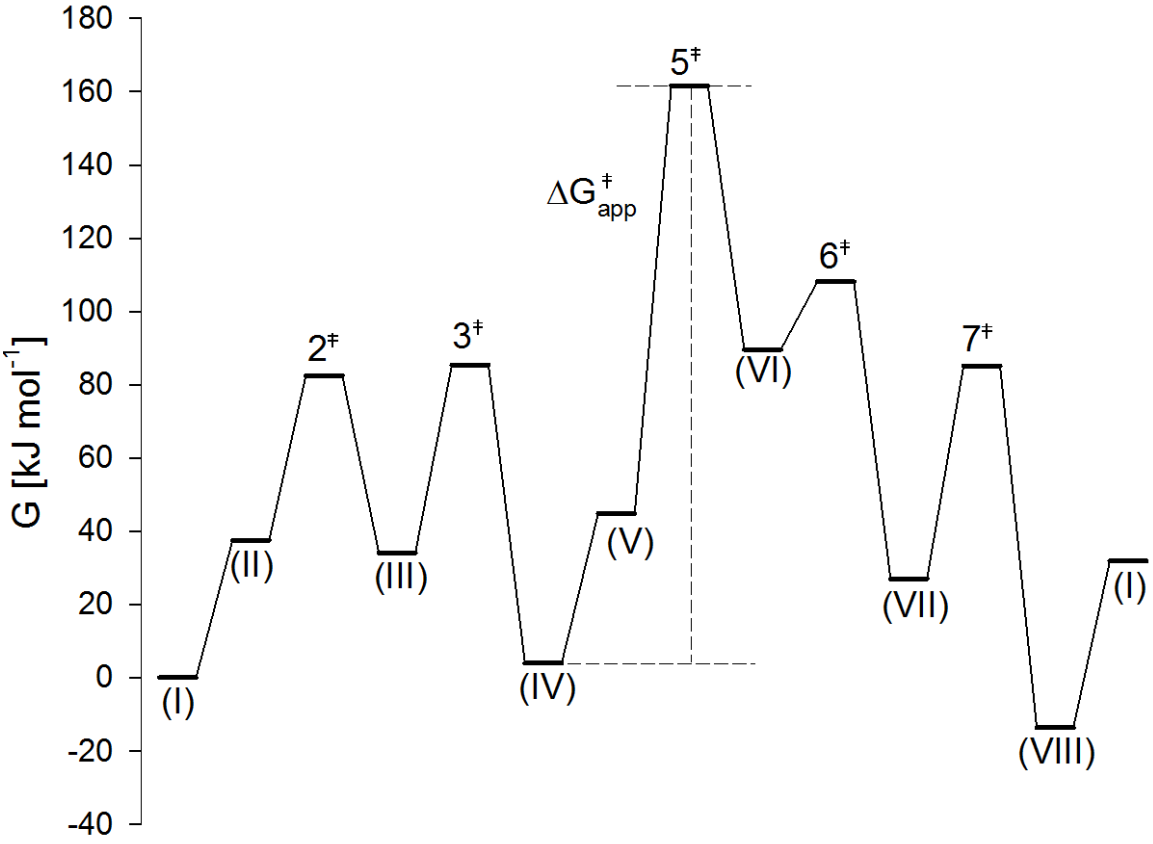

Figure S6.8 Free energy (343 K) diagram for aldol condensation of *n*-butanal over a SiO_2-C_3-NHR catalyst calculated at the ωB97X-D/6-311++G(3df,3pd) level of theory [kJ mol^{-1}]. The elementary steps are labeled according to the reaction mechanism in Scheme 6.1. The C-C bond formation step ($5^{‡}$) is done in the presence of water. The difference in free energy between the resting state (IV) and the rate limiting transition state ($5^{‡}$) is denoted as $\Delta G_{app}^{‡}$.

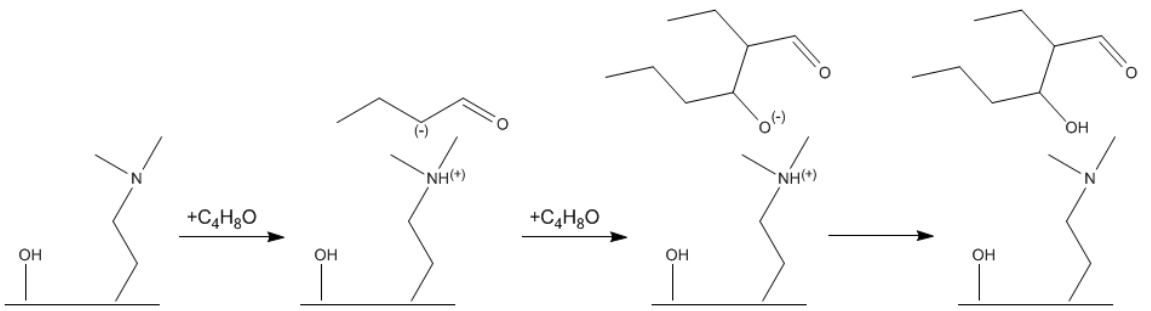

Scheme S6.1 Proposed aldol reaction mechanism using tertiary amine supported silica catalysts

6.7 References

[1] D. E. Cane. *Chem. Rev*. **1990**, 90, 1089-1103.

[2] S. Kraut. *Annu. Rev. Biochem*. **1977**, 46, 331-345.

[3] E. L. Marglefesky, R. K. Zeidan, M. E. Davis. *Chem. Soc. Rev*. **2008**, 37, 1118-1126.

[4] W. Notz, F. Tanaka, C. F. Barbas. *Acc. Chem. Res*. **2004**, 37, 580-591.

[5] S. Shylesh, W. R. Thiel. *ChemCatChem*. **2011**, 3, 278-287.

[6] N. A. Brunelli, C. W. Jones. *J. Catal*. **2013**, 308, 60-72.

[7] Y. Kubota, K. Goto, S. Miyata, Y. Goto, Y. Fukushima, Y. Sugi, *Chem. Lett*. **2003**, 32, 234-235.

[8] J. D. Bass, A. Solovyov, A. J. Pascall, A. Katz. *J. Am. Chem. Soc*. **2006**, 128, 3737-3747.

[9] K. Shimizu, E. Hayashi, T. Inokuchi, T. Kodama, H. Hagiwara, Y. Kitayama. *Tetrahedron Lett*. **2002**, 43, 9073-9075.

[10] R. K. Zeidan, M. E. Davis. *J. Catal*. **2007**, 247, 379-382.

[11] N. A. Brunelli, K. Venkatasubbaiah, C. W. Jones. *Chem. Mater*. **2012**, 24, 2433-2442.

[12] S. Shylesh, A. P. Singh. *J. Catal*. **2006**, 244, 52-64.

[13] M. Kruk, L. Cao. *Langmuir* **2007**, 23, 7247-7254.

[14] S. Shylesh, D. G. Hanna, S. Werner, A. T. Bell. *ACS Catal*. **2012**, 2, 487-493.

[15] S. A. Didas, A. R. Kulkarni, D. S. Sholl, C. W. Jones. *ChemSusChem*. **2012**, *5*, 2058-2064.

[16] S. Farsadpour, L. T. Ghoochany, S. Shylesh, G. Dorr, A. Seifert, S. Ernst, W. R. Thiel. *ChemCatChem*. **2012**, 4, 401-407.

[17] B. List. *Acc. Chem. Res*. **2004**, 37, 548-557.

[18] M. Singh, N. Zhou, D. Paul, K. Klabunde. *J. Catal*. **2008**, 260, 371-379.

[19] K. Kandel, S. M. Althaus, C. Peeraphadit, T. Kobayashi, B. G. Trewyn, M. Pruski, I. I. Slowing. *J. Catal*. **2012**, 291, 63-68.

[20] A. Corma, R. M. Martin-Aranda. *J. Catal*. **1991**, 130, 130-137.

[21] T. Yamamoto, T. Tanaka, T. Funabiki, S. Yoshida. *J. Phys. Chem. B.* **1998**, 102, 5830-5839.

[22] J. M. Rosenholm, T. Czuryszkiewicz, F. Kleitz, J. B. Rosenholm, M. Linden. *Langmuir* **2007**, 23, 4315-4323.

[23] K. Motokura, M. Tada, Y. Iwasawa. *Chem. Asian J*. **2008**, 3, 1230-1236.

[24] E. Papier. *Adsorption on Silica Surfaces,* Marcel Dekker Inc, **2000**.

[25] N. A. Brunelli, S. A. Didas, K. Venkatasubbaiah, C. W. Jones. *J. Am. Chem. Soc*. **2012**, 134, 13950-13953.

[26] S. Bahmanyar, K. N. Houk, *J. Am. Chem. Soc*. **2001**, 123, 11273-11283.

[27] J. L. Reymond, *J. Mol. Catal. A. Enzymatic*. **1998**, 5, 331-337.

[28] M. Wiesner, G. Upert, G. Angelici, H. Wennemers, *J. Am. Chem. Soc*. **2010**, *132*, 6-7.

[29] Meier, W. M. *Z. Kristallogr*. **1967**, 115, 439-450.

[30] A. Behn, P. M. Zimmerman, A. T. Bell, M. Head-Gordon. *J. Chem. Phys.* **2011**, 135, 224108.

[31] Y. Shao, et al. *Phys. Chem. Chem. Phys.* **2006**, 8, 3172−3191.

Chapter 7

An Experimental and Theoretical Study of *n*-butanal Self-Condensation over Ti Species Supported on Silica

Abtract

The effects of the coordination environment and connectivity of Ti on the rate *n*-butanal self-condensation over Ti-silica catalysts were investigated. Characterization of Ti-incorporated SBA-15 catalysts by XANES, UV-VIS, and Raman spectroscopy revealed that the Ti was isolated and tetrahedrally coordinated at low Ti weight loadings but was present as dispersed anatase at higher weight loadings. A comparison of the activity of these catalysts for aldol condensation demonstrated that isolated Ti sites are more active than hexacoordinated sites. The connectivity of tetrahedral Ti species was also found to have an effect on the rate of aldol condensation, Ti-O-Ti dimers being less active than isolated titanol species. The connectivity of tetrahedral Ti was altered by impregnating either Cp_2TiCl_2 or $Ti(O^iPr)_4$ precursors onto a silica support material at low Ti weight loadings. A decrease in activity was observed as the weight loading of Ti was increased for catalysts synthesized by the impregnation of Cp_2TiCl_2 because dimers were formed by the condensation of neighboring titanols. The catalyst synthesized by impregnating $Ti(O^iPr)_4$ onto SBA-15 was less active for aldol condensation than that prepared using Cp_2TiCl_2, and exhibited a higher activation energy because this precursor readily forms dinuclear Ti species. However, the activity could be increased by dehydroxylating the support prior to the impregnation of $Ti(O^iPr)_4$, thus decreasing the fraction of Ti dimers that could form after calcination. A kinetic H/D isotope effect was observed over isolated titanol and Ti dimer catalysts suggesting that α-H abstraction is the rate-determining step. This conclusion is supported by theoretical analysis of the reaction mechanism. In agreement with experimental results, the calculated activation barrier for butanal condensation over a Ti dimer is roughly two times greater than that over Ti-OH sites. The cause for this difference was explained by energy decomposition analysis of the enolate formation step which showed that there is a large energetic penalty for the substrate to distort over the Ti-O-Ti dimer than the Ti-OH monomer.

7.1 Introduction

Aldol condensation of aldehydes has become a subject of considerable interest because this reaction enables the formation of carbon-carbon bonds in compounds used as chemical intermediates and alternative fuels. For example, ~3 x 10^6 tons of the hydrogenated aldol product 2-ethylhexanol are produced annually for use as a plasticizer, solvent, or diesel additive [1,2], and this product could be readily upgraded via esterification to produce a diesel fuel with a favorable cetane number [3,4]. The production of 2-ethylhexanol is generally carried out by aldol condensation of *n*-butanal and the subsequent hydrogenation of the resulting 2-ethylhexenal.

Previous studies have shown that acid-base bifunctionality plays a crucial role in the catalysis of aldol condensation [5-8]. The presence of basic amine and acidic carboxyl

groups on homogeneous amino acid catalysts such as proline have been shown to be very effective for aldol condensation [9]. Bulk metal oxides are also promising heterogeneous aldol condensation catalysts due to the presence of robust Lewis acid and Brønsted base pairs. In particular, the anatase phase of titanium dioxide has been shown to be active and selective for aldol condensation [10]. IR studies have observed a significant shift of the carbonyl peak from 1722 to 1691 cm^{-1} upon the adsorption of acetaldehyde onto the surface of anatase, indicating that the carbonyl group is strongly bound to Lewis acidic Ti sites [11]. Strong adsorption of the aldehyde to the surface facilitates the subsequent H-abstraction step in the aldol mechanism by polarizing the carbonyl bond, causing the alpha proton to become more acidic [8]. Barteau and coworkers have shown that the activity of the TiO_2 (001) surface for the aldol condensation of acetaldehyde increases as more surface oxygen sites are exposed via progressive oxidation of the surface [12]. This suggests that the surface oxygen acts as a Brønsted base in abstracting the alpha proton of the aldehyde. Anatase is thus an active catalyst for aldol condensation due to its ability to adsorb the aldehyde at Lewis acid Ti sites and abstract the alpha-proton at the Brønsted basic surface oxygen sites. In another study by Barteau and coworkers, it was reported that the selectivity for aldol condensation of acetaldehyde was higher on the {114}-faceted (001) rutile surface, which exposes 4, 5, and 6-coordinate Ti, than on the {011} facet, which exposes only 5-coordinate Ti (59% and 31%, respectively) [13]. However, anatase powder was found to have even higher selectivity (75%) and activity for this reaction [13]. It is, therefore, evident that the coordination of Ti in titania has a strong effect on the activity and selectivity of Ti sites for aldol condensation.

The purpose of the study was to elucidate the role of the local coordination and connectivity of Ti sites on the activity of these sites for aldol condensation. Silica-titania catalysts with a well-defined active site were synthesized by incorporating Ti into the framework of SBA-15. These catalysts were characterized by XANES, UV-Vis, and Raman spectroscopy and then the kinetics of *n*-butanal self-condensation were investigated in order to determine the effects of coordination environment. These studies revealed that isolated, tetrahedrally coordinated titanol sites are more active than tetrahedrally coordinated Ti dimer species and octahedrally coordinated Ti sites present on the dispersed nanoparticles of anatase. The insights gained from the current study demonstrate the importance of Ti coordination and connectivity on the activity of Ti species as catalysts for the self-condensation of *n*-butanal.

7.2 Methods

7.2.1 Catalyst Preparation

Titanium was incorporated into the framework of SBA-15 by direct hydrothermal synthesis. Tetraethoxysilane (TEOS, Aldrich) and titanium isopropoxide (Aldrich) were used as the Si and Ti sources, respectively, and Pluronic P123 triblock (Aldrich) co-polymer was used as the structure-directing agent. In a typical synthesis procedure, 4.0 g of P123 was added to 70.0 mL of 0.2 M HCl solution to yield a transparent solution at 313 K. Then 9.0 g of tetraethoxysilane and the required amount of titanium isopropoxide (Si/Ti molar ratio = 5-50) were added dropwise and the resulting gel mixture was stirred for another 24 h. The gel was then crystallized at 393 K for 24 h. The final solid was

filtered, washed with water, and dried at 383 K overnight. Finally, the samples were calcined at 823 K for 6 h. These catalysts are referred to as *x*-Ti–SBA-15, where *x* denotes the dispersion of titanium (atoms nm^{-2}).

Catalysts were also synthesized by incipient-wetness impregnation. Mesoporous SBA-15 (850 m^2 g^{-1}, average pore diameter 60 Å) [14] was impregnated with either $Ti(O^iPr)_4$ (Aldrich, 99.999%) or Cp_2TiCl_2 (Aldrich, 97%) dissolved in toluene (Alfa Aesar, anhydrous 99.8% pure). In a typical synthesis procedure, a titanium loading of 0.45 wt% was achieved using roughly 30 mg (g support)$^{-1}$ precursor in the solution. These catalysts are referred to as 0.07-Ti-Pr/SBA-15 and 0.07-Ti-Cp/SBA-15, respectively. Amorphous SiO_2 (Silicycle, 500 m^2 g^{-1}, average pore diameter 60 Å) was pretreated at 373 K or 1023 K and was then impregnated using $Ti(O^iPr)_4$. These catalysts are referred to as 0.07-Ti-Pr/SiO_2-373K and 0.07-Ti-Pr/SiO_2-1023K, respectively. All impregnated catalysts were dried at 393 K for 12 h and calcined in 100 cm^3 min^{-1} of air (Praxair) for 823 K for 6 h.

7.2.2 Gas-phase Self-condensation of n-butanal

Measurements of reaction rates were performed in a 6.35 mm OD quartz tube containing an expanded section (~12.7 mm OD, ~20 mm length). A plug of quartz wool was placed below the catalyst bed to hold the powder in place. The reactor was heated by a ceramic furnace with external temperature control and the catalyst bed temperature was measured with a K-type thermocouple sheathed in a quartz capillary placed in direct contact with the catalyst bed.

Prior to reaction, the catalyst was heated to the reaction temperature at a rate of 2 K min^{-1} in pure He (Praxair, 99.999%) flowing at 150 cm^3 min^{-1} at STP. The feed to the reactor consisted of *n*-butanal (TCI, 98%) and He (Praxair, 99.999%). For kinetic isotope experiments, *n*-butanal-2,2-d_2 (CDN Isotopes, 98%) was used as the feed. A filled 1 mL syringe connected to a syringe pump (Cole-Palmer, 74900 series) was used to inject *n*-butanal into a heated port through which He was continuously flowing. All experiments were carried out at a total gas pressure of 1 atm. The total gas flow rate was typically 150 cm^3 min^{-1} at STP. Using these conditions, the conversion of aldehyde was always less than 10%. Reaction products were analyzed using an Agilent 6890N gas chromatograph containing a bonded and crosslinked (5%-Phenyl)-methylpolysiloxane capillary column (Agilent, HP-1) connected to a flame ionization detector (FID).

7.2.3 Catalyst Characterization

Ti content was determined by inductively coupled plasma optical emission spectroscopy (ICP-OES) conducted at Galbraith Laboratories in Knoxville, TN.

Nitrogen adsorption isotherms were performed using a Micromeritics Gemini VII surface area and pore volume analyzer. The specific surface area and pore size were calculated using the Brunauer-Emmet-Teller (BET) equation and Barrett-Joyner-Halenda (BJH) equations.

X-ray absorption spectroscopy (XAS) measurements were performed at the Advanced Photon Source at Argonne National Laboratory (ANL) on beam line 10-BM. Measurements were performed at the Ti K-edge. The Ti edge energy was taken as the first inflection point of the main absorption peak. The energy was referenced to a pure Ti foil placed between the two ionization chambers located after the sample. The catalysts

and reference materials, TiO_2 anatase (Aldrich) and titanium silicate-1 (TS-1) were diluted with boron nitride, an inert and relatively X-ray transparent material, in order to achieve an absorbance of ~2.5 because such an absorbance provides optimal signal to noise ratio [15]. Samples were placed in a controlled-atmosphere cell, heated to 473 K in the presence of flowing gas [16], and then cooled to ambient conditions before collecting the XAS data. The XAS data were analyzed with the IFEFFIT software and its complementary Athena GUI [17,18].

Diffuse reflectance UV-VIS spectra were acquired using a Fischer Scientific EVO 300 spectrometer equipped with a Praying Mantis reflectance chamber. Spectra were referenced to the diffuse reflectance spectrum of Teflon.

Raman spectra were recorded at ambient conditions using a confocal Raman microscope (LabRam HR, Horiba Jobin Yvon) equipped with a 532 nm HeNe laser operated at a power of 50 mW.

7.2.4 Theoretical Calculations

The models chosen to represent Ti monomer and dimer active sites are shown in Scheme 7.1. To mimic the rigidity of the silica support, all geometry optimizations were performed with relaxation of only the Ti atoms, the O atoms in the first coordination sphere, and the H atom of the titanol group. Geometry optimizations and single-point energy calculations were performed using density functional theory (DFT) at the ωB97X-D [19,20] /LANL2DZ and ωB97X-D/CRENBL levels of theory, respectively. Enthalpies at reaction temperature were determined by taking zero point vibrational and temperature corrections into account using the rigid rotor harmonic oscillator (RRHO) approximation. Entropies were determined using a quasi-RRHO approach proposed by Grimme, which replaces the vibrational entropy for modes with frequencies <100 cm^{-1} by the entropy for a corresponding free-rotor [21]. All calculations were carried out using Q-Chem software package [22]. The partial charges on atoms were calculated using natural bond orbital (NBO) analysis [23]. The structures of reaction intermediates were hypothesized a priori and then refined by standard geometry optimizations. The transition structures connecting intermediates were found by the freezing-string method [24] followed by local optimization.

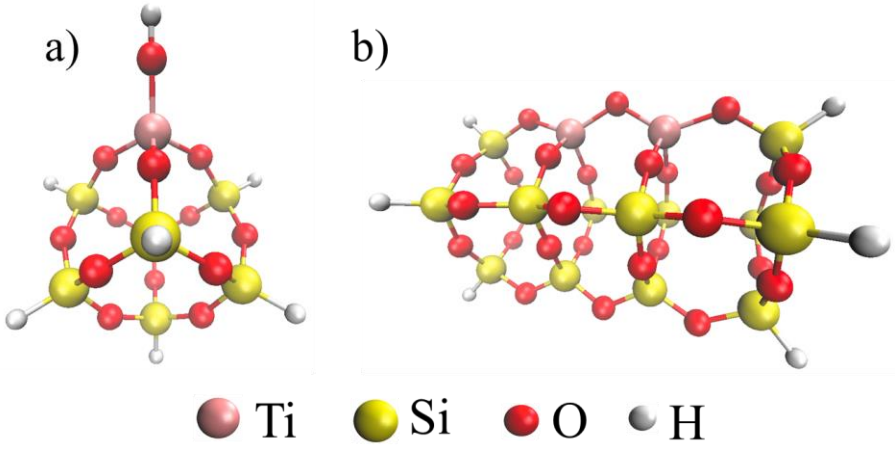

Scheme 7.1 Cluster model of the tetrahedral (a) isolated titanol and the (b) Ti dimer.

7.3 Results and Discussion

7.3.1 Catalyst Characterization

The Ti loading, surface area, and pore volume of each catalyst are shown in Table 7.1. The weight loading was varied from 0.11-4.5 wt % in order to change the dispersion of Ti on SBA-15 support. The pore volumes and surface areas of the incorporated and impregnated catalysts for a given Ti weight loading are very similar.

The coordination of Ti in the incorporated Ti–SBA-15 catalysts was probed by X-ray absorption spectroscopy. Previous studies have demonstrated that the pre-edge feature can be used reliably to determine the coordination number of Ti in various oxide compounds [25]. Figure 7.1 shows the Ti XANES region for three samples as well as two Ti standards, TS-1 and TiO_2 anatase. The spectrum of 0.07-Ti–SBA-15 exhibits a single pre-edge feature at 4971 eV similar to that observed in the spectrum of TS-1, indicating that Ti is tetrahedrally coordinated within the framework [26]. The spectrum of 0.3-Ti–SBA-15 has a strong feature at 4971 eV and a small shoulder at 4975 eV, while the spectrum of 0.7-Ti–SBA-15 matches that of bulk TiO_2 anatase. The three peaks at 4969, 4972, and 4975 eV in the spectrum of anatase are due to the transition of 1s core electrons to $1t_{ig}$, $2t_{2g}$, and $3e_g$ molecular orbitals [26]. Thus, the coordination environment of Ti changes from tetrahedral in 0.07-Ti–SBA-15 to distorted octahedral in 0.7-Ti–SBA-15 as the Ti weight loading is increased.

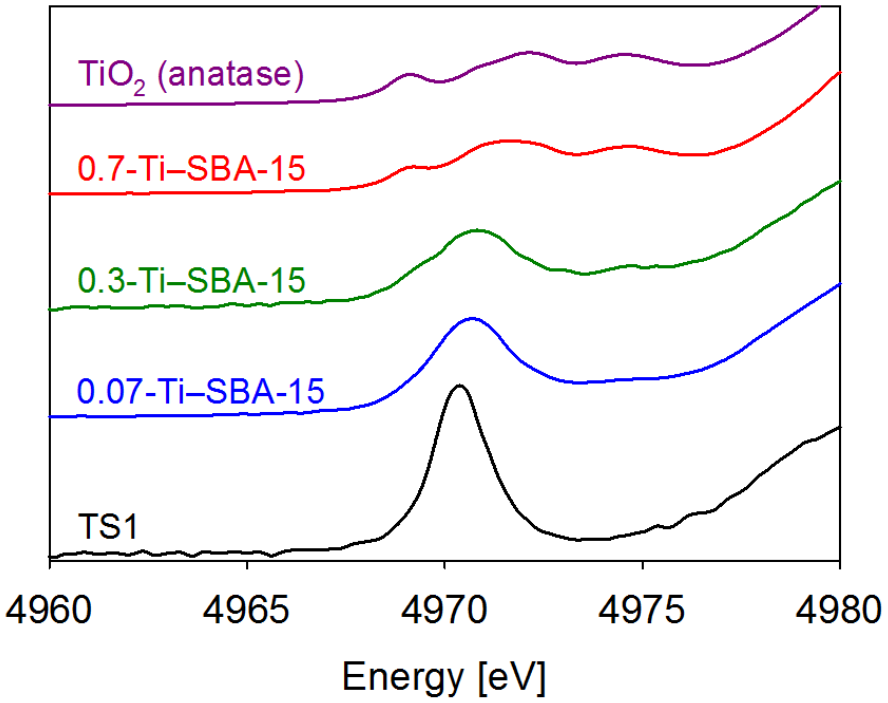

Figure 7.1 XANES spectra of (–) TS1, (–) 0.07-Ti–SBA-15, (–) 0.3-Ti–SBA-15, (–) 0.7-Ti–SBA-15, and (–) TiO_2 anatase.

Table 7.1 Chemical and physical properties of different *x*-Ti—SBA-15 catalysts.

Sample	Si/Ti Ratio[a]	Ti Content (wt. %)[b]	Ti Dispersion (Ti/nm^2)	BET Surface Area (m^2/g)	Pore Volume (cm^3/g)
0.02-Ti–SBA-15	50	0.11	0.016	836	0.75
0.07-Ti–SBA-15	25	0.44	0.065	826	0.73
0.3-Ti–SBA-15	10	1.85	0.27	789	0.67
0.7-Ti–SBA-15	5	4.50	0.67	715	0.49
0.07-Ti-Cp/SBA-15	--	0.42	0.062	805	0.73
0.3-Ti-Cp/SBA-15	--	1.74	0.26	746	0.63
0.07-Ti-Pr/SBA-15	--	0.45	0.067	800	0.70
SBA-15	--	--	--	850	0.93

[a] Expected, [b] Actual (ICP results)

The UV-Visible diffuse reflectance spectra of Ti–SBA-15 and TiO_2 anatase are shown in Figure 7.2. 0.02-Ti–SBA-15 and 0.07-Ti–SBA-15 exhibit peaks in the range of 210-230 nm due to the ligand-to-metal charge transfer (LMCT) from oxygen to tetrahedral Ti (IV) [27]. Zhao and coworkers have reported that this band provides evidence that Ti is tetrahedrally coordinated and has been incorporated into the framework of SBA-15 [28]. As the Ti loading increases, the peak maximum of the absorption is red-shifted to higher wavelengths, approaching that of anatase. Previous studies have reported that this shift can be attributed to partially polymerized hexacoordinated Ti species [29,30]. Consistent with previous UV-Visible studies of dispersed TiO_2 nanoparticles on SiO_2, the peak position of the sample containing the highest weight loading of Ti, 0.7-Ti–SBA-15, is blue-shifted from that of anatase due to quantum-size effects [31,32].

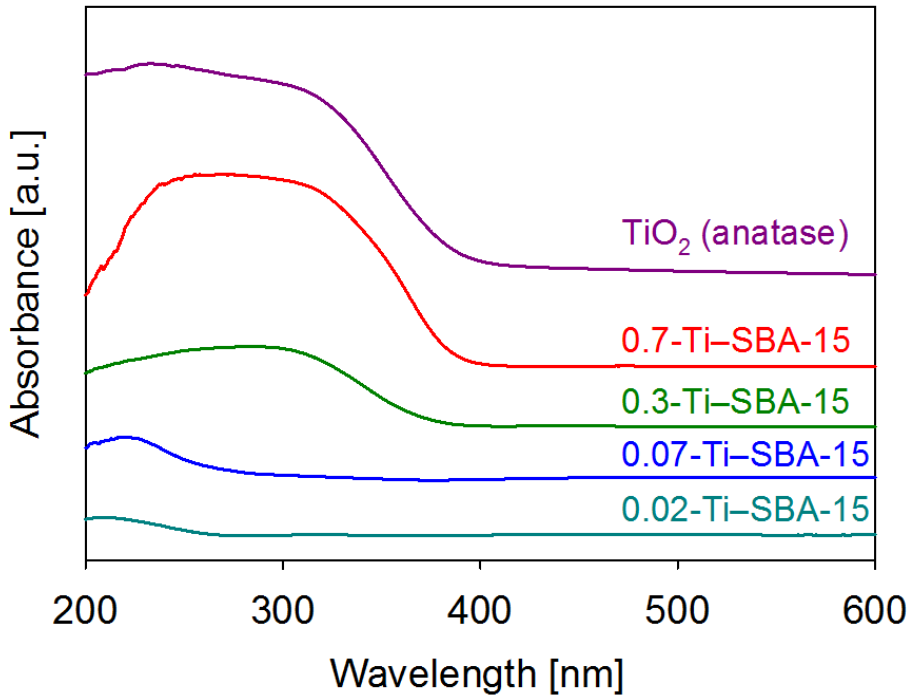

Figure 7.2 UV-Vis spectra of (–) 0.02-Ti–SBA-15, (–) 0.07-Ti–SBA-15, (–) 0.3-Ti–SBA-15, (–) 0.7-Ti–SBA-15, and (–) TiO_2 anatase.

Figure 7.3 shows the Raman spectra of SBA-15, *x*-Ti–SBA-15 and TiO_2 anatase. The spectrum of SBA-15 exhibits peaks at 485 and 975 cm^{-1} which are attributed to the stretching vibrations of four-membered siloxane linkages (Si-O-Si) and surface silanols (O_3Si-OH), respectively [33]. The spectrum of 0.02-Ti–SBA-15 is indistinguishable from the spectrum of SBA-15 because of the very low weight loading of Ti. The spectrum of 0.07-Ti–SBA-15 exhibits small deviations from the spectrum of pristine SBA-15. The peaks at 485 and 975 cm^{-1} are slightly more intense and broader for 0.07-Ti–SBA-15 than for SBA-15 and a weak peak near 140 cm^{-1} becomes apparent. Similar observations have been reported by Turek and coworkers, who observed an increase in the intensity of a peak at 970 cm^{-1} as more Ti was substituted into silicalite [34]. The weak peak around 140 cm^{-1} is the most sensitive fingerprint for anatase and indicates the formation of Ti-O-Ti bonds. Samples with higher Ti loadings than 0.07-Ti–SBA-15 exhibit the four characteristic peaks of anatase at 145, 400, 520, 650 cm^{-1} due to the E_g symmetric stretching, the B_{1g} symmetric bending, the A_{1g} anti-symmetric bending, and the E_g vibrations of Ti-O-Ti bonds, respectively [35]. Although the XRD spectra for these catalysts only indicate the presence of anatase at the highest weight loading (see refer to Figure S7.1 in the Supporting Information), the Raman spectra suggest that a fraction of the titanium on the 0.3 and 0.7 Ti–SBA-15 catalysts is present as anatase.

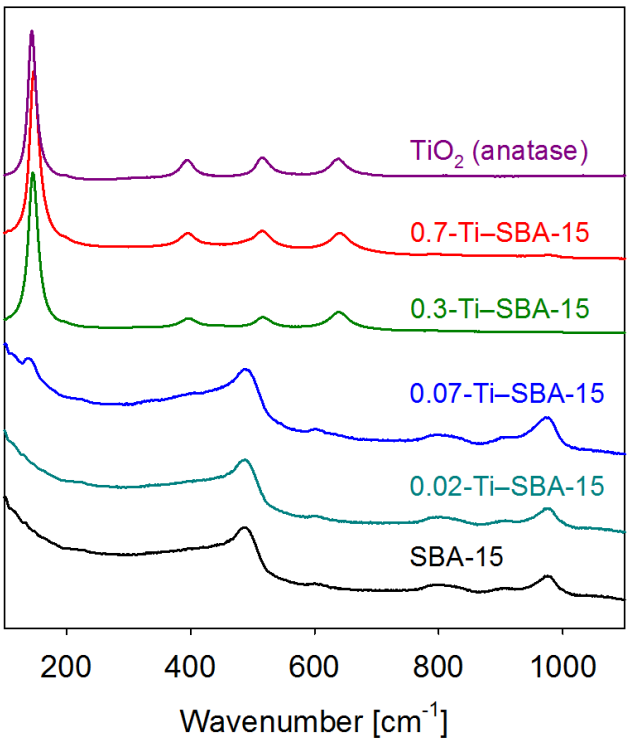

Figure 7.3 Raman spectra of (–) SBA-15, (–) 0.02-Ti–SBA-15, (–) 0.07-Ti–SBA-15, (–) 0.3-Ti–SBA-15, (–) 0.7-Ti–SBA-15, and (–) TiO_2 anatase.

7.3.2 Catalytic Activity of x-Ti–SBA-15 and x-Ti/SBA-15 Catalysts

Experiments were conducted under mild conditions to ensure differential conversion so that catalyst deactivation and secondary aldol reactions could be minimized. The only product observed under any of the conditions investigated was the dehydrated aldol product, 2-ethlyhexenal. Figure 7.4 shows the activity versus time-on-stream for the most active catalyst, 0.02-Ti–SBA-15. After a brief induction period, the catalyst remains stable for at least 3 h. If deuterated *n*-butanal-2,2-d_2 is reacted over this catalyst, a kinetic isotope effect of $k_H/k_D = 2.4$ is observed suggesting that the alpha C-H bond is involved in the transition state of the rate-limiting elementary step. α-H abstraction is relevant to aldol condensation and will be discussed in the context of the reaction mechanism (see Section 7.3.3).

The activities of *x*-Ti–SBA-15 catalysts are shown in Figure 7.5. As the weight loading of Ti increases, the turnover frequency decreases monotonically. However, no activity was observed in the absence of Ti. Comparison of the activity of 0.02-Ti–SBA-15 and 0.7-Ti–SBA-15 coupled with the results of the characterization of these samples suggests that isolated tetrahedral Ti sites are more active than hexacoordinated Ti sites. As shown in Figure S7.2 in the Supporting Information, *n*-butanal desorbs at a lower temperature over 0.7-Ti–SBA-15 than 0.07-Ti–SBA-15. Therefore, hexacoordinated Ti sites may be less active than isolated four-coordinated Ti sites because the adsorption of butanal is less favorable at coordinatively saturated sites. A theoretical study comparing the adsorption of formaldehyde onto different Ti sites on the (001) plane of TiO_2 anatase

supports this assertion [36]. The results of this study found that the most favorable binding involved the Lewis acid-base interaction between the coordinatively unsaturated Ti (+4) sites and oxygen of the carbonyl group. Hence, the remainder of this study will focus on the more active tetrahedrally coordinated Ti catalysts.

Interestingly, the activity of 0.02-Ti–SBA-15 is higher than that of 0.07-Ti–SBA-15 despite the evidence from XANES and UV-Visible spectroscopy suggesting that both these catalysts contain predominantly isolated tetrahedrally coordinated Ti. This finding leads to the proposal that, in addition to the coordination environment, the connectivity of the Ti site also has an effect on the catalytic activity – tetrahedral Ti-O-Ti sites being less active than isolated tetrahedral Ti sites. In order to test this hypothesis, catalysts were synthesized by incipient wetness impregnation using either $Ti(O^iPr)_4$ or Cp_2TiCl_2 precursors. The literature suggests that the latter precursor can be used to synthesize site-isolated catalysts with high Ti loading [37]. However, as shown by Entry 2 and 3 of Table 7.2, the activity of 0.07-Ti-Cp/SBA-15 is two times higher than that of the 0.3-Ti-Cp/SBA-15 catalyst. The TOF values are similar to what was observed in incorporated 0.07-Ti–SBA-15 and 0.3-Ti–SBA-15, respectively. Previous experimental and theoretical studies have reported that Cp_2TiCl_2 reacts with the silanol groups of mesoporous silica to yield a $(\equiv SiO)_3TiCp$ intermediate, which subsequently forms isolated $(\equiv SiO)_3TiOH$ species after calcination [16,38]. Since the Cp_2TiCl_2 precursor is known to react facilely with the support [16], and the UV-Vis spectra of these catalysts indicates that Ti is tetrahedrally coordinated (see Supporting Information), it is unlikely that the coordination number of Ti changes with loading. However, as the surface density of Ti increases, it is feasible that during calcination neighboring titanols condense to form tetrahedral dimers. Based upon our experimental evidence and previous theoretical studies [38], the dinuclear Ti species shown in Scheme 7.1 was chosen to represent Ti dimer although other dimer structures may be possible. In accordance with the stated hypothesis, the decrease in activity for catalysts with higher Ti weight loading is attributed to the formation of tetrahedrally coordinated Ti dimers.

Table 7.2 Activity (TOF), apparent activation energy (kJ mol^{-1}), and partial pressure dependencies of Ti silica catalysts. P_{Total} = 101.325 kPa

Entry	Sample	TOF[a] (10^{-4} s^{-1})	Activation Energy[b] (kJ mol^{-1})	Partial Pressure Dependence[c]
1	0.07-Ti–SBA-15	10.5	60	0.05
2	0.07-Ti-Cp/SBA-15	11.4	59	0.10
3	0.3-Ti-Cp/SBA-15	5.70	55	0.15
4	0.07-Ti-Pr/SBA-15	2.90	120	0.20
5	0.07-Ti-Pr/SiO_2-373K	4.05	61	0.15
6	0.07-Ti-Pr/SiO_2-1023K	8.10	58	0.10

[a] T = 353 K, $P_{n\text{-}butanal}$ = 0.2 kPa, balance He
[b] T = 343-363 K, $P_{n\text{-}butanal}$ = 0.2 kPa, balance He
[c] T = 353 K, $P_{n\text{-}butanal}$ = 0.1-0.4 kPa, balance He

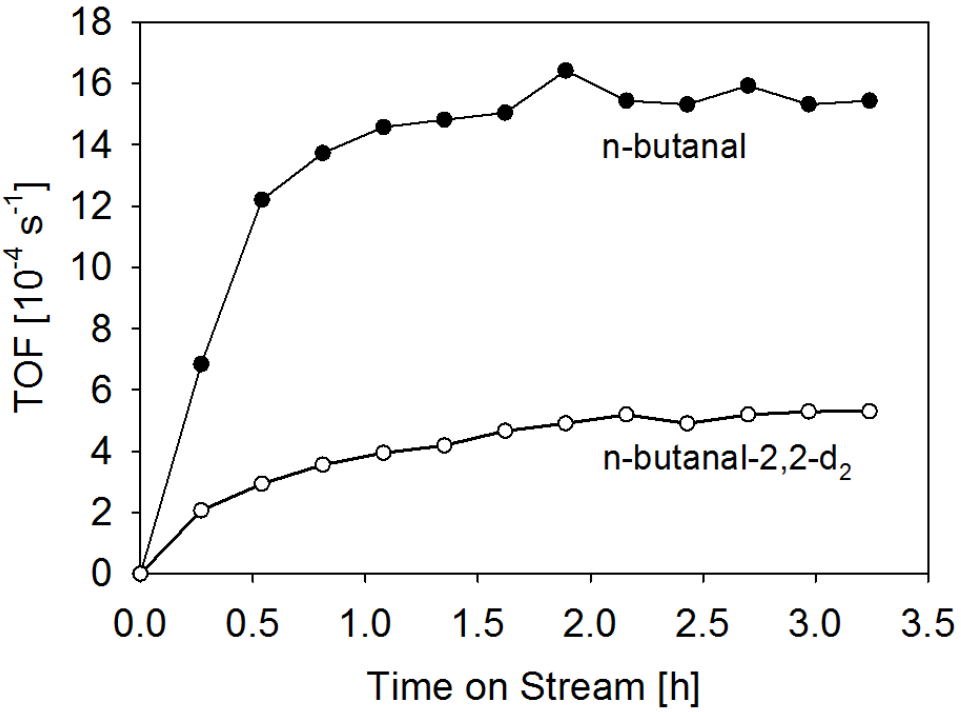

Figure 7.4 Time on stream study over 0.02-Ti–SBA-15 catalyst. T = 353 K, P_{Total} = 101.3 kPa, $P_{n\text{-}butanal}$ = 0.2 kPa (●) *n*-butanal (○) *n*-butanal-2,2-d_2, balance He. Catalyst mass = 0.02 g. Total gas flow rate at STP = 150 cm^3 min^{-1}.

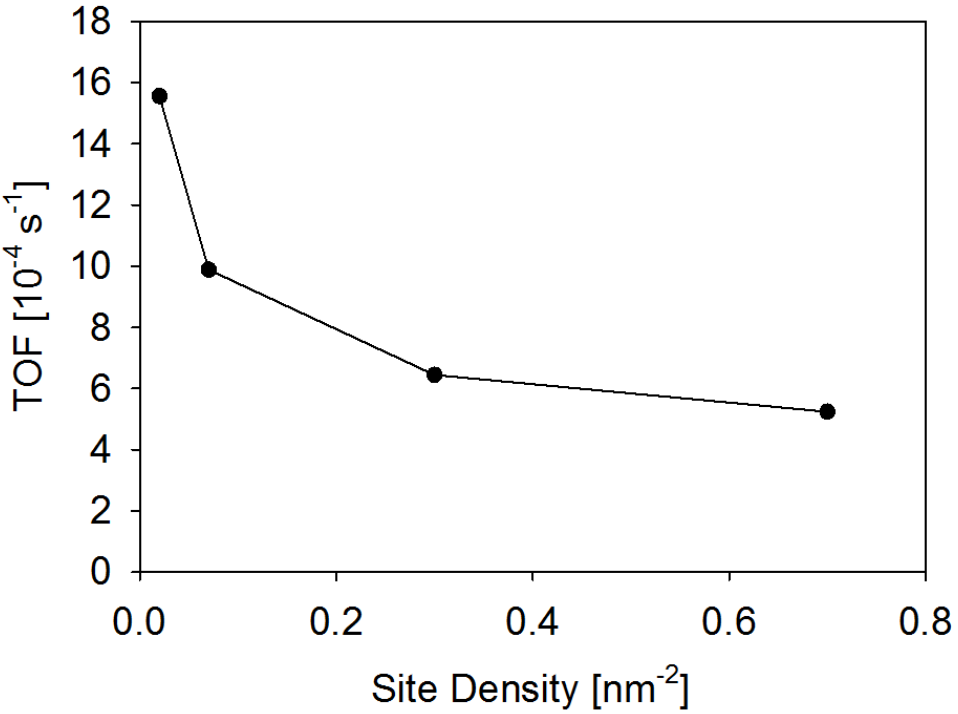

Figure 7.5 Effect of the Ti site density on the activity of *x*-Ti–SBA-15 catalysts for aldol condensation. T = 353 K, P_{Total} = 101.3 kPa, $P_{n\text{-}butanal}$ = 0.2 kPa τ = 4.2 ms (mol Ti / mol feed rate)

Impregnation was also conducted with a $Ti(O^iPr)_4$ precursor because previous literature indicates that this precursor reacts with surface silanol groups to form dinuclear Ti complexes [39]. The probability of forming Ti dimers with this precursor is high since $Ti(O^iPr)_4$ is known to exist as an oligomer in solution [40]. Furthermore, Scott and coworkers have proposed that $Ti(O^iPr)_4$ does not follow simple ligand exchange with the support as other metal precursors do, but rather a grafted Ti monomeric species reacts with $Ti(O^iPr)_4$ to form a dinuclear Ti complex [39]. The UV-Vis spectrum of the catalyst synthesized by impregnation of $Ti(O^iPr)_4$ onto SBA-15 shows that Ti is tetrahedrally coordinated (see Supporting Information); however, this catalyst was the least active, as shown by Entry 4 of Table 7.2, supporting the hypothesis that tetrahedral Ti dimers are less than active than Ti monomers. Furthermore, the apparent activation energy of 0.07-Ti-Pr/SBA-15 was 120 kJ mol^{-1}, which is two times greater than what was measured for the incorporated 0.7–Ti–SBA-15 catalyst. Despite the large difference in the apparent activation energy, both catalysts show a kinetic isotope effect ($k_H/k_D = 2$ is observed over 0.07-Ti-Pr/SBA-15 catalyst) and both are roughly zero order in *n*-butanal.

In an effort to produce isolated Ti species, $Ti(O^iPr)_4$ was impregnated onto amorphous silica pretreated at different temperatures. The purpose of the pretreatment was to dehydroxlate the support in order to spatially separate the silanol groups, thereby increasing the average distance between possible locations at which $Ti(O^iPr)_4$ could graft. The silanol group density was quantified using ^{29}Si MAS NMR as reported previously [41]. Silica pretreated at 373 K and 1023 K contains 4 and 1.6 OH/nm^2, respectively. As shown by Entries 5 and 6 of Table 7.2, the TOF of 0.07-Ti-Pr/SiO_2-1023K was roughly twice as high as 0.07-Ti-Pr/SiO_2-373K, demonstrating that dehydroxylation of the silica support has a significant effect on the catalytic activity. Similarly, the activity of 0.07-Ti-Pr/SiO_2-373K was greater than that of 0.07-Ti-Pr/SBA-15, indicating that there is an inverse correlation between the activity and the density of silanol groups of the support (SBA-15 contains 5 OH/nm^2). Although the Raman spectra of these catalysts exhibits peaks characteristic of anatase, 0.07-Ti-Pr/SiO_2-1023K shows an additional peak characteristic of isolated Ti around 940 cm^{-1} (see Supporting Information). Therefore, the fraction of isolated Ti is dependent upon the silanol density. Additionally, the apparent activation energy for 0.07-Ti-Pr/SiO_2 matches that of both the 0.02-Ti–SBA-15 and 0.07-Ti–SBA-15, but is much lower than that of the 0.07-Ti-Pr/SBA-15 catalyst. These results suggest that a majority of the catalytic activity for Ti-Pr/SiO_2 occurs at isolated Ti sites, which are more active than tetrahedrally coordinated Ti-O-Ti sites.

7.3.3 Catalytic Mechanism for Aldol Condensation

The mechanism proposed for aldol condensation over isolated Ti sites is shown in Scheme 7.2. The reaction sequence begins with the adsorption of butanal via Reaction 1. As described previously, the adsorption occurs through a Lewis acid-base interaction between the nucleophilic oxygen of the carbonyl group and the electrophilic Ti (Species B). The strength of this interaction polarizes the carbonyl causing the carbon to become more electrophilic and α-H to be more acidic. The increase in acidity facilitates α-H abstraction by the Brønsted base oxygen to form a bound water and enolate intermediate as shown in Reaction 2. In Reaction 3, the Ti becomes a saturated hexacoordinated species by adsorbing a second molecule of butanal. The polarization of the carbonyl bond induces nucleophilic attack by the enolate to the electrophilic carbon resulting in the

formation of a C-C bond in Reaction 4. The aldol product is formed in Reaction 5 when the bound water acts as a Brønsted acid, and desorbs from the active site in Reaction 6. Under reaction conditions, the aldol product readily undergoes dehydration to form the thermodynamically favored product 2-ethylhexenal [11,42].

The kinetic isotope effect observed for both 0.07-Ti–SBA-15 and 0.07-Ti-Pr/SBA-15 provides evidence that enolate formation is a kinetically relevant step. If it is assumed that the adsorption step is quasi-equilibrated, the rate of 2-ethylhexenal formation is given by:

$$r_P = \frac{K_1 k_2 P_{n-butanal} L}{1 + K_1 P_{n-butanal}} \quad (1)$$

where K_1 is the equilibrium constant for Reaction 1, k_2 is the rate constant for Reaction 2, and L is the number of active sites. The zero-order partial pressure dependence on n-butanal suggests that the surface is saturated with adsorbed aldehyde, and therefore the rate expression can be simplified to:

$$r_P = k_2 L \quad (2)$$

suggesting that the apparent activation barrier represents the intrinsic barrier for enolate formation.

7.3.4 Theoretical Modeling of Tetrahedral Titanol and Ti Dimer Sites

To understand why isolated Ti sites are more active and have a much lower activation barrier than Ti dimer sites, a theoretical analysis of the aldol condensation reaction pathway was performed for both isolated titanol and a dinuclear Ti species. Since the β– and γ–C of *n*-butanal are inert in aldol condensation and the gas phase de-protonation energy of butanal and ethanal are similar [43,44], ethanal was used as a model reactant to reduce the computational cost.

Using the isolated titanol cluster, the mechanism shown in Scheme 7.2 was found to describe the minimum-energy pathway. The changes in Gibbs free energy calculated for the reaction temperature of 353 K are shown in Figure 6 and the changes in enthalpy along the reaction pathway are shown in Figure 7.7. Since the surface is saturated with adsorbed butanal, as indicated by the zero order partial pressure dependence on *n*-butanal, the reference state was chosen to include one aldehyde adsorbed to the Ti, and another molecule of hydrogen bonded to the hydroxyl of an adjacent silanol. Figure 6 shows that α-H abstraction has the largest free energy barrier in the reaction sequence, indicating that enolate formation is the rate-determining step. This conclusion is consistent with the observed kinetic isotope effect. The calculated activation energy for α-H abstraction is 64 kJ mol^{-1}, in good agreement with the value of 60 kJ mol^{-1} determined experimentally. Excellent agreement between theory (123 kJ mol^{-1}) and experiment (120 kJ mol^{-1}) was also found for the barrier of enolate formation over the dinuclear Ti species. Interestingly, the large difference of 60 kJ mol^{-1} in the activation energy between monomer and dimer species cannot be rationalized on the basis of the Lewis acidity of

the Ti or the Lewis basicity of the oxygen responsible for the α-H abstraction. As shown in Table 7.3, the charges on Ti in monomer and dimer species upon aldehyde absorption are comparable, indicating that the Lewis acidity of both sites is similar. Even though the calculated proton affinity of the oxygen of Ti-O-Ti is 35 kJ mol^{-1} more basic than the oxygen of titanol, the Ti dimer exhibits a much higher barrier for α-H abstraction. To provide an explanation for this phenomenon, an energy decomposition analysis of the enolate-formation step was performed for the monomer and dimer species. The results of this analysis, shown in Figure 7.8, suggest that the geometric distortion penalty for transitioning from state B to state $B^{\ddagger}$ is 48 kJ mol^{-1} greater for the dimer than for the monomer. Therefore, the activation energy for the dimer is much larger than for the monomer mainly because of geometric constraints. Even though the oxygen of the dimer is a stronger base than that of the titanol, it is less able to readily reach the α-H because of the rigidity of the Ti-O-Ti bridge. Conversely, the titanol is more flexible, resulting in the more facile formation of the enolate.

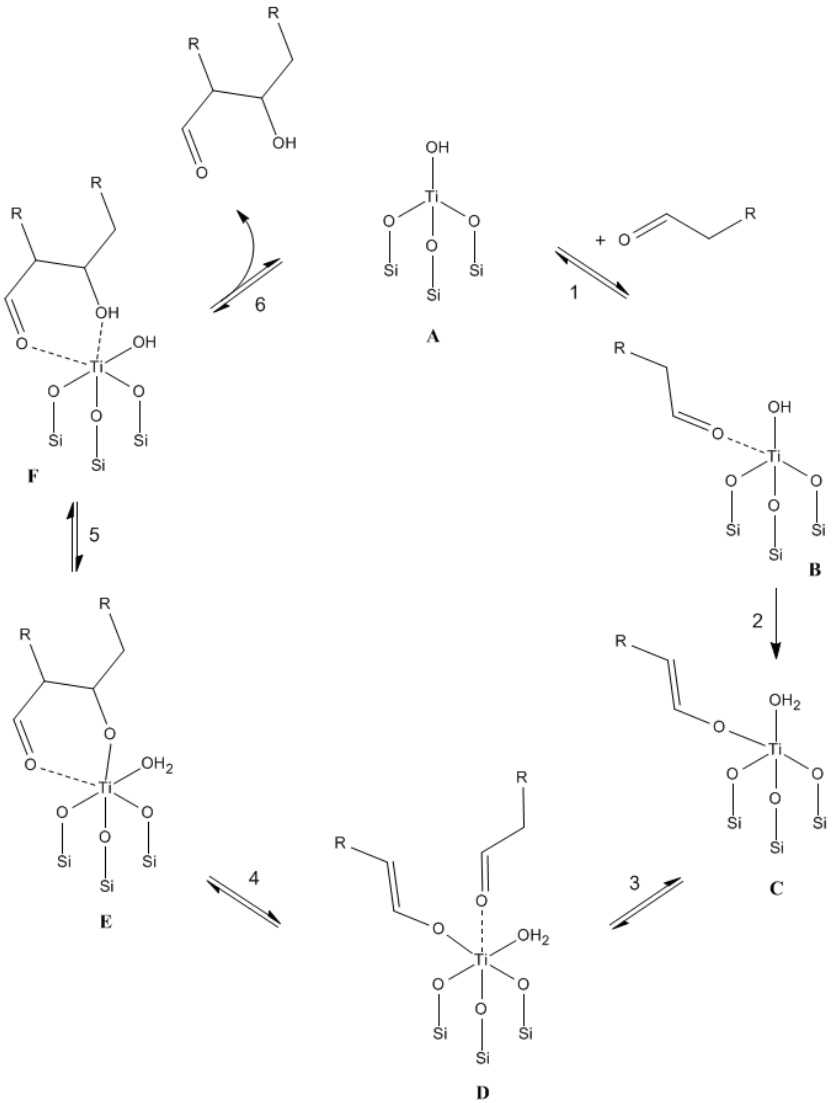

Scheme 7.2. Mechanism of aldol condensation over an isolated titanol. R = CH_2CH_3.

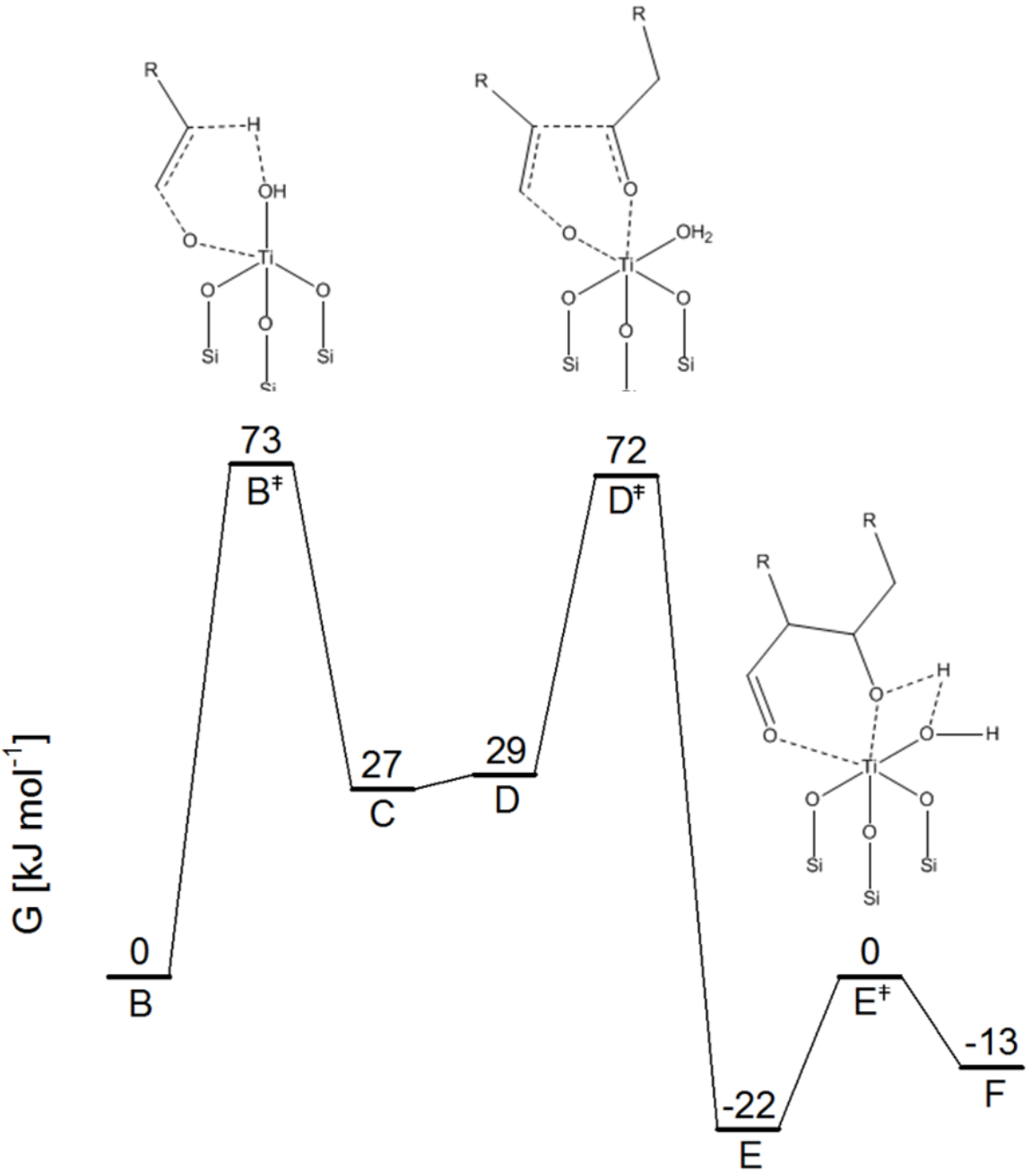

Figure 7.6 Free-energy (353 K) diagram for aldol condensation over an isolated titanol (where R = H). The elementary steps are labeled according to the reaction mechanism shown in Scheme 7.2.

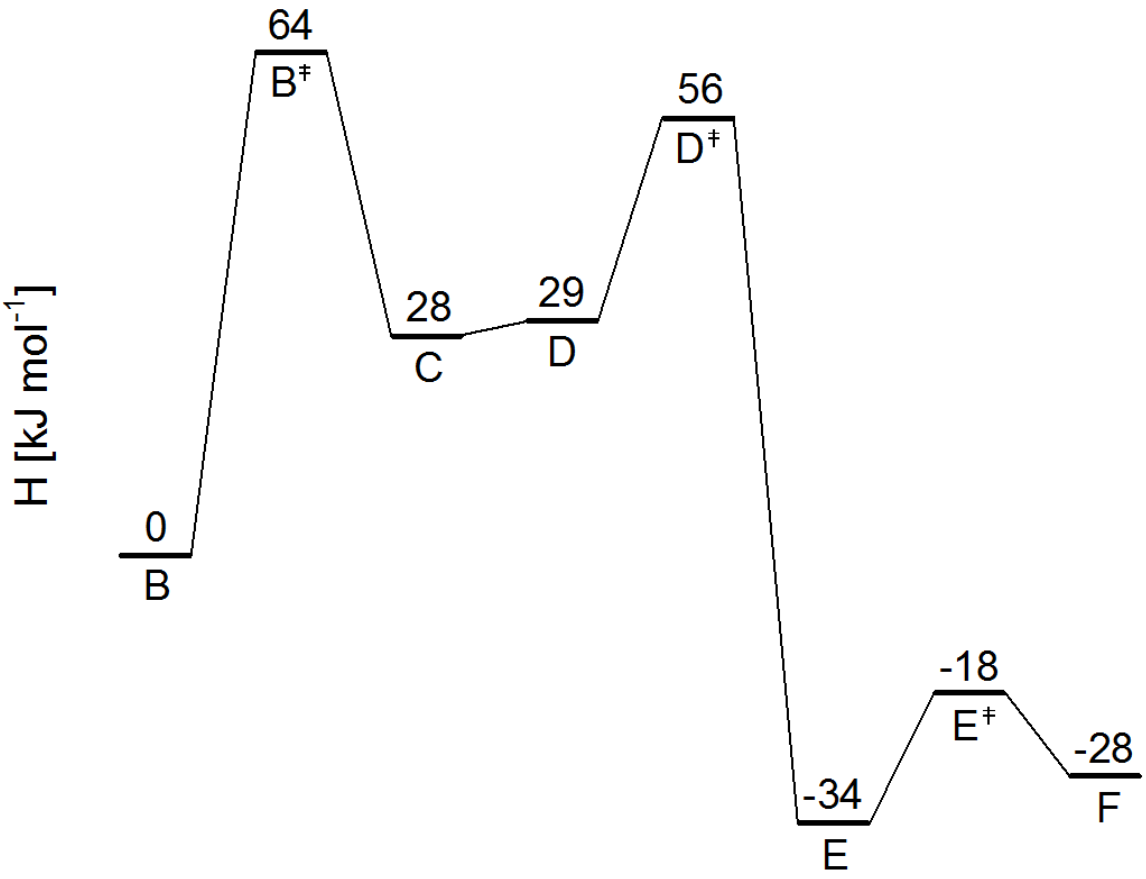

Figure 7.7 Enthalpy (353 K) diagram for aldol condensation over an isolated titanol (where R = H). The elementary steps are labeled according to the reaction mechanism shown in Scheme 7.2.

Table 7.3 Lewis acid and base properties of the isolated titanol monomer and the Ti dimer.

Species	Charge of Ti (au)	Proton Affinity (kJ mol^{-1})	$\Delta H^{\ddagger}$ (kJ mol^{-1})
Monomer	1.85	-835[a]	64
Dimer	1.86	-869[b]	120

[a] Proton affinity of the oxygen of the titanol group
[b] Proton affinity of the oxygen bridge in a Ti-O-Ti dimer

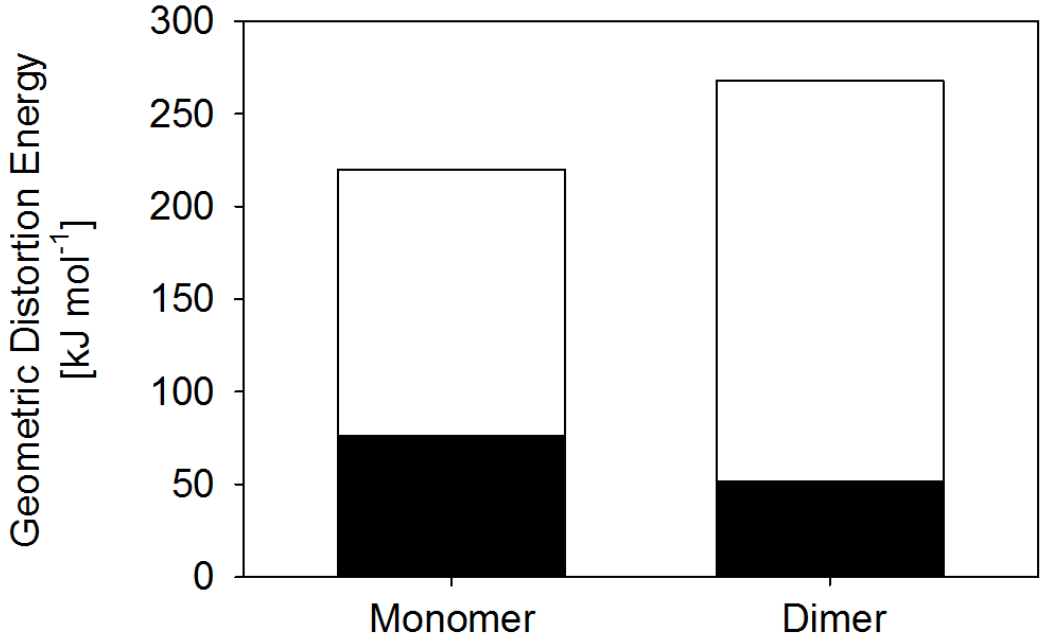

Figure 7.8 Energy decomposition analysis of enolate formation over isolated titanol monomer and dimer species.

7.4 Conclusions

The effects of Ti coordination environment and connectivity on the rate of *n*-butanal self-condensation were investigated over Ti-Si catalysts. The aldol condensation activity of the incorporated Ti atoms was found to decrease with increasing weight loading of Ti. Characterization of the catalysts containing Ti incorporated into the framework of mesoporous SBA-15 showed that at low Ti weight loadings, Ti is isolated and tetrahedrally coordinated while at high loadings, Ti is present in the form of hexacoordinately dispersed anatase. This result demonstrates that isolated Ti sites are more active than hexacoordinate sites because, as shown by *n*-butanal temperature programmed desorption, coordinatively saturated Ti sites bind the aldehyde less strongly.

The connectivity of tetrahedral Ti species was also found to have an effect on the rate of aldol condensation, Ti-O-Ti dimers being less active than isolated titanol species. The connectivity was altered by impregnating either Cp_2TiCl_2 or $Ti(O^iPr)_4$ precursors onto a silica support material. The former precursor tends to form isolated sites while the latter precursor leads to dinuclear Ti species. A decrease in activity was observed as the weight loading of Ti was increased for catalysts synthesized by using Cp_2TiCl_2 as the Ti precursor. This result suggests that dimers are formed by the condensation of neighboring titanols at high Ti loadings. The catalyst synthesized by grafting $Ti(O^iPr)_4$ onto SBA-15 is less active because such precursors readily form the less active dinuclear Ti species. It is also shown that isolation of Ti sites can be achieved by dehydroxylating the support in order to achieve a larger average spacing between silanol groups. Catalyst synthesized by impregnating $Ti(O^iPr)_4$ on dehydroxlated SiO_2 pretreated at 1023 K were

almost as active as the catalysts containing site-isolated Ti prepared using Cp_2TiCl_2, and exhibited the same activation energy.

Consistent with the observed kinetic isotope effect, theoretical analysis of the aldol mechanism over an isolated titanol group demonstrates that α-H abstraction from an adsorbed butanal is the rate-determining step. The rate expression derived from this mechanism is zero order in *n*-butanal concentration and only a function of the rate coefficient for the rate-determining step. The calculated activation barriers for enolate formation over isolated titanol and Ti dimer species are in excellent agreement with those determined from experiment and support the experimental finding that Ti-O-Ti sites, which have a much higher activation barrier for α-H abstraction, are less active than Ti-OH sites. Energy decomposition analysis of the enolate formation step shows that although the oxygen present on the Ti-O-Ti dimer is more basic than the oxygen of the Ti monomer, there is a large energetic penalty for the substrate to distort over the Ti-O-Ti dimer. The oxygen of the titanol is less rigid and is therefore able to bend more easily to abstract the α-H and form the enolate.

7.5 Acknowledgements

This work was supported by the XC^2 program funded by BP. The authors would like to thank the Prof. T. Don Tilley for providing TS-1 and Eric Bloch for his assistance in performing TGA.

7.6 Supporting Information

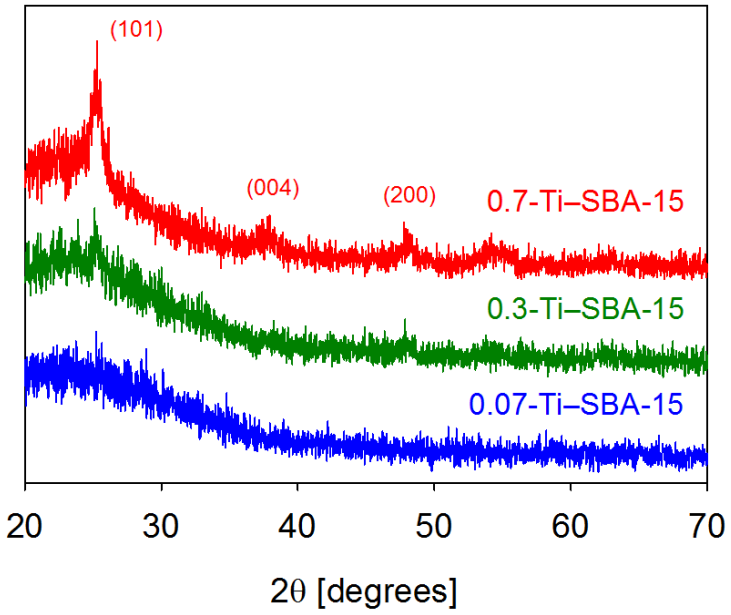

Figure S7.1 XRD of x-Ti—SBA-15 catalysts obtained with a Siemens D5000 diffractometer using Cu Kα radiation. Data were collected in the range 20° < 2θ < 70° with a step size of 0.02°.

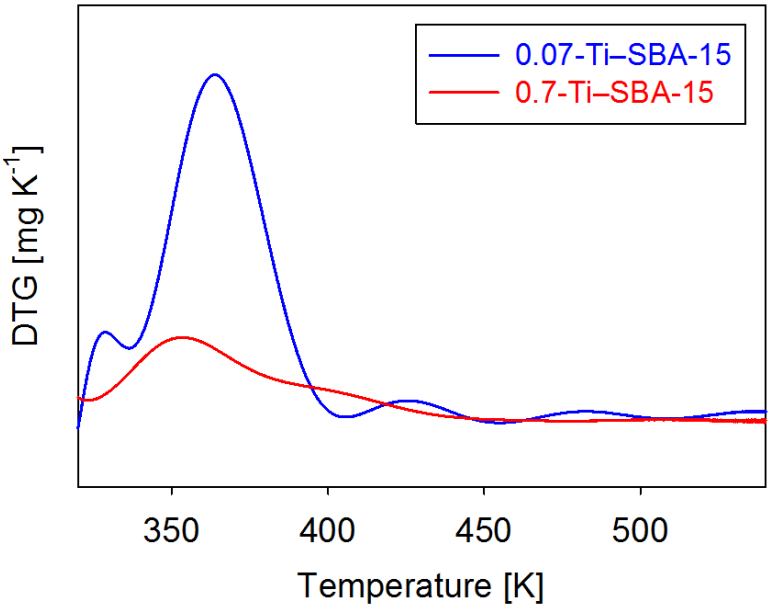

Figure S7.2 TGA of *n*-butanal soaked 0.07 and 0.7-Ti—SBA-15 catalysts obtained with a TA Instruments TGA 5000 instrument. Spectra are normalized by total weight of

catalyst. Samples were held in a platinum pan under nitrogen atmosphere and heated at 2 K min^{-1}.

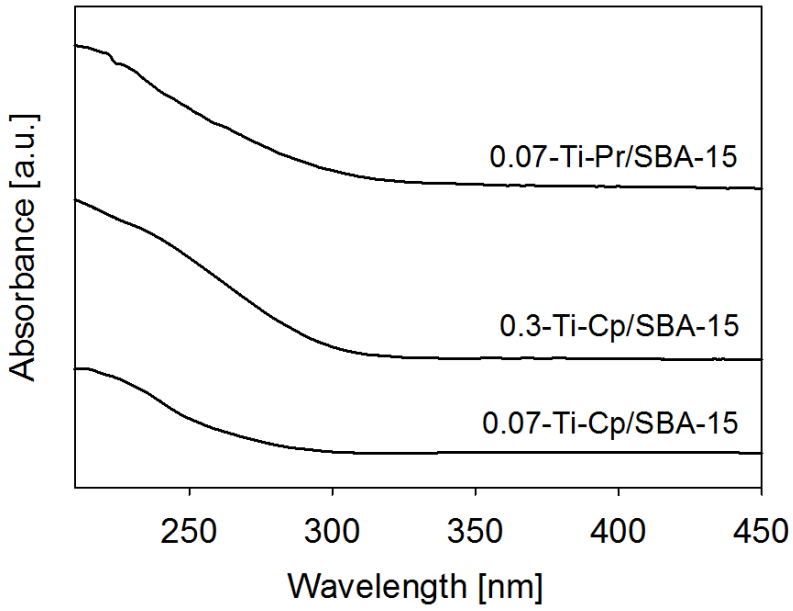

Figure S7.3 UV-Vis Spectra of 0.07-Ti-Cp/SBA-15, 0.3-Ti-Cp/SBA-15, 0.07-Ti-Pr/SBA-15 catalysts.

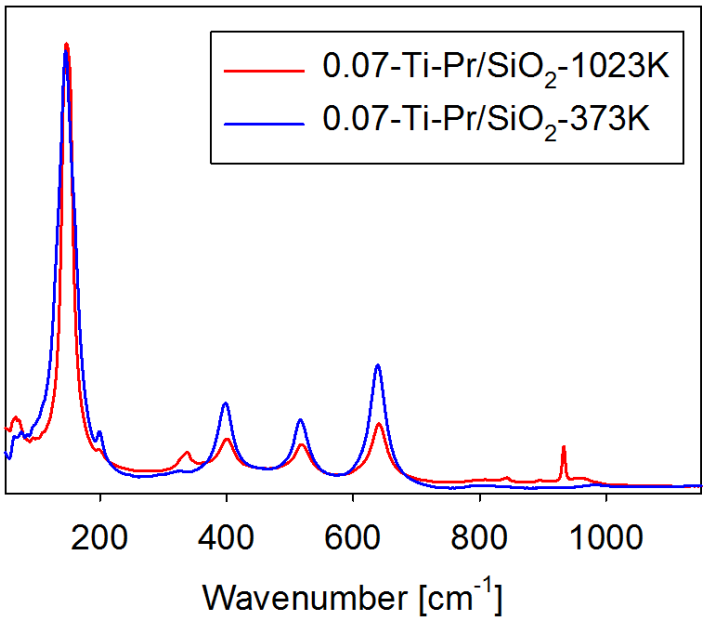

Figure S7.4 Raman Spectra of 0.07-Ti-Pr/SiO_2-373K and 0.07-Ti-Pr/SiO_2-1023K catalysts.

7.7 References

[1] J. A. Kent. in: *Handbook of Industrial Chemistry and Biotechnology, 12th ed.,* Springer, New York, **2012**.

[2] B. J. Arena, J. S. Holmgren. *Direct Conversion of butyraldehyde to 2-ethylhexanol-1*. US5258558 A, **1992**.

[3] A. A. Kiss, A. C. Dimian, G. Rothenberg. *Adv. Synth. Catal.* **2006**, 348, 75-81.

[4] G. Knothe, A. C. Matheaus, T. W. Ryan III. *Fuel* **2003,** 82, 971-975.

[5] K. Tanabe. *J. Chin. Chem. Soc.* **1998**, 45, 597-602.

[6] K. Tanabe, T. Yamaguchi. *Catal. Today* **1994**, 20, 185-198.

[7] S. Shylesh, W. R. Thiel. *ChemCatChem* **2011**, 3, 278-287.

[8] E. Iglesia, D. G. Barton, J. A. Biscardi, M. J. L. Gines, S. L. Soled. *Catal. Today* **1997**, 38, 339-360.

[9] B. Noziere, A. Cordova. *J. Phys. Chem. A* **2008**, 112, 2827-2837.

[10] J. E. Rekoske, M. A. Barteau. *Ind. Eng. Chem. Res.* **2011**, 50, 41-51.

[11] M. Singh, N. Zhou, D. K. Paul, K. J. Klabunde. *J. Catal.* **2008**, 260, 371-379.

[12] H. Idriss, M. A. Barteau. *Catal. Lett.* **1996**, 40, 147-153.

[13] H. Idriss, K. S. Kim, M. A. Barteau. *J. Catal.* **1993**, 139, 119-133.

[14] M. Kruk, L. Cao. *Langmuir* **2007**, 23, 7247-7254.

[15] S. D. Kellys, D. Hesterberg, B. Ravel. in: *Soil Science Society of America,* Madison, WI, **2008**.

[16] R. E. Jentoft, S. E. Deutsch, B. C. Gates. *Rev. Sci. Instrum.* **1996**, 67, 2111-2112.

[17] B. Ravel, M. Newville. *J. Synchrotron Rad.* **2005**, 12, 537-541.

[18] M. Newville. *J. Synchrotron Rad.* **2001**, 8, 96-100.

[19] J. D. Chai, M. Head-Gordon. *Phys. Chem. Chem. Phys.* **2008**, 10, 6615-6620.

[20] J. D. Chai, M. Head-Gordon. *J. Chem. Phys.* **2008**, 128, 084106-084115.

[21] S. Grimme. *Chem. Eur. J.* **2012**, 18, 9955-9964.

[22] Y. Shao, et al. *Phys. Chem. Chem. Phys.* **2006**, 8, 3172-3191.

[23] J. P. Foster, F. Weinhold. *J. Am. Chem. Soc.* **1980**, 102, 7211-7218.

[24] A. Behn, P. M. Zimmerman, A. T. Bell, M. Head-Gordon. *J. Chem. Phys.* **2011**, 135, 224108.

[25] F. Farges, G. E. Brown Jr., J. J. Rehr. *Phys. Rev. B* **1997**, 56, 1809-1819.

[26] J. S. Hwang, J. S. Chang, S. E. Park, K. Ikeue, M. Anpo. *Top. Catal.* **2005**, 35, 311-319.

[27] J. Jarupatrakorn, T. D. Tilley. *J. Am. Chem. Soc.* **2002**, 124, 8380-8388.

[28] G. Li, X. S. Zhao. *Ind. Eng. Chem. Res.* **2006**, 45, 3569-3573.

[29] T. Blasco, A. Corma, M. T. Navarro, J. Perez Pariente. *J. Catal.* **1995**, 156, 65-74.

[30] G. Petrini, A. Cesana, G. De Alberti, F. Genoni, G. Leofanti, M. Padovan, G. Paparatto, P. Roffia. *Stud. Surf. Sci. Catal.* **1991**, 68, 761-766.

[31] A. Fernandez, J. Leyrer, A. R. Gonzalez-Elipe, G. Munuera, H. Knozinger. *J. Catal.* **1988**, 112, 489-494.

[32] Z. Luan, L. Kevan. *J. Phys. Chem. B* **1997**, 101, 2020-2027.

[33] Z. Laun, E. M. Maes, P. A. W. van der Heide, D. Zhao, R. S. Czernuszewicz, L. Kevan. *Chem. Matt.* **1999**, 11, 3680-3686.

[34] G. Deo, A. M. Turek, I. E. Wachs, D. R. C. Huybrechts, P. A. Jacobs. *Zeolites* **1993**, 13, 365-373.

[35] J. Yan, G. Wu, N. Guan, L. Li, Z. Li, X. Cao. *Phys. Chem. Chem. Phys.* **2013**, 15, 10987-10988.

[36] H. Liu, X. Wang, C. Pan, K. M. Liew. *J. Phys. Chem. C* **2012**, 116, 8044-8053.

[37] G. Calleja, R. van Grieken, R. Garcia, J. A. Melero, J. Iglesias. *J. Mol. Catal. A* **2002**, 182-183, 215-225.

[38] P. E. Sinclair, G. Sankar, C. R. A. Catlow. *J. Phys. Chem. B* **1997**, 101, 4232-4237.

[39] A. Omar Bouh, G. L. Rice, S. L. Scott. *J. Am. Chem. Soc.* **1999**, 121, 7201-7210.

[40] K. B. Sharpless, S. S. Woodard, M. G. Fin. *Pure & Appl. Chem.* **1983**, 55, 1823-1836.

[41] S. Shylesh, D. G. Hanna, S. Werner, A. T. Bell. *ACS Catal.* **2012**, 2, 487-493.

[42] J. McMurry. in: *Organic Chemistry,* Thomson Learning, Pacific Grove, **2004,** 859-860.

[43] "Acetaldehyde." NIST. http://webbook.nist.gov/cgi/cbook.cgi?ID=C75070&Units=SI&Mask=8#Thermo-React (accessed March 17, 2014).

[44] "Butanal." NIST. http://webbook.nist.gov/cgi/cbook.cgi?ID=C123728&Units=SI&Mask=8#Thermo-React (accessed March 17, 2014).